Minimum Design Requirements for Insulated Concrete Form Wall Systems

Ray Yu

A thesis

submitted in partial fulfillment of the

requirements for the degree of

Master of Science in Civil Engineering

University of Washington

2021

Reading Committee:

Dr. Dawn Lehman, Co-Chair

Dr. Laura Lowes, Co-Chair

Dr. Paolo Calvi

Dr. Scott Campbell, NRMCA, External Member

Program Authorized to Offer Degree:

Civil & Environmental Engineering

University of Washington

Abstract

Minimum Design Requirements for Insulated Concrete Form Systems

Ray Yu

Co-Chairs of the Supervisory Committee:
Professor Dawn Lehman
Professor Laura Lowes
Civil & Environmental Engineering

Insulated concrete form (ICF) walls are used in low- to mid- rise construction and are cost-competitive with wood and masonry walls. In addition, these wall systems meet increasingly strict insulation requirements in building codes and therefore have the potential to be more cost-effective than wood construction. There is one drawback, however, and that is that their minimum reinforcing requirements are determined by ACI 318-19, including maximum spacing limits and minimum reinforcement ratios. These reinforcement requirements exceed what is required to meet strength demands. As such, there is a need to investigate the required spacing and amount of reinforcement. In addition, there is an interest in using steel fibers to replace some of the wall reinforcement. Previous studies have not investigated these design parameters.

This research project utilized non-linear finite element modeling (FEM) to investigate the impact of reducing minimum steel requirements as well as the use of steel fiber in planar walls. The FEM was based on prior work and validated using in-plane and out-of-plane tests. The wall models were subjected to monotonically increasing shear in the out-of-plane direction and a constant, distributed axial load at the top of the wall. The reference wall geometry was selected to meet a

single bay of a one-story structure as well as future test specimens. Using the validated modeling approach and reference geometry, a parametric study was conducted to investigate the impact of the following design parameters on the structural response of the wall: (1) bar spacing, (2) number of curtains of steel, as well as (3) steel fiber dosage in conjunction with the first two variables. The research findings are as follows: (1) the peak strength of the wall is determined by the tensile capacity of the plain or fiber-reinforced concrete (FRC), (2) the bar spacing and the number of curtains of steel only impact the residual strength increase after cracking, and (3) it appears possible to use FRC with starter bars for some walls as this concrete provides shear, moment and axial capacity and the starter bars transfers the forces to the foundation. The findings suggest more economical bar layouts for ICF walls are possible without compromising the structural response.

TABLE OF CONTENTS

LIST OF FIGURES

LIST OF TABLES

ACKNOWLEDGEMENTS

The funding for this research was provided by the National Ready Mix Concrete Association.

I would like to thank my professors, Dawn Lehman and Laura Lowes for their advice and guidance over the last two years. I also would like to thank Scott Campbell for providing insight on ICF construction.

I am grateful for Nikki Lewis and Muzi Zhao for their help and patience in aiding in my understanding of LS-DYNA. I would like to thank my friends and roommates for their encouragement and support throughout the entire pandemic and the few months before the pandemic.

Lastly, I would like to thank my parents for all their support throughout my entire life. I am truly blessed to have them by my side.

Chapter 1. INTRODUCTION

Insulated concrete form (ICF) walls are used in low- and mid-rise construction. Reinforced concrete structural walls possess high strength and stiffness, allowing for resistance to low-to-moderate seismic demands. However, this wall system must meet ACI code minimum requirements for bar spacings and reinforcement ratios despite structural analysis predicting lower requirements. ACI limits the spacing to 18 in. whereas masonry allows a spacing up to 48 in.

Although there has been substantial research on the in-plane response of walls, there is a limited amount of research done on the out-of-plane response of RC walls, and almost none examining the impact of the minimum reinforcement requirements. Roller (1996) states that it "appears that existing code provisions for minimum quantities of reinforcing steel are based solely on engineering judgment and have no apparent technical basis." The goal of this research is to determine and quantify whether the ACI requirements for reinforcing steel are overly restrictive in the design of minimally reinforced concrete walls loaded in the out-of-plane direction.

This study used commercial software program LS-DYNA for finite element models. Zhao et al. (2021) showed that LS-DYNA can capture stiffness, strength, and deformation capacity for reinforced columns well. In addition, LS-DYNA has a concrete damage plastic model which has a bilinear tensile softening model which can be used to model reinforced and fiber reinforced concrete after cracking. The finite element model was developed and calibrated by simulating the results of three in-plane loaded wall specimens and four out-of-plane loaded specimens. This validated model was used to conduct a parameter study on splice vs continuous reinforcement, bar spacings, number of curtains of steel, the presence of bond-slip equation, and steel fiber content. The results provide design implications that would reduce the cost of an ICF wall system.
The primary objectives of this research are:

- To develop a high-resolution finite element model to predict stiffness, strength, and deformation capacity of wall test specimens.
- To conduct a parameter study on walls with varying longitudinal bar spacings, the number of curtains of steel, the use of a bond-slip equation, and varying steel fiber contents.

- To provide new design recommendations for spacing of reinforcement in ICF walls that can aid in reducing the cost of ICF wall construction.

This research was conducted in two phases: (1) model development and validation and (2) parameter study of reinforced and FRC walls subjected to out-of-plane loading.

Chapter 2 details the modeling approach and validation of the finite element (FE) model. A discussion of the constitutive material models, model layout, mesh scheme, and loading protocol are given. This modeling approach was used to model an experimental data set of 3 in-plane loaded walls and 4 out-of-plane loaded walls. An analysis was conducted between the measured and simulated response and damage pattern and progression to determine the accuracy of the modeling approach.

Chapter 3 details the parameter study conducted on reinforced concrete specimens. The geometry and material properties of the reference wall were selected from discussion with practicing engineers. The varying parameters were longitudinal bar spacing, the number of curtains of steel, and the presence of a bond-slip equation. The load-displacement response, tensile damage pattern, and steel stresses and strains were investigated.

Chapter 4 details the parameter study conducted on fiber reinforced concrete specimens. The same reference wall geometry from Chapter 3 was used. The varying parameters were longitudinal bar spacing, number of curtains of steel, and varying steel fiber contents. One aspect of this study that is unique is the fiber dosages; where most studies use volumes of 1.5% or above, this study included lower volumes of 0.5 and 1.0% to enhance constructability as others have noted constructability issues with higher dosages. For each parameter, the load-displacement response, tensile-damage pattern, and steel stresses and strains were investigated.

Chapter 5 summarizes all the presented research. Key conclusions and recommendations for future work for modeling and physical testing are presented to improve the design procedures of ICF walls in low-seismic regions.

Chapter 2. MODELLING APPROACH AND VALIDATION

This chapter presents the finite element modeling approach used to simulate the nonlinear response of the concrete walls considered in this study: lightly reinforced concrete walls constructed using a traditional concrete mix, lightly reinforced concrete walls constructed using steel fiber reinforced concrete, and concrete walls constructed using steel fiber reinforced concrete (FRC) without reinforcing bars. The LS-DYNA software (LSTC, 2006) was used for all simulations. This software has multiple features that make it ideally suited to the current project and has been shown to accurately simulate the stiffness, strength, and deformation capacity of reinforced concrete components exhibiting multiple failure models (Zhao et al. 2021).

A primary feature that makes the software well suited for the current project is the three-dimensional concrete constitutive model, concrete damage plasticity model (CDPM), also referred to as MAT273 that simulates strength loss due to crushing and cracking and employs the crushing and fracture energies with a mesh-dependent length to minimizes the mesh-dependency of the simulation results. This concrete model was adapted to simulate the response of FRC walls, by adjusting the fracture energy and shape of the post-peak stress-strain tension response using the results of Woo et al. (2014) and Markalikova et al. (2020).

In addition to the concrete model, LS-DYNA provides unique features for modeling reinforcing steel; specifically reinforcing can be modeled using beam-type elements to enable simulation of buckling under compressive loading as well as yielding under tension loading, though buckling was not a significant response mode for the current study. Additionally, reinforcing steel elements can be embedded in concrete solid elements using a contact surface model calibrated to represent the bond stress versus slip behavior in the direction parallel to the bar axis. Finally, the LS-DYNA software employs a dynamic explicit solution algorithm that enables a simulation to progress through phases of the response history that include significant stiffness and strength loss, which for reinforced concrete walls results from concrete crushing, concrete cracking, bond strength loss, and/or steel yielding as well as load reversal.

Sections 2.1 – 2.7 provide a detailed presentation of the modeling approach used to investigate the behavior of lightly reinforced and fiber-reinforced walls as well as validation of this modeling approach. Section 2.1 presents the finite element meshes used for the simulations and boundary conditions including imposed displacement histories. Section 2.2 presents the concrete, reinforcing steel, and bond material models. Section 2.3 presents previous research done on LS-DYNA using the CDPM material model. Section 2.4 presents the in-plane reinforced concrete wall validation. Section 2.5 presents the out-of-plane reinforced concrete wall validation. Section 2.6 presents the calibration of the concrete constitutive model to simulate the response of fiber-reinforced concrete with low fiber volumes. Section 2.7 presents the validation of the fiber-reinforced concrete model for FRC components.

2.1 Finite Element Mesh and Boundary Conditions

There are limited studies on the out-of-plane behavior of RC walls; thus, data from concrete wall models subjected to in-plane lateral loading were used also to validate the model. Figures 2.1 and 2.2 show the two models used to validate the nonlinear finite element modeling approach via comparison of simulated and measured responses. Figure 2.1 shows the finite element mesh used to simulate the response of a reinforced concrete wall subjected to constant axial loading and in-plane lateral loading; simulated lateral loading was applied via monotonically increasing displacement demand while laboratory lateral loading was applied via a cyclic displacement history. Figure 2.3 shows the finite element mesh used to simulate the response of reinforced concrete walls/slabs subjected to out-of-plane loading via monotonically increasing out-of-plane displacement demand.

2.1.1. FE Meshes

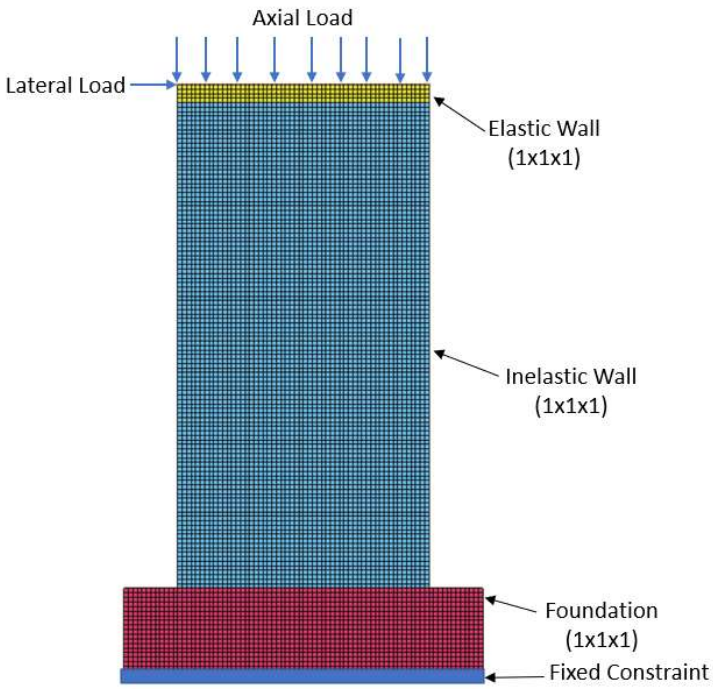

Figure 2.1.[1] Finite element mesh and boundary conditions for simulation of walls subjected to in-plane axial and lateral loading

[1] Note that individual element sizes are provided in inches, i.e. (1x1x1) indicates and solid element that is 1 in. x 1 in. x 1 in.

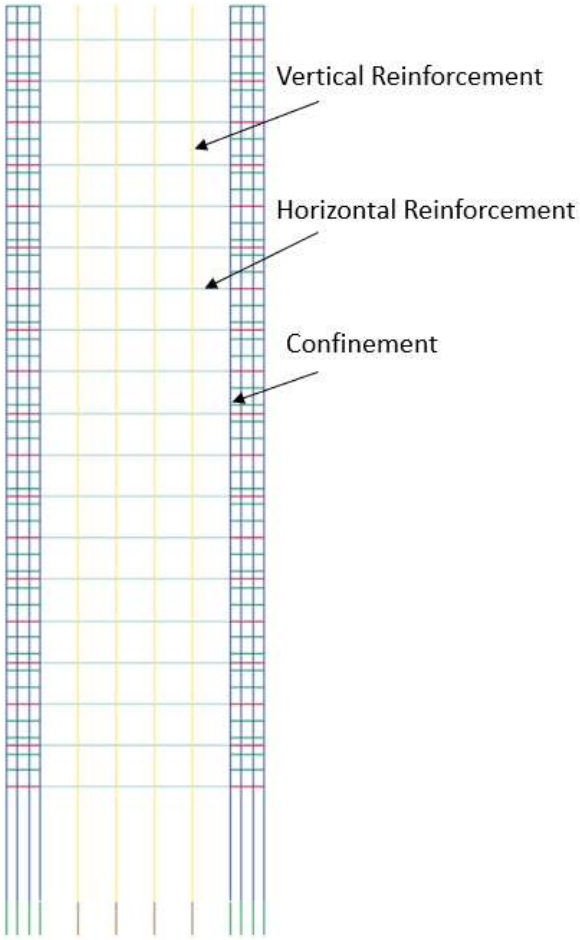

Figure 2.2. Reinforcement Layout for In-plane loaded walls

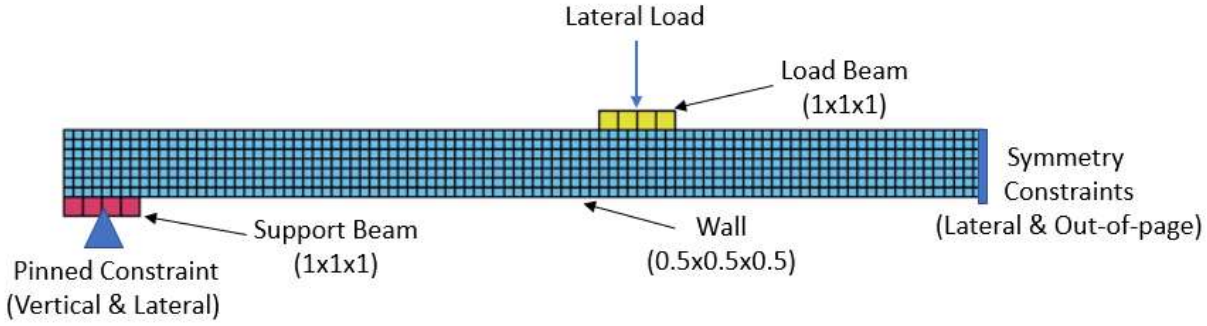

Figure 2.3. Finite element mesh and boundary conditions for simulation of walls subjected to monotonic out-of-plane lateral loading

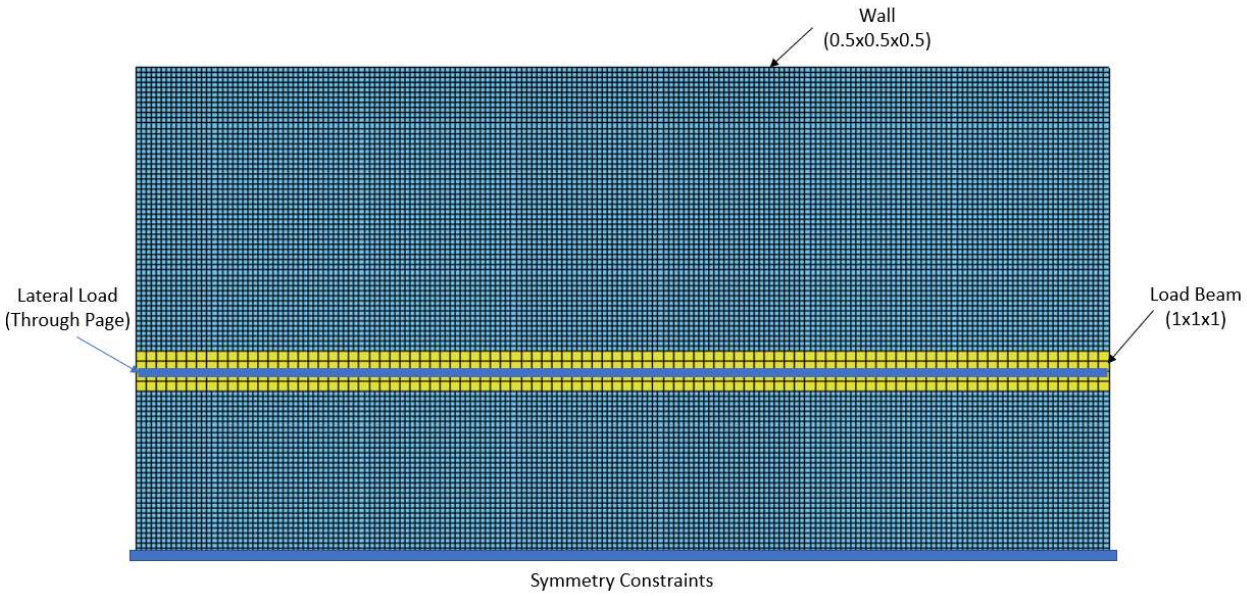

Figure 2.4. In-plane view of finite element mesh and boundary conditions for simulation of walls subjected to monotonic out-of-plane lateral loading.

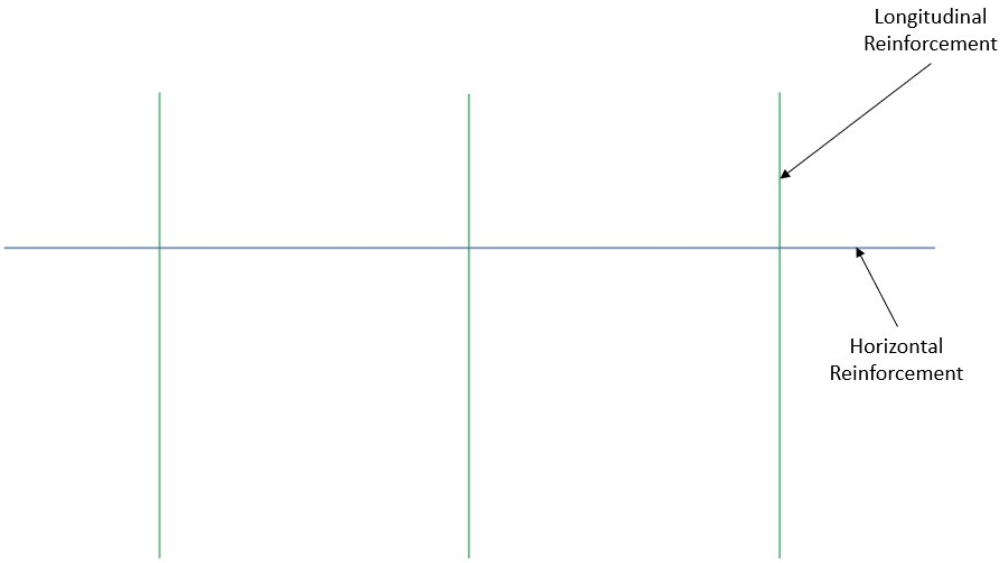

Figure 2.5. Reinforcement Layout for out-of-plane loaded walls

In all of the models, finite element meshes comprised solid concrete elements and steel beam elements embedded in the solid concrete elements via a contact surface model calibrated to

represent concrete-steel bond-slip behavior, as shown in Figures 2.2 and 3.5. The steel beam embedded is the same for non-confined and confined reinforcement. The concrete material response was defined to be inelastic in most of the model, but elastic at locations where loads were applied, or reactions developed; in all cases, the elastic response was observed in the laboratory at these locations (Table 2.1). Solid concrete elements were 8-node solid elements representing a constant stain field and employing a reduced integration scheme to prevent element locking with 1 quadrature point and with Flanagan-Belytschko stiffness form hour-glass control. The hourglass control coefficient was set to 0.03 to prevent hour-glassing modes and limit stiffening. Beam elements were Hughes-Liu beam elements with 2 nodes and with cross-section integration.

Concrete solid element dimensions were chosen to provide a sufficient number of elements to represented variation in stress-strain fields that could be expected to determine response (Figure 2.1 and 2.3). A mesh refinement study for out-of-plane loaded walls was conducted to determine adequate mesh size. The mesh refinement study results are given in Figure 2.6. From the mesh refinement study, a mesh size of 0.5 in. by 0.5 in. adequately represented the stress and strain fields associated with the out-of-plane flexural loading. The 0.25 in. by 0.25 in. mesh provided adequate results but sacrificed efficiency as it was longer to run.

For the wall loaded in the in-plane direction (Figure 2.1), solid concrete elements measured 1 in. by 1 in by 1 in.; this element size resulted in 4-6 elements along the in-plane length of the compression zone, 6-8 elements along the in-plane length of the boundary element, and 4-6 elements through the thickness of the wall, where response varied due to confined and unconfined concrete. Solid concrete elements throughout the remainder of the model were also 1 in. by 1 in. by 1 in.

For the wall loaded in the out-of-plane direction (Figure 2.3), solid concrete elements measured 0.5 in. by 0.5 in. by 0.5 in.; this element size resulted in 7-13 elements along the out-of-plane thickness (vertical direction in Figure 2.3), 144 -192 elements along the length (through the page in Figure 2.3), and 90 elements along the height (lateral direction in Figure 2.3).

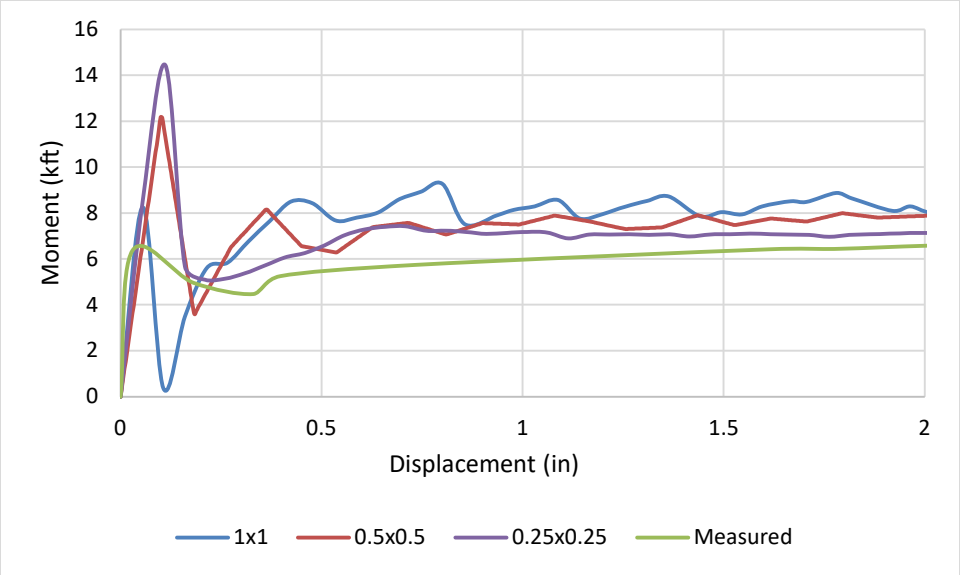

Figure 2.6. Mesh Refinement Study of out-of-plane loaded walls

Table 2.1. Wall properties for RC wall validation

Material Type	Element Type	Region (Model Type)	Mesh Size (inches)
Elastic (MAT 001)	Constant Stress Solid Element (ELFORM 1)	Elastic Top Region (In-Plane)	1x1x1
		Support Beam (Out-of-Plane)	1x1x1
		Load Beam (Out-of-Plane)	1x1x1
Concrete Damage Plasticity (MAT 273)	Constant Stress Solid Element (ELFORM 1)	Inelastic Wall Region (In-Plane)	1x1x1
		Foundation (In-Plane)	1x1x1
		Wall (Out-of-Plane)	0.5x0.5x0.5
Plastic-Kinematic (MAT 003)	Hughes-Liu Beam (ELFORM 1)	Steel Beam Elements (In-Plane and Out-of-Plane)	1.5

The steel reinforcement was embedded into the concrete elements by the LS-DYNA command CONSTRAINED_BEAM_IN_SOLID. The steel elements were modeled as beam elements with a bilinear stress-strain model. The steel elements are 2 node elements with linear moment distribution and constant axial distribution. LS-DYNA restricts beam element sizes less than 1 unit length when conducting LS-DYNA model checking. Due to this constraint, 1.5 in. length elements

were used for beam elements to ensure model stability. LS-DYNA determines the nodal displacements for embedded elements based on the nodal displacements of nearby master (material in which the steel is embedded) element nodes. The embedded element mesh is not required to line up with the master element mesh.

For walls loaded in-plane, the bond was modeled for the longitudinal reinforcement in the foundation and inelastic wall regions. Within the foundation, the bottom two elements (3.0 in.) of each vertical reinforcing bar model were modeled as perfectly bonded to the concrete to provide a fixed anchorage. This anchorage was provided to ensure that no slippage occurred in the foundation for stresses to develop along the height of the reinforcing bars. For the walls loaded in the out-of-plane direction, the bond model was used to connect all reinforcement to wall concrete.

The bond was modeled by creating an axial coupling force function of the bond-slip and then implementing that to the beam embedded in solid. The bond only has slip along the length of the bar and has no relative movement between the concrete and steel perpendicular to the bar. There was a significant difference in the behavior of the wall models when the bond model was applied in the longitudinal reinforcement. However, when comparing models with the bond model applied to the transverse reinforcement, there was a negligible difference in wall behavior. The longitudinal reinforcement provides strength in flexure, whereas the transverse reinforcement provides strength in shear. Since the models simulated exhibited primarily flexural behavior, the bond model was only used for the longitudinal reinforcement.

The wall subjected to in-plane loading was subjected to a constant axial load applied via load control at the top of the wall and a monotonically increasing lateral displacement demand applied via displacement control. The bottom of the foundation was fixed in all three directions and rotations and the top of the wall was fixed in the out-of-plane direction; these boundary conditions were considered to represent the boundary conditions in the laboratory. For these walls, the computational demand of the simulations could have been reduced by exploiting the plane of symmetry located at the interior of the wall; however, the simulations were not sufficiently computationally demanding to warrant this.

For the out-of-plane wall/slabs symmetry was exploited and the fem model comprised only half of the wall/slab and the symmetric boundary condition; Figure 2.3 shows the location of symmetric boundary conditions as well as the loading beam and reaction support. To represent laboratory loading, a line load was applied at the center of the loading beam via displacement control. The support beam had a line of elements (out of plane direction in Figure 2.3) fixed in the vertical and out-of-plane direction. The symmetric boundary was fixed in the lateral direction and had one point fixed in the out-of-plane direction to account for symmetry.

2.2 MATERIAL MODELS

2.2.1 *Concrete Material Model*

The modeling employs the concrete damage-plastic model originally developed by Grassl et al. (2006) and incorporated into LS-DYNA as CDPM and MAT273 model name in LS-DYNA. This model characterizes concrete stress-strain response under cyclic loading including strength loss due to crushing, cracking, and crack-surface slip. The model combines an effective stress-based plasticity model with a strain-based damage model and employs different damage parameters for compression and tension.

Compression response is simulated using a continuum plastic-damage model. The response is nonlinear elastic to peak followed by strength loss, accumulation of plastic deformation, which manifests as non-zero strain following unloading to zero stress, and accumulation of damage, which manifests as a reduced unloading stiffness. Parameters defining concrete compressive response are

- Concrete compressive strength, f'_c
- Concrete elastic modulus E_c, defined per ACI 318-19 as $E = 57{,}000\sqrt{f'_c}$ per ACI 318-19, with E and f'_c in (psi)
- Compressive strain softening behavior coefficient, which is the intersection between the tangential line of the compressive strain softening curve and the x-axis, defined per Zhao et al. (2021) recommendations, $E_{fc} = 0.0025$

Figures 2.7 and 2.8 show the behavior of the concrete model in compression.

The tensile response is simulated using a continuum damage model. Material response is elastic to tensile strength followed by strength and stiffness loss. Like the compressive model, the loss in stiffness is characterized by a tensile damage parameter that progresses from zero damage and unloading stiffness equal to the elastic modulus to complete damage with essentially zero stiffness. Parameters defining tensile response are

- Concrete tensile strength f_t defined per ACI 318-19 as, $f_t = 7.5\sqrt{f'_c}$ (psi) per ACI 318-19
- Concrete fracture energy (Figure 2.9), G_f, define per *fib Model Code* as $G_f = \frac{73 f_c^{0.18}}{145}$ (f'c in Mpa, result in psi)
- Hardening parameters per LS-DYNA default
- Bilinear tensile softening curve with the following equations

$$w_f = 4.444 \frac{G_f}{f_t}$$

$$w_{f1} = 0.15 w_f$$

$$f_{t1} = 0.3 f_t$$

- ECC (Eccentricity Parameter), which controls the shape of the deviatoric shape, with the following equations:

$$ECC = \frac{1+\varepsilon}{2-\varepsilon} \quad \varepsilon = \frac{f_{t(f_{bc}{}^2 - f'_c{}^2)}}{f_{bc}(f_c{}^2 - f_t{}^2)} \quad f_{bc} = 1.16 f'_c$$

LS Dyna supports multiple post-peak envelopes; for this study, the bilinear envelop was chosen. Figure 2.9 shows the behavior of the concrete model in tension.

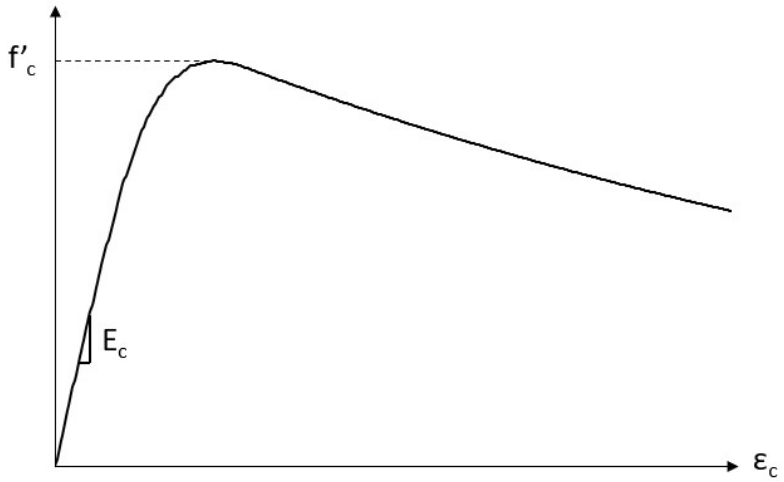

Figure 2.7. CDPM concrete compressive response

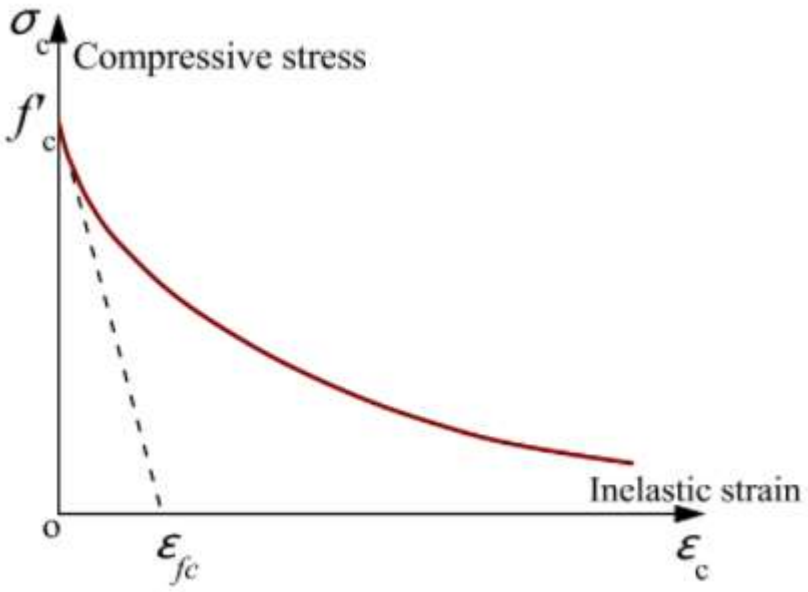

Figure 2.8. CDPM compressive softening curve

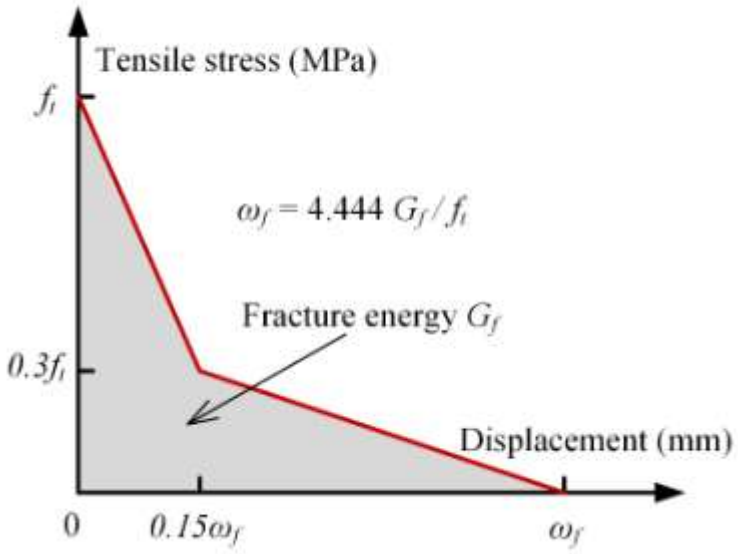

Figure 2.9. CDPM bilinear tensile softening curve

2.2.2 *Reinforcing Steel*

The reinforcing steel was modeled using a one-dimensional plasticity model with kinematic hardening. Es is defined as 29,000 ksi. Ep was defined as the slope between the point of yielding

and the point of ultimate strength in the experiments. Kinematic hardening was used since the yield surface of the steel reinforcement will only translate and not increase in size during the simulation. Figure 2.10 shows the idealized stress-strain relationship for this material model.

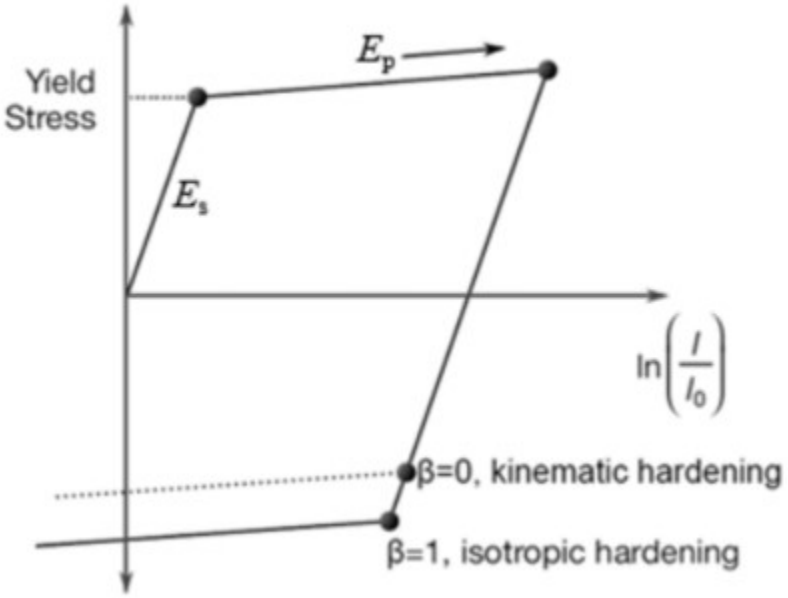

Figure 2.10. Reinforcing Steel material model

2.2.3 *Bond-Slip Model*

The bond-slip model developed by Murcia-Delso et al (2011) and the LS-DYNA implementation of this model by Zhao et al. (2021) were used to model load transfer, parallel to the bar axis, between concrete and embedded reinforcing steel. Perfect load transfer is assumed in the direction perpendicular to the bar axis.

Figure 2.11 shows the envelope of the bar-slip model developed by Mucia-Delso (2011). This envelope was developed using data from pull-out tests employing a single reinforcing bar embedded in a concrete cylinder $15d_b$ long by 3 ft in diameter. Bar sizes used in the tests were 35, 43, and 57 mm, but the model was extrapolated to simulate the response of bars ranging in size from 16 to 57 mm (No. 5 to No. 18).

Parameters required to calibrate the model for a specific bar size are:

- S_R, clear rib spacing of bar, $S_R = 0.5d_b$, where d_b is the diameter of the reinforcing bar

- τ_{max}, maximum bond strength, $\tau_{max} = 1.163 f'_c{}^{3/4}$ (in MPa), where f'c is the concrete compressive strength
- S_{peak}, the slip at τ_{max}, $S_{peak} = 0.07 d_b$

For most of the wall models in this thesis, #4 (13 mm) reinforcement was used. Due to the minimal size difference, the Murcia-Delso bond model was used for this research.

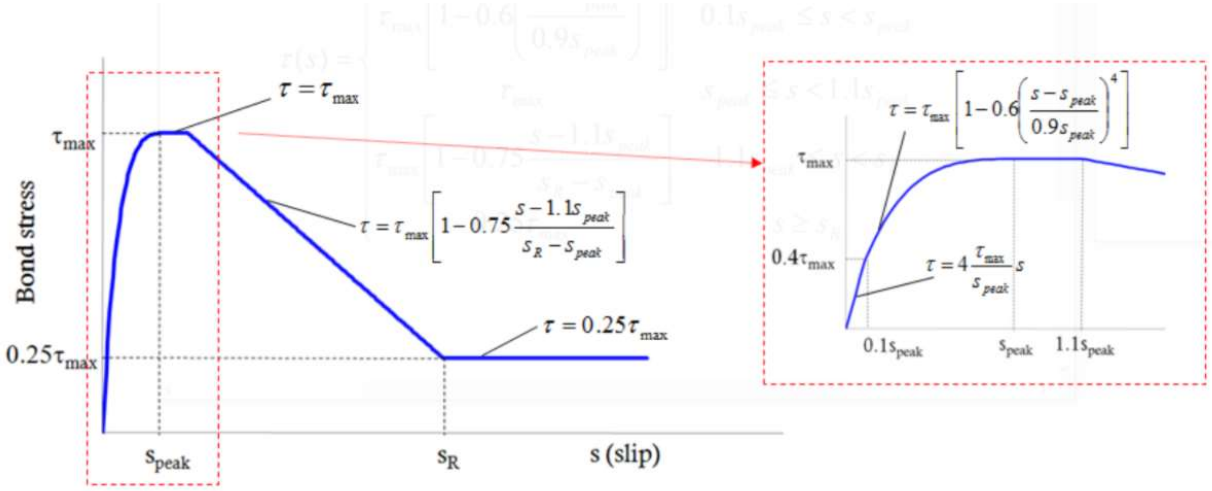

$$\tau(s) = \begin{cases} 4\dfrac{\tau_{\max}}{s_{peak}} s & s < 0.1 s_{peak} \\ \tau_{\max}\left[1 - 0.6\left(\dfrac{s - s_{peak}}{0.9 s_{peak}}\right)^4\right] & 0.1 s_{peak} \le s < s_{peak} \\ \tau_{\max} & s_{peak} \le s < 1.1 s_{peak} \\ \tau_{\max}\left[1 - 0.75\dfrac{s - 1.1 s_{peak}}{s_R - s_{peak}}\right] & 1.1 s_{peak} \le s < s_R \\ 0.25\tau_{\max} & s \ge s_R \end{cases}$$

Figure 2.11. Bond slip model and corresponding equations

Zhao et al. (2021) implemented this bond model by adding a function to the embedment of steel reinforcement into the concrete. This was done by creating a function characterized from Figure 2.11. This function was then applied to the beam in solid constraint in LS-DYNA to account for the bond-slip between the steel reinforcement and concrete elements.

The bond model was not used for all reinforcing bars and all locations. The bond model was not used for horizontal reinforcement because i) horizontal bar anchorage is accomplished primarily using physical mechanisms (i.e., hooks and 90-degree bends), ii) horizontal reinforcement slip has minimal impact global response, and iii) this reduces the computation demand of the simulations. The bond-slip model was also not used for the bottom two steel reinforcement elements in the foundation, to ensure steel anchorage within the foundation.

2.2.4 *Other Model Parameters*

For meshing schemes that have multiple mesh sizes between solid elements, a tied node to surface contact was used to tie the nodes from the smaller mesh to the larger mesh. This allows for the transfer of strains and stresses along the interface between the different meshes.

The steel reinforcement was embedded into the concrete by constrained beam in solid. This was done to ensure proper embedment of the steel into the concrete elements, as well as implementing the bond equation.

2.2.5 *Dynamic explicit solution algorithm*

For the models, a dynamic explicit solution algorithm was used. The dynamic explicit algorithm is a time-based simulation where a timestep dictates the intermediate steps to a solution and data is taken at each specified data point. The simulation obtains a solution at each timestep and then moves on to the next timestep without requiring convergence. This allows for faster runtime and more data points than implicit solutions. The minimum timestep is determined by LS-DYNA by the equations shown in Figure 2.12. The timestep used in the simulations is $0.9\Delta t_{min}$. The more allotted time to simulation, the smoother the simulation gets. This is due to longer simulations having more timesteps in between each data point, allowing for more precise calculations.

$$c_{3D-continuum} = \sqrt{\frac{E(1-\nu)}{(1+\nu)(1-2\nu)\rho}}$$ dilatational wave

E = Young's modul
ν = Poisson's ratio
ρ = specific mass density

Critical time step :

$$\triangle t_{min} = \frac{l}{c}$$

Figure 2.12. LS-DYNA formulation of minimum timestep

2.3 SIMULATIONS USING LS-DYNA CDPM

Zhao et al. (2021) simulated the concrete damage plasticity model in cyclic compression, cyclic tension, and tension-compression for RC columns and concrete-filled steel tubes (CSFT). The concrete-damage plasticity model in LS-DYNA produced results similar to the measured results. Peak strength and deformation capacity from the simulated results match the test results. Figure 2.13 shows the comparison of cyclic tension and compression models from Zhao et al. (2021) Figure 2.14 shows the LS-DYNA model developed from Zhao et al. (2021) and its comparison with a RC column test. Figures 2.15 and 2.16 show the LS-DYNA model developed by Zhao et al. (2021) and its comparison with CFST.

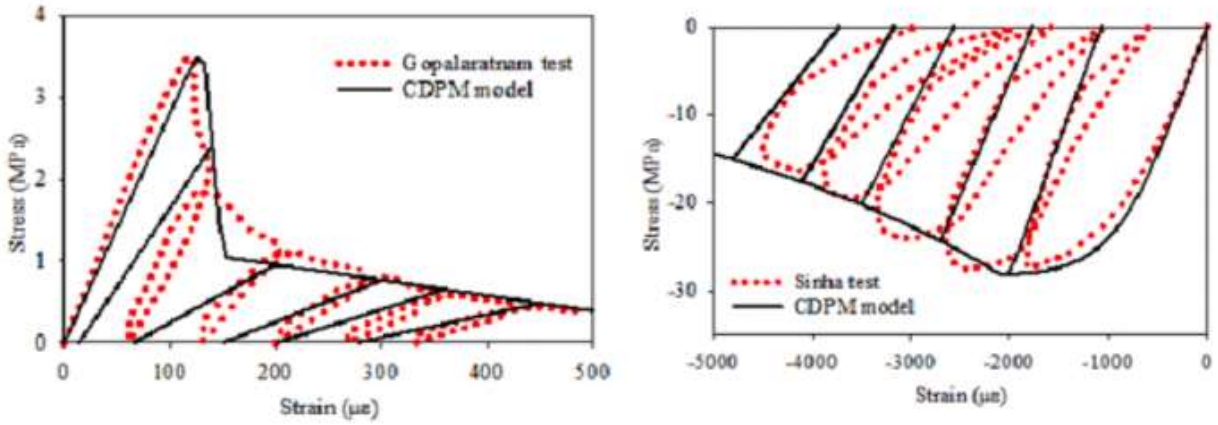

Figure 2.13. Cyclic compression and cyclic tension simulation comparisons from Zhao et al. (2021)

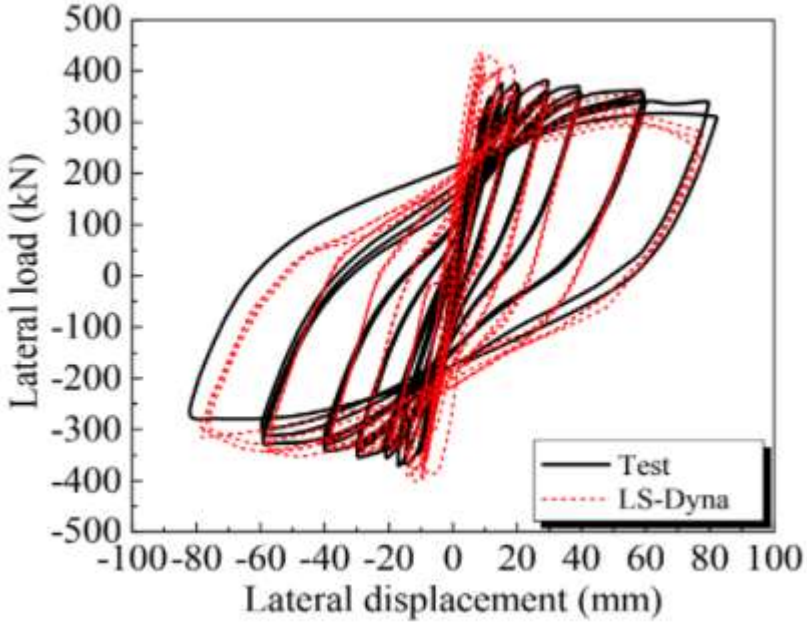

Figure 2.14. Comparison of simulated and measured response of RC Column from Zhao et al. (2021)

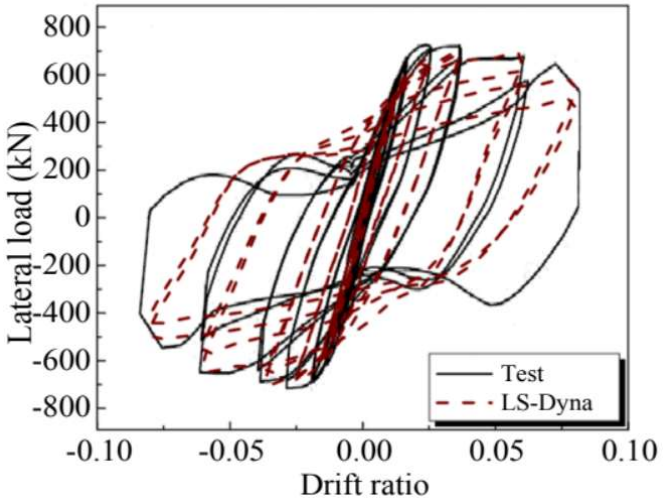

Figure 2.15. Comparison of simulated and measured response of CFST from Zhao et al. (2021) with Roeder Specimen III

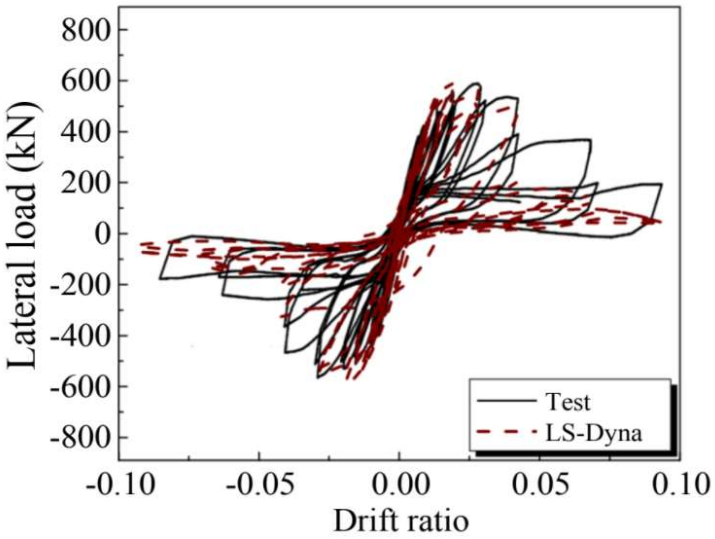

Figure 2.16. Comparison of simulated and measured response of CFST from Zhao et al. (2021) with Roeder Specimen II

2.4 IN-PLANE REINFORCED CONCRETE WALL VALIDATION

2.4.1 *Introduction*

Table 2.2 lists the *in-plane* laboratory tests of reinforced concrete walls used to validate the modeling approach. The test specimens in Table 2.2 were chosen due to the relatively low longitudinal reinforcement ratios in these walls; all test specimens in Table 2.2 were subjected to constant axial load and quasi-static cyclic lateral loading applied under displacement control. Specimen RW1 was tested by Thomsen and Wallace (2004). was designed and tested to investigate displacement-based design approaches. Specimen C1 tested by Lu et al. (2016) was designed to investigate the ductility of lightly reinforced walls subjected to reversed cyclic loading. Specimen CP1 tested by Sevilla et al. (2019) was designed to investigate the behavior of a lightly reinforced wall subjected to axial and cyclic lateral loading.

2.4.2 *Experimental Test Specimens*

Specimen RW1 (Thomsen and Wallace) is used commonly to calibrate and validate simulation methods. For the current study, the wall provides a lightly reinforced web region (ρ_l = 0.45%) as well as a high axial load ratio, (10%) both of which may be found in ICF construction. Wall C1 was modeled due to its uniformly distributed reinforcement and low reinforcement ratio (ρ_l = 0.5%). Wall CP1 has a low longitudinal reinforcement ratio and 14.3 in. spacing of longitudinal reinforcement (ρ_l = 0.37%).

Figure 2.17 provides the test set-up for specimen RW1. Figure 2.18 provides the test set-up for specimen C1. Figures 2.19 provide the test setup for specimen CP1.

Table 2.2. Wall specimens used for model validation

Specimen	Author	f'c (ksi)	h/l	Axial Load Ratio (constant) (%)	ρ_l (%)	Bar Spacing (in.)	Δ_u (%)
RW1	Thomsen et al. (2004)	4.00	3.10	10	1.13	7.5	2.26
C1	Lu et al. (2016)	5.58	2.00	3.5	0.53	8.9	2.50
CP1	Sevilla et al. (2019)	3.80	2.55	3.5	0.37	14.3	3.50

Note: Variables in the table: h is the height of the wall, l is the length of the wall, ρ_l is the longitudinal reinforcement ratio, and Δ_u is the drift at end of the test.

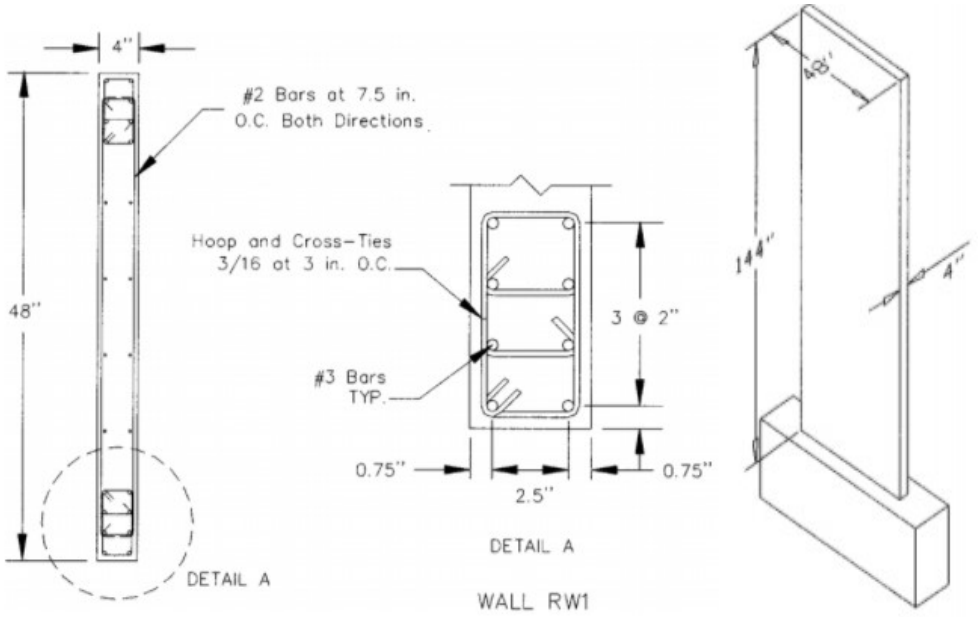

Figure 2.17. Wall layout of RW1

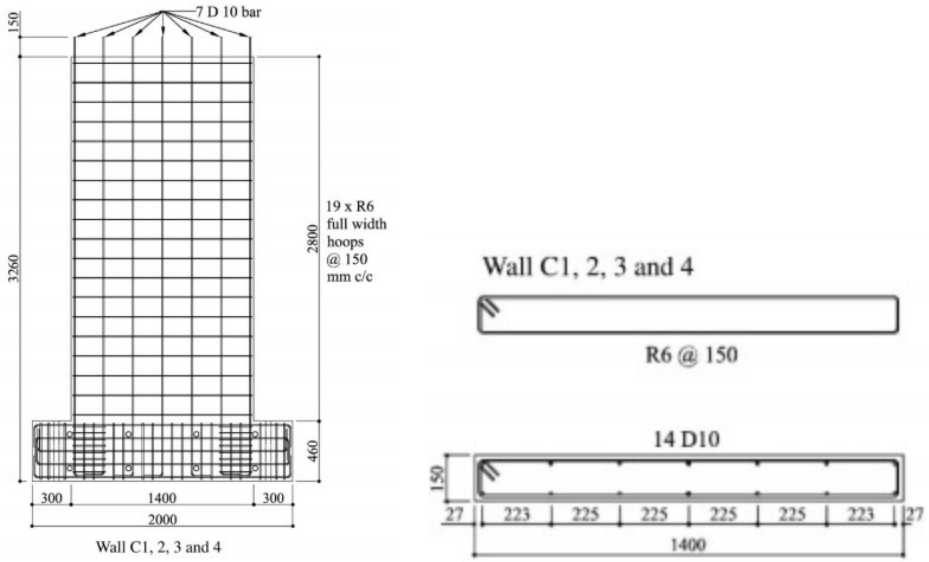

Figure 2.18. Wall layout of C1

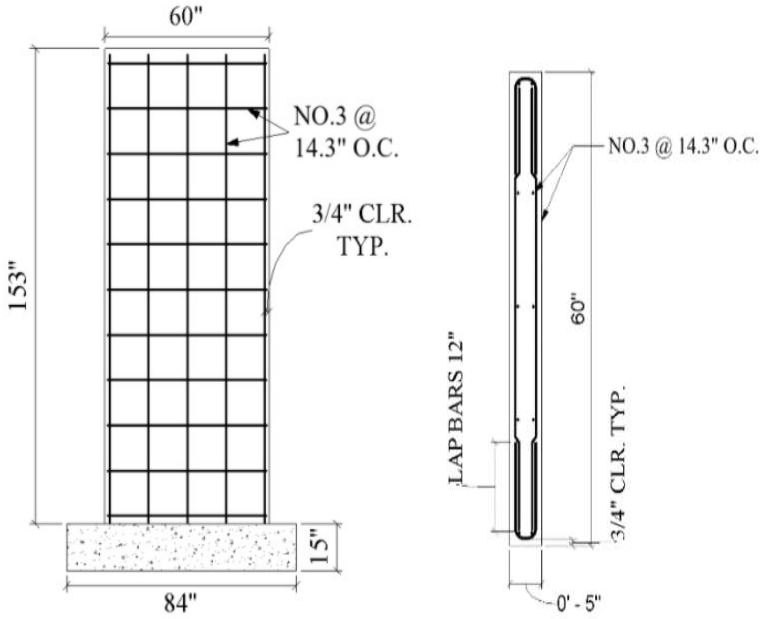

Figure 2.19. Wall layout of CP1

2.4.3 *Simulation Results*

Laboratory response history for the case of loading in the positive direction and the observed crack patterns at the end of the test for RW1 are provided in Figures 2.20 and 2.23. Figures 2.21 and 2.24 show the load-displacement and tensile damage comparisons for C1. Figures 2.22 and 2.25 compare simulated and measured load-displacement history and tensile damage patterns for CP1. Figures 2.20 -2.22 also show the simulated load-displacement history (blue) for the case of constant axial load and monotonically increasing displacement demand.

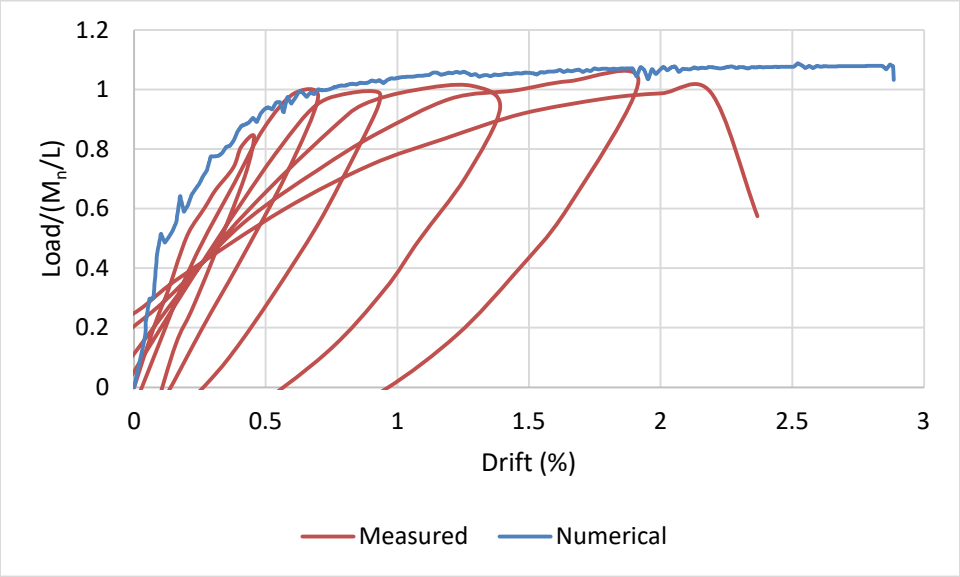

Figure 2.20. Load-drift history of RW1

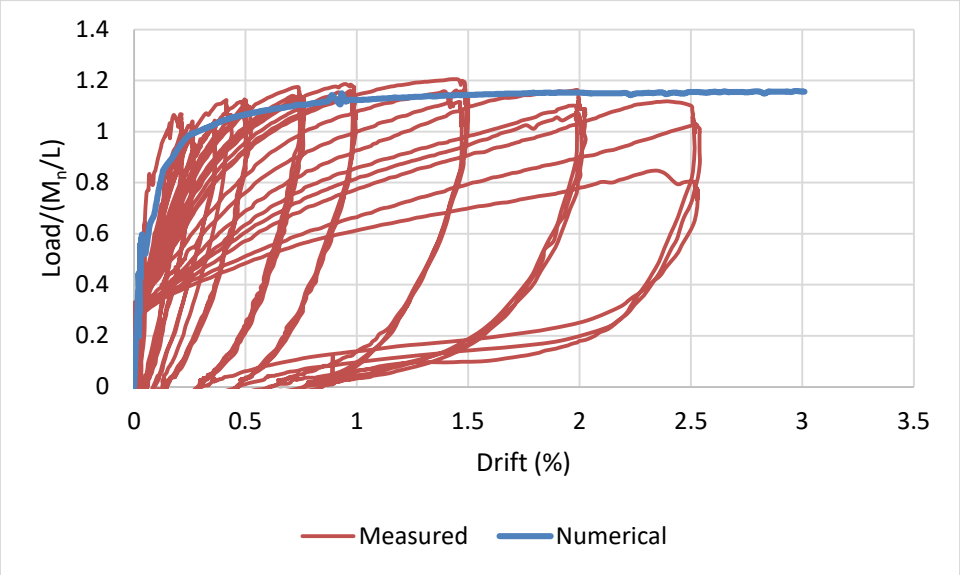

Figure 2.21. Load-drift history of C1

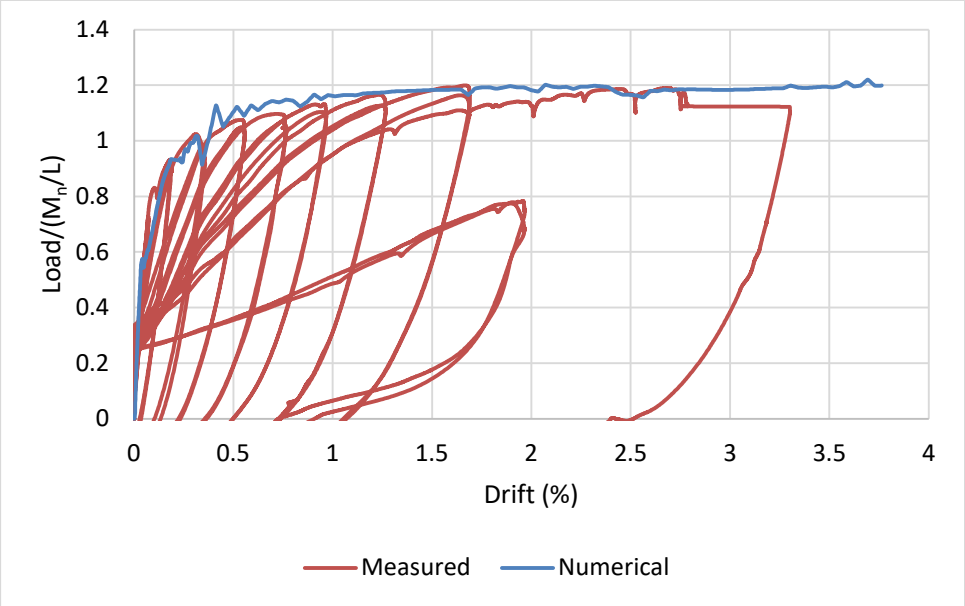

Figure 2.22. Load-drift history of CP1

Overall, there is good correlation between simulated and measured responses for all three models. The data in Figures 2.20-2.22 show that for Specimens RW1, C1, and CP1, initial stiffness is simulated well by the LS-DYNA model; the simulated strength is slightly lower than measured for Specimen C1, but simulated strength is similar for Specimens RW1 and CP1. Maximum strength and post-yield hardening are also simulated well. All three models sustain deformation capacities beyond what was sustained in the measured response because the model does not simulate the cyclic response of including bar fracture.

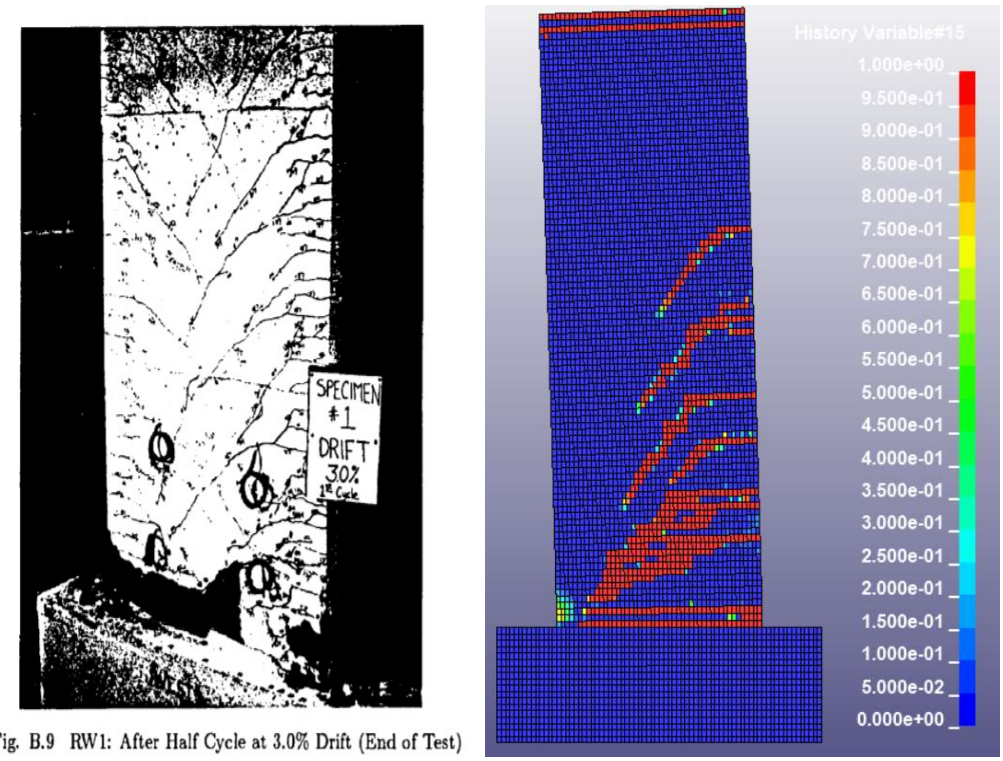

Fig. B.9 RW1: After Half Cycle at 3.0% Drift (End of Test)

Figure 2.23. Comparison of damage from RW1

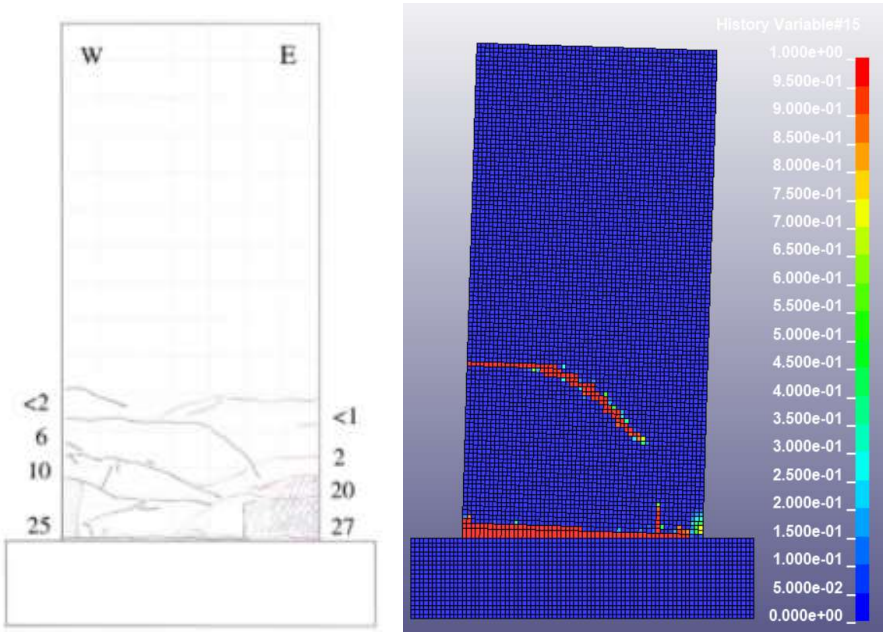

Figure 2.24. Comparison of damage from C1

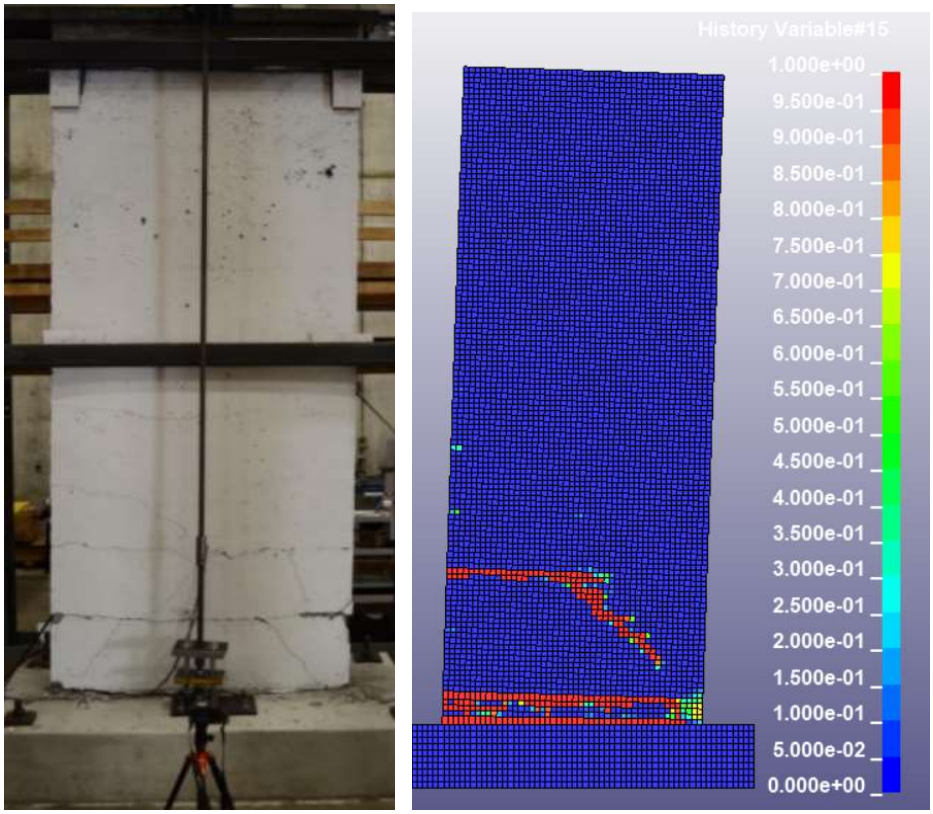

Figure 2.25. Comparison of damage from CP1

The simulated tensile damage histories are similar to the observed damage of the tests. RW1 does have more flexural cracking that occurs during the simulation. This could be due to RW1 being more slender than the other walls and having more reinforcement in the wall. This allows for higher moment demands along the height of the wall, which allows for more areas to achieve cracking stresses. Walls C1 and CP1 have damage at the wall-foundation interface and one flexural crack.

2.4.4 *In-Plane Model Validation Conclusions*

Overall, the models for in-plane loaded tests match the results. The load-displacement histories are similar and reach the same peak strengths, however, failure is not simulated in the models, as bar failure mechanisms were not modeled. The tensile damage histories see the flexural cracks that were seen in the laboratory setting. The LS-DYNA model accurately represents the behavior of the in-plane loaded tests.

2.5 OUT-OF-PLANE REINFORCED CONCRETE WALL VALIDATION

2.5.1 *Introduction*

The laboratory test program conducted by Roller (1996) was also used to validate the modeling approach for the current study. Roller tested four lightly reinforced concrete walls subjected to monotonically increasing out-of-plane plane loading to investigate the impact of bar spacing on wall behavior. Walls were subjected to out-of-plane loading via a four-point bending test with loading applied under displacement control without any axial load applied; walls were tested to large drifts and in some cases data includes loss of strength.

Roller did note potential issues with the test specimens. The issues are as follows:

- Horizontal rows of form ties used in walls created horizontal planes of weakness.
- "Less than ideal" concrete consolidation was noted in some specimens, compromising tensile strength. The specific tests that were compromised were not identified

2.5.2 *Experimental Test Specimens*

Table 2.3 provides material properties, configuration data, and provides measured, calculated, and simulated strengths, and measured and simulated drift capacity. Figure 2.27 shows wall configurations. Figure 2.26 shows the test set up in the laboratory.

Table 2.3. Wall specimens from Roller, 1996 for RC wall validation

Specimen	f'_c (ksi)	h/l^4	ρ_l (%)	Bar Spacing (in.)	Δ_{max} [3](%)	M_n [1] (k-ft)	M_{cr} [2] (k-ft)	M_{max} (k-ft)	$M_{residual}$ (k-ft)
R1	5.36	0.94	0.18	32	5.55	6.15	8.97	9.16	8.35
R2	5.36	0.94	0.12	24	5.00	4.76	11.7	12.2	8.40
R3	5.36	0.90	0.06	48	3.50	7.75	30.9	35.0	12.0
R4	5.36	1.25	0.01	36	5.55	6.52	16.6	17.9	10.7

Notes:

1. M_n is the nominal flexural strength calculated per ACI 318-19.
2. Mcr is the cracking strength calculated per ACI 318-19
3. Δ_{max} is the max displacement applied in the laboratory
4. h/l is the height to length ratio where the length is the cross-section length provided from the wall configuration (Figure 2.27) and the height is the dimension given from the test set-up (Figure 2.26)

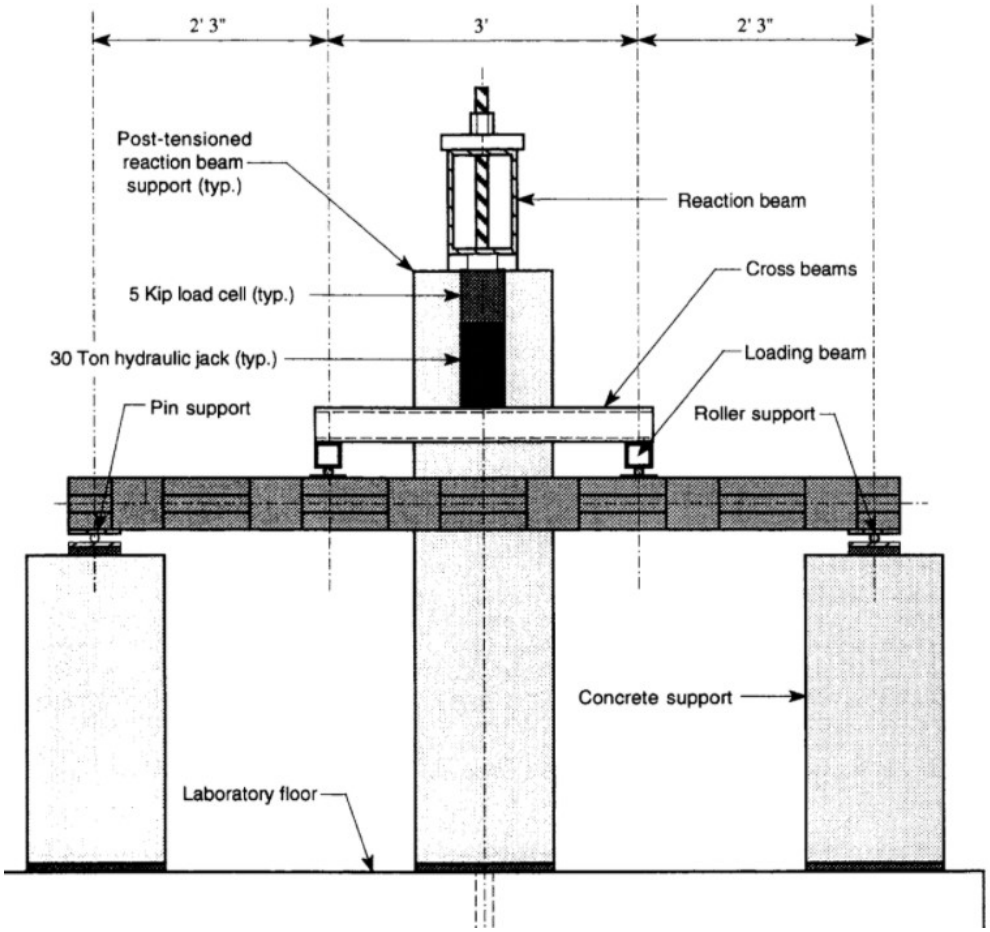

Figure 2.26. Roller, 1996 wall test set-up

Wall	ρ_l (%)	Wall Configuration
R1	0.18	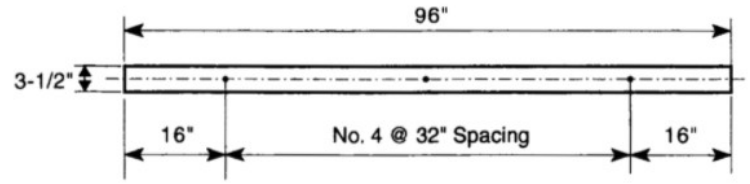
R2	0.12	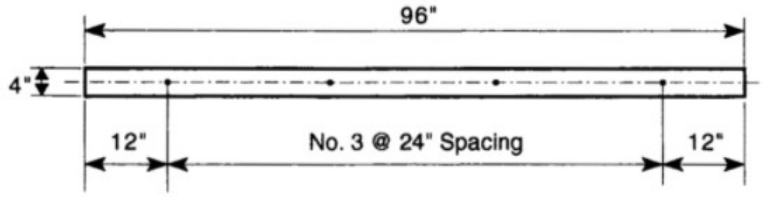
R3	0.06	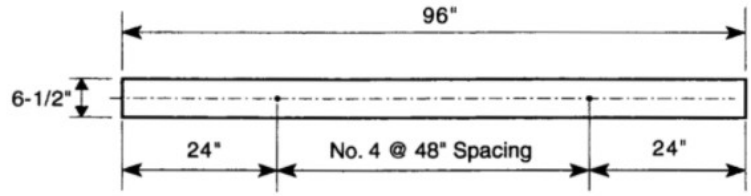
R4	0.10	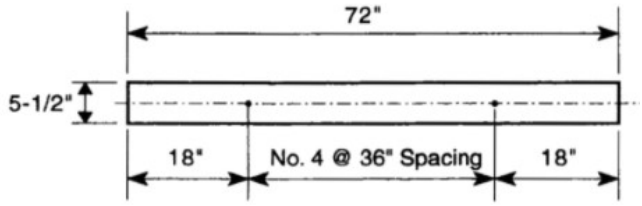

Figure 2.27. List of cross-sections for Roller walls

Note: Cross-Section shown is for out-of-plane dimension

2.5.3 *Simulation of Roller Walls R1-R4*

The Roller (1996) test program consists of four lightly reinforced concrete walls subjected to four-point bending, in the out-of-plane direction, with loading applied monotonically under displacement control to large displacement. Individual walls varied only in longitudinal reinforcement bar size and spacing. In the laboratory, walls exhibited distributed cracking within the constant moment region of the four-point bend test; laboratory instrumentation was limited to measurement of the applied load and deflection of the wall at mid-span. data maximum wall strength, post-peak wall strength and hardening, and capacity at drift demands in excess of 4%.

Figures 2.28 – 2.31 show measured and simulated responses for the tests. In the laboratory, test specimens exhibited essentially a linear-elastic response to peak strength followed by significant strength loss associated with distributed cracking in the constant moment region of the test

specimen; post-peak, residual strength was maintained to maximum displacement to test termination. Figure 2.32 shows the typical simulated tensile damage pattern. No compression damage was observed in the laboratory or the simulations. The overall general behavior of the walls is as follows:

- Simulated maximum strength achieved prior to concrete cracking, this strength is consistent with the cracking moment calculated using the tensile capacity of the concrete defined equal to 7.5*sqrt(fc) (see Table 2.3). Simulated strength is higher than the measured strength; this is possibly due to poor concrete consolidation during casting or to the rapid onset of strength loss that limited the researcher's abilities to accurately measure maximum strength in the laboratory Roller (1996).
- Simulation results show a large drop in strength after the formation of the first crack. This is due to the rapid loss of concrete tensile strength associated with concrete crack opening and crack propagation and to the low reinforcement ratio which results in only a modest increase in total steel tension force at large displacement demands associate with large crack width openings.
- A relatively stable residual post-cracking strength is achieved at a drift demand of approximately 0.75%, both in the laboratory tests and the simulations.

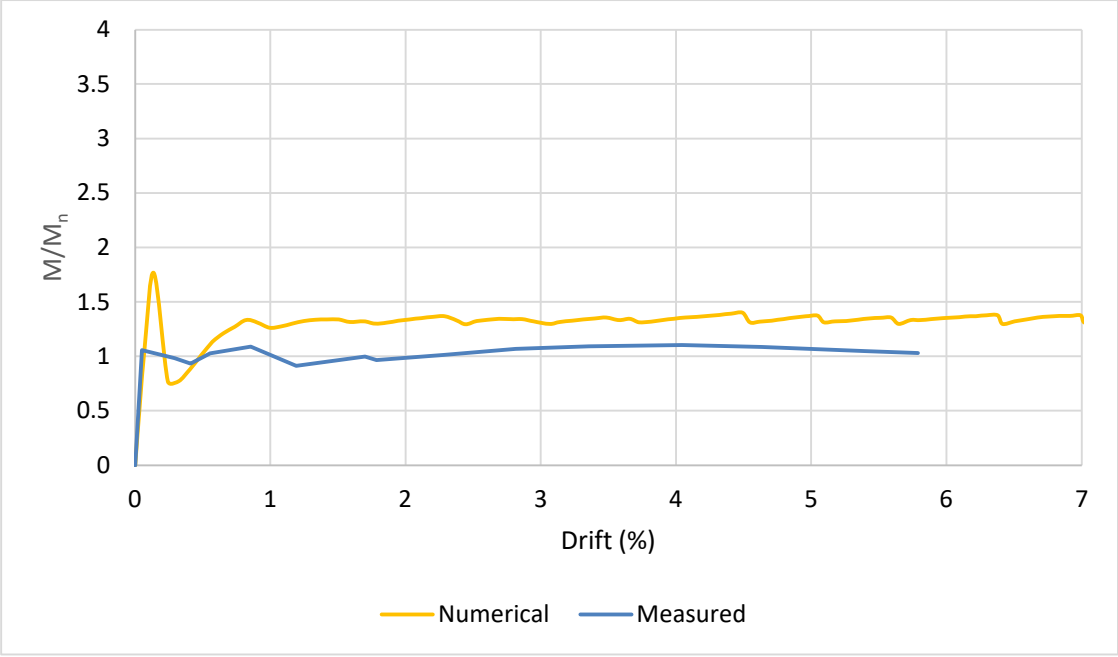

Figure 2.28. Load-drift history of R1

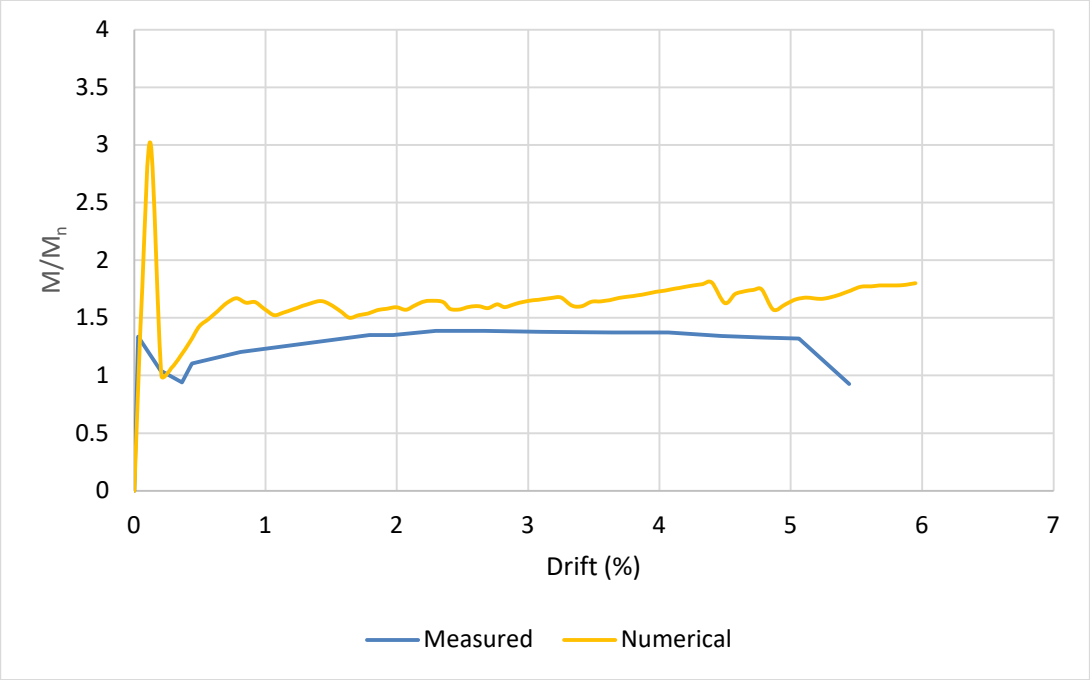

Figure 2.29. Load-drift history of R2

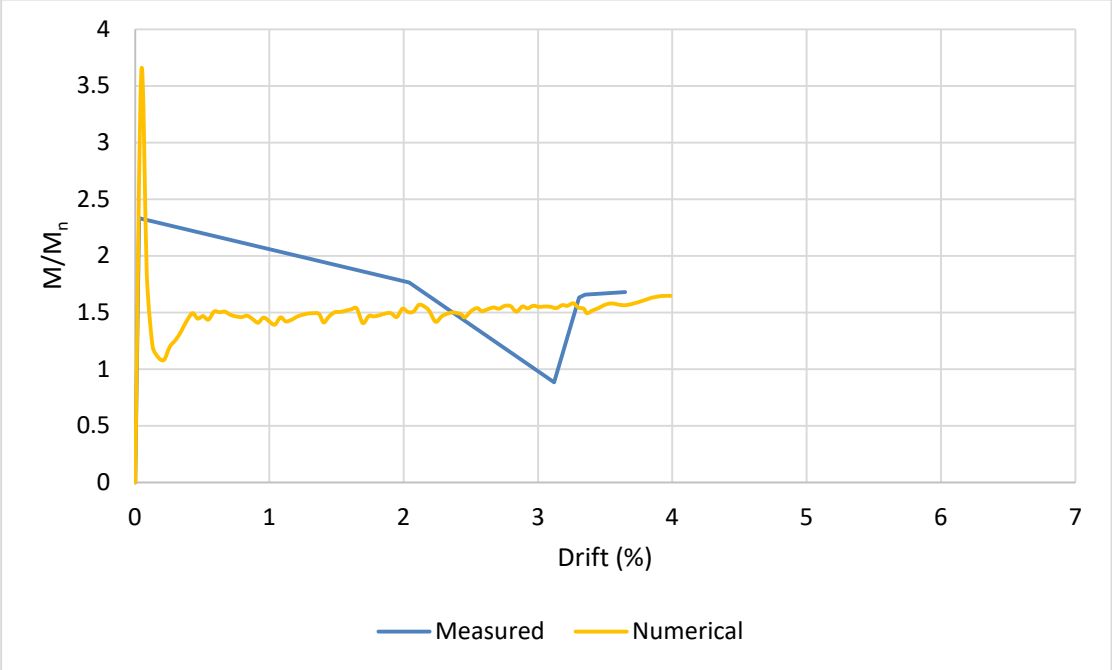

Figure 2.30. Load-drift history of R3

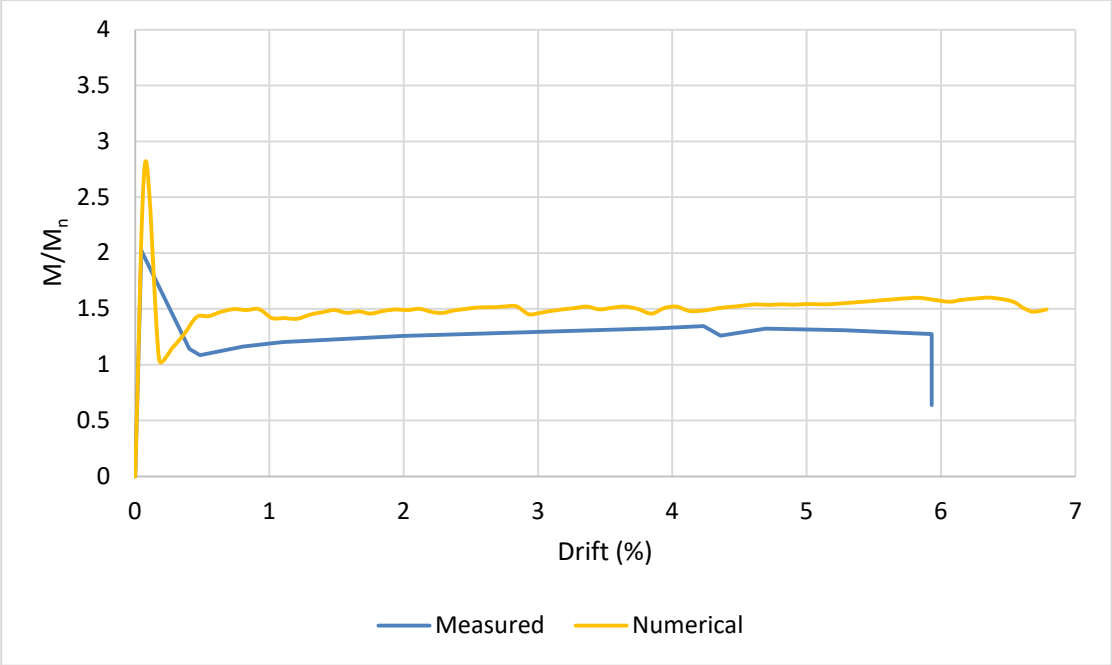

Figure 2.31. Load-drift history of R4

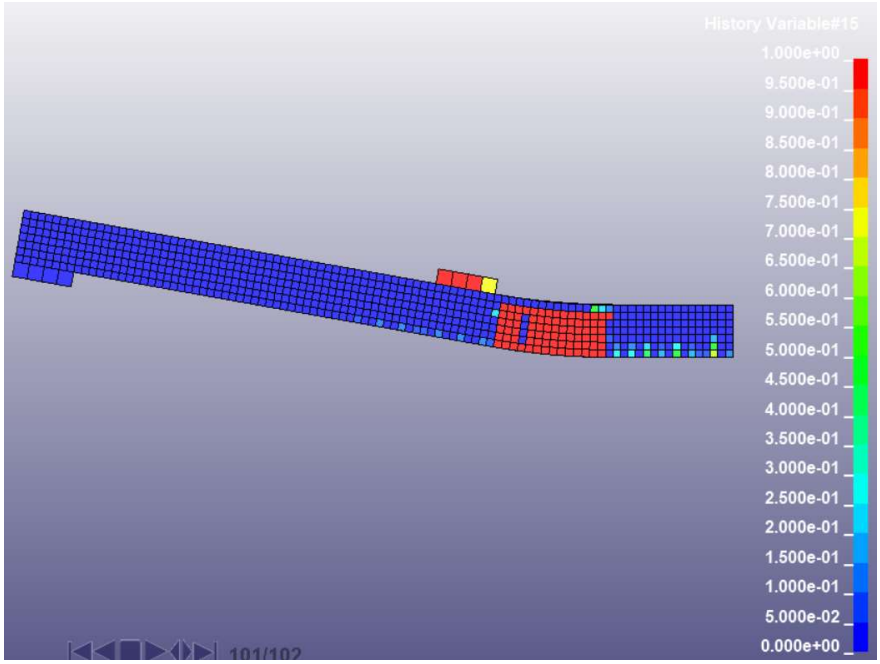

Figure 2.32. General tensile damage history for Roller walls

The following observations were made from the models:

- All the Roller wall simulations maintain their residual capacity post-cracking, suggesting that the out-of-plane loaded can maintain residual post-peak capacity when subjected to large deformation demands.

- The failure mechanisms of each wall were not captured. The simulated walls maintained strength past the failure seen in the measured results.
- All walls maintained at minimum $1.35M_n$ to larger displacement demands

From the results, reduced reinforcement requirements for ICF construction meet structural demands. The walls maintain strength post-cracking and achieve larger cracking strengths. A parametric study for this reduction in steel reinforcement will be discussed in Chapter 3.

2.5.4 *Model Validation Conclusions*

Overall, the LS-DYNA simulations matched the results of the measured tests well for out-of-plane walls. The initial stiffness and residual capacity to large deformations were well model and were similar to what was seen in the test. The out-of-plane models achieved higher peak strength than the measured tests. This could be due to the consolidation issues that were observed during the experiment. In addition, the post-peak capacity of the models was higher than measured results, but that too can be attributed to the consolidation issues of the tests. The tensile damage is concentrated at the constant moment region. The LS-DYNA model does not model the failure mechanism of out-of-plane walls since all models were able to maintain capacity past the point where failure occurred in the measured tests.

2.6 Fiber Reinforced Concrete Wall Model Definition

The data above show that lightly reinforced concrete walls exhibit significant strength loss at cracking. Fiber reinforced concrete with hooked steel fibers and low fiber content was investigated as means of reducing strength loss at cracking and increasing post-cracking strength in comparison with traditional concrete. Only hooked steel fibers were considered in this study, as hooked ends provide greater transfer across open cracks, and hooked steel fibers provide more hook strength and, thus, more gradual deterioration in tension strength once cracking occurs. Additionally, FRC with low fiber content, which is less expensive and more easily placed than FRC with high fiber content, offers the potential for walls without reinforcement and reduced overall wall cost as labor would not be required to place reinforcing steel for FRC only walls.

To date, limited research has addressed finite element modeling of components constructed using FRC and FRC with hooked steel fibers and low fiber content, in particular. This research uses the pre-existing concrete damage plasticity model presented in Section 2.2 and alters the post-peak tensile behavior curve to simulate the greater tensile strength and fracture energy provided by FRC.

2.6.1 *Introduction to FRC*

Previous research to investigate the behavior of fiber reinforced concrete has primarily employed three-point bending tests. Studies by Woo et al. (2014), Marcalikova et al. (2020), Vandewalle (2007), Kim and Bordelon (2016), and Kazemi et al. (2007) all suggest the use of fiber reinforced concrete increases the overall tensile strength and fracture energy of concrete, providing less rapid strength loss with increasing strain demands. The studies conducted were of notched beam tests with varying fiber content ratios of 0.5, 1.0, and 1.5% fiber content. Woo et al (2014). and Marcalikova et al. (2020) provide data characterizing tensile strength and fracture energy as a function of fiber content for hooked steel fibers; data from these studies were used to develop a method for calibrating the tension response curve for the CDPM material model to simulate the response of FRC.

2.6.2 *Modeling FRC Behavior for Simulation of Lightly Reinforced FRC Walls*

Simulation of walls constructed with FRC requires the definition of the material parameters used in the concrete damage plasticity model in LS-DYNA. Since the response of the FRC walls is controlled by the concrete tensile response, material parameters characterizing the tensile response were considered. The compressive response of FRC is assumed to have very little impact on model behavior, and the parameters remain the same as mentioned in Section 2.2.

Data from Woo et al. (2014), Marcalikova et al. (2020), Vandewalle (2007), Kim and Bordelon (2016), and Kazemi et al. (2007) were considered in characterizing the tensile response of FRC for simulations. Ultimately, data from Woo et al. (2014) and Maracalikova et al. (2020) were used for this research. Woo et al. (2014) provided a basis of a trilinear post-peak tensile response curve for FRC, while Marcalikova et al. (2020) provided fracture energies and tensile strengths corresponding to increases in fiber content. Other research provided details confirming the results

from Woo et al. (2014) and Marcalikova et al. (2020) but did not provide relationships detailing fracture energy and tensile strength to fiber content nor tensile post-peak modeling parameters.

The LS-DYNA damage-plasticity model employs a bilinear post-peak tension response curve. The trilinear post-peak tensile response curve presented by Woo et al. (2014) was converted to a bilinear curve and the fracture energy relationships provided by Marcalikova et al. (2020) were used to define the area under the curve as a function of fiber content. Figure 2.33 shows the trilinear response curve from Woo et al. (2014). Specifically, these two sources were used to define the parameters f_t, w_{f1}, f_{t1}, and w_f. in Figure 2.34 that define the tension post-peak response curve for the LS-DYNA CDPM (see Section 2.2 for discussion of the model) as follows;

- $G_{f,fiber}$ per Marcalikova et al. (2020) as

  $$G_{f,fiber} = 20FC \times G_{f,RC} \quad \text{(Eq. 2.1)}$$

  where FC is the fiber content percentage and $G_{f,RC}$ is the fracture energy of concrete
- $f_{t,fiber}$ per Marcalikova et al. (2020) as

  $$f_{t,fiber} = 1.65FC + f_{t,RC} \quad \text{(Eq. 2.2)}$$

  where $f_{t,RC}$ is the tensile strength of concrete using equations detailed in Section 2.2
- f_{t1} per Woo et al. (2014), average f_t value from the second line of the trilinear curve as

  $$f_{t1} = 0.4f_{t,fiber} \quad \text{(Eq. 2.3)}$$
- w_{f1} per Woo et al. (2014), average crack width value from the second line of the trilinear curve as

  $$w_{f1} = 0.25 \text{ mm} \quad \text{(Eq. 2.4)}$$

w_f was estimated by obtaining the area under the curve from w_{f1} and f_{t1} values and making the total area under the bilinear response equal to the predicted G_f. Figure 2.34 shows the FRC post-peak tensile response.

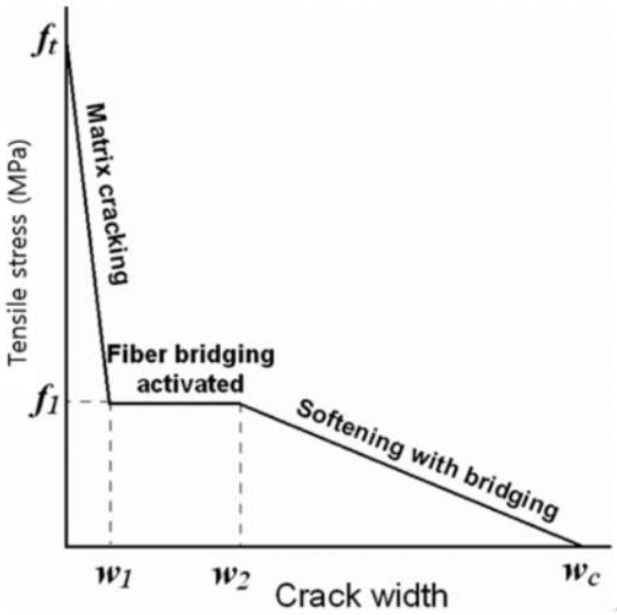

Figure 2.33. Trilinear Tensile response curve from Woo et al (2014)

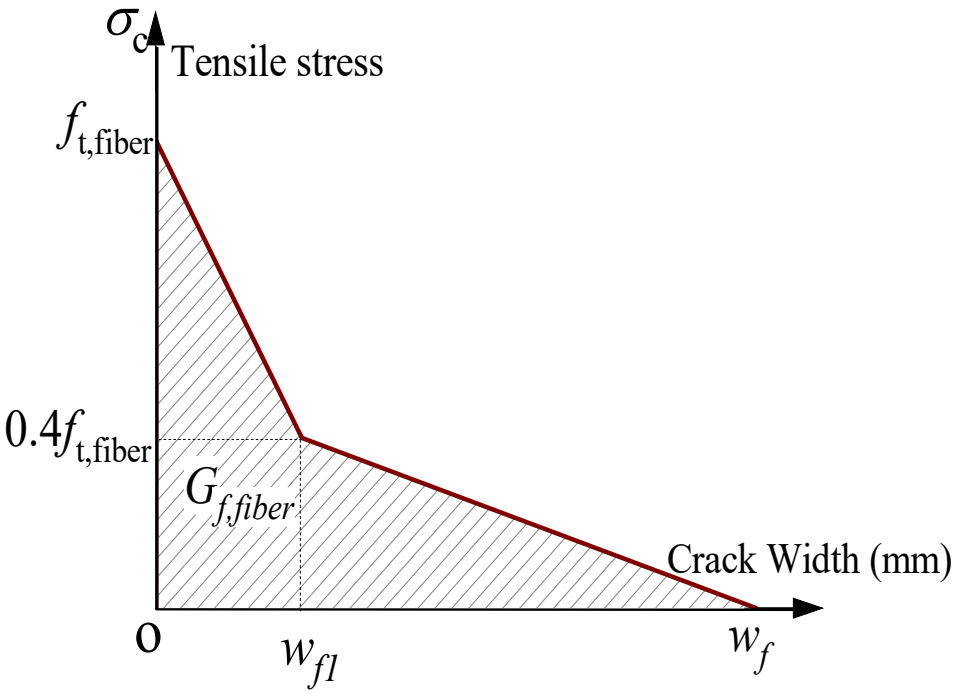

Figure 2.34. FRC bilinear response curve for use in CDPM

The rest of the concrete material model values were defined using the same approach presented in Section 2.2 for plain concrete.

2.7 FIBER REINFORCED CONCRETE WALL VALIDATION

The FRC material model was validated by comparing simulated and measured response histories for nine notched beam tests conducted by Marcalikova et al. (2020). All of the Marcalikova et al. (2020) tests employed the same notched beam specimen; Figure 2.35 shows the notch-beam test used in the experiment and Figure 2.36 shows the FEM model used to simulate this notched beam test specimen. The model was composed of a fine mesh region comprising 1.5 x 1.5 x 1.5 mm elements in the region above the 3 mm wide notch and a coarse-mesh region comprising 5 x 5 x 5 mm solid elements elsewhere.

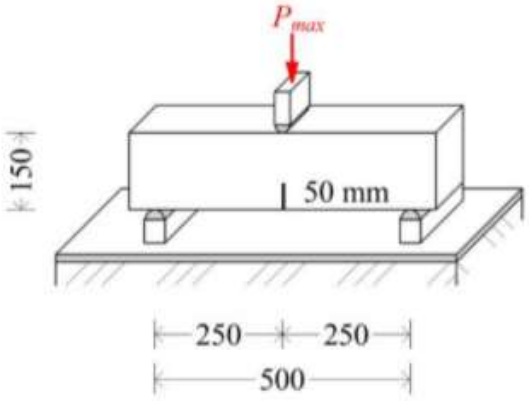

Figure 2.35. Marcalikova et al. (2020) notch-beam test set-up

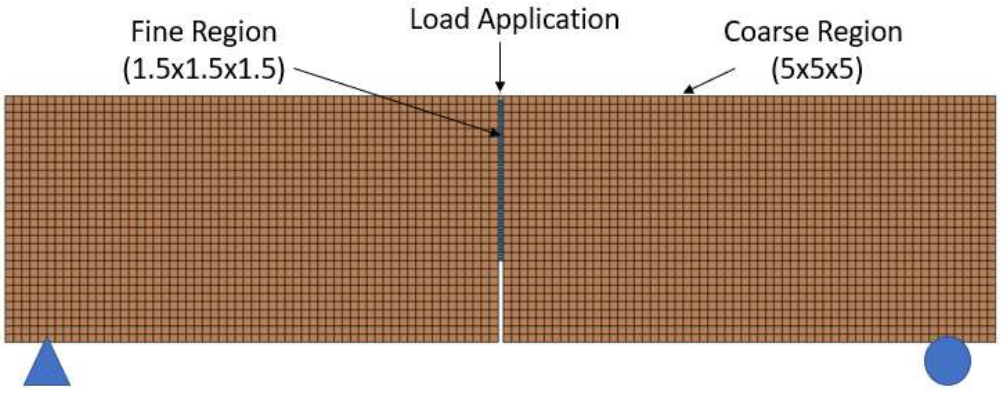

Figure 2.36. Notch-beam model

Figure 2.37 shows the nine tests conducted by Marcalikova et al. (2020) comprised three specimens each constructed of plain concrete (Black lines in plot), FRC with straight fibers (Green lines in plot), and FRC with hooked fibers (Blue lines in plot). The model developed was to simulate the results of the hooked fibers (blue). The measured results for hooked fibers have high variations of strength. The FRC model simulates the average peak strength well and then simulates strength deterioration that is similar to the average of the three hooked fiber tests. The strength deterioration post-peak matches the results well.

Additional simulations were done to see the impact of the w_{fl} value on the predicted response on the notch beam models. Due to the extrapolation of w_{fl} from a trilinear curve, differing w_{fl} values were simulated to account for rapid and less rapid strength capacity loss post-crack. A range of 0.15 – 0.5 mm was used for the w_{fl} value. The f_t, f_{t1}, and G_f values remained the same, whereas the w_f value was adjusted accordingly. The results replicate behavior as expected from the post-peak tensile model. The lower the w_{fl} value, the lower the peak strength, but it maintains a higher post-peak strength than those with higher w_{fl} values. Figure 2.38 shows the results from the differing w_{fl} values.

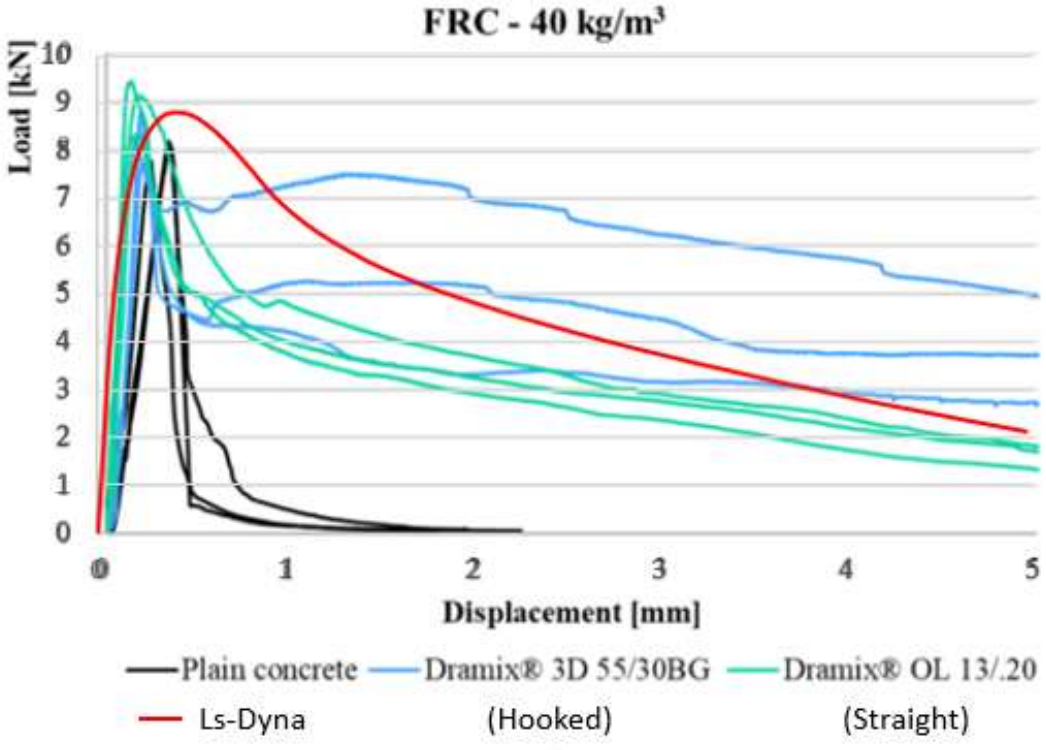

Figure 2.37. Comparison of FRC model

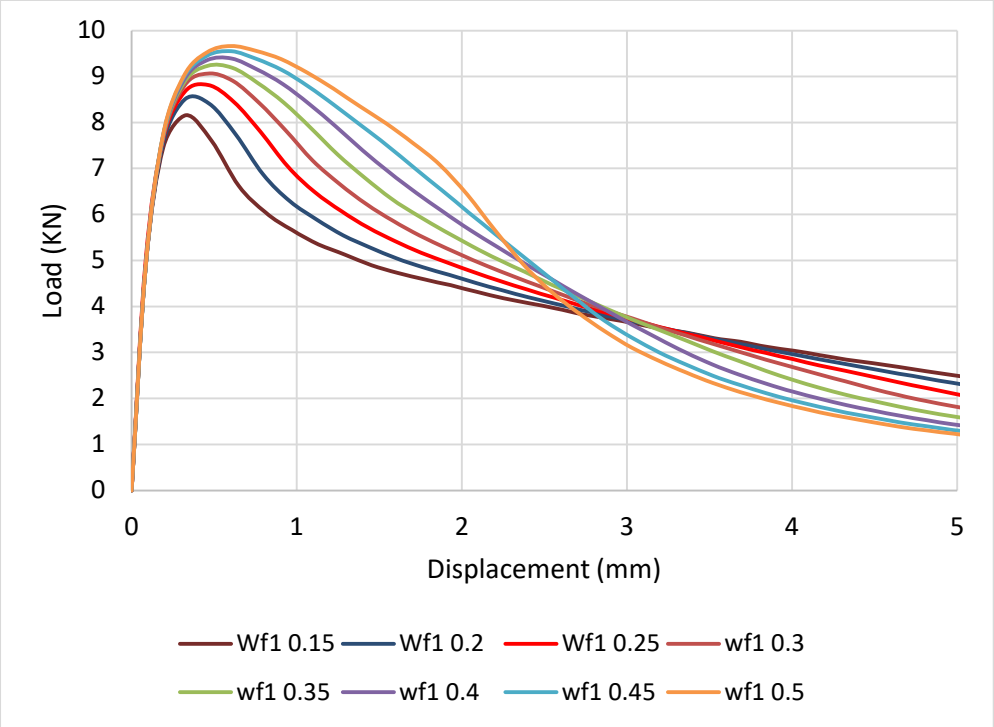

Figure 2.38. Comparison of differing wf1 values on notch beam behavior

2.8 CONCLUSIONS

From both validations of reinforced and FRC walls, the models accurately represent the test data. The model parameters for reinforced concrete suggested by Zhao et al. (2021) and LS-DYNA match test data. A FRC model calibrated by Woo et al. (2014) and Marcalikova et al. (2020) predicts FRC response well and will be used to model FRC walls. Moving forward, a parametric study of out-of-plane loaded walls will be conducted for walls using this modeling approach.

Chapter 3. PARAMETRIC STUDY OF RC WALLS

This chapter focuses on the parametric study of the modeling of RC walls with minimal longitudinal reinforcement loaded in the out-of-plane direction using LS-DYNA. This parametric study investigates the presence of modeling bond-slip, the difference in modeling continuous and spliced reinforcement, bar spacings, and the number of curtains of steel reinforcement. Load-drift histories, steel strains, and tensile damage histories were used to investigate the impact of the varying parameters.

Section 3.1 discusses the reference specimen used for the study. Section 3.2 provides an overview of the study parameters including a list of all model configurations. Section 3.3 discusses the results from each set of parameters investigated.

3.1 SELECTION OF REFERENCE SPECIMEN

The geometry, materials, and loading of the reference model were intended to model a one-story wall. The reinforcement spacing and based on three information sources:

- Advisory panel members were consulted to determine the geometry and size of the reinforcement.
- ACI requirements: The maximum vertical reinforcement spacing is 18 in. The $\rho_{l,min}$ value is 0.12%. The minimum cover requirement is 0.75 in.

3.1.1 *Reference Wall Properties*

The reference model has the following geometry, reinforcement, and material strengths. The reinforcing steel was size No. 4 reinforcement with a yield strength of 60 ksi. The compressive strength of the concrete was 4 ksi. The wall height was 10 ft, the length was 112 in, the thickness was 6 in. The reference model had one curtain of No. 4 longitudinal and transverse reinforcement spaced at 18 in. Table 3.1 lists the wall details.

Table 3.1. Reference wall details

Variable		Value
Wall Geometry	H (in.)	120
	L (in.)	112
	t (in.)	6
Steel Reinforcement	Bar Size	No. 4
	Bar Spacing (in.)	18
	Curtains of Steel	1
Material Properties	f_y (ksi)	60
	f'_c (ksi)	4
Loading Properties	P (%)	2

3.1.2 *Reference Wall Modelling Properties*

There are two regions up the height of the wall. The lower, finer mesh region uses 0.5x0.5 in. elements over the lower 40 in. of the wall height. The finer mesh region 40 in. height was determined by a mesh refinement study. Above this fine region, was a plastic wall region followed by an elastic wall region with steel loading plates attached to both sides of the wall along the length. Below the wall, consisted of a plastic foundation. These regions were all 1x1 in. meshes. Table 3.2 lists the element and material models used in LS-DYNA and Figure 3.1 shows the model.

Table 3.2. Element and material models used

Region	Element Type	Constitutive Model	Mesh Size
Steel Loading Plate	Constant Stress Solid Element (ELFORM 1)	Elastic (MAT 001)	1x1x1
Elastic Coarse			1x1x1
Inelastic Coarse		Concrete Damage Plastic (MAT 273)	1x1x1
Inelastic Fine			0.5x0.5x.0.5
Foundation			1x1x1
Steel Reinforcement	Hughes-Liu Beam (ELFORM 1)	Plastic-Kinematic (MAT 003)	1.5

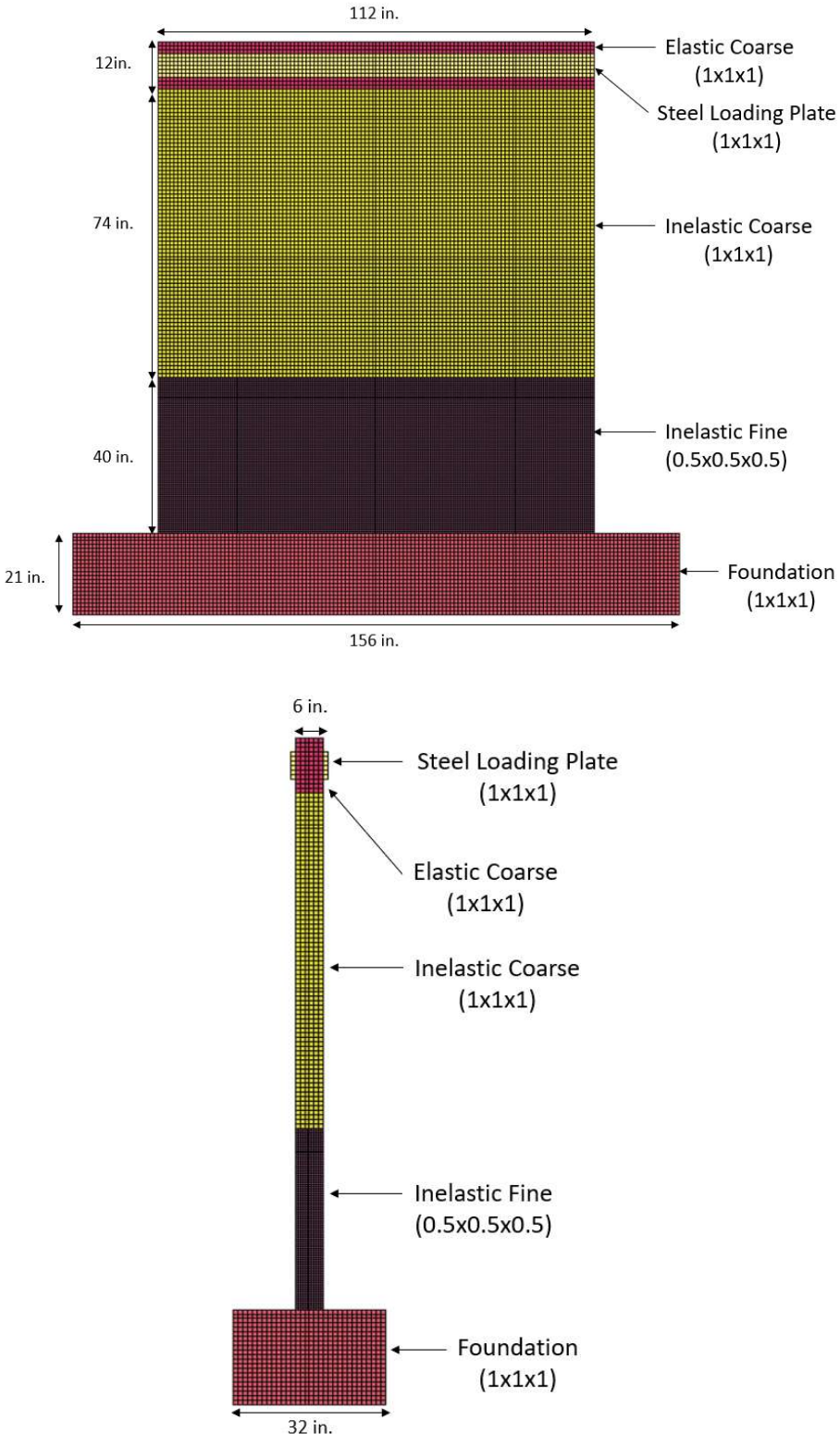

Figure 3.1. Model properties and layout

3.2 Overview of Study Parameters

The parametric study was conducted to investigate the impact of bar spacing, curtains of steel, splices, and modeling bond on the response of the walls subjected to out-of-plane loading including strength, deformability, and damage pattern. The following describes the objective of studying each parameter.

- Bar Spacing – Current ACI requirements allow for a maximum bar spacing of 18 in. Masonry and precast concrete allow for bar spacings of 48 in. Due to the large difference in maximum bar spacings, RC walls may not be economically feasible. The bar spacing can affect strength capacity post concrete cracking, so spacings of 18, 24, 36, and 48 in. were studied.
- Number of Curtains of Steel – The number of curtains of steel was studied to see the effect of steel location on the behavior of walls. Typical ICF construction uses a single curtain of steel at the center of the wall. Due to the placement of this bar, the steel may not engage like in a typical concrete wall section when there are multiple curtains of steel.
- Perfect or Modeled Bond – The use of mathematical expression to simulate bond was used to investigate its effect on the behavior and tensile damage histories.
- Spliced or Continuous Bars – The effect of having a bar splice at the wall-foundation interface was studied. In typical construction, the foundation is cast first with dowel bars. The wall is then cast. The presence of spliced bars is to simulate construction practice.

Table 3.3 provides the values of each parameter. The model design indicates:

- Bar Spacing (18, 24, 36, and 48 in.)
- Number of curtains of steel (1 and 2 curtains)
- Bond Equation Used (Modelled Bond {MB} and Perfect Bond (No Bond Equation) {PB})
- Spliced (S) or Continuous (C) Reinforcement
- Fiber Content Ratio (0.0%), to distinguish from FRC walls

For example, Model W18_1_PB_C_0 has 18 in. spaced continuous bars with one curtain steel modeled with perfect bond and 0% fiber content.

Table 3.3. RC wall models

Model ID	Bar Spacing	Curtains of Steel	No. of Longitudinal Bars	ρ_l (%)	Bond	Spliced?
W18_1_MB_C_0	18	1	7	0.21	MB	C
W24_1_MB_C_0	24		6	0.18		
W36_1_MB_C_0	36		4	0.12		
W48_1_MB_C_0	48		3	0.09		
W18_2_MB_C_0	18	2	14	0.42		
W24_2_MB_C_0	24		12	0.36		
W36_2_MB_C_0	36		8	0.24		
W48_2_MB_C_0	48		6	0.18		
W18_2_PB_C_0	18		14	0.42	PB	
W24_2_PB_C_0	24		12	0.36		
W36_2_PB_C_0	36		8	0.24		
W48_2_PB_C_0	48		6	0.18		
W18_2_MB_S_0	18		14	0.42	MB	S
W24_2_MB_S_0	24		12	0.36		
W36_2_MB_S_0	36		8	0.24		
W48_2_MB_S_0	48		6	0.18		

3.3 Reinforced Concrete Wall Comparisons

The following results were used to compare the wall models:

- Normalized load-drift history to 1% drift – The reaction taken from the foundation base was normalized to the flexural strength at cracking (M_{CR}) which was plotted against the drift corresponding to displacement at the top of the wall.
- Tensile damage history – The tensile damage was obtained by utilizing history variable 15 created by the concrete constitutive model at peak strength and 1% drift. History variable 15 is the tensile damage history from CDPM in LS-DYNA. The user must specify LS-DYNA to return certain history variables to receive the output. The tensile damage is an element history detailing the tensile damage of an element ranging from 0 to 1, where 1 represents fully damaged concrete without any tensile capacity and 0 represents concrete that has not reached peak strength and subsequently has no damage.

- Steel stresses – The steel stresses were taken at the wall ends and wall-foundation interface at peak strength, 0.5%, and 1.0% drifts. Figure 3.2 details where the approximate location of peak strength, 0.5%, and 1.0% drift occur on the load-drift history.

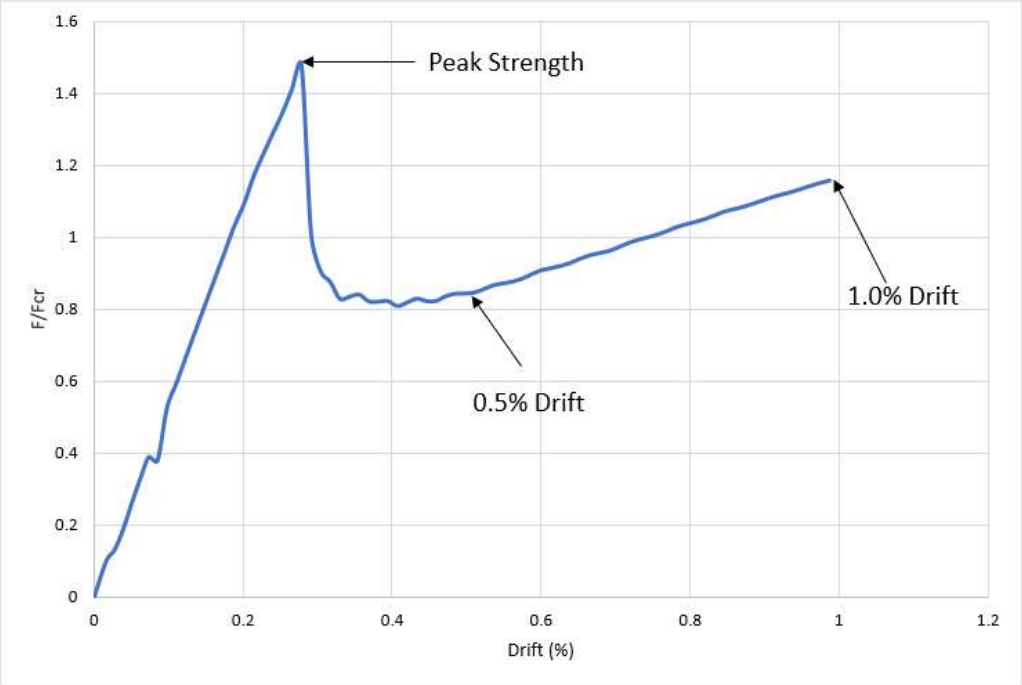

Figure 3.2. Locations of data obtained for tables and figures

3.4 PERFECT VS MODELLED BOND

Bond-slip behavior impacts the flexural and shear response of RC components. Typical modeling techniques embed the reinforcing bar nodes into the concrete nodes, resulting in a "perfect-bond" model (i.e., the strain of the bar and the concrete is the same). For components where: (1) the flexural bond demand is high due to moment along the length/height of the specimen, and/or (2) there is large demand due to anchorage to transfer the demand to an adjacent component. This section investigated the response of models with and without the bond modeled.

For the models for which the bond was modeled, the bond-slip model proposed by Murcia-Delso et al. (2011) was used. The equations corresponding to the model are given in Section 2.2 of

Chapter 2. The model was implemented between the longitudinal reinforcement and concrete in the wall and foundation. The bond model was not implemented for the transverse reinforcement.

Figure 3.3 provides a comparison of the load-drift history to 1% drift between the perfect-bond and modeled-bond models with continuous reinforcement. Figures 3.4-3.6 provide the stress in the reinforcing bars at peak strength, 0.5%, and 1% drifts. Figure 3.7 provides the strain histories for the end reinforcing bars. Figures 3.8-3.11 provide the tensile damage history at peak strength and 1% drift between the 48 in. spaced reinforcing bar wall models.

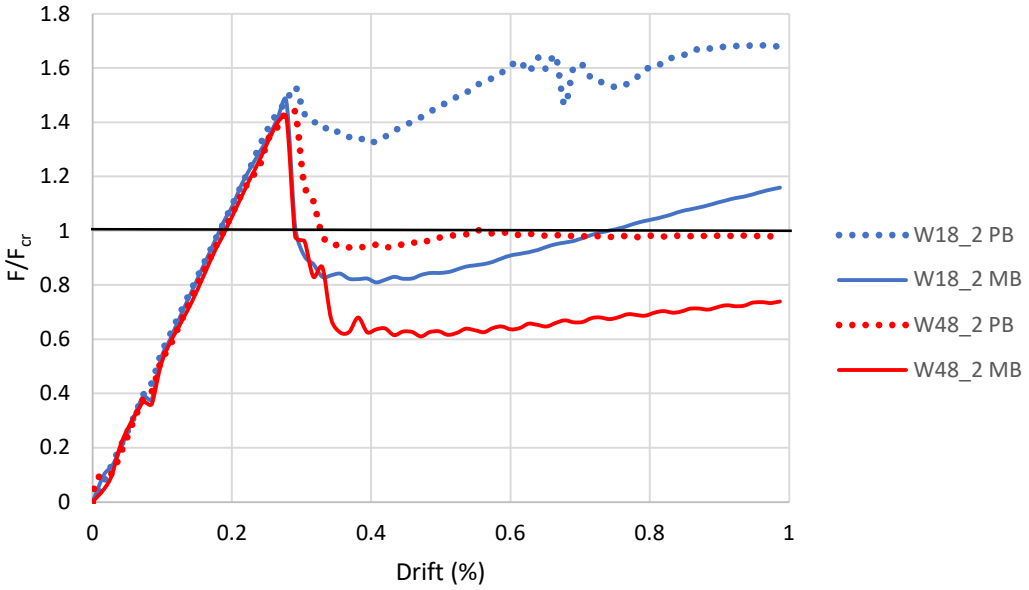

Figure 3.3. Load-drift history for perfect bond and modeled bond models

Table 3.4 provides values of the loading history at full cracking, residual (0.5% drift), and simulation end. The models will use a shortened notation listing the spacing, number of curtains, and bond equation used. The following observations are made:

- The peak strength normalized by the force corresponding to developing the ACI cracking moment (F_{max}/F_{cr}) ranged from 1.42 to 1.53. On average, the models with perfect bond had a strength ratio of 1.50, and the models with modeled bond had a strength ratio of 1.46. The perfect bond models are slightly stronger than the modeled bond models.

- The residual strength at 0.5% drift is impacted by the bond model; all models with perfect bond had a higher residual strength. This higher residual strength results from the higher steel strain at cracking for the numerical models with perfect bond
- The residual strength at 0.5% drift was normalized to the peak strength (F_{min}/F_{cr}). For the models with perfect bond, this ratio ranged from 0.65 to 0.87; the values increased with a decrease in steel spacing. For the models with modeled bond, the ratio ranged from 0.43 to 0.55; again, the values increased with a reduction in bar spacing.
- The post-cracking response is quantified by considering: (1) the ratio of the strength at 1% drift to the minimum strength ($F_{1\%}/F_{min}$) and (2) the ratio of the strength at 1% drift to the maximum strength ($F_{1\%}/F_{max}$). For models with perfect bond, the average ratios were 1.16 and 0.87 for minimum and maximum strengths, respectively. For models with modeled bond, the average ratios were 1.31 and 0.63 for minimum and maximum strengths, respectively. In all cases, there is some stiffening that occurs after residual strength.

.

Table 3.4. Load and Drift values at full cracking, residual, and simulation end between RC modeled and perfect bond

Model Designation	Peak			0.5% Drift (Residual Strength)			1% Drift (End of Simulation)		
	Drift (%)	F_{max} (kips)	F_{max}/F_{cr}	F_{min} (kips)	F_{min}/F_{max}	F_{min}/F_{cr}	$F_{1\%}$ (kips)	$F_{1\%}/F_{max}$	$F_{1\%}/F_{min}$
W18_2_MB	0.28	3.93	1.48	2.15	0.55	0.81	3.08	0.78	1.43
W24_2_MB	0.28	3.89	1.46	1.91	0.49	0.72	2.54	0.65	1.33
W36_2_MB	0.28	3.90	1.47	1.79	0.46	0.67	2.27	0.58	1.27
W48_2_MB	0.28	3.78	1.42	1.64	0.43	0.62	1.97	0.52	1.20
Average			1.46		0.48	0.71		0.63	1.31
COV			0.02		0.11	0.11		0.18	0.07
W18_2_PB	0.29	4.07	1.53	3.52	0.87	1.33	4.46	1.10	1.27
W24_2_PB	0.29	4.03	1.52	3.05	0.76	1.15	3.63	0.90	1.19
W36_2_PB	0.29	3.97	1.49	2.74	0.69	1.03	3.10	0.78	1.13
W48_2_PB	0.29	3.82	1.44	2.49	0.65	0.94	2.61	0.68	1.05
Average			1.50		0.74	1.11		0.87	1.16
COV			0.03		0.13	0.15		0.21	0.08

Table 3.5 presents a comparison of the three strength ratios for the companion models, where companion models have the same spacing with different approaches to modeling bond. The perfect bond models have higher strengths post-peak.

Table 3.5. Wall strength comparisons of the use of bond equation and perfect bond

Model Designation	F_{mb}/F_{pb}		
	Peak	0.5% Drift	1% Drift
W18_2	0.97	0.61	0.69
W24_2	0.96	0.63	0.70
W36_2	0.98	0.65	0.73
W48_2	0.99	0.66	0.75
Average	0.98	0.64	0.71
COV	0.01	0.03	0.03

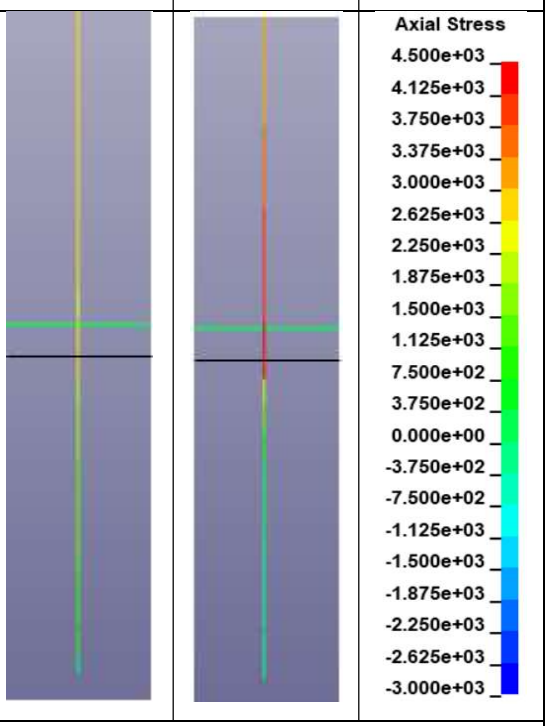

Figure 3.4. Steel Stress at Peak of W48_2 Companion Models
Black line indicates wall-foundation interface

Modeled Bond	Perfect Bond	Scale (ksi)
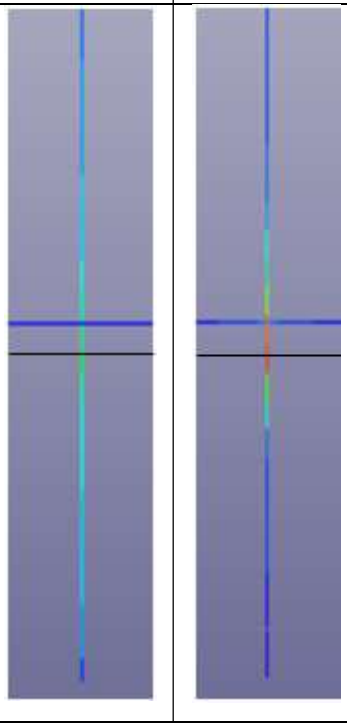		

Figure 3.5. Steel Stress at 0.5% drift of W48_2 Companion Models
Black line indicates wall-foundation interface

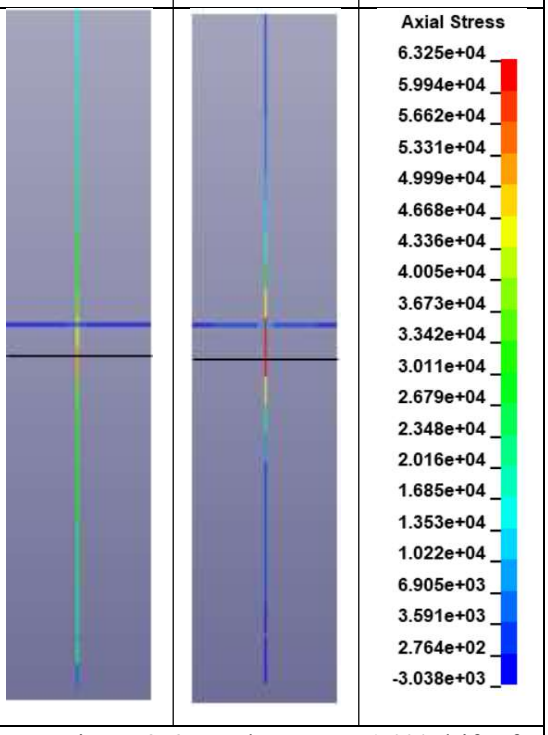

Figure 3.6. Steel Stress at 1.0% drift of W48_2 Companion Models
Black line indicates wall-foundation interface

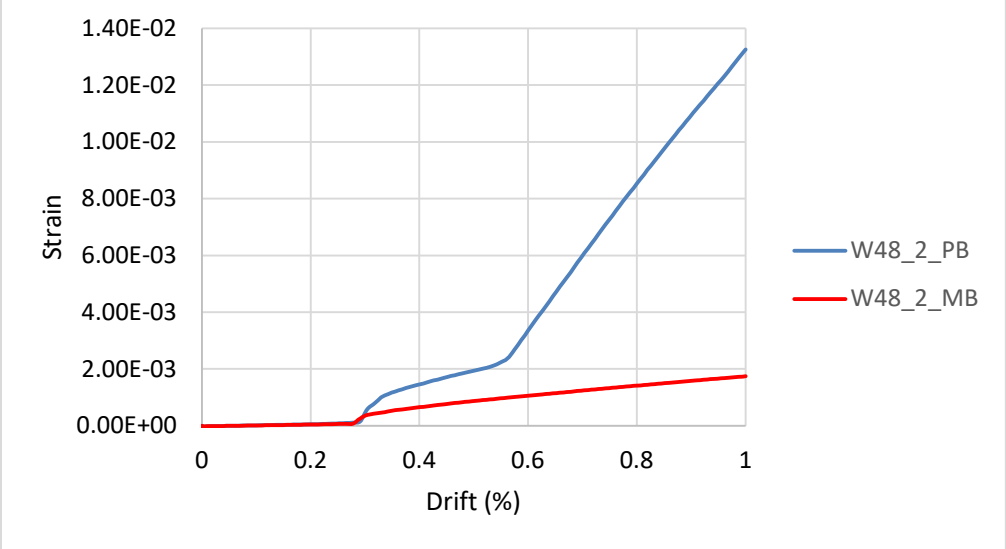

Figure 3.7. Strain histories of W48_2 companion models for the extreme tensile reinforcing bar at the base of the wall

The perfect bond walls have larger peak strength and residual strength values than the modeled bond walls. The walls with 18 in. spacing and 2 curtains of steel have strengths of 4.07 and 3.93 kips for perfect and modeled bond models, respectively. The steel stresses are also larger in the perfectly bonded models as well at 0.5 and 1.0% drifts. The perfect bond walls had more distributed tensile damage up the height of the wall, whereas modeled bond walls see tensile damage concentrated at the wall-foundation interface.

From the results, the bond will be modeled since it is clear that it makes a difference in the response and it is expected that it better simulates the response.

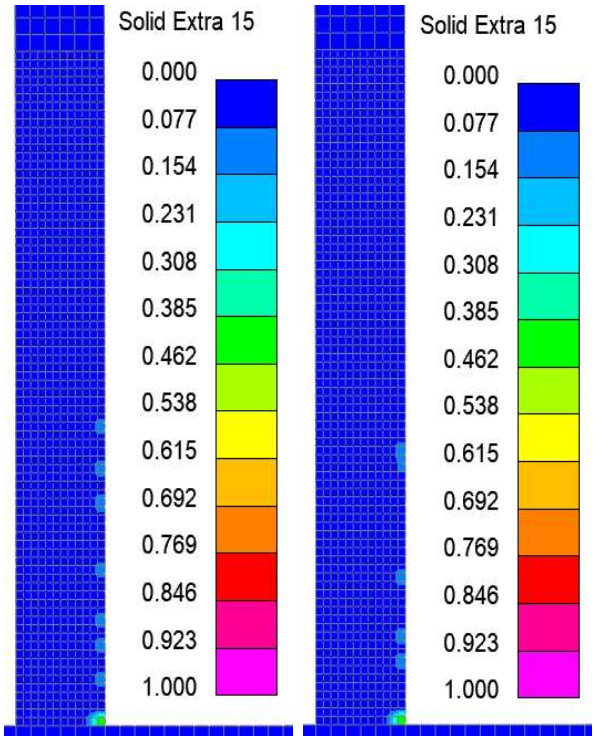

Figure 3.8. Tensile damage of W48_2_MB and W48_2_PB at peak strength for the lower 40 in. of wall

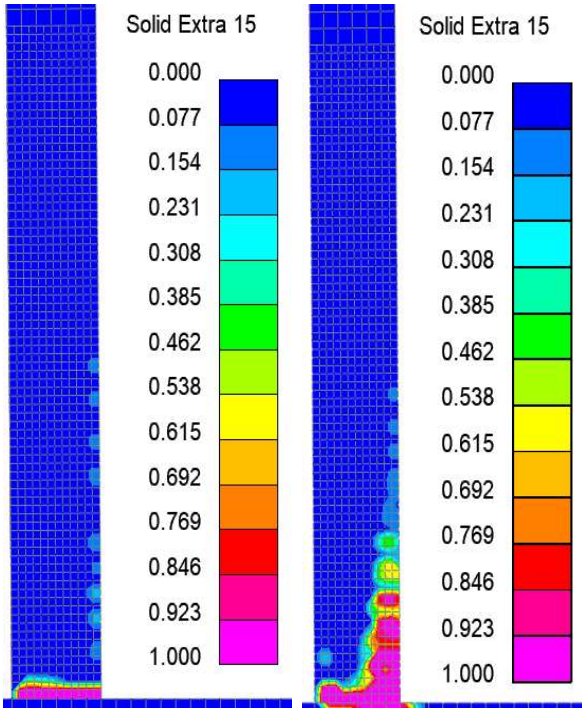

Figure 3.9. Tensile damage of W48_2_MB and W48_2_PB at 1% drift for the lower 40 in. of wall

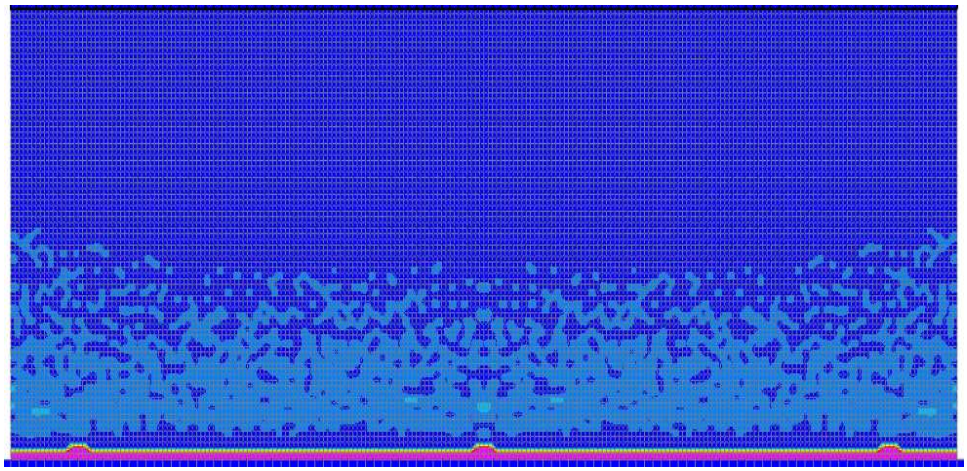

Figure 3.10. Tensile damage of W48_2_MB at 1% drift for the lower 40 in. of wall

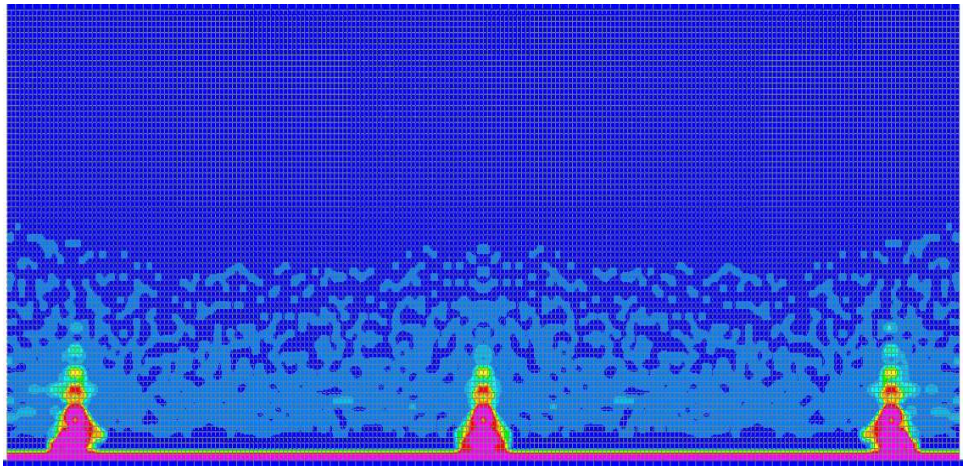

Figure 3.11. Tensile damage of W48_2_PB at 1% drift for the lower 40 in. of wall

3.5 Spliced vs Continuous Reinforcing Bars

In typical wall construction, the foundation is cast first with longitudinal starter bars extending from the foundation into the wall. The wall is then cast. Typical modeling uses continuous reinforcement to model longitudinal steel bar behavior. This study investigated the response of models with spliced and continuous longitudinal reinforcement at the wall-foundation interface.

For the models with the wall splice modeled, the lap length was determined from ACI 318-19 Table 25.4.2.3. This was done to ensure sufficient steel reinforcement was given to achieve maximum strengths. This length was also in accordance with ACI 318-19 Table 25.5.2.1 for bar splices.

Figure 3.12 provides a comparison of the load-drift history to 1% drift between the spliced and continuous bars. Figures 3.13-3.15 show the strains of the end reinforcing bars at peak strength, 0.5%, and 1% drift. Figure 3.16 provides the strain histories for the end reinforcing bars. Figures 3.17-3.20 provide the tensile damage history at peak strength and 1% drift for models with 48 in. spacings.

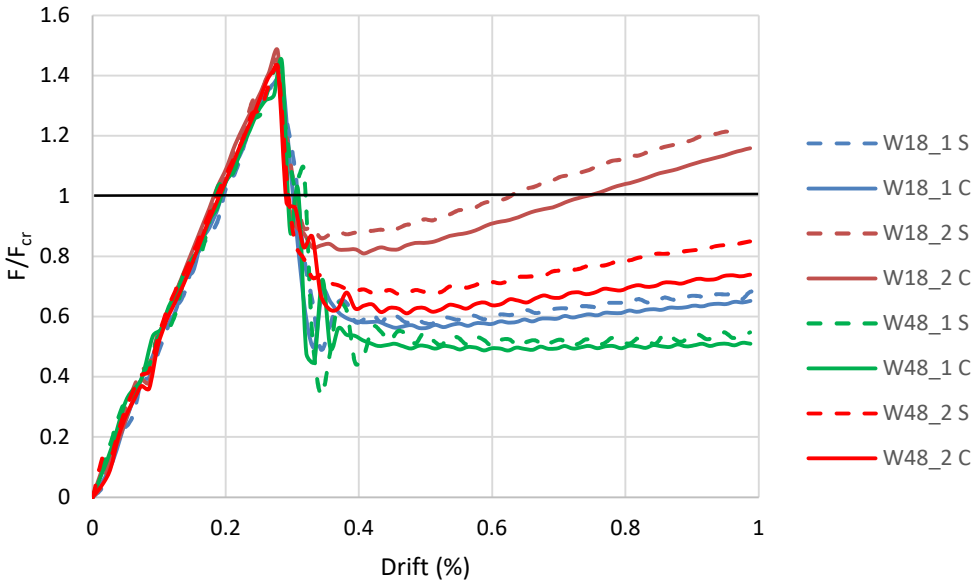

Figure 3.12. Load-drift history for spliced and continuous reinforcement

Table 3.6 provides values of the strengths at full cracking, residual (0.5% drift), and 1% drift. The table will use a shortened notation detailing the spacing, number of curtains, spliced or continuous reinforcement. The following observations are made:

- The models reached approximately the same peak strength. The peak strength is independent of bar splice.
- The peak strength normalized by the force corresponding to developing the ACI cracking moment (F_{max}/F_{cr}); the ratio ranged from 1.36 to 1.48. On average, the models with spliced bars had a strength ratio of 1.41 and the models with continuous bars had a strength ratio of 1.44.
- The post-peak minimum strength and the drift corresponding to this value were the same and did not depend on the configuration of the reinforcing bar.
- To investigate the strength loss after peak, the minimum strength was normalized to the peak strength (F_{min}/F_{cr}). For the models with spliced reinforcement, this ratio ranged from 0.38 to 0.63 with the values increasing with a decrease in steel spacing of the longitudinal reinforcement. For the models with continuous reinforcement, the ratio ranged from 0.34 to 0.55; again, the values increased with a decrease in bar spacing. The difference in

minimum strength for the models between spliced and continuous reinforcement is minimal.

- The post-cracking response was investigated by considering: (1) the ratio of the strength at 1% drift to the minimum strength ($F_{1\%}/F_{min}$) and (2) the ratio of the strength at 1% drift to the maximum strength ($F_{1\%}/F_{max}$). For models with spliced reinforcement, the average ratios were 1.21 and 0.53 for minimum and maximum strengths, respectively. For models with continuous reinforcement, the average ratios were 1.19 and 0.58 for minimum and maximum strengths, respectively.

Table 3.6. Load and Drift values at full cracking, residual, and simulation end of RC spliced and continuous reinforcement

Model Designation	Peak			0.5% Drift (Residual Strength)			1% Drift (End of Simulation)		
	Drift (%)	F_{max} (kips)	F_{max}/F_{cr}	F_{min} (kips)	F_{min}/F_{max}	F_{min}/F_{cr}	$F_{1\%}$ (kips)	$F_{1\%}/F_{max}$	$F_{1\%}/F_{min}$
W18_1_C	0.28	3.72	1.40	1.50	0.40	0.56	1.73	0.47	1.15
W18_2_C		3.93	1.48	2.15	0.55	0.81	3.08	0.78	1.43
W48_1_C		3.84	1.44	1.31	0.34	0.49	1.36	0.35	1.04
W48_2_C		3.78	1.42	1.64	0.43	0.62	1.97	0.52	1.20
Average			1.44		0.43	0.62		0.53	1.21
COV			0.02		0.21	0.22		0.34	0.14
W18_1_S	0.28	3.60	1.36	1.54	0.43	0.58	1.82	0.51	1.18
W18_2_S		3.85	1.45	2.44	0.63	0.92	3.22	0.84	1.32
W48_1_S		3.77	1.42	1.45	0.38	0.55	1.46	0.39	1.01
W48_2_S		3.80	1.43	1.81	0.48	0.68	2.26	0.59	1.25
Average			1.41		0.48	0.68		0.58	1.19
COV			0.03		0.23	0.25		0.33	0.11

Table 3.7 provides three strength ratios for the companion models, where companion models have the same spacing with different reinforcement configurations. The spliced reinforcement models have about the same strengths as the continuous reinforcement models.

Table 3.7. Wall strength comparisons of spliced and continuous reinforcement

Model Designation	Peak Fs/Fc	0.5% Drift Fs/Fc	1% Drift Fs/Fc
W18_1	0.97	1.03	1.05
W18_2	0.98	1.13	1.05
W48_1	0.98	1.11	1.07
W48_2	1.01	1.10	1.15
Average	0.98	1.09	1.08
COV	0.02	0.04	0.04

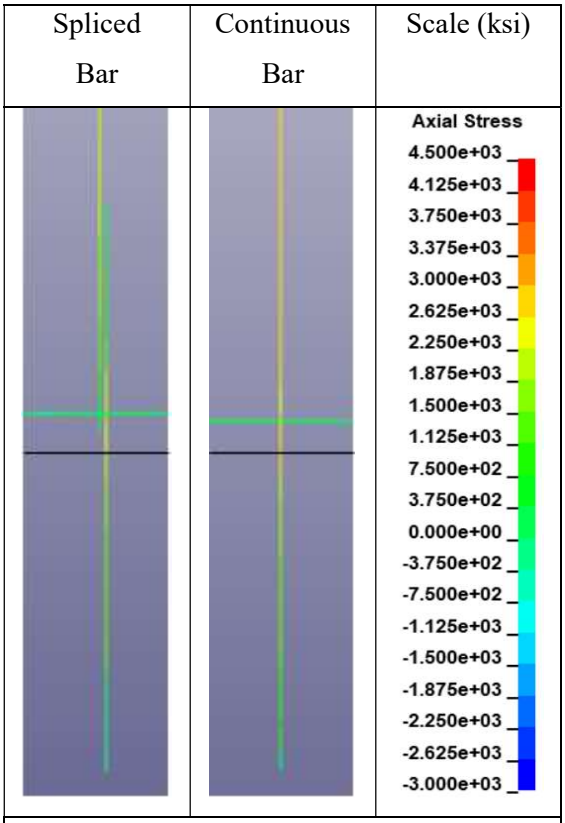

Figure 3.13. Steel Strains at Peak Strength of W48_2 companion models Black line indicates wall-foundation interface

Spliced Bar	Continuous Bar	Scale (ksi)
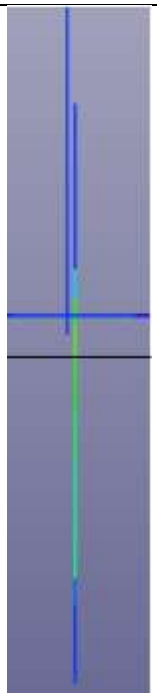	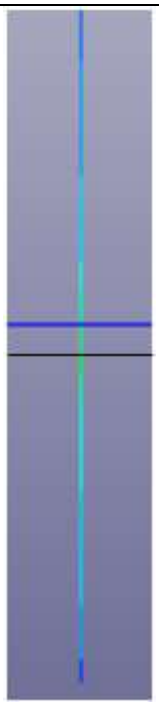	

Figure 3.14. Steel Strains at 0.5% drift of W48_2 companion models
Black line indicates wall-foundation interface

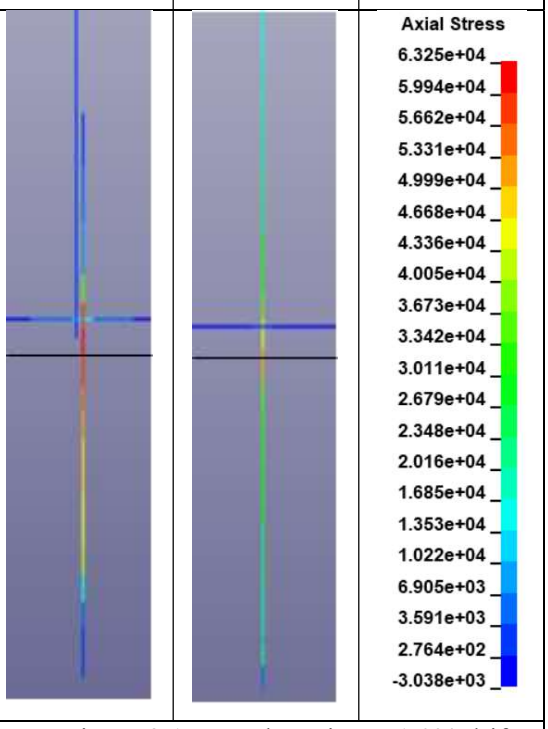

Figure 3.15. Steel Strains at 1.0% drift of W48_2 companion models
Black line indicates wall-foundation interface

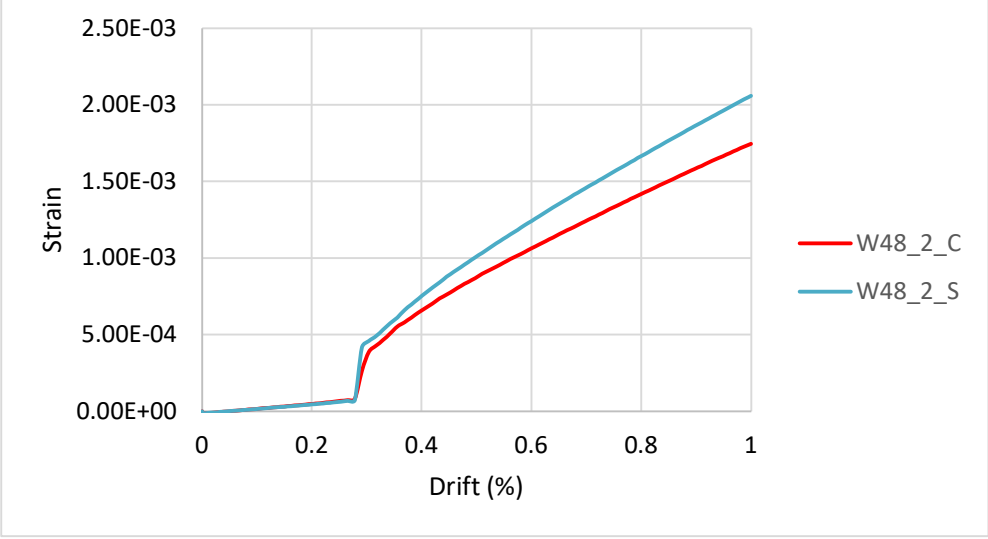

Figure 3.16. Strain histories of spliced and continuous reinforcement models for the extreme tensile reinforcing bar at the base of the wall

The steel stresses are greater in the spliced bar models for post-peak behavior at 0.5 and 1.0% drifts. At peak, the steel strains are very similar and are less than 5 ksi. For spliced bar models, there is additional damage up the height of the wall along the locations of longitudinal reinforcement. Continuous bar models only sustain damage at the wall-foundation interface.

From the results, the presence of a bar splice does not have a large effect on the strength and behavior of the wall models. It is simpler to model continuous reinforcement than spliced reinforcement. Continuous reinforcement will be used for the remainder of this parametric study.

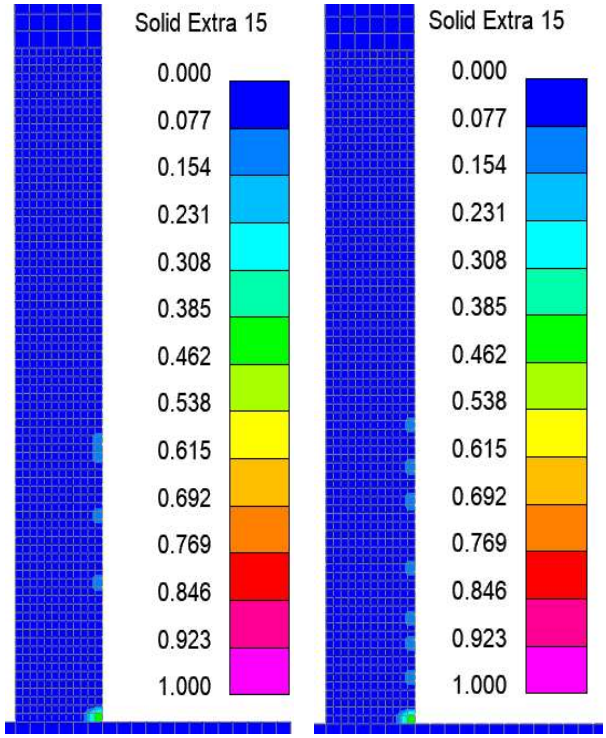

Figure 3.17. Tensile damage of W48_2_S and W48_2_C at peak strength for lower 40 in. of wall

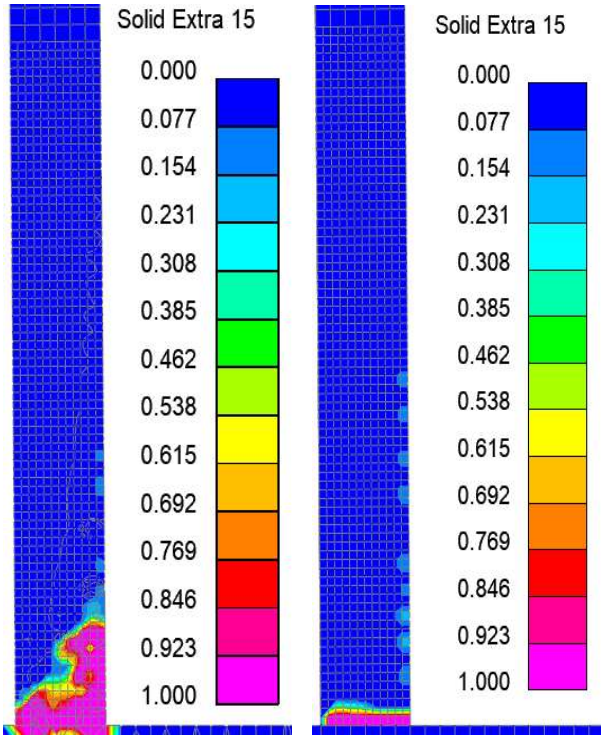

Figure 3.18. Tensile damage of W48_2_S and W48_2_C at 1% drift for lower 40 in. of wall

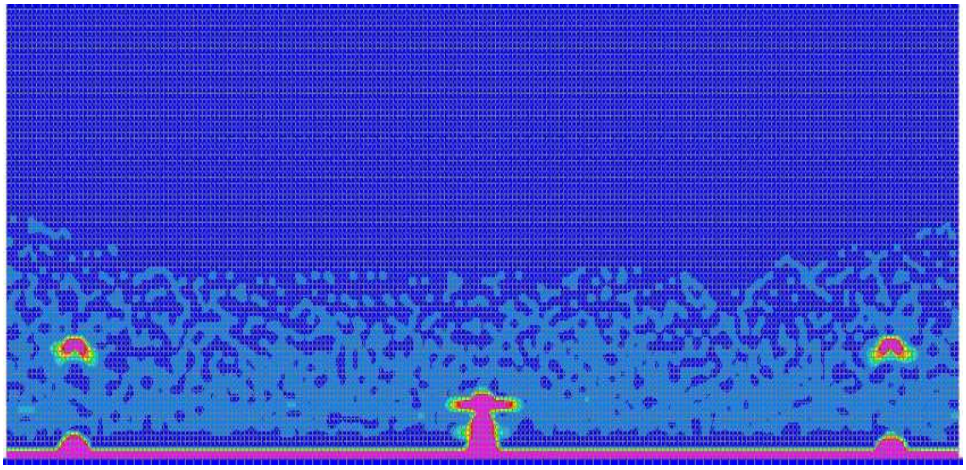

Figure 3.19. Tensile damage of W48_2_S at 1% drift for lower 40 in. of wall

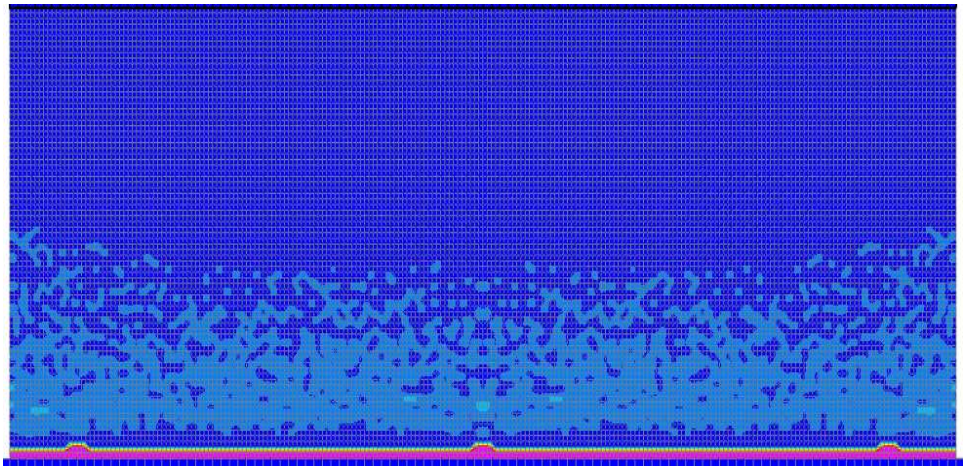

Figure 3.20. Tensile damage of W48_2_C at 1% drift for lower 40 in. of wall

3.6 One vs Two Curtains of Steel of Reinforcement

The placement of the steel through the thickness will impact the response of the wall. In walls with one curtain of steel, the curtain is placed in the center of the wall thickness. In walls with two curtains of steel, each curtain of steel reinforcement is placed 0.75 in. cover from each surface in accordance with ACI 318-19. This section investigated the influence of the curtains of steel and reinforcement ratio and subsequent response. The evaluation compares the force-drift response, longitudinal steel stresses, and the crack pattern as determined by the tension damage parameter.

Figure 3.21 provides a comparison of the load-drift history to 1% drift between the one and two curtains of steel models. Figures 3.22-3.24 shows stresses in the reinforcing bars at peak strength, 0.5%, and 1% drift. Figure 3.25 provides the strain histories for the end reinforcing bars. Figures 3.26-3.29 provide the tensile damage history at peak strength and 1% drift for models with 48 in. spacing.

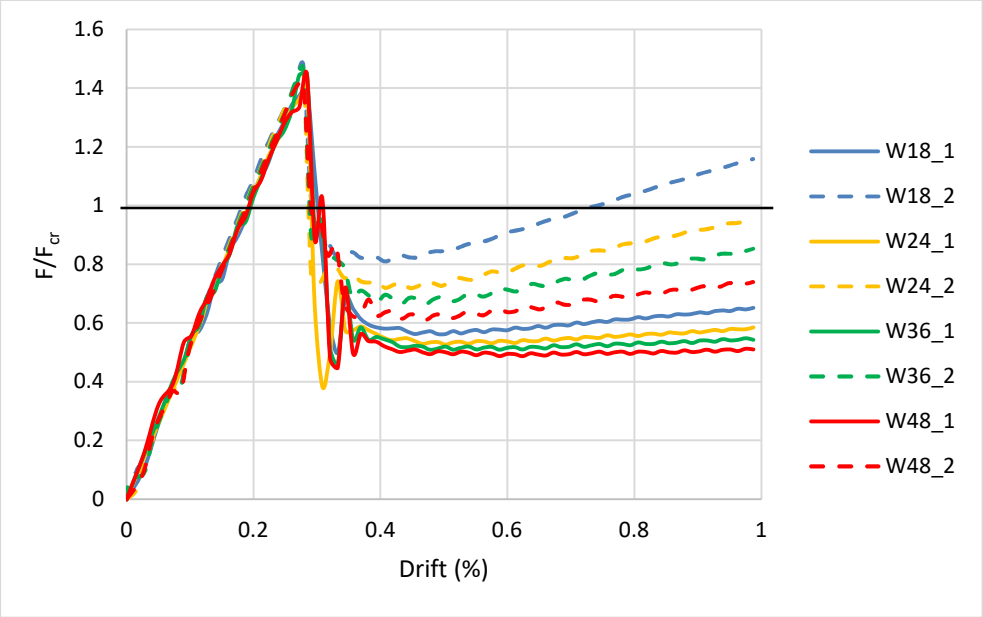

Figure 3.21. Load-drift history for one and two curtains of steel models

Table 3.8 provides values of the loading history at full cracking, residual (0.5% drift), and 1% drift. The table will use a shortened notation detailing the spacing and number of curtains. The following observations are made:

- The models all reached approximately the same peak strength. The maximum strength does not depend on the number of curtains of steel reinforcement.
- The peak strength normalized by the force corresponding to developing the ACI cracking moment ranged (F_{max}/F_{cr}) from 1.40 to 1.48. On average, the models with one curtain of steel had a strength ratio of 1.42 and the models with two curtains of steel had a strength ratio of 1.46. The ratio did not depend on the number of curtains.
- To understand the strength loss after peak, the minimum strength was normalized to the peak strength (F_{min}/F_{cr}). For the models with one curtain of steel, this ratio ranged from 0.34 to 0.40 with the values increasing with a decrease in steel spacing. For the models with two curtains of steel, the ratio ranged from 0.43 to 0.55; again, the values increased with a decrease in bar spacing. There is an increase in the residual strength as there are more curtains of steel in the model.
- The post-cracking response is quantified by considering: (1) the ratio of the strength at 1% drift to the minimum strength ($F_{1\%}/F_{min}$) and (2) the ratio of the strength at 1% drift to the

maximum strength ($F_{1\%}/F_{max}$). For models with one curtain of steel, the average ratios were 1.09 and 0.41 for minimum and maximum strengths, respectively. For models with two curtains of steel, the average ratios were 1.31 and 0.63 for minimum and maximum strengths, respectively. The one curtain of steel models see little post-crack stiffening, whereas the two curtains of steel models see a significant amount of post-crack stiffening.

Table 3.8. Load and Drift values at full cracking, residual, and simulation end of RC one and two curtains of reinforcement

Model Designation	Peak			0.5% Drift (Residual Strength)			1% Drift (End of Simulation)		
	Drift (%)	F_{max} (kips)	F_{max}/F_{cr}	F_{min} (kips)	F_{min}/F_{max}	F_{min}/F_{cr}	$F_{1\%}$ (kips)	$F_{1\%}/F_{max}$	$F_{1\%}/F_{min}$
W18_1	0.28	3.72	1.40	1.50	0.40	0.56	1.73	0.47	1.15
W24_1		3.74	1.41	1.40	0.37	0.53	1.56	0.42	1.11
W36_1		3.84	1.44	1.35	0.35	0.51	1.44	0.38	1.07
W48_1		3.84	1.44	1.31	0.34	0.49	1.36	0.35	1.03
Average			1.42		0.37	0.52		0.41	1.09
COV			0.01		0.07	0.06		0.13	0.05
W18_2	0.28	3.93	1.48	2.15	0.55	0.81	3.08	0.78	1.43
W24_2		3.89	1.46	1.91	0.49	0.72	2.54	0.65	1.33
W36_2		3.90	1.47	1.79	0.46	0.67	2.27	0.58	1.27
W48_2		3.78	1.42	1.64	0.43	0.62	1.97	0.52	1.20
Average			1.46		0.48	0.71		0.63	1.31
COV			0.02		0.11	0.11		0.18	0.07

Table 3.9 presents a comparison of the three strength ratios for the companion models, where companion models have the same spacing with different reinforcement configurations.

Table 3.9. Wall strength comparisons of one and two curtains of reinforcement

Model Designation	Peak F1c/F2c	0.5% Drift F1c/F2c	1% Drift F1c/F2c
W18	0.95	0.70	0.56
W24	0.96	0.73	0.61
W36	0.98	0.75	0.63
W48	1.02	0.80	0.69
Average	0.98	0.75	0.62
COV	0.03	0.06	0.09

One Curtain	Two Curtains	Scale (ksi)
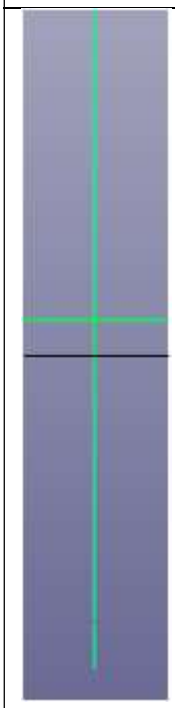	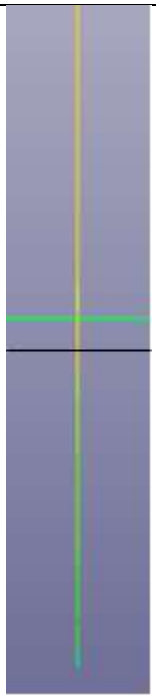	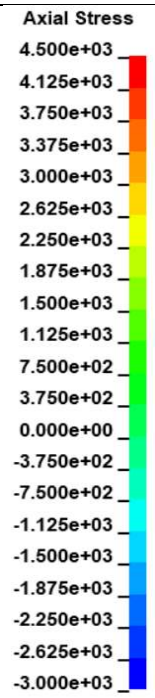

Figure 3.22. Steel Strains at Peak Strength of W48 companion models Black line indicates wall-foundation interface

One Curtain	Two Curtains	Scale (ksi)
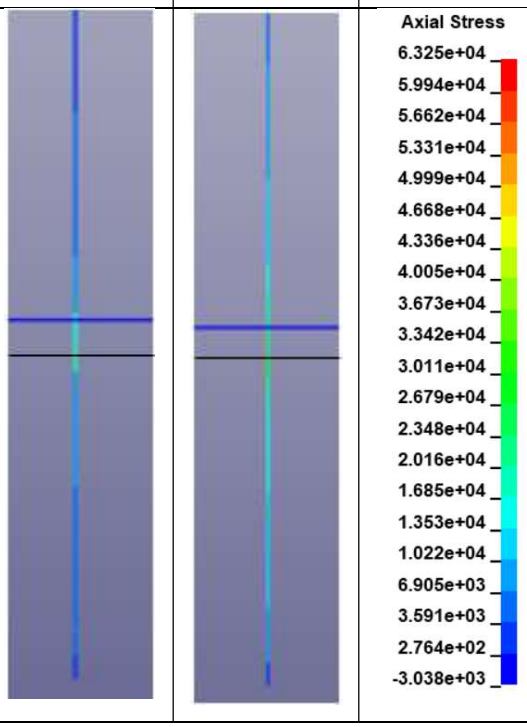		

Figure 3.23. Steel Strains at 0.5% drift of W48 companion models
Black line indicates wall-foundation interface

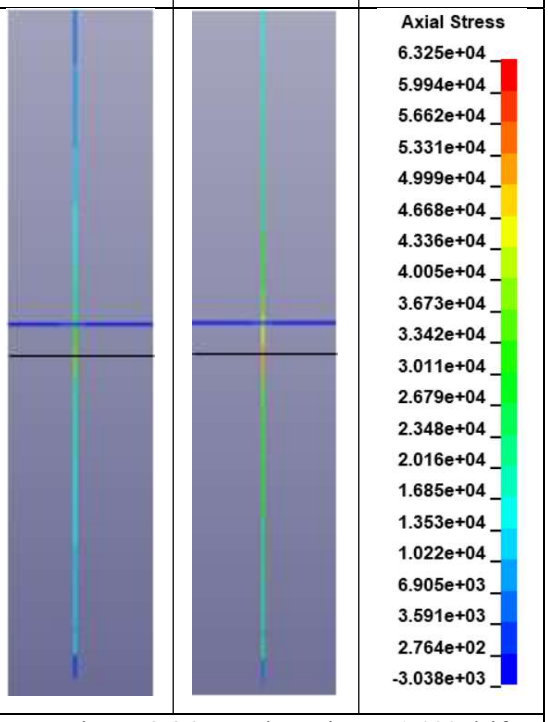

Figure 3.24. Steel Strains at 1.0% drift of W48 companion models
Black line indicates wall-foundation interface

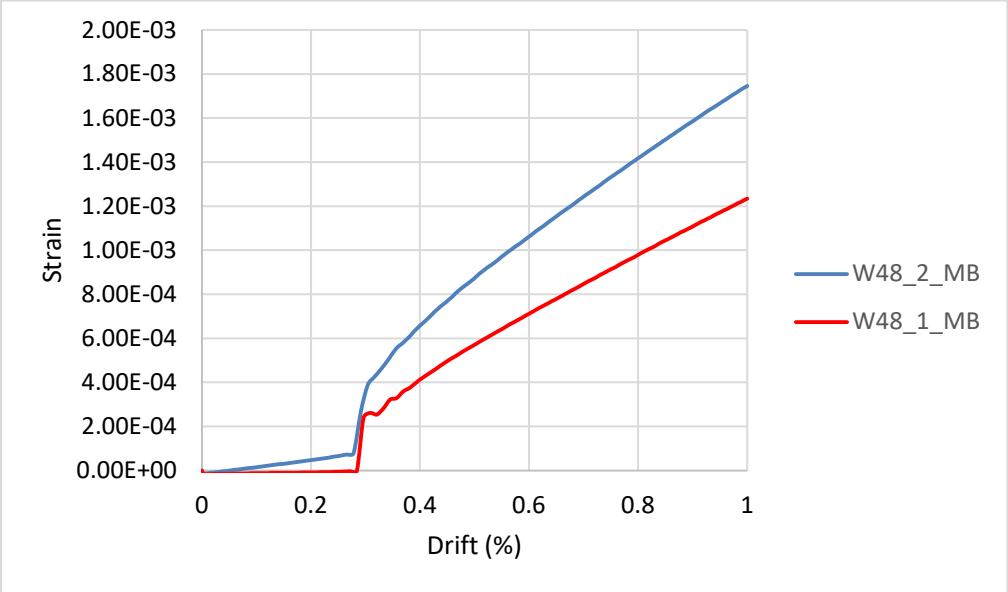

Figure 3.25. Strain Histories between W48 companion models for the extreme tensile reinforcing bar at the base of the wall

The one curtain of steel models have less strength at 0.5% and 1.0% drift. The steel stresses are less in the one curtain of steel models as well at 1.0% drift. The tensile damage patterns between the two model types are about the same as seen in Figures 3.27: Tensile Damage of W48_1 and W48_2 at 1% drift. Both see concentrated damage at the wall-foundation interface.

From the results, the number of curtains of steel impacts the post-cracking strength capacity of the wall. One curtain of steel will be used for the remainder of this parametric study.

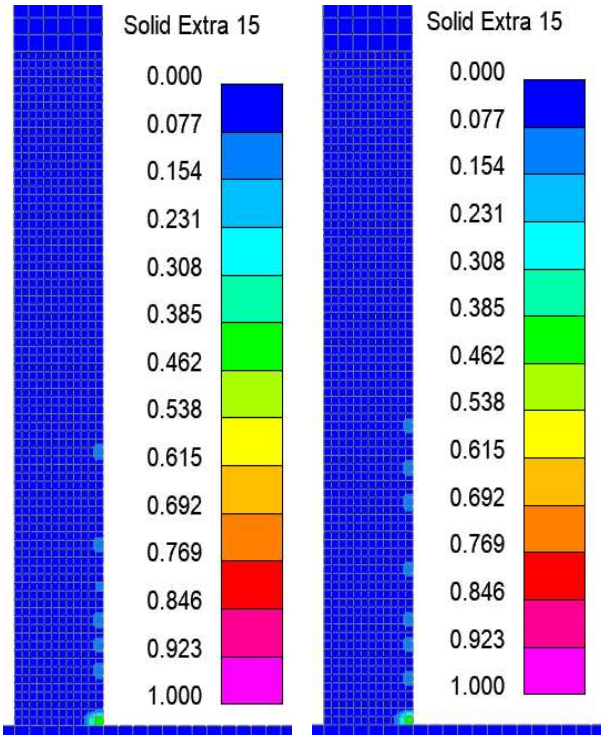

Figure 3.26. Tensile damage of W48_1 and W48_2 at peak strength for lower 40 in. of wall

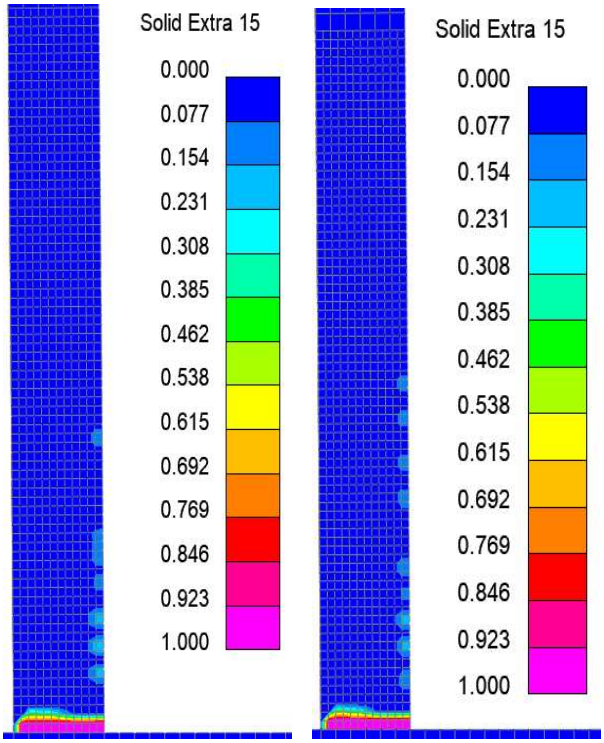

Figure 3.27. Tensile damage of W48_1 and W48_2 at 1% drift for lower 40 in. of wall

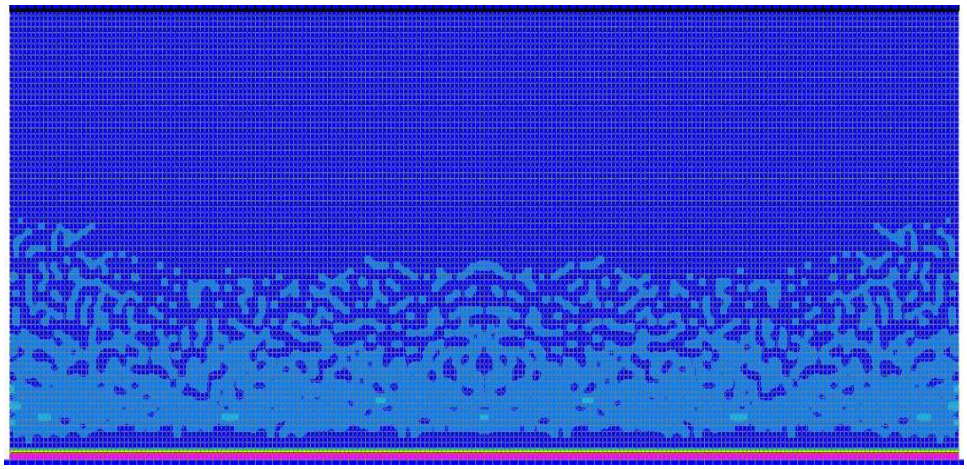

Figure 3.28. Tensile damage of W48_1 at 1% drift for lower 40 in. of wall

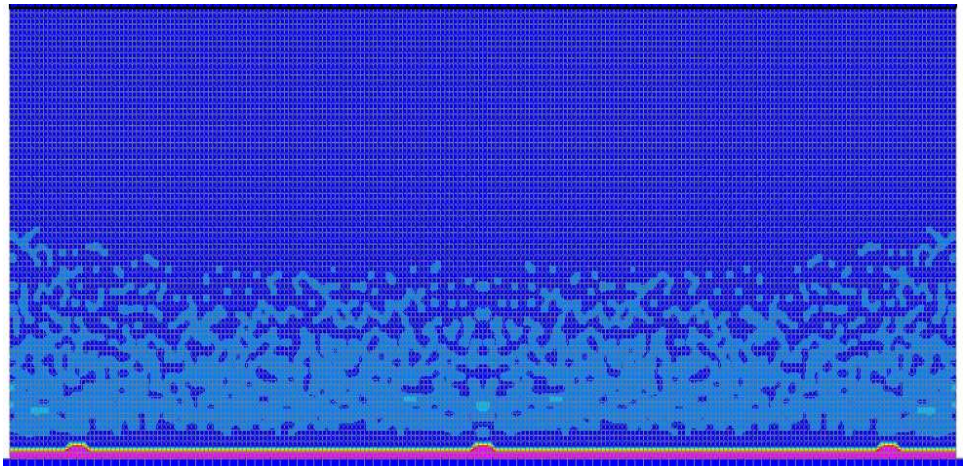

Figure 3.29. Tensile damage of W48_2 at 1% drift for lower 40 in. of wall

3.7 Bar Spacing of Longitudinal Reinforcement

Bar spacing impacts the longitudinal reinforcement ratio of a wall. The larger the reinforcement ratio, the stronger the wall is, as there is more steel to resist the tensile forces in the wall. This section investigated the response of models with varying reinforcement spacings of 18, 24, 36, and 48 in. The evaluation compares the force-drift response, longitudinal steel stresses, and the crack pattern as determined by the tension damage parameter.

The maximum bar spacing in ACI 318-19 is 18 in. Masonry code requirements allow for 48 in. longitudinal bar spacings. Bar spacings up to 48 in. were modeled, including spacings of 18, 24, 36, and 48 in.

Figure 3.30 provides a comparison of the load-drift history to 1%. Figures 3.31-3.33 provide the stresses in the reinforcing bars at peak strength, 0.5%, and 1% drift between 18 and 48 in. spacings. Figure 3.34 provides the strain histories for the end reinforcing bars. Figures 3.35-3.38 provide the distribution of tensile damage parameter at peak strength and 1% drift for models with 18 and 48 in. spacings.

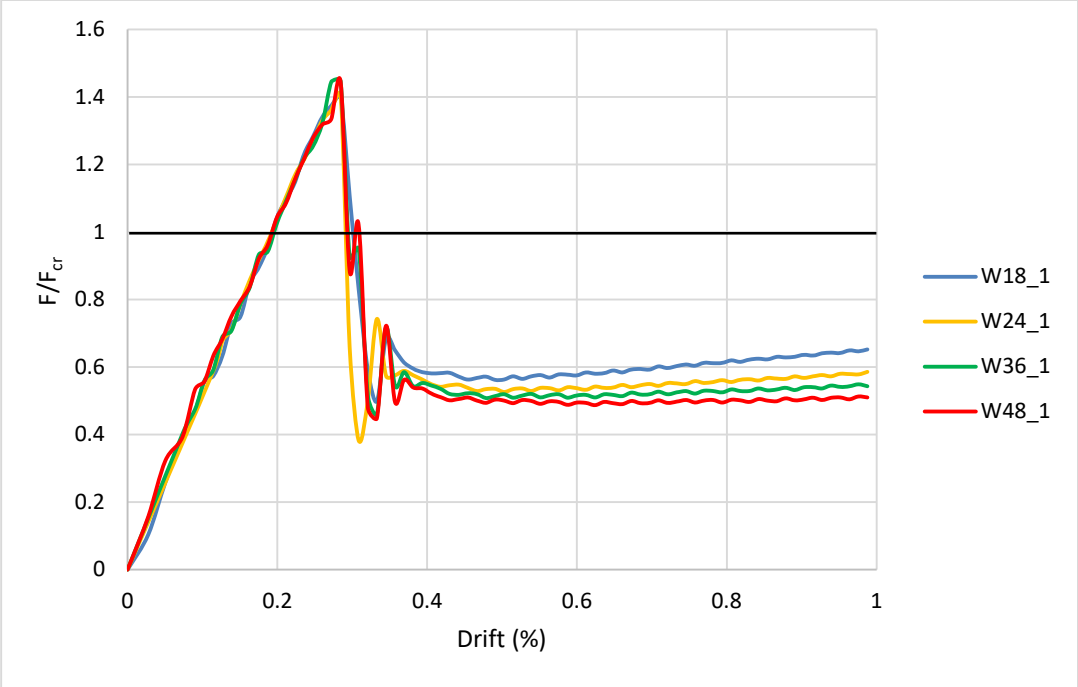

Figure 3.30. Load-drift history for single curtains of steel models

Table 3.10 provides values of the loading history at full cracking, residual, and simulation end. The table will use a shortened notation detailing the spacing and number of curtains.

The following observations are made:

- The models all reached approximately the same peak strength. The peak strength is not dependent on steel spacings.
- The peak strength normalized by the force corresponding to developing the ACI cracking moment (F_{max}/F_{cr}) ranged from 1.40 to 1.44. On average, the models had a strength ratio of 1.42. The normalized strength is approximately the same for the 18, 24, 36, and 48 in. spacings.
- The minimum strength was normalized to the peak strength (F_{min}/F_{cr}). This ratio ranged from 0.34 to 0.40 with the values increasing with a decrease in steel spacing.
- The post-cracking response is quantified by considering: (1) the ratio of the strength at 1% drift to the minimum strength ($F_{1\%}/F_{min}$) and (2) the ratio of the strength at 1% drift to the maximum strength ($F_{1\%}/F_{max}$). The average ratios were 1.09 and 0.41 for minimum and maximum strengths, respectively. The range of ratios for minimum strength was 1.03 to

1.15 and the range of ratios for the maximum strength was 0.35 to 0.47. The spacing has little impact on post-peak behavior as there is little post-peak stiffening in the models.

Table 3.10. Load and Drift values at full cracking, residual, and simulation end of RC reinforcement spacings

Model Designation	Peak			0.5% Drift (Residual Strength)			1% Drift (End of Simulation)		
	Drift (%)	F_{max} (kips)	F_{max}/F_{cr}	F_{min} (kips)	F_{min}/F_{max}	F_{min}/F_{cr}	$F_{1\%}$ (kips)	$F_{1\%}/F_{max}$	$F_{1\%}/F_{min}$
W18_1	0.28	3.72	1.40	1.50	0.40	0.56	1.73	0.47	1.15
W24_1	0.28	3.74	1.41	1.40	0.37	0.53	1.56	0.42	1.11
W36_1	0.28	3.84	1.44	1.35	0.35	0.51	1.44	0.38	1.07
W48_1	0.28	3.84	1.44	1.31	0.34	0.49	1.36	0.35	1.03
Average			1.42		0.37	0.52		0.41	1.09
COV			0.01		0.07	0.06		0.13	0.05

Table 3.11 presents a comparison of the three strength ratios for models with 24, 36, and 48 in. spaced models normalized by the model with 18 in. spaced model.

Table 3.11. Wall strength comparisons of 1 curtain of steel normalized by W18_1 strength

Model Designation	Peak F/F18	0.5% Drift F/F18	1% Drift F/F18
W24	1.00	0.93	0.90
W36	1.03	0.90	0.83
W48	1.03	0.87	0.79
Average	1.02	0.90	0.84
COV	0.01	0.03	0.7

W18_1	W48_1	Scale (ksi)
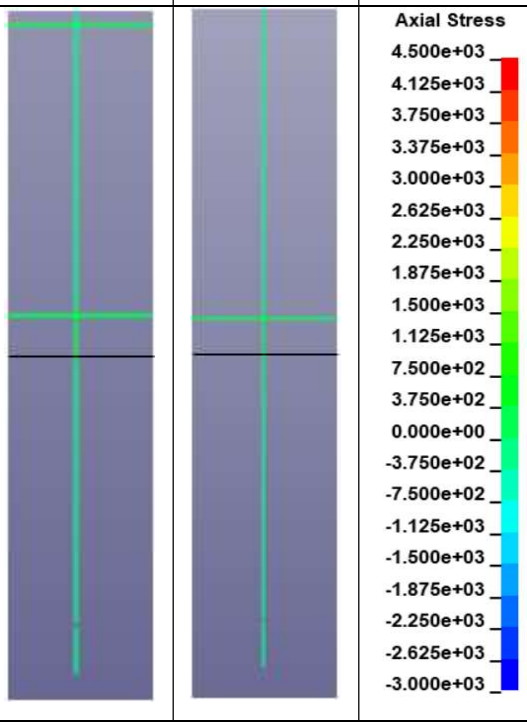		

Figure 3.31. Steel Strains at Peak Strength of W18_1 and W48_1
Black line indicates wall-foundation interface

W18_1	W48_1	Scale (ksi)
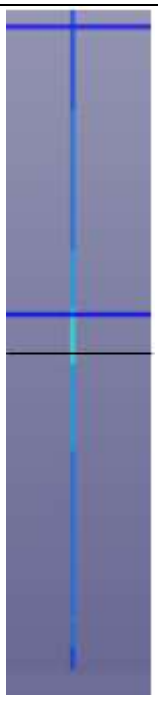	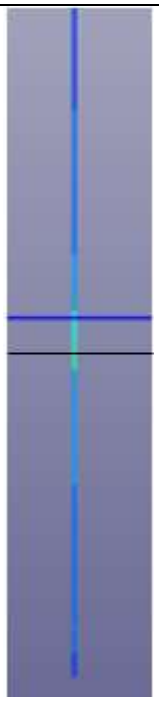	

Figure 3.32. Steel Strains at 0.5% drift of W18_1 and W48_1
Black line indicates wall-foundation interface

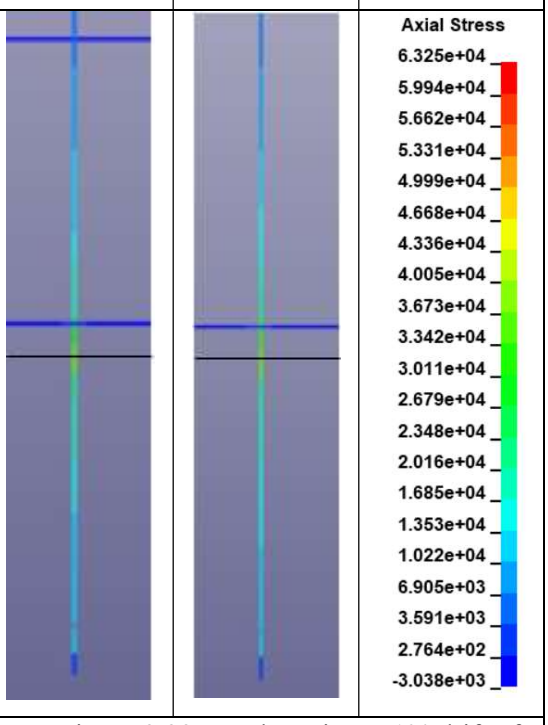

Figure 3.33. Steel Strains at 1% drift of W18_1 and W48_1
Black line indicates wall-foundation interface

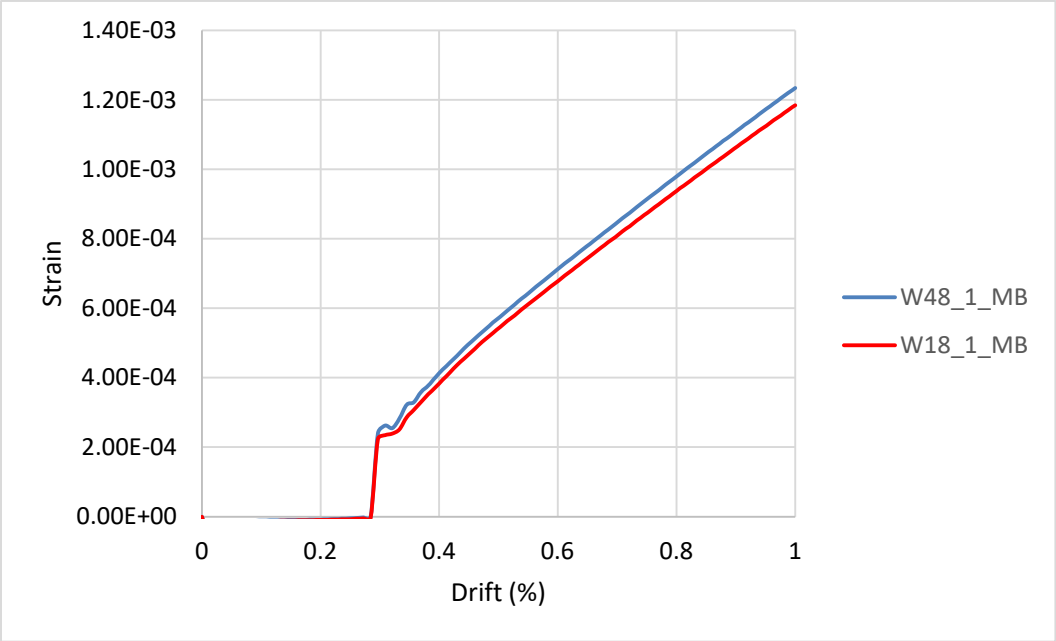

Figure 3.34. Strain histories between W18_1 and W48_1 for the extreme tensile reinforcing bar at the base of the wall

As steel spacing increases, there is a slight decrease in strength at 0.5% and 1.0% drift. The steel stresses are approximately the same for 18, 24, 36, and 48 in. spacings. The distribution of tensile damage values for the four spacings are approximately the same. Both see concentrated damage at the wall-foundation interface, but no change in tensile damage up the height of the wall.

From the results, the longitudinal bar spacing has little impact on the post-cracking strength capacity of the wall. A wall with 48 in. spaced bars, one curtain of steel, continuous reinforcement, and modeled bond should be suitable for the design of ICF walls.

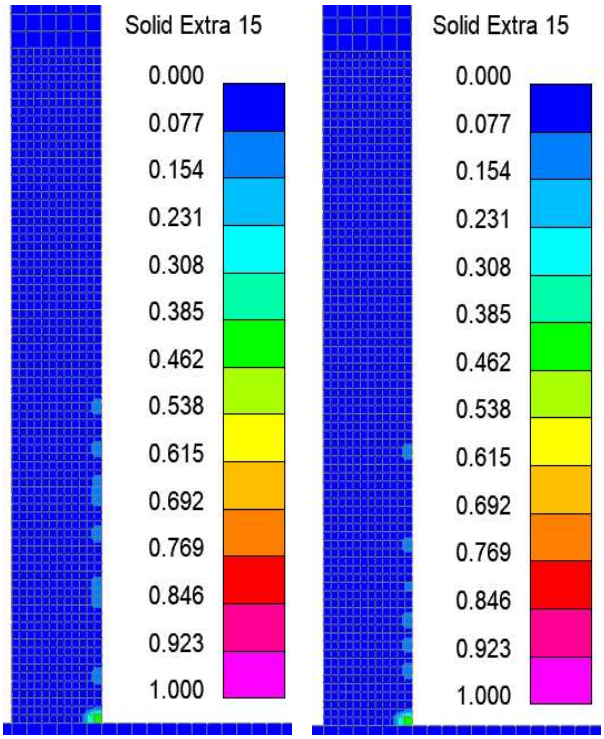

Figure 3.35. Tensile damage of W18_1 and W48_1 at peak strength for lower 40 in. of wall

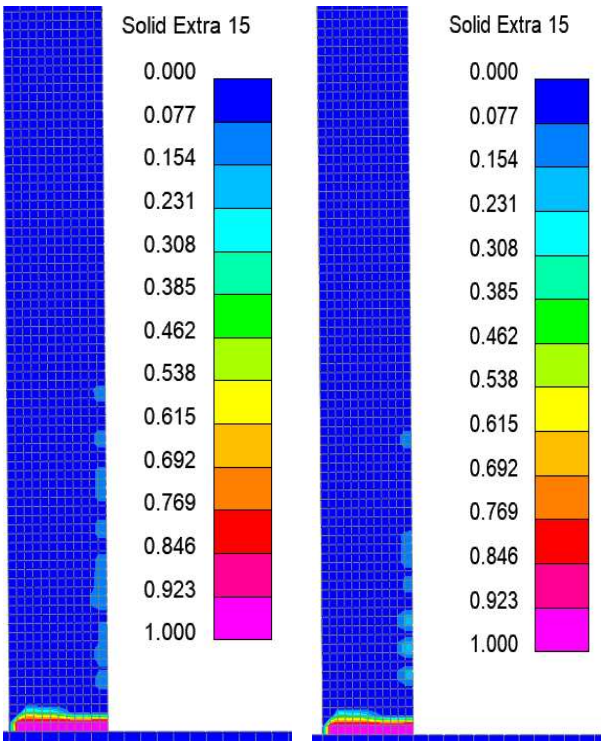

Figure 3.36. Tensile damage of W18_1 and W48_1 at 1% drift for lower 40 in. of wall

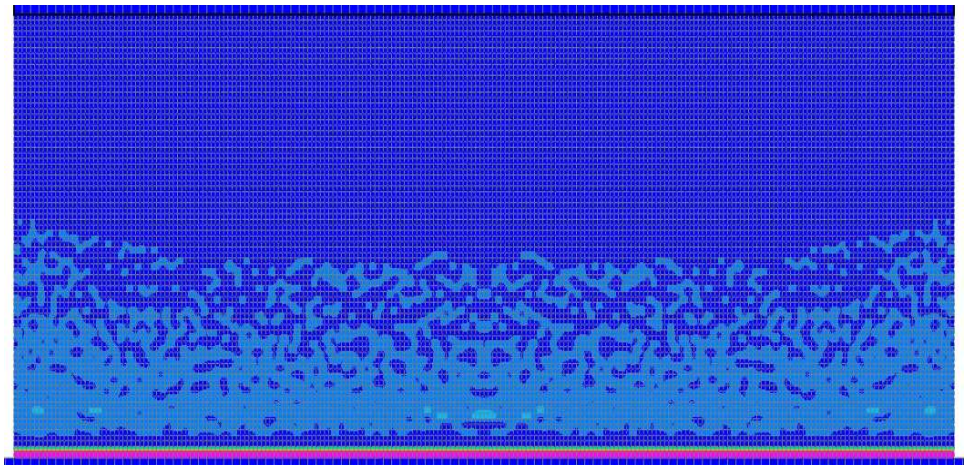

Figure 3.37. Tensile damage of W18_1 at 1% drift for lower 40 in. of wall

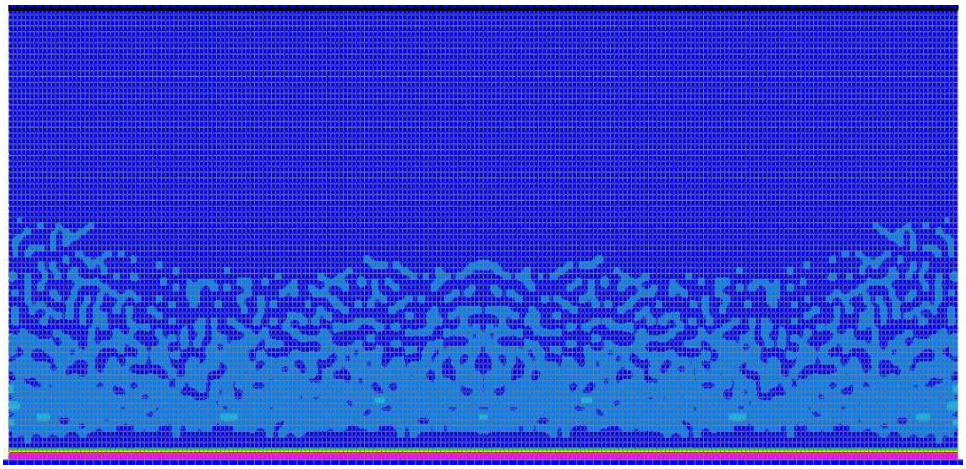

Figure 3.38. Tensile damage of W48_1 at 1% drift for lower 40 in. of wall

Chapter 4. PARAMETRIC STUDY OF FRC WALLS

This chapter focuses on the parametric study of FRC walls with minimal or no longitudinal reinforcement using LS-DYNA. All the models were subjected to combined axial and out-of-plane loading.

This parametric study investigates the following study parameters:

1. Fiber content percentage,
2. Continuous vs. spliced reinforcement
3. Bar spacing
4. The number of curtains of longitudinal reinforcement.

For each study parameter, the following are used to evaluate the differences in the structural behavior: (1) load-drift history, (2) longitudinal steel strains including maximum and history, and (3) tensile damage states as selected drift levels.

The information presented in this chapter is similar to Chapter 3. Section 4.1 focuses on the study parameters and model configurations investigated. Section 4.2 discusses the results from each set of parameters investigated.

4.1 Overview of Modeling Approach and Study Parameters of FRC Walls

Fiber contents of 0.5, 1.0, and 1.5% were investigated. The walls have the same geometry and wall detailing as the models in Chapter 3 and are shown in Figure 3.1.

For the FRC models, the foundation concrete strength was increased. The wall concrete with fiber results in a larger tensile strength which could result in unintended damage to the foundation. As such, the foundation concrete was increased to meet the tensile strength of the FRC to prevent full cracking.

The following parameters were studied to investigate the strength capacity and tensile damage of the concrete walls:

- Bar Spacing – Current ACI requirements limit the bar spacing to 18 in or less according to ACI 318-19 11.7.3.1. Masonry allows for bar spacings of 48 in and precast allows for bar spacings of 30 in. for interior walls according to ACI 318-19 11.7.3.2. Due to the large difference in maximum bar spacings, RC walls may not be economical relative to masonry or wood construction. The prior analyses from Chapter 3 indicate that bar spacing can affect strength capacity post concrete cracking, so spacings of 18 and 48 in. were studied. Spacings of 24 and 36 in. were not investigated, as the amount steel of does not have a significant impact on the flexural strength.
- Number of Curtains of Steel – The number of curtains of steel was studied to see the effect of steel location on the behavior of walls. Typical ICF construction uses a single curtain of steel at the center of the wall. The use of two curtains of steel places the reinforcement at the maximum moment arm where a single curtain of steel is located at the neutral axis depth and therefore does not provide flexural strength before cracking. The results from Chapter 3 indicate that the more longitudinal reinforcement in the wall, the wall will have larger post-peak strengths.
- Starter Bars Only – A starter bar starting in the foundation and terminating in the wall was studied. This was done to allow for the transfer of forces and to account for construction practices. Typically, the foundation is cast before the wall and has dowel bars sticking out of the foundation to connect with the wall reinforcement to allow for the transfer of forces. This configuration also has less reinforcement in the wall, as the reinforcing bars are only at the base of the wall.
- Fiber Content Percentage: The fiber content percentage was studied to see the impact of increasing fiber content percentage on wall behavior. Fiber content increases the tensile capacity of concrete which should allow for less reinforcement needed and potentially no reinforcement in the wall.
- Spliced or Continuous Bars – The effect of having a bar splice at the wall-foundation interface was studied. In typical construction, the foundation is cast first with dowel bars. The wall is then cast. The presence of spliced bars is to simulate construction practice. The results from Chapter 3 indicate that this should not have a large impact on wall behavior.

From the study parameters, FRC wall models were developed. Table 4.1 details the matrix for FRC walls. Each model is defined by the following parameters:

- Bar Spacing (0 (Starter Bars), 18, and 48 in.)
- Number of curtains of steel (0 (Starter Bars), 1, and 2 curtains)
- Type of bond equation applied (Bond Equation {MB} and not modelled {0})
- Spliced (S) or Continuous (C) reinforcement
- Fiber Content Ratio (0.0, 0.5, 1.0, and 1.5%)

For example, Model W18_1_B_C_1.0 has 18 in. spaced, continuous longitudinal bars with one curtain steel; the bars are modeled using perfect bond; the fiber content is 1.0% of the concrete volume.

Table 4.1. FRC models

Model ID	Splice (S) or Continuous (C)	Bar Spacing	Curtains of Steel	Fiber Content (%)
W18_1_MB_C_0.0	C	18	1	0.0
W18_2_MB_C_0.0			2	
W48_1_MB_C_0.0		48	1	
W48_2_MB_C_0.0			2	
W18_1_MB_S_0.5	S	18	1	0.5
W18_2_MB_S_0.5			2	
W48_1_MB_S_0.5		48	1	
W48_2_MB_S_0.5			2	
W0_0_0_0_0.5	C	Starter Bars	Starter Bars	0.5
W0_0_0_0_1.0				1
W0_0_0_0_1.5				1.5
W18_1_MB_C_0.5		18	1	0.5
W18_1_MB_C_1.0				1
W18_1_MB_C_1.5				1.5
W48_1_MB_C_0.5		48		0.5
W48_1_MB_C_1.0				1
W48_1_MB_C_1.5				1.5
W18_2_MB_C_0.5		18	2	0.5
W18_2_MB_C_1.0				1
W18_2_MB_C_1.5				1.5
W48_2_MB_C_0.5		48		0.5
W48_2_MB_C_1.0				1
W48_2_MB_C_1.5				1.5

The following results were used to compare the wall models:

- Normalized load-drift history to 1% drift – The reaction taken from the foundation base was normalized to the flexural strength at cracking (M_{CR}) which was plotted against the drift corresponding to displacement at the top of the wall.
- Tensile damage history – The tensile damage was obtained by utilizing history variable 15 created by the concrete constitutive model at peak strength and 1% drift.
- Steel stresses – The steel stresses were taken at the wall ends and wall-foundation interface at peak strength and 1.0% drifts.

4.2 SPLICED VS. CONTINUOUS REINFORCING BARS

In typical wall construction, the foundation is cast first with longitudinal starter bars extending from the foundation into the wall. The wall is then cast. Typical modeling uses continuous reinforcement to model longitudinal steel bar behavior. This study investigated the response of models with spliced and continuous longitudinal reinforcement at the wall-foundation interface.

For the models with the wall splice modeled, the lap length was determined from ACI 318-19 Table 25.4.2.3. This was done to ensure sufficient steel reinforcement was given to achieve maximum strengths. The spliced was modeled by having the bars spaced at one bar diameter length between another along the length of the wall. This length was also in accordance with ACI 318-19 Table 25.5.2.1 for bar splices. Table 4.2 lists the models investigated for this section

Table 4.2. List of spliced and continuous models with 0.5% fiber content

Model ID	Splice (S) or Continuous (C)	Bar Spacing	Curtains of Steel	Fiber Content (%)
W18_1_MB_S_0.5	S	18	1	0.5
W18_2_MB_S_0.5			2	
W48_1_MB_S_0.5		48	1	
W48_2_MB_S_0.5			2	
W18_1_MB_C_0.5	C	18	1	
W18_2_MB_C_0.5			2	
W48_1_MB_C_0.5		48	1	
W48_2_MB_C_0.5			2	

Figure 4.1 provides a comparison of the normalized load-drift history to 1% drift between the spliced and continuous bars with fiber content of 0.5%. Figure 4.2 and 4.3 provides the strains in the reinforcing bars at peak strength and 1% drift. Figure 4.4 provides the strain histories for the end reinforcing bars. Figures 4.5-4.10 provide the tensile damage histories at peak strength and 1% drift for the models with 48 in. spaced reinforcing bars (W48_2_MB_C_0.5 and W48_2_MB_S_0.5).

In Figure 4.1, the solid lines indicate continuous reinforcement; dashed lines indicate spliced reinforcement. There is no discernible difference between the continuous and spliced reinforcement. The model designations do not have the type of bond used, as all the models in this section have modeled bond. For FRC models, the bond equation was not modified to account for FRC, although research suggests fiber can improve bond response. The more steel reinforcement in the wall, the higher post-peak strength is observed, which is consistent with the findings in Chapter 3.

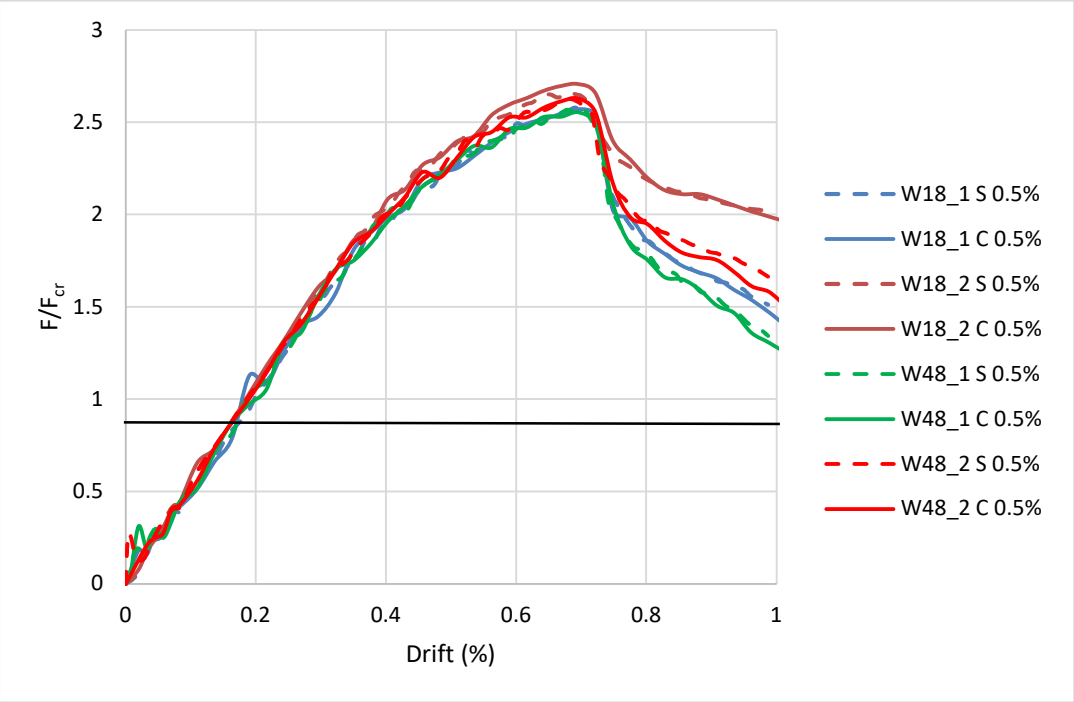

Figure 4.1. Load-drift history for spliced and continuous reinforcement

Table 4.3 provides values of the loading history at peak strength and 1% drift, which was the end of the simulation for all models. The models will use a shortened notation listing the spacing, the number of curtains, fiber content used, and spliced or continuous reinforcement. The following observations are made:

- The models all reached approximately the same peak strength, suggesting the peak strength does not depend on the presence of bar splice or continuous bars.

- The peak strength normalized by the force corresponding to developing the ACI cracking moment (F_{max}/F_{cr}) ranged from 2.55 to 2.65. The normalized strength was approximately the same for spliced and continuous reinforcing bar models.
- The post-cracking response is quantified by considering the ratio of the strength at 1% drift to the maximum strength ($F_{1\%}/F_{max}$). For models with spliced reinforcement, the average of this ratio was 0.63. For models with continuous reinforcement, the average of this ratio was 0.60. In all cases, the strength at 1% drift decreased with a reduction in the number of curtains of steel and spacing of the longitudinal reinforcement; this is the same conclusion for the models without fiber, discussed in Chapter 3.

Table 4.3. Load and Drift values at peak strength and simulation end of FRC spliced and continuous reinforcement

Model Designation	**Peak**			**1% Drift (End of Simulation)**	
	Drift (%)	**F_{max} (kips)**	**F_{max}/F_{cr}**	**$F_{1\%}$ (kips)**	**$F_{1\%}/F_{max}$**
W18_1_C_0.5	0.70	6.83	2.57	3.91	0.57
W18_2_C_0.5	0.70	7.19	2.70	5.28	0.73
W48_1_C_0.5	0.70	6.78	2.55	3.47	0.51
W48_2_C_0.5	0.70	6.98	2.63	4.20	0.60
Average			2.61		0.60
COV			0.03		0.15
W18_1_S_0.5	0.69	6.85	2.58	4.02	0.59
W18_2_S_0.5	0.69	7.05	2.65	5.36	0.76
W48_1_S_0.5	0.69	6.80	2.56	3.57	0.53
W48_2_S_0.5	0.69	6.98	2.63	4.42	0.63
Average			2.61		0.63
COV			0.02		0.15

Table 4.4 presents a comparison of the two strength ratios for the companion models, where companion models have the reinforcement with (F_s) and without a splice (F_c).

Table 4.4. Wall strength comparisons of spliced and continuous reinforcement

Model Designation	**Peak F_s/F_c**	**1% Drift F_s/F_c**
W18_1	1.00	1.03
W18_2	0.98	1.02
W48_1	1.00	1.03
W48_2	1.00	1.05
Average	1.00	1.03
COV	0.01	0.02

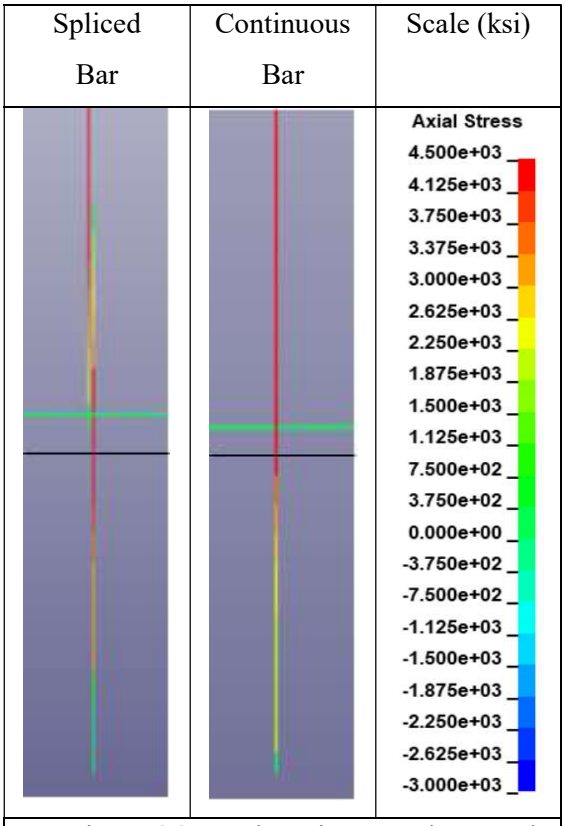

Figure 4.2. Steel Strains at peak strength of W48_2 companion models
Black line indicates wall-foundation interface

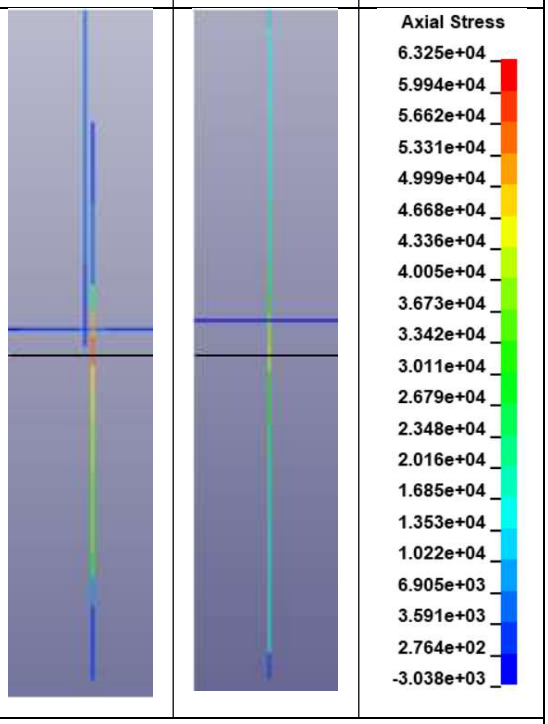

Figure 4.3. Steel Strains at 1% drift of W48_2 companion models
Black line indicates wall-foundation interface

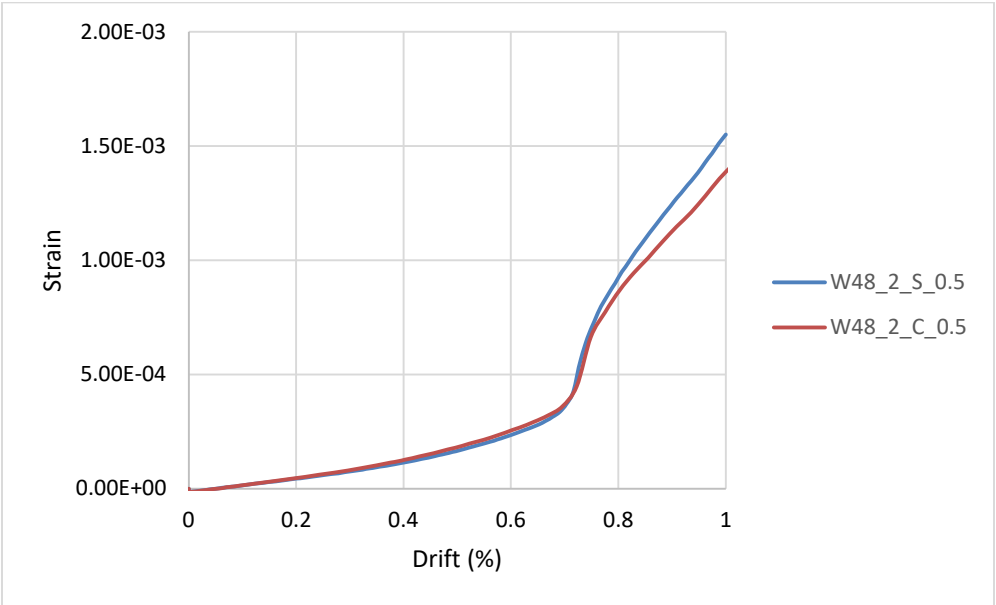

Figure 4.4. Strain histories for spliced and continuous reinforcement models for the extreme tensile reinforcing bar at the base of the wall

The spliced and continuous bar models have approximately the same strengths at peak and 1% drift. The steel stresses do not reach yield in any of the simulations. At peak, the steel strains are very similar and are less than 5 ksi.

The tensile damage histories are the same for spliced and continuous bar models, as there is distributed tensile damage (cracking) throughout the height of the wall as seen in Figure 4.6. This is likely due to the FRC model allowing for more concrete tensile residual capacity post-cracking.

From the results, the presence of a bar splice does not have a large effect on the strength, force-drift response, and cracking (distribution of damage) of the wall models. Because it is simpler and requires less computational time to model continuous reinforcement than spliced reinforcement, continuous reinforcement will be used for the remainder of this parametric study.

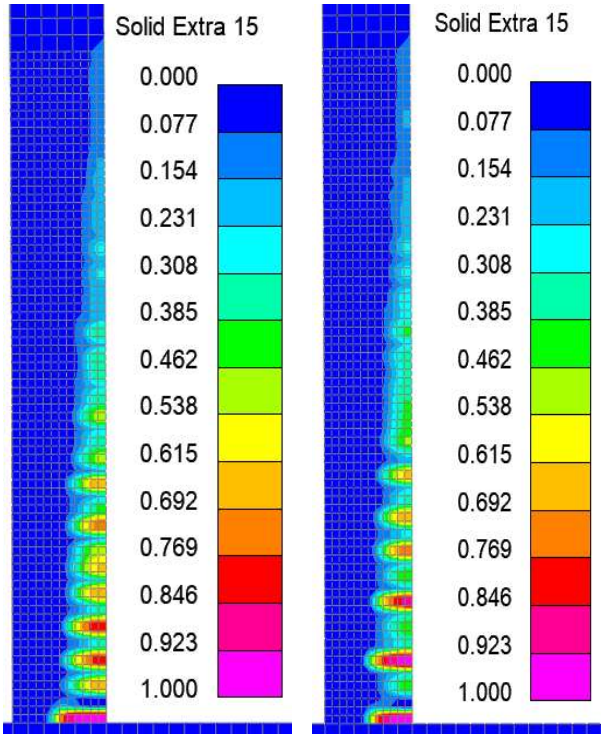

Figure 4.5. Tensile damage of W48_2_S and W48_2_C at peak strength for lower 40 in. of wall

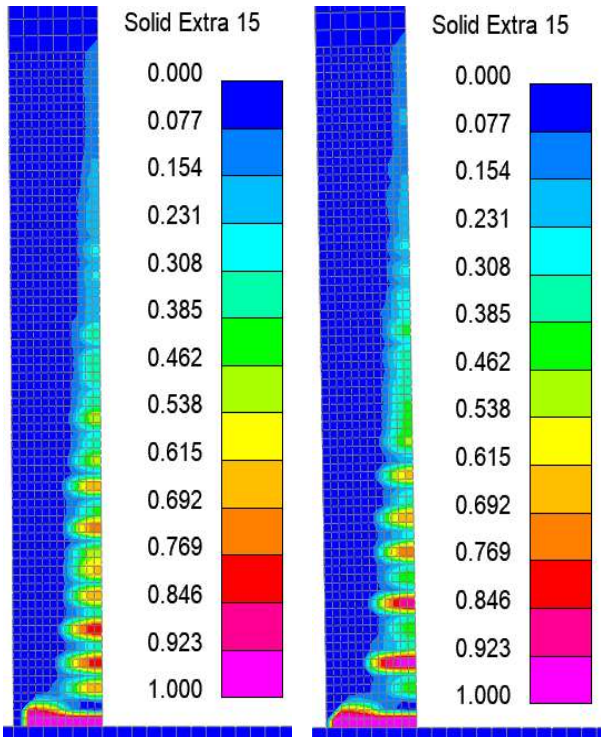

Figure 4.6. Tensile damage of W48_2_S and W48_2_C at 1% drift for lower 40 in. of wall

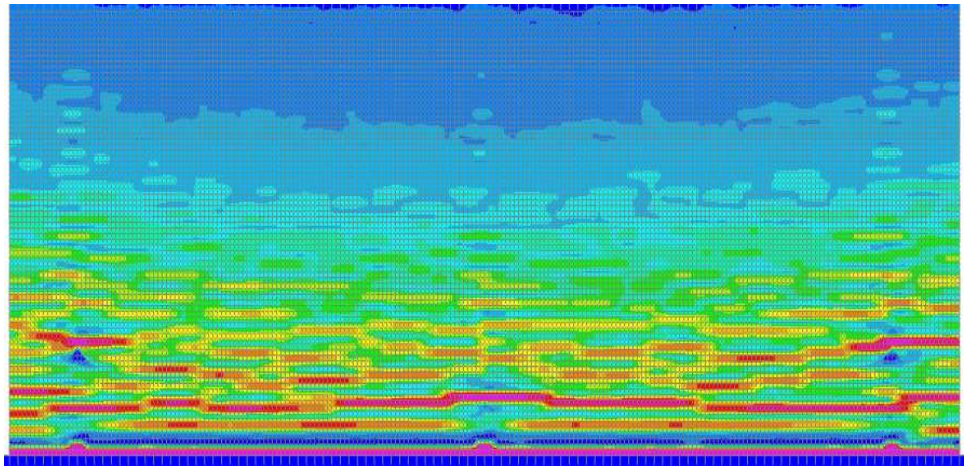

Figure 4.7. Tensile damage of W48_2_S at peak strength for lower 40 in. of wall

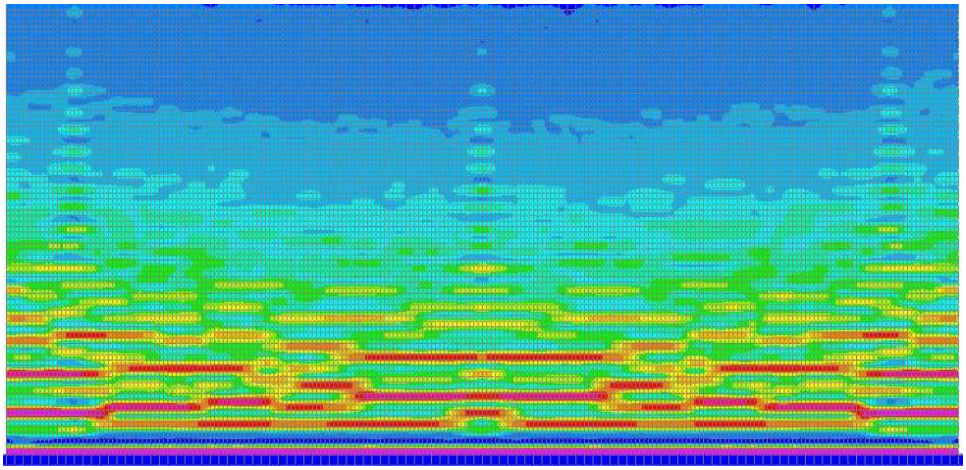

Figure 4.8. Tensile damage of W48_2_C at peak strength for lower 40 in. of wall

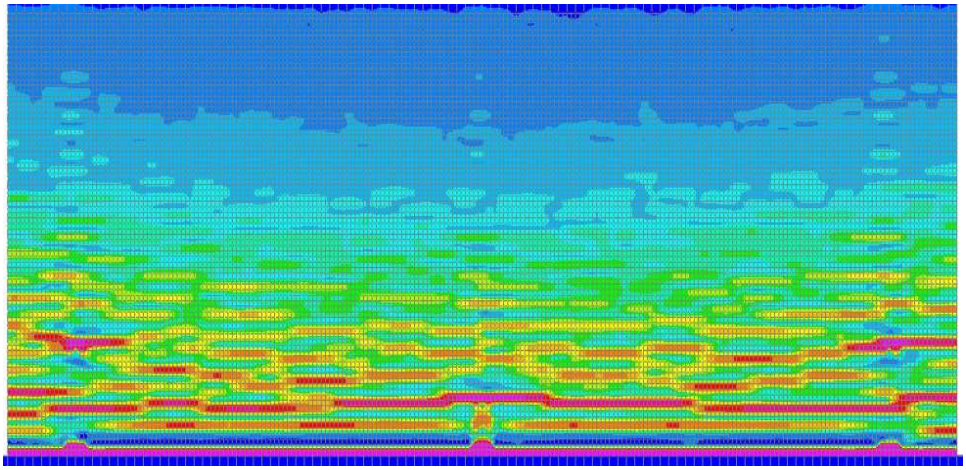

Figure 4.9. Tensile damage of W48_2_S at 1% drift for lower 40 in. of wall

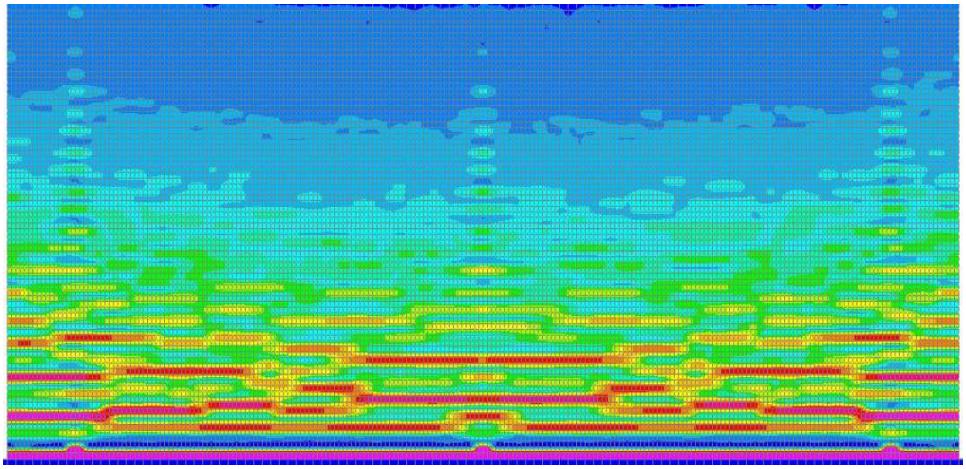

Figure 4.10. Tensile damage of W48_2_C at 1% drift for lower 40 in. of wall

4.3 FIBER CONTENT

FRC concrete has more tensile capacity than RC because the fibers reduce the crack openings of the concrete, allowing for the concrete to carry more tension. Various fiber content percentages were examined to see the overall effect of having fiber in concrete. The modeling of FRC is outlined in Section 2.6. This section investigated the response of models with varying fiber content percentages. The evaluation compares the force-drift response, longitudinal steel stresses, and the crack pattern as determined by the tension damage parameter.

The FRC models were modeled for fiber content percentages of 0.5, 1.0, and 1.5%. These percentages were determined from the data from Marcalikova et al. (2020) and Woo et al. (2014) as they also investigate fiber content percentages of the same amount. Table 4.5 lists the models compared in this section.

Table 4.5. List of models for comparison of fiber content

Model ID	Splice (S) or Continuous (C)	Bar Spacing	Curtains of Steel	Fiber Content (%)
W18_1_MB_C_0.0	C	18	1	0.0
W18_2_MB_C_0.0			2	
W48_1_MB_C_0.0		48	1	
W48_2_MB_C_0.0			2	
W0_0_0_0_0.5		Starter Bars	Starter Bars	0.5
W0_0_0_0_1.0				1
W0_0_0_0_1.5				1.5
W18_1_MB_C_0.5		18	1	0.5
W18_1_MB_C_1.0				1
W18_1_MB_C_1.5				1.5
W48_1_MB_C_0.5		48		0.5
W48_1_MB_C_1.0				1
W48_1_MB_C_1.5				1.5
W18_2_MB_C_0.5		18	2	0.5
W18_2_MB_C_1.0				1
W18_2_MB_C_1.5				1.5
W48_2_MB_C_0.5		48		0.5
W48_2_MB_C_1.0				1
W48_2_MB_C_1.5				1.5

Figure 4.11 provides a comparison of the normalized load-drift history to 1% drift between RC and FRC with 0.5, 1.0, and 1.5% fiber content. Figures 4.12 and 4.13 provide the strains in the reinforcing bars at peak strength and 1% drift. Figure 4.14 provides the strain histories for the end reinforcing bars. Figures 4.15 – 4.24 provide the tensile damage histories at peak strength and 1% drift between the 48 in. spaced reinforcing bar wall models (W48_1_MB__C_0.0, W48_1_MB_C_0.5, W48_1_MB_C_1.0, and W48_1_MB_C_1.5).

Table 4.6 provides values of the loading history at peak strength and simulation end. The models will use a shortened notation listing the spacing, number of curtains, and fiber content used. The following observations are made:

- The FRC models achieved larger strengths than the RC models. Increasing fiber content percentage also leads to an increase in strength as well.
- The peak strength normalized by the force corresponding to developing the ACI cracking moment (F_{max}/F_{cr}) ranged from 1.40 to 1.48 for RC models, 2.55 to 2.7 for 0.5% fiber content, 3.02 to 3.19 for 1.0% fiber content, and 3.44 to 3.65 for 1.5% fiber content. The average ratios were 1.44 for RC, 2.60 for 0.5% fiber content, 3.08 for 1.0% fiber content, and 3.51 for 1.5% fiber content. Overall, increasing fiber content percentage leads to a higher peak strength in the wall.
- The post-cracking response is quantified by considering the ratio of the strength at 1% drift to the maximum strength ($F_{1\%}/F_{max}$). The average ratios were 0.53 for RC, 0.57 for 0.5% fiber content, 0.70 for 1.0% fiber content, and 0.74 for 1.5% fiber content. An increase in fiber content percentage leads to a larger post-peak strength at 1% drift.

In Figure 4.11, the solid lines indicate 0.5% fiber content, double lines indicate 0.0% fiber content, dashed lines indicated 1.0% fiber content, and dotted lines indicated 1.5% fiber content. An increase in fiber content leads to an increase in strength. The model designations do not have the type of bond used and spliced or continuous reinforcement, as all the models in this section have modeled bond and continuous reinforcement. For FRC models, the bond equation was not modified to account for FRC, although research suggests fiber can improve bond response. The more steel in the wall, the higher post-peak strength is observed, which is consistent with the findings in Chapter 3.

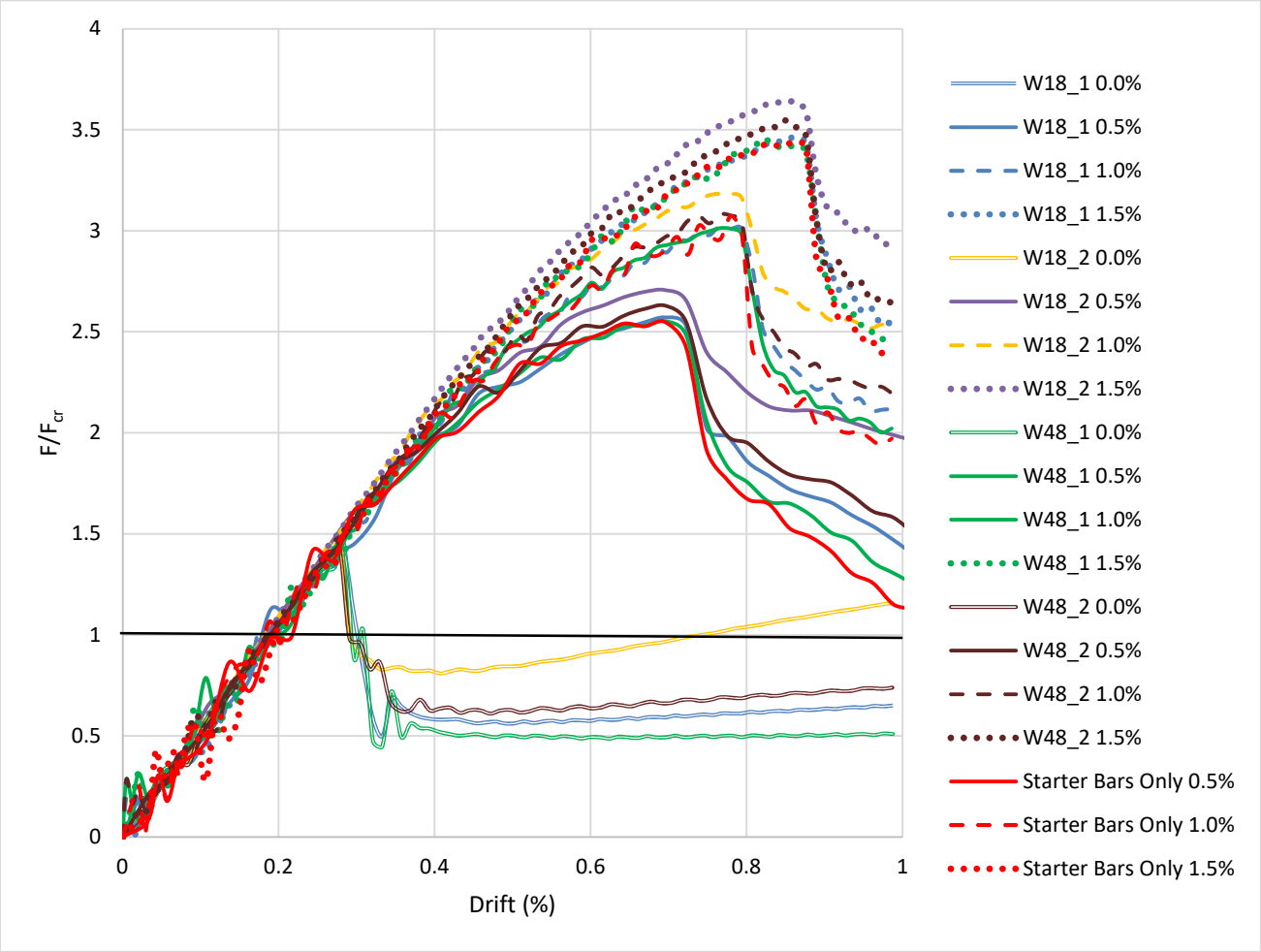

Figure 4.11. Load-drift history for RC, 0.5, 1.0, and 1.5% fiber content

Table 4.6. Load and Drift values at peak strength and simulation end of FRC fiber content

Model Designation	Peak			1% Drift (End of Simulation)	
	Drift (%)	F_{max} (kips)	F_{max}/F_{cr}	$F_{1\%}$ (kips)	$F_{1\%}/F_{max}$
W18_1_0.0	0.28	3.72	1.40	1.73	0.47
W18_2_0.0	0.28	3.93	1.48	3.08	0.78
W48_1_0.0	0.28	3.84	1.45	1.36	0.35
W48_2_0.0	0.28	3.78	1.43	1.97	0.52
Average			1.44		0.53
COV			0.02		0.34
W0_0_0.5	0.70	6.77	2.55	3.06	0.45
W18_1_0.5	0.70	6.83	2.57	3.91	0.57
W18_2_0.5	0.70	7.19	2.70	5.28	0.73
W48_1_0.5	0.70	6.78	2.55	3.47	0.51
W48_2_0.5	0.70	6.98	2.63	4.20	0.60
Average			2.60		0.57
COV			0.02		0.18
W0_0_1.0	0.78	8.17	3.08	5.24	0.64
W18_1_1.0	0.77	8.03	3.03	5.63	0.70
W18_2_1.0	0.78	8.46	3.19	6.72	0.79
W48_1_1.0	0.78	8.01	3.02	5.37	0.67
W48_2_1.0	0.77	8.19	3.09	5.84	0.71
Average			3.08		0.70
COV			0.02		0.08
W0_0_1.5	0.86	9.13	3.44	6.35	0.70
W18_1_1.5	0.86	9.20	3.47	6.77	0.74
W18_2_1.5	0.86	9.66	3.65	7.78	0.81
W48_1_1.5	0.82	9.18	3.46	6.50	0.71
W48_2_1.5	0.85	9.42	3.55	7.03	0.75
Average			3.51		0.74
COV			0.02		0.06

Table 4.7 presents a comparison of the two strength ratios for companion models of fiber contents of 0.5, 1.0, and 1.5% to RC models.

Table 4.7. Wall strength comparisons of FRC and RC concrete

Model Designation	Peak F_{FRC}/F_{RC}	1% Drift F_{FRC}/F_{RC}
W18_1_0.5	1.84	2.26
W18_2_0.5	1.83	1.71
W48_1_0.5	1.77	2.55
W48_2_0.5	1.85	2.13
Average	1.82	2.16
COV	0.02	0.16
W18_1_1.0	2.16	3.25
W18_2_1.0	2.15	2.18
W48_1_1.0	2.09	3.95
W48_2_1.0	2.17	2.96
Average	2.14	3.09
COV	0.02	0.24
W18_1_1.5	2.47	3.91
W18_2_1.5	2.46	2.52
W48_1_1.5	2.39	4.78
W48_2_1.5	2.49	3.56
Average	2.45	3.69
COV	0.02	0.25

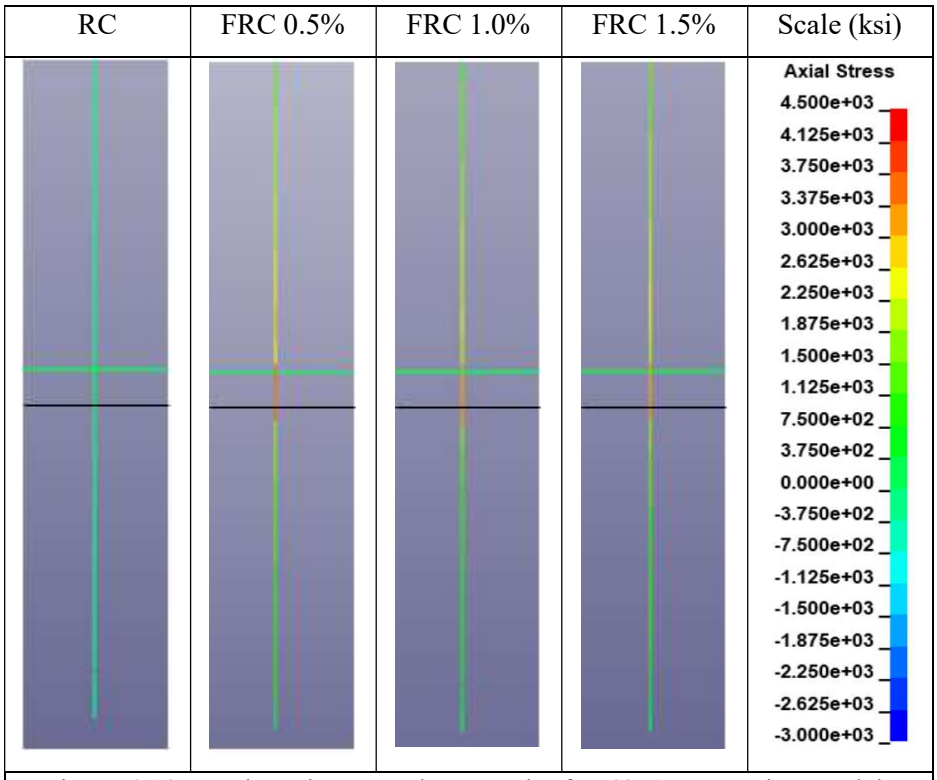

Figure 4.12. Steel Strains at Peak Strength of W48_1 companion models
Black line indicates wall-foundation interface

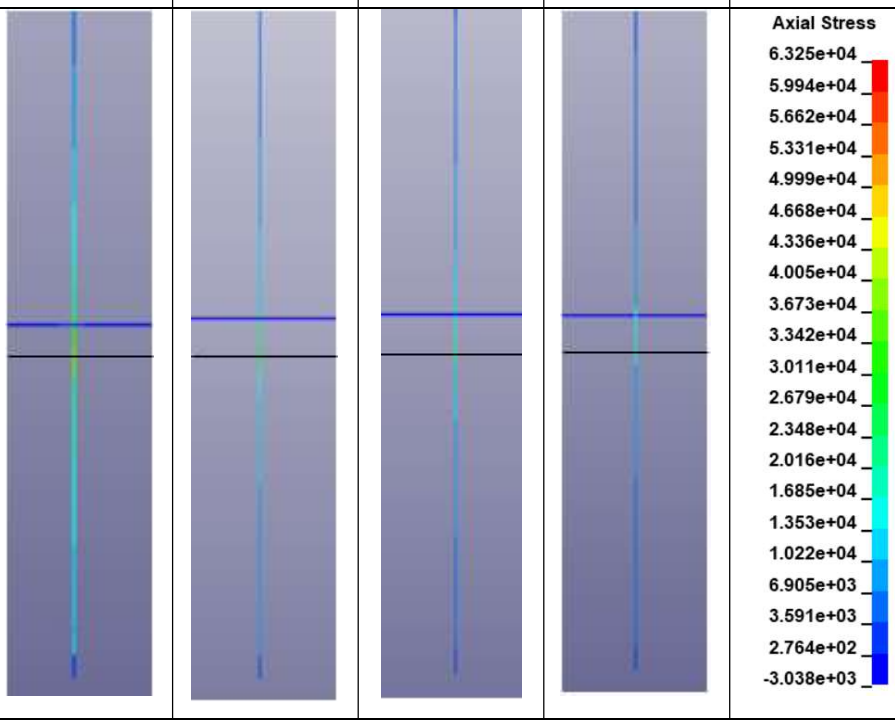

Figure 4.13. Steel Strains at 1% drift of W48_1 companion models
Black line indicates wall-foundation interface

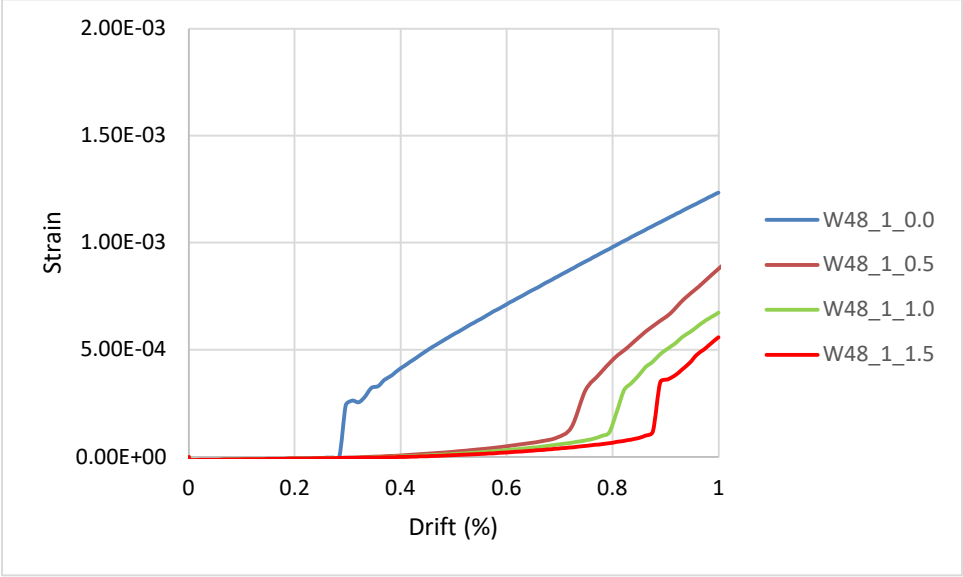

Figure 4.14. Strain histories for W48_1 companion models with different fiber content percentages for the extreme tensile reinforcing bar at the base of the wall

The FRC models have larger strengths at peak and 1% drift than RC models. In addition, increasing fiber content leads to larger strengths at peak and 1% drift as well. At peak strength, there is little steel stress occurring in longitudinal reinforcement. At 1% drift, the RC model's longitudinal reinforcement has more stress than the FRC models. The tensile damage histories are the same for all three fiber content percentages and models with fiber see much more distributed damage along the height of the wall when compared to the RC models.

From the results, increasing fiber contents leads to higher peak strengths and residual capacity at 1% drift. All three fiber content percentages are suitable for the design of ICF walls. A fiber content of 0.5% will be used for the remainder of the thesis, as it provides adequate strength and is the most economical choice of the three fiber content percentages.

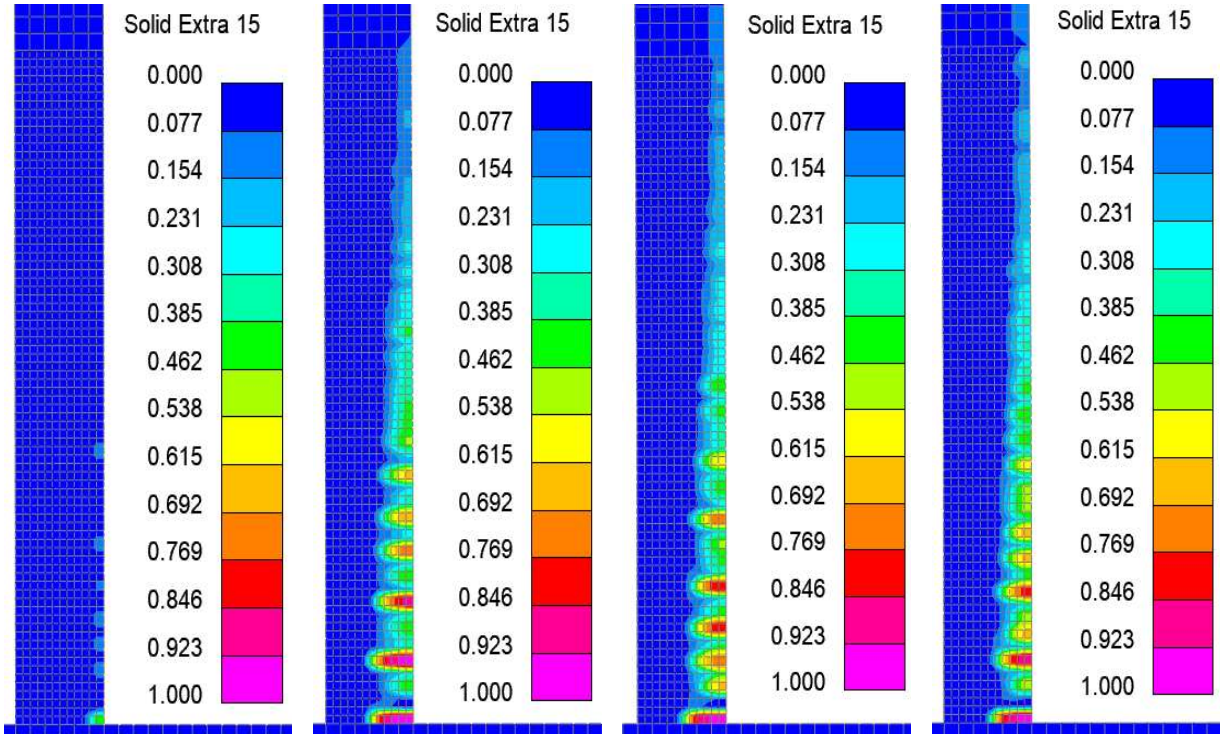

Figure 4.15. Tensile damage of W48_1_0.0, W48_1_0.5, W48_1_1.0, and W48_1_1.5 at peak strength for lower 40 in. of wall

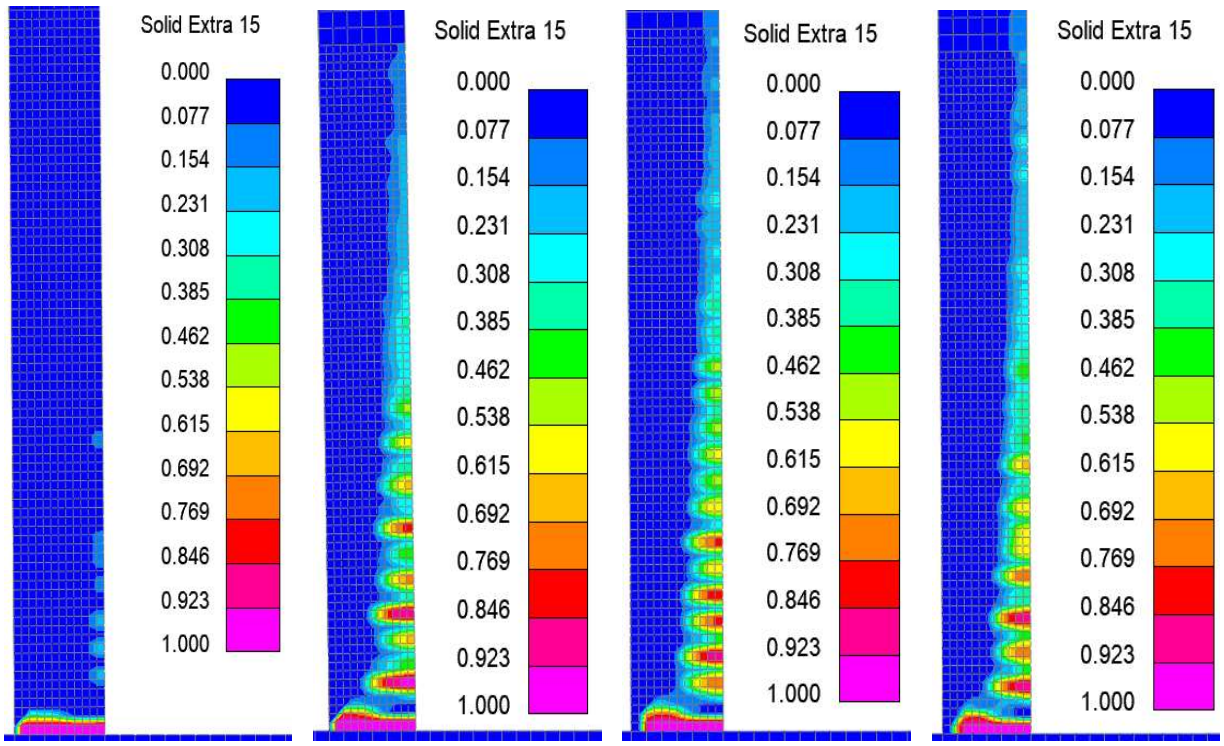

Figure 4.16. Tensile damage of W48_1_0.0, W48_1_0.5, W48_1_1.0, and W48_1_1.5 at 1% drift for lower 40 in. of wall

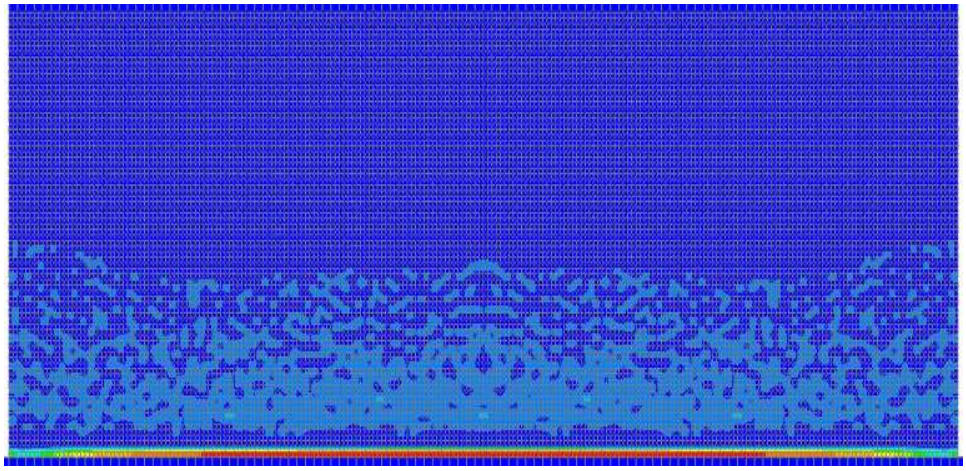

Figure 4.17. Tensile damage of W48_1_0.0 at peak strength for lower 40 in. of wall

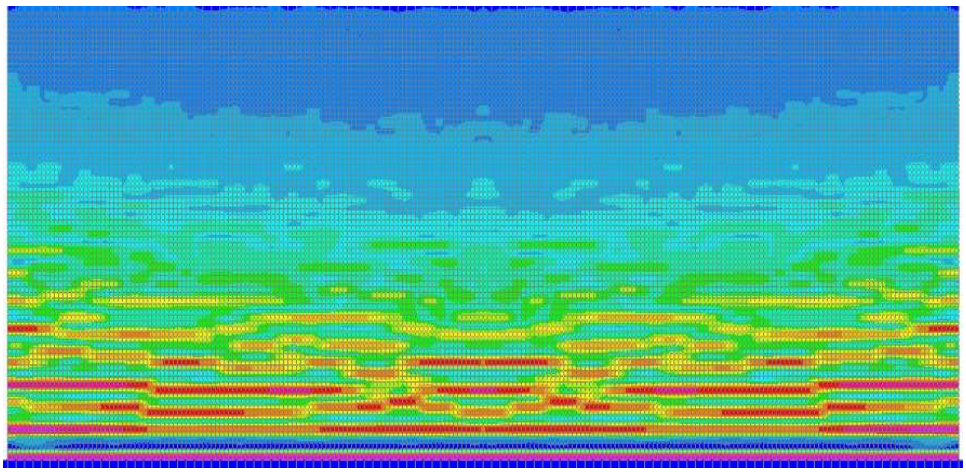

Figure 4.18. Tensile damage of W48_1_0.5 at peak strength for lower 40 in. of wall

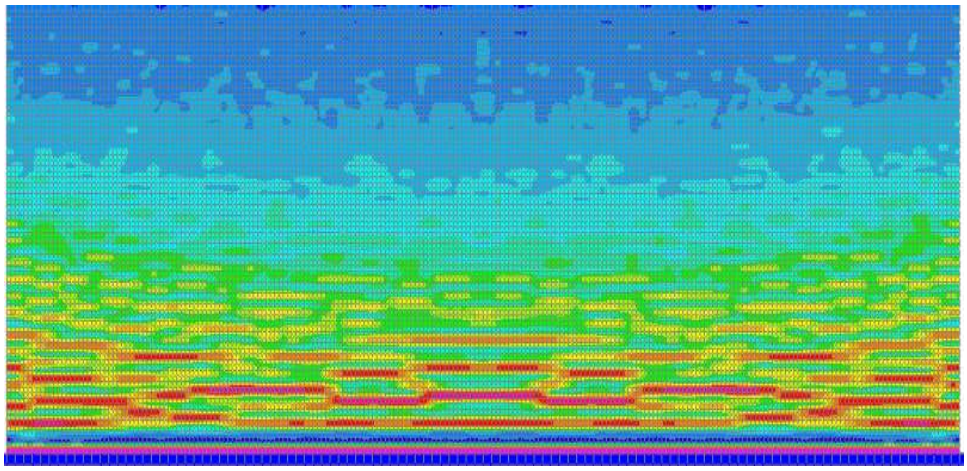

Figure 4.19. Tensile damage of W48_1_1.0 at peak strength for lower 40 in. of wall

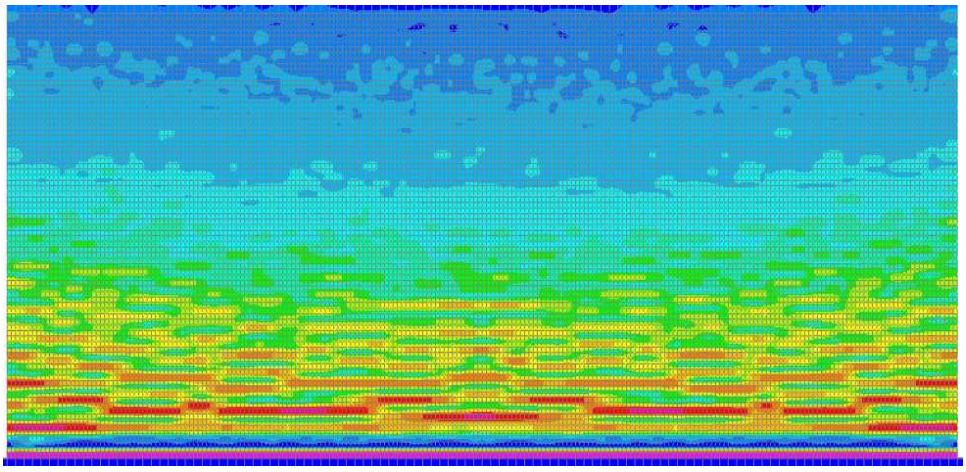

Figure 4.20. Tensile damage of W48_1_1.5 at peak strength for lower 40 in. of wall

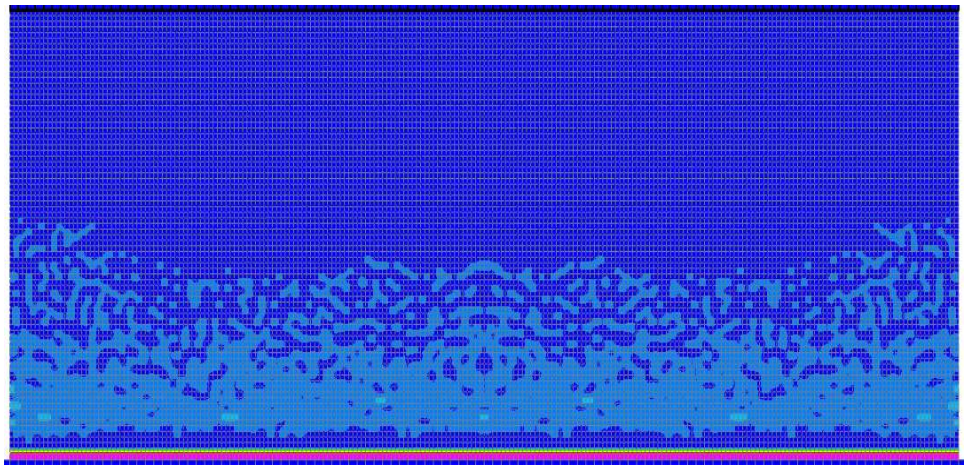

Figure 4.21. Tensile damage of W48_1_0.0 at 1% drift for lower 40 in. of wall

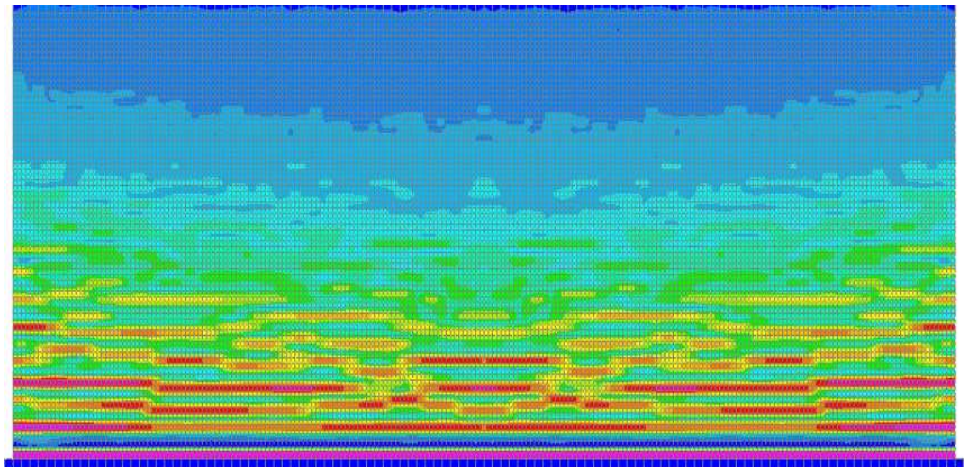

Figure 4.22. Tensile damage of W48_1_0.5 at 1% drift for lower 40 in. of wall

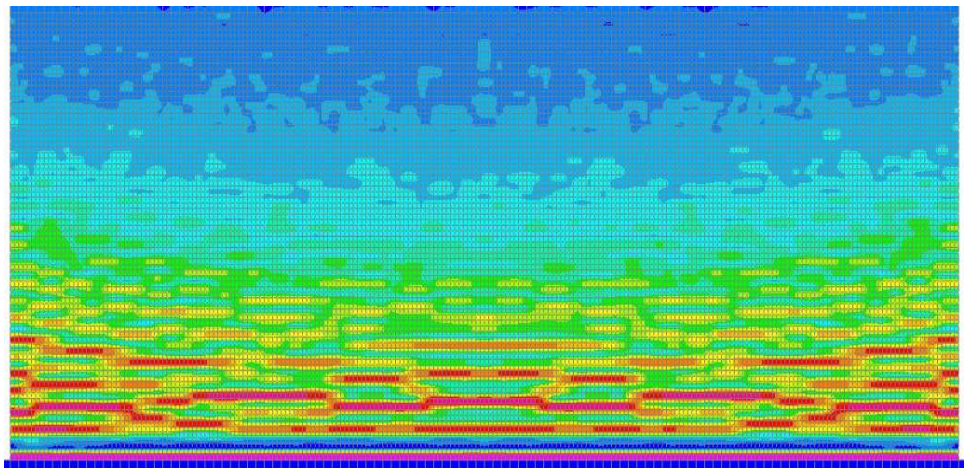

Figure 4.23. Tensile damage of W48_1_1.0 at 1% drift for lower 40 in. of wall

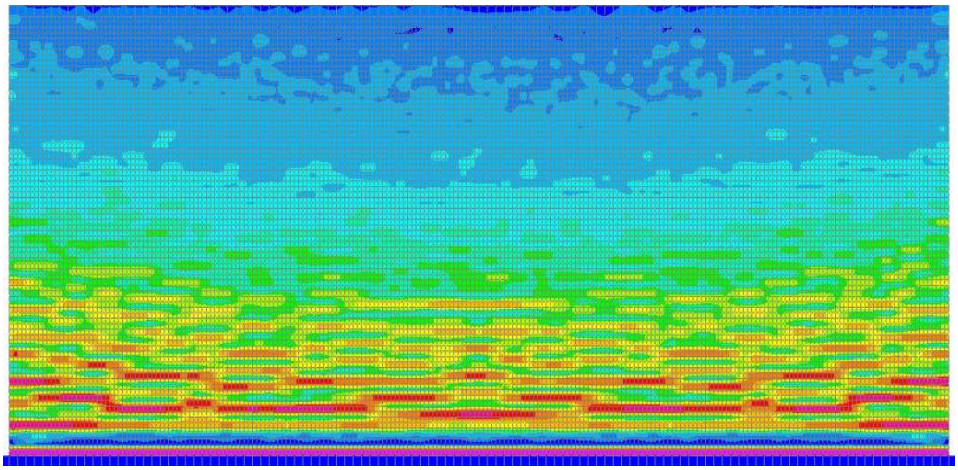

Figure 4.24. Tensile damage of W48_1_1.5 at 1% drift for lower 40 in. of wall

4.4 Reinforcement Configuration

Traditional RC walls use reinforcement to increase the tensile capacity of RC structures. In FRC, the concrete has an increased tensile capacity which could allow for walls with reinforcement ratios and spacings that do not meet ACI 318-19 requirements. This section investigates spacings of 18 in. with one and two curtains of steel, 48 in. with one and two curtains of steel, and starter bars only in the wall. The evaluation compares the force-drift response, the crack pattern as determined by the tension damage parameter, and steel strains.

The only spacing configurations that meet ACI 318-19 requirements are the 18 in. spaced models. In section 3.3, it was found that walls with 48 in. spacing with one curtain of steel for RC walls was sufficient for ICF construction. Due to increased tensile capacity from FRC, walls with starter bars may be sufficient for ICF construction. Table 4.8 lists the models used for comparison in this section.

Table 4.8. List of models for comparison of reinforcement configuration

Model ID	Splice (S) or Continuous (C)	Bar Spacing	Curtains of Steel	Fiber Content (%)
W0_0_0_0_0.5	C	Starter Bars	Starter Bars	0.5
W18_1_MB_C_0.5		18	1	
W48_1_MB_C_0.5		48		
W18_2_MB_C_0.5		18	2	
W48_2_MB_C_0.5		48		

Figure 4.25 provides a comparison of the normalized load-drift history to 1% drift for starter bars only, 18 in. spacing with one and two curtains of steel, and 48 in. spacing with one and two curtains of steel. Figures 4.26 - 4.31 provide the tensile damage histories at peak strength and 1% drift between the starter bars and 48 in. spaced single curtain reinforcing bar wall models (W0_0_0_0_0.5 and W48_1_MB_C_0.5).

Table 4.9 provides values of the loading history at full cracking and simulation end. The models will use a shortened notation listing the spacing, number of curtains, and fiber content. The following observations are made:

- Higher peak strength was achieved with more longitudinal steel reinforcement in the wall.
- The peak strength normalized by the force corresponding to developing the ACI cracking moment (F_{max}/F_{cr}) ranged from 2.55 to 2.70, and the average ratio was 2.60. Overall, increasing the amount of steel in the wall increases the peak strength.
- The post-cracking response is quantified by considering the ratio of the strength at 1% drift to the maximum strength ($F_{1\%}/F_{max}$). The ratios ranged from 0.45 to 0.73, and the average ratio was 0.57. Increasing the amount of steel in the wall increased post-peak strength in the wall.

In Figure 4.25, the solid lines one curtain of steel, the dashed lines indicate two curtains of steel, brown indicates starter bars only, red indicates 48 in. spacings and blue indicates 18 in. spacings. An increase in fiber content leads to an increase in strength. The model designations do not have the type of bond used and spliced or continuous reinforcement, as all the models with reinforcement in this section have modeled bond and continuous reinforcement. For FRC models, the bond equation was not modified to account for FRC, although research suggests fiber can

improve bond response. The more steel in the wall, the higher post-peak strength is observed, which is consistent with the findings in Chapter 3.

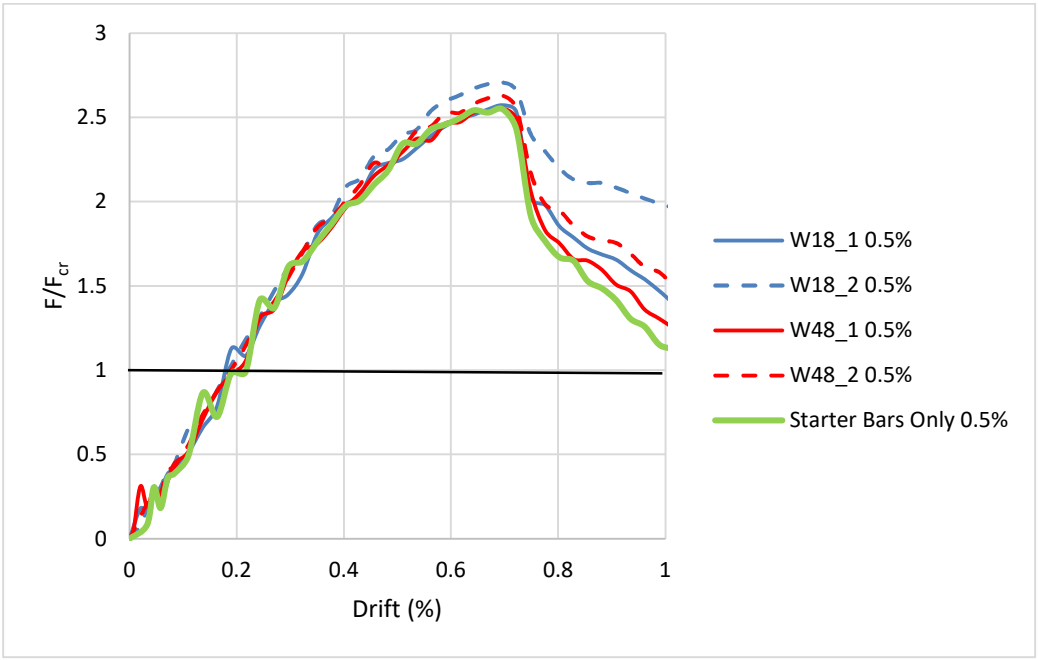

Figure 4.25. Load-drift history for various reinforcement configurations

Table 4.9. Load and Drift values at peak strength and simulation end of FRC reinforcement layouts

Model Designation	ρ_l (%)	Peak			1% Drift (End of Simulation)	
		Drift (%)	F_{max} (kips)	F_{max}/F_{cr}	$F_{1\%}$ (kips)	$F_{1\%}/F_{max}$
W0_0_0.5	0.00	0.70	6.77	2.55	3.06	0.45
W18_1_0.5	0.21	0.70	6.83	2.57	3.91	0.57
W18_2_0.5	0.42	0.70	7.19	2.70	5.28	0.73
W48_1_0.5	0.09	0.70	6.78	2.55	3.47	0.51
W48_2_0.5	0.18	0.70	6.98	2.63	4.20	0.60
Average				2.60		0.57
COV				0.02		0.18

The FRC models with more reinforcement have larger strengths at peak and post-peak. The tensile damage histories for the reinforcement configurations are approximately the same. There is

distributed damage along the height of the wall with the portion at the wall-foundation interface having the most amount of damage.

From the results, increasing the amount of longitudinal reinforcement increases the strength capacity of the wall. Walls without any steel reinforcement achieve similar peak strengths to those with steel reinforcement. All reinforcement configurations are suitable for the design of ICF walls. A FRC wall without any steel reinforcement is recommended for ICF construction, as it provides adequate strength and is the most economical choice of any steel reinforcement configuration.

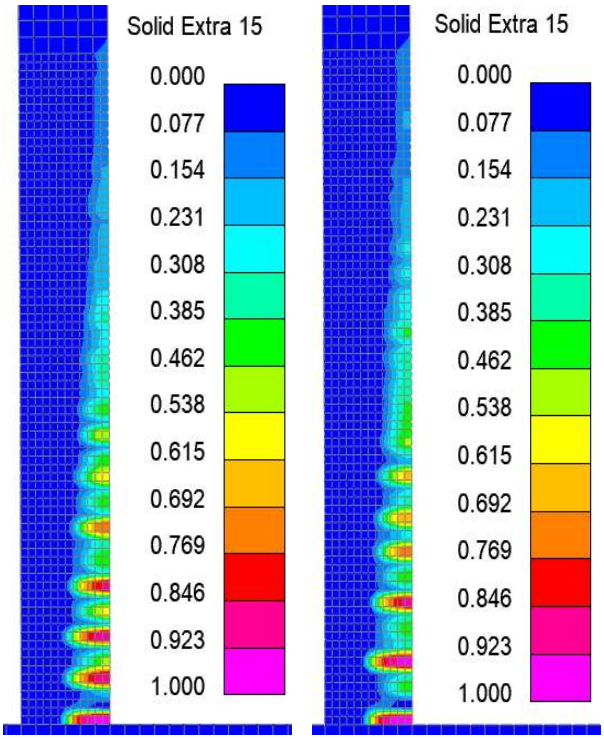

Figure 4.26. Tensile damage of W0_0_0.5 and W48_1_0.5 at peak strength for lower 40 in. of wall

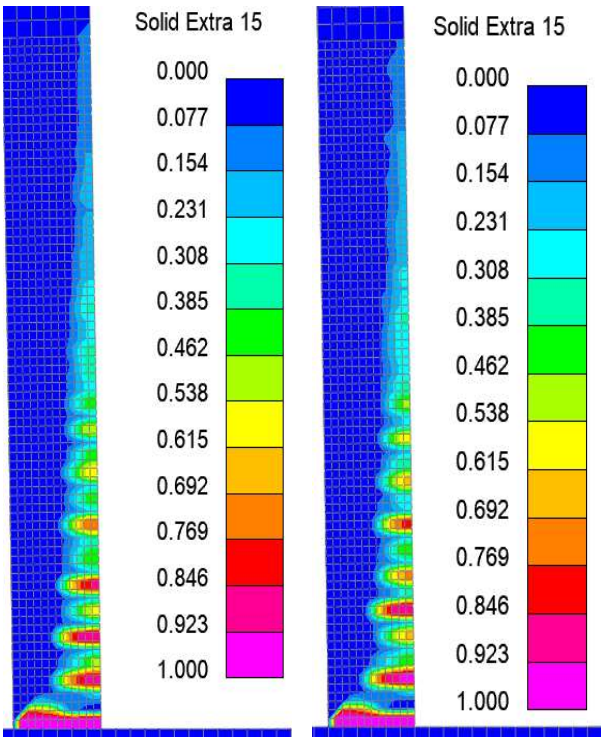

Figure 4.27. Tensile damage of W0_0_0.5 and W48_1_0.5 at 1% drift for lower 40 in. of wall

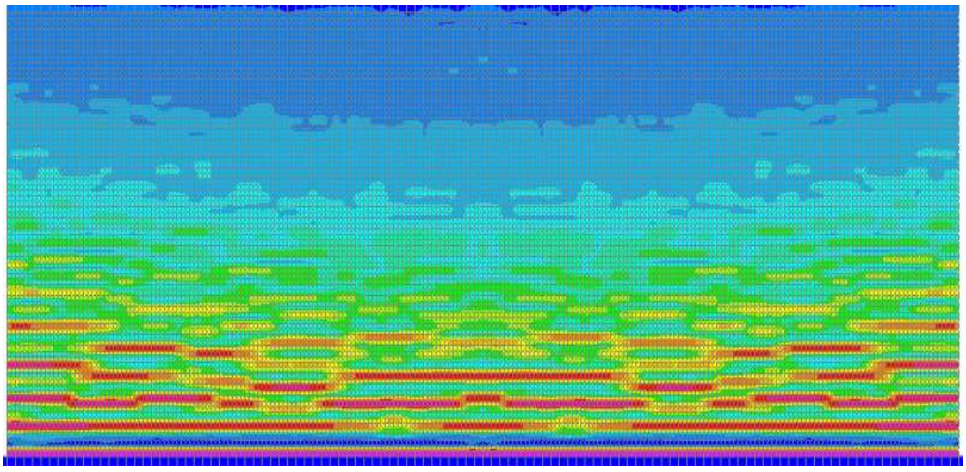

Figure 4.28. Tensile Damage of W0_0_0.5 at peak strength for lower 40 in. of wall

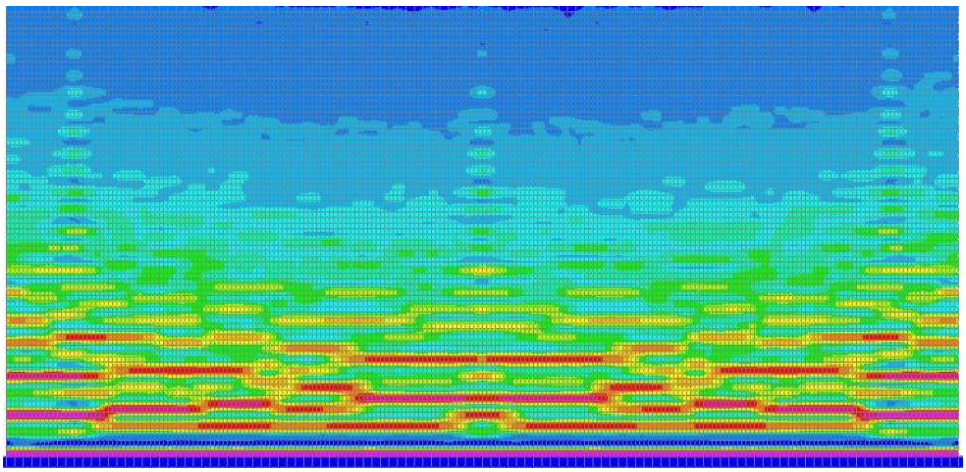

Figure 4.29. Tensile Damage of W48_1_0.5 at peak strength for lower 40 in. of wall

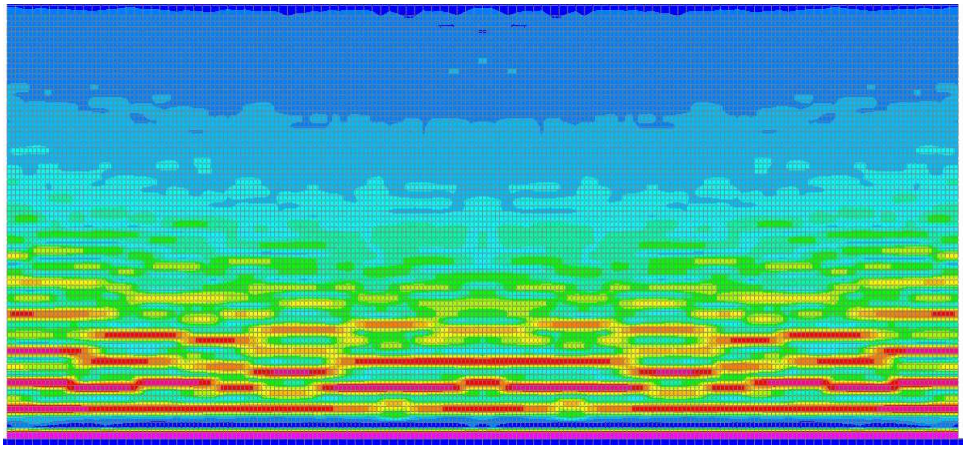

Figure 4.30. Tensile Damage of W0_0_0.5 at 1% drift for lower 40 in. of wall

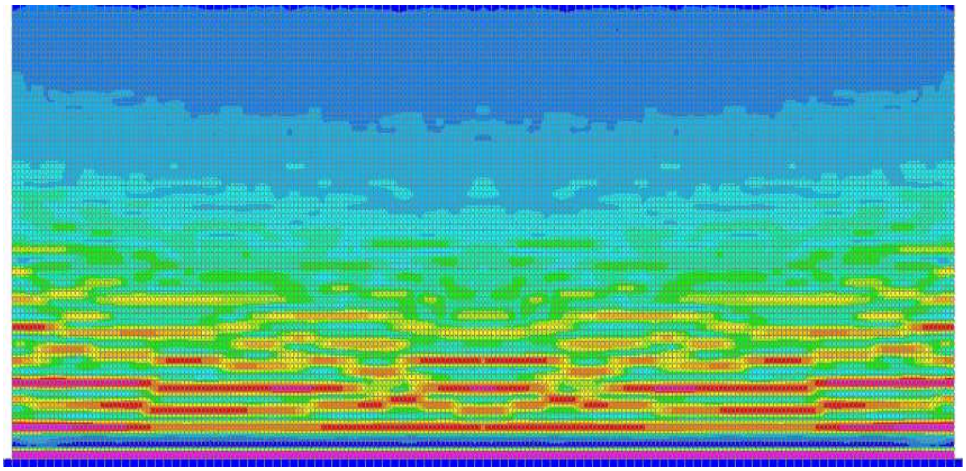

Figure 4.31. Tensile Damage of W48_1_0.5 at 1% drift for lower 40 in. of wall

Chapter 5. SUMMARY, CONCLUSIONS, AND RECOMMENDATIONS FOR FUTURE WORK

The research presented here uses a validated finite element model to investigate the flexural behavior at peak and residual strength of minimally reinforced concrete walls loaded in the out-of-plane direction. The primary objectives of the research presented were:

1. To develop a nonlinear finite element model capable of predicting, the stiffness, strength, and deformation capacity of wall test specimens.
2. To use this model to test the impact of differing steel reinforcement layouts on ICF walls.
3. To develop a FRC model to test its impact on ICF walls.

From this work, it can be seen that the peak strength is controlled by concrete tensile strength, and residual strength is controlled by longitudinal reinforcement.

Section 5.1 provides a summary of the research conducted, Section 5.2 provides conclusions on the research conducted, and Section 5.3 provides potential future to further understand lightly reinforced walls loaded in the out-of-plane direction.

5.1 RESEARCH SUMMARY

5.1.1 *Model Development and Evaluation*

LS-DYNA was used to develop a FE model for this research. Using 3 in-plane and 4 out-of-plane loaded walls, a modeling approach was developed and calibrated. Model development determined appropriate levels of mesh refinement and strategies to minimize explicit dynamic fluctuation.

The models simulate the envelope of the cyclic response curve, tensile damage history, and deformation capacity well. The models did not capture failure mechanisms in any of the simulations. This may be due to the fact the models were run only monotonically, making it difficult for the reinforcement to buckle and subsequently fracture.

5.1.2 *Parametric Study to Investigate Effect of Minimal Steel Reinforcement*

An extensive study was conducted to see the impact of increasing steel spacing and the number of curtains of steel. Model parameters tested were splice vs continuous reinforcement modeling, use of bond equation, reinforcing bar spacing, and curtains of bar reinforcement. The results indicate that one curtain with 48 in. spacing with modeled bond and continuous reinforcement should provide ample strength capacity to the wall. The tensile damage is primarily concentrated at the base of the wall. However, peak strength is achieved in these walls before cracking, so walls should be designed for the cracking load and drift. The results indicate that reinforcement spacings larger than the minimum ACI reinforcement spacings should be suitable for ICF walls.

5.1.3 *Parametric Study to Investigate Effect of FRC*

An extensive study was conducted to see the impact of using FRC for ICF walls. The model parameters tested were spliced vs continuous reinforcement modeling, reinforcing bar spacing, curtains of bar reinforcement, and fiber content percentage. The results indicate that the use of FRC increases the overall strength and drift capacity of the wall. The tensile damage is distributed along the height of the wall. The foundation concrete tensile strength must match that of the FRC wall to prevent damage in the foundation. It was found that a wall with a fiber content of 0.5% without any steel reinforcement is suitable for ICF construction. The results indicate that the use of FRC should be suitable for ICF walls.

5.1.4 *Study Limitations*

The limitations to this study are:

1. Inability to model failure mechanisms – The model validation walls were unable to model failure mechanisms of bar buckling and bar fracture. This inability to capture this behavior allows for the models to show larger drift capacities that were seen in the tests.
2. Inability to model shrinkage and creep – The reinforcing bars aid in the resistance to shrinkage and creep damage. In cases for walls with little reinforcement and starter bars only, there could be more shrinkage and creep damage in the walls when compared to walls with more reinforcement. This damage that occurs before loading could have an impact on the wall capacity, as there is already some damage in the wall.

5.2 CONCLUSIONS

5.2.1 *Modeling Conclusions*

- The presence of the bond-slip equation reduces the residual capacity of the specimens. This slip makes the steel strains to be less than the concrete strains. Less strain in the steel leads to less steel stress and thus less capacity of the wall.
- For modeling in LS-DYNA, continuous reinforcing bars should be used. There is little difference between the behavior of spliced and continuous reinforcing bars for RC models. The same peak strengths and post-peak residual behavior were observed. Using continuous reinforcement also simplifies the model development process.

5.2.2 *RC Wall Conclusions*

- The location of the longitudinal reinforcement has an impact on the residual capacity post-cracking. When two layers of steel reinforcement are provided, post-crack hardening occurs whereas one layer of steel reinforcement is provided, the residual strength remains constant. In addition, the smaller the bar spacing, the larger increase in residual strength.
- Steel reinforcement requirements outlined by ACI codes are over-restrictive on the design of RC walls subject to low seismic loads. Models that met ACI code requirements saw the same behavior with non-ACI compliant models until peak strength. In the post-peak residual region, hardening occurred in ACI compliant models whereas constant residual strength was maintained in non-ACI compliant models. It is recommended that these code provisions be reviewed for walls subject to low seismic loads.
- For reinforced concrete walls, the tensile damage is primarily at the base of the wall regardless of steel layout. The reduced bar spacings saw a slight decrease in residual strength, which is expected as there is less steel reinforcement to carry tensile load.

5.2.3 *FRC Wall Conclusions*

- The use of FRC increases strength and drift capacity and is a viable solution to reduce cost in ICF wall construction. However, concrete mix workability must be considered before design.

- The same behavior is seen in FRC walls with reinforcement and FRC walls with starter bars. The behavior at peak strength is the same. The more reinforcement in the FRC wall, the higher residual capacity observed.

5.3 FUTURE WORK

5.3.1 *Future Modelling*

- Fiber contents of 0.125 and 0.25%: Fiber contents of 0.5% or higher were used in previous research. This amount of fiber may have workability issues, so investigating the impact of less fiber on wall behavior would be beneficial to the ICF industry.
- Wall Lengths: For 48 in. spaced specimens, the wall length could only fit two 48 in. spaces (3 layers of steel). A larger wall length would be beneficial in understanding wall behavior as there would be more layers of steel as a wall would have in practice.
- Non-planar walls: In typical construction, walls have other walls frame into each other providing some lateral or out-of-plane resistance. Modeling a non-planar may be able to capture this effect and provide better detail for wall behavior.

5.3.2 *Future Laboratory Testing*

- 2 tests studying bar spacings at 18 and 48 in. with 1 curtain of steel. This is to confirm the findings of the research presented in this thesis.
- 1 test studying bar spacings at 48 in. with 2 curtains of steel. This is to confirm the findings of the research presented in this thesis.
- 1 test studying the effect of removing transverse steel. This research did not remove any transverse steel in the reinforced concrete walls. Removing transverse steel could lead to cost benefits as there would be fewer materials and fewer hours needed to prepare the wall for a concrete pour.
- 1 test studying bar spacings at 48 in. with 1 curtain of steel with low shrinkage add-mixtures. Shrinkage was not investigated in this research. This low-shrinkage add-mixture would be investigated to limit cracking before the wall is being loaded. Since there is little steel to act in tension, the reduction of cracks could allow for more tensile capacity in the wall.

- 3 tests studying differing fiber content percentages of 0.125%, 0.25%, and 0.5%. Most research on FRC is done for fiber content percentages higher than 0.5%. This can lead to workability issues when pouring the concrete. Fiber content percentages less than 0.5% should be tested to see its effect on concrete tensile capacity.
- 2 tests studying fiber content percentages without any longitudinal reinforcement, but with dowel bars. To have a wall without any longitudinal reinforcement, dowel bars must be placed for the transfer of forces from the wall to the foundation.

BIBLIOGRAPHY

ACI 318-19, Building Code Requirements for Structural Concrete, *American Concrete Institute*, 2019.

Alarcon, C., et al. "Effect of Axial Loads in the Seismic Behavior of Reinforced Concrete Walls with Unconfined Wall Boundaries." *Engineering Structures*, vol. 73, 2014, pp. 13–23., doi:10.1016/j.engstruct.2014.04.047.

Carrillo, J., Pincheira, J. and Alcocer, S. "Behavior of low-rise, steel fiber-reinforced concrete thin walls under shake table excitations." *Engineering Structures*, 138, 2017.

Correal, J., Herran, C., Carrillo, J., Reyes, J. and Hermida, G. "Performance of hybrid fiber-reinforced concrete for low-rise housing with thin walls." *Construction and Building Materials*, 185, 2018.

Dazio, Alessandro, et al. "Quasi-Static Cyclic Tests and Plastic Hinge Analysis of RC Structural Walls." *Engineering Structures*, vol. 31, no. 7, 2009, pp. 1556–1571., doi:10.1016/j.engstruct.2009.02.018.

Deng, Kai Lai, et al. "Quasi-Static Test of Reinforced Concrete Shear Wall with Low Concrete Strength and Reinforcement Ratio." *Applied Mechanics and Materials*, vol. 188, 2012, pp. 106–111., doi:10.4028/www.scientific.net/amm.188.106.

Grassl, Peter, and Milan Jirasek. "Damage-Plastic Model for Concrete Failure." *International Journal of Solids and Structures*, vol. 43, 2006.

Grassl, P., et al. "A Damage-Plasticity Model for the Dynamic Failure of Concrete." *Eurodyn 2011, 8th International Conference on Structural Dynamics*, 2011.

Grassl, Peter, et al. "CDPM2: A Damage-Plasticity Approach to Modelling the Failure of Concrete." *International Journal of Solids and Structures*, vol. 50, 2013.

Han, S. W., et al. "Seismic Behaviour of Structural Walls with Specific Details." *Magazine of Concrete Research,* vol. 54, no. 5, 2002, pp. 333–345., doi:10.1680/macr.2002.54.5.333.

International Federation for Structural Concrete (fib). CEB-FIB model code 2010 (MC22010). Berlin, Germany: Ernst & Sohn, 2013.

Ireland, M.G., et al. "Experimental Investigations of a Selective Weakening Approach for the Seismic Retrofit of R.C. Walls." *2007 NZSEE Conference*, 2007.

Kazemi, M. T., Fazileh, F., & Ebrahiminezhad, M. A. (2007). Cohesive crack model and Fracture energy Of Steel-Fiber-Reinforced-Concrete Notched Cylindrical Specimens. *Journal of Materials in Civil Engineering, 19*(10), 884-890. doi:10.1061/(asce)0899-1561(2007)19:10(884)

Kim, M., & Bordelon, A. (2015). Determination of total fracture energy for fiber-reinforced concrete. *ACI Spec. Publ., 300*, 1-16.

LSTC. Keyword User's Manual, Volume I. *Livermore*, CA, USA: Version 12 R12.0.0. 2020.

LSTC. Keyword User's Manual, Volume II. *Livermore*, CA, USA: Version 12 R12.0.0. 2020.

LSTC. Theory Manual. *Livermore*, CA, USA, 2006.

Lu, Yiqiu, et al. "Cyclic Testing of Reinforced Concrete Walls with Distributed Minimum Vertical Reinforcement." *Journal of Structural Engineering*, vol. 143, no. 5, 2016, p. 04016225., doi:10.1061/(asce)st.1943-541x.0001723.

Lu, Yiqiu, and Richard S. Henry. "Numerical Modelling of Reinforced Concrete Walls with Minimum Vertical Reinforcement." *Engineering Structures*, vol. 143, 2017.

Luna, Bismarck N., et al. "Seismic Behavior of Low-Aspect-Ratio Reinforced Concrete Shear Walls." *ACI Structural Journal*, 2015.

Marcalikova, Z., Cajka, R., Bilek, V., Bujdos, D., & Sucharda, O. (2020). Determination of mechanical characteristics for fiber-reinforced concrete with straight and hooked fibers. *Crystals, 10*(6), 545. doi:10.3390/cryst10060545

Murcia-Delso, Juan, et al. "Modeling the Bond-Slip Behavior of Confined Large-Diameter Reinforcing Bars." *III ECCOMAS Thematic Conference on Computational Methods in Structural Dynamics and Earthquake Engineering*, 2011.

Murcia-Delso, Juan, and P. Benson Shing. "Bond-Slip Model for Detailed Finite-Element Analysis of Reinforced Concrete Structures." *Journal of Structural Engineering*, vol. 141, no. 4, 2015.

PCA100-2017, Prescriptive Design of Exterior Concrete Walls. *Portland Cement Association*, 2017.

Roller, J. "Design Criteria for Insulating Concrete Form Wall Systems," *PCA Serial No. 2073*, Portland Cement Association, Skokie, IL, USA, 1996.

Sevilla, Rory de, et al. "Feasibility of a Fiber Reinforced Polymer Retrofit for Non-Ductile Concrete Walls." *2019 SEAOC Convetion Proceedings*, 2019.

Thomsen, John H., and John W. Wallace. “Displacement-Based Design of Slender Reinforced Concrete Structural Walls—Experimental Verification.” *Journal of Structural Engineering*, vol. 130, no. 4, 2004, pp. 618–630., doi:10.1061/(asce)0733-9445(2004)130:4(618).

Vandewalle, L. (2007). Postcracking Behaviour of Hybrid Steel Fiber Reinforced Concrete. *Proceedings of FraMCoS-6,* 1367-1375.

Woo, S., Kim, K., & Han, S. (2014). Tensile cracking constitutive model of steel fiber reinforced concrete (sfrc). *KSCE Journal of Civil Engineering, 18*(5), 1446-1454. doi:10.1007/s12205-014-0335-3

Woo, Sang-Kyun, et al. “Tensile Cracking Constitutive Model of Steel Fiber Reinforced Concrete (SFRC).” *KSCE Journal of Civil Engineering*, vol. 18, no. 5, 2014.

Zhao, Mu-zi, et al. “Modeling Recommendations for RC and CFST Sections in LS-DYNA Including Bond Slip.” *Engineering Structures*, Volume 229, 2021.

APPENDIX A

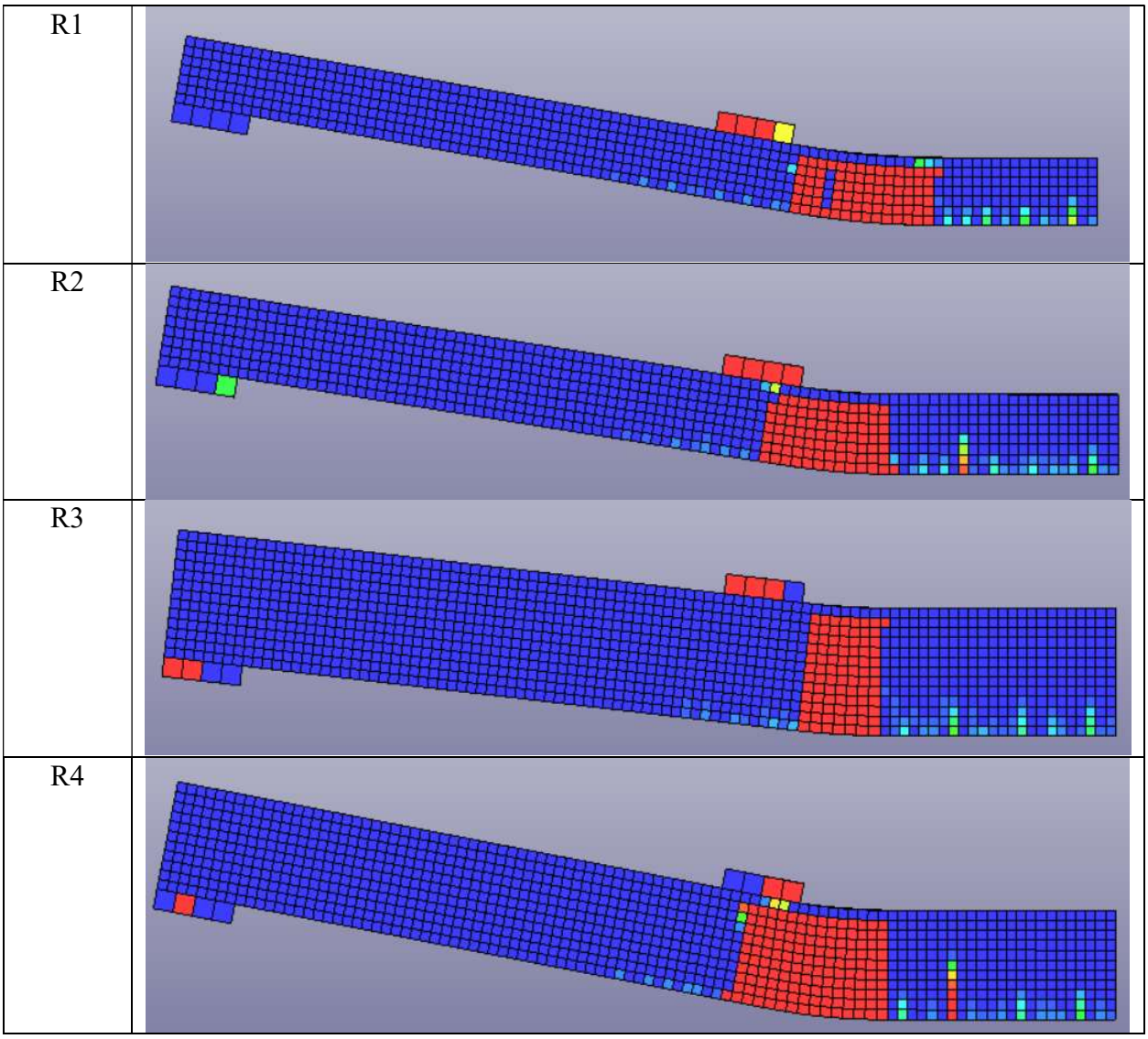

Figure A.1. Tensile Damage Results for Roller Walls

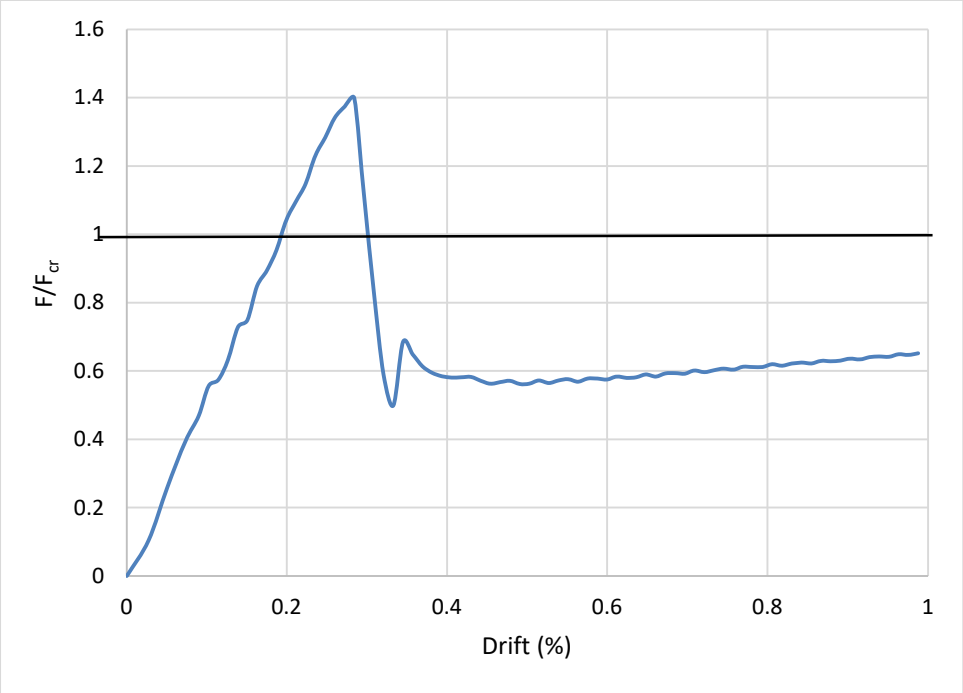

Figure A.2. Load Displacement History of W18_1_MB_C_0

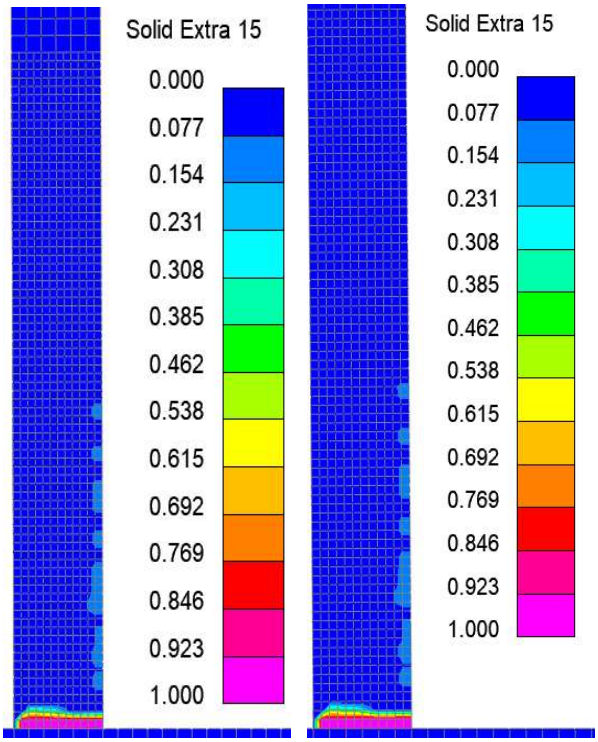

Figure A.3. Tensile Damage of W18_1_MB_C_0 at 0.5% and 1% Drift

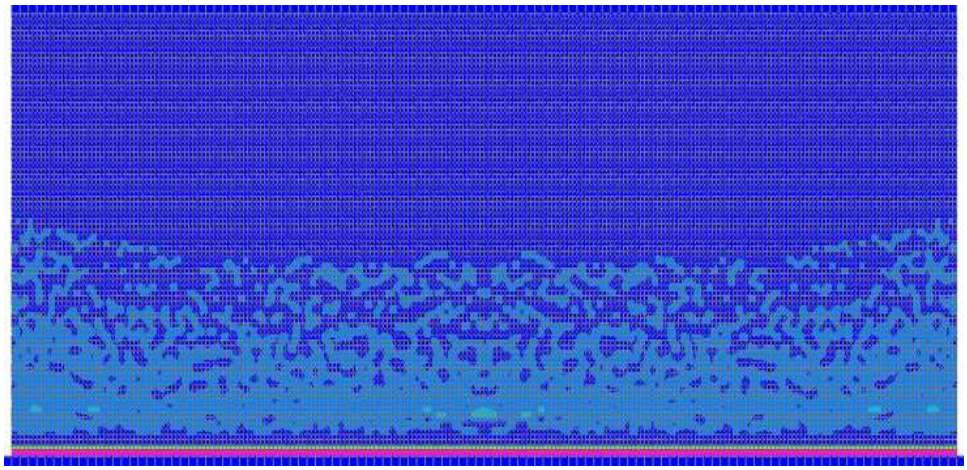

Figure A.4. Tensile Damage of W18_1_MB_C_0 at 1.0% Drift

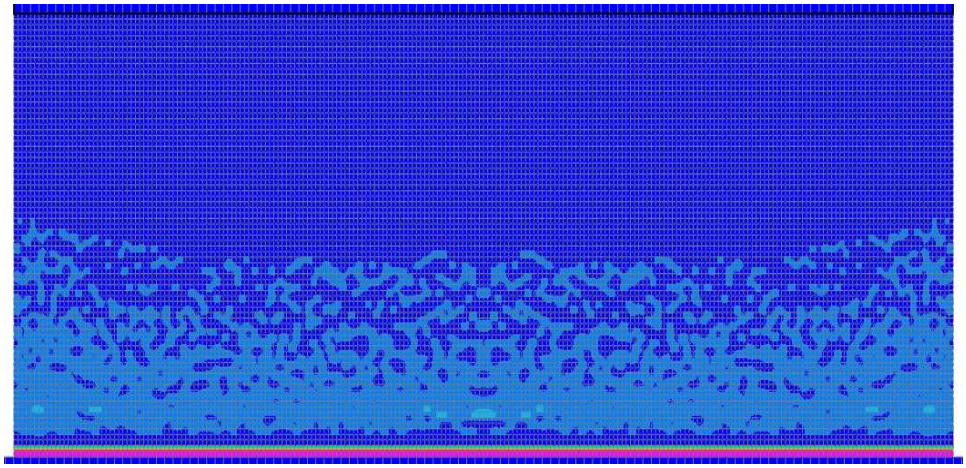

Figure A.5. Tensile Damage of W18_1_MB_C_0 at 0.5% Drift

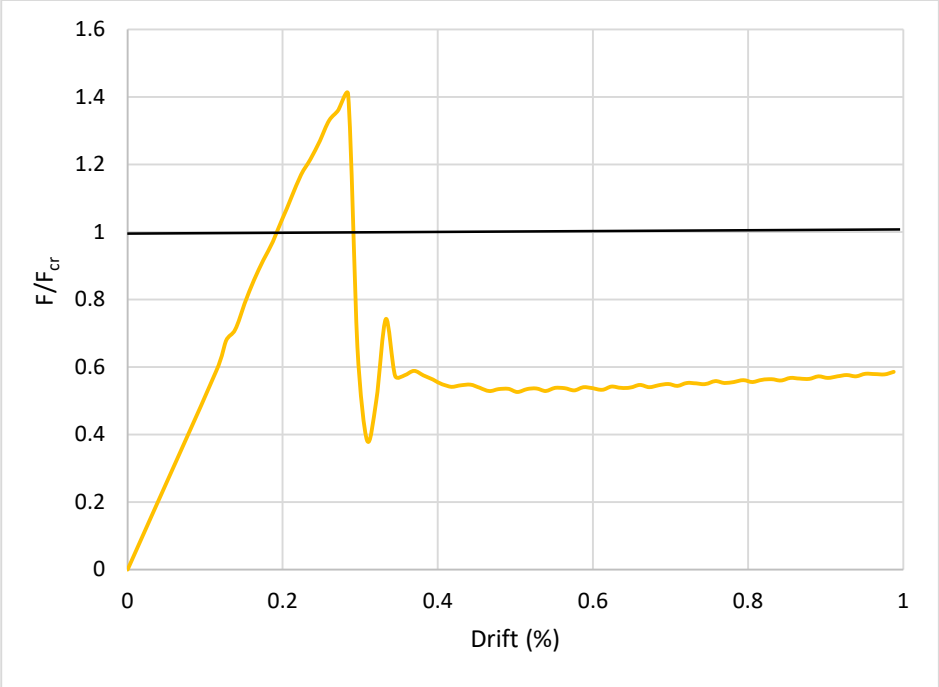

Figure A.6. Load Displacement History of W24_1_MB_C_0

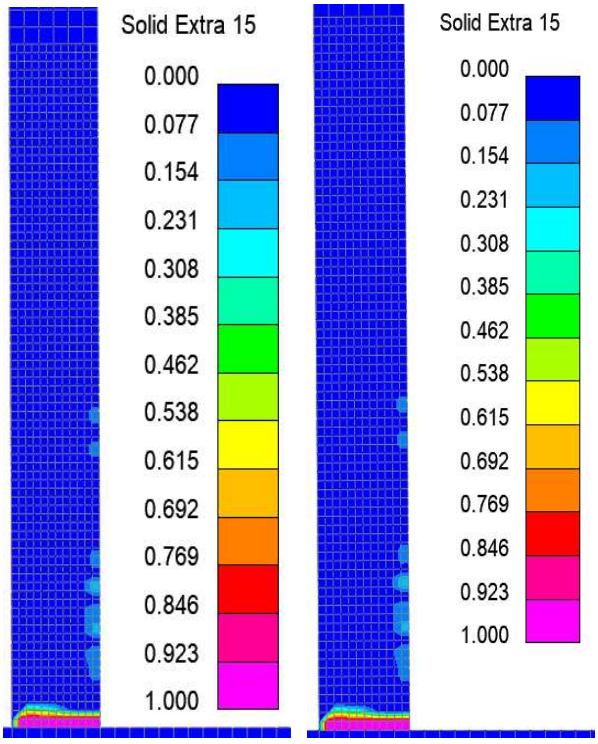

Figure A.7. Tensile Damage of W24_1_MB_C_0 at 0.5% and 1% Drift

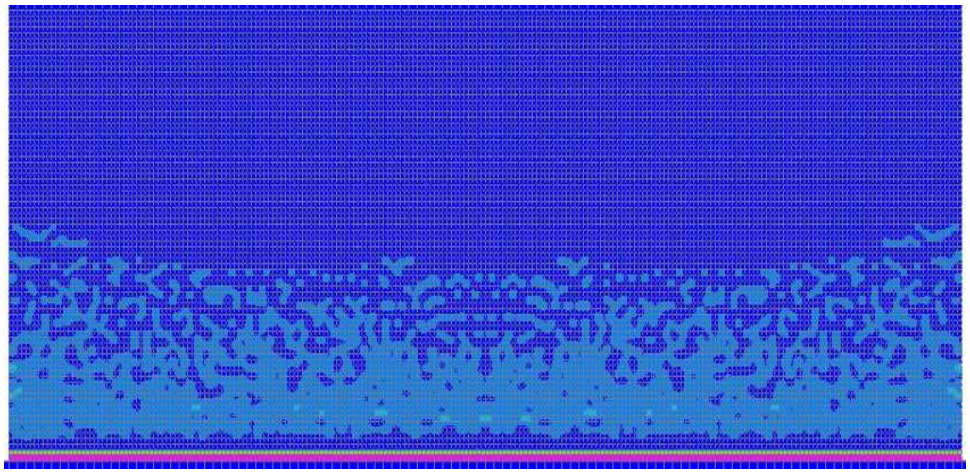

Figure A.8. Tensile Damage of W24_1_MB_C_0 at 0.5% Drift

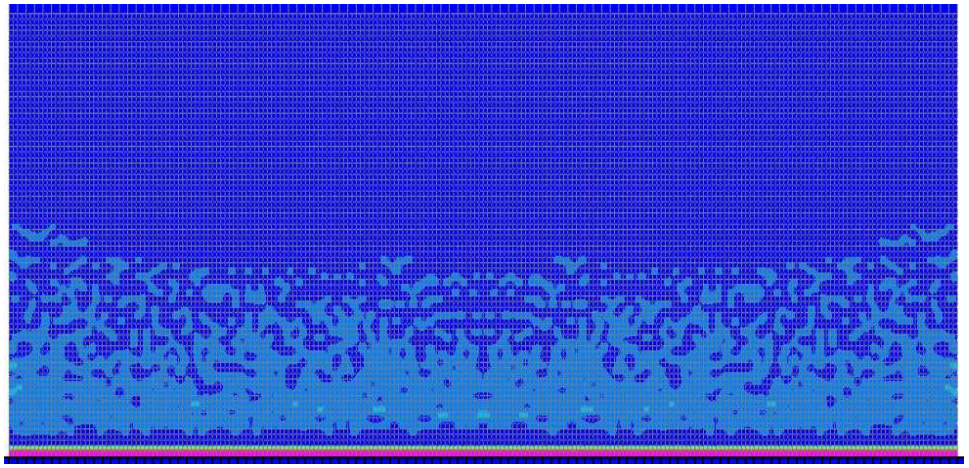

Figure A.9. Tensile Damage of W24_1_MB_C_0 at 1.0% Drift

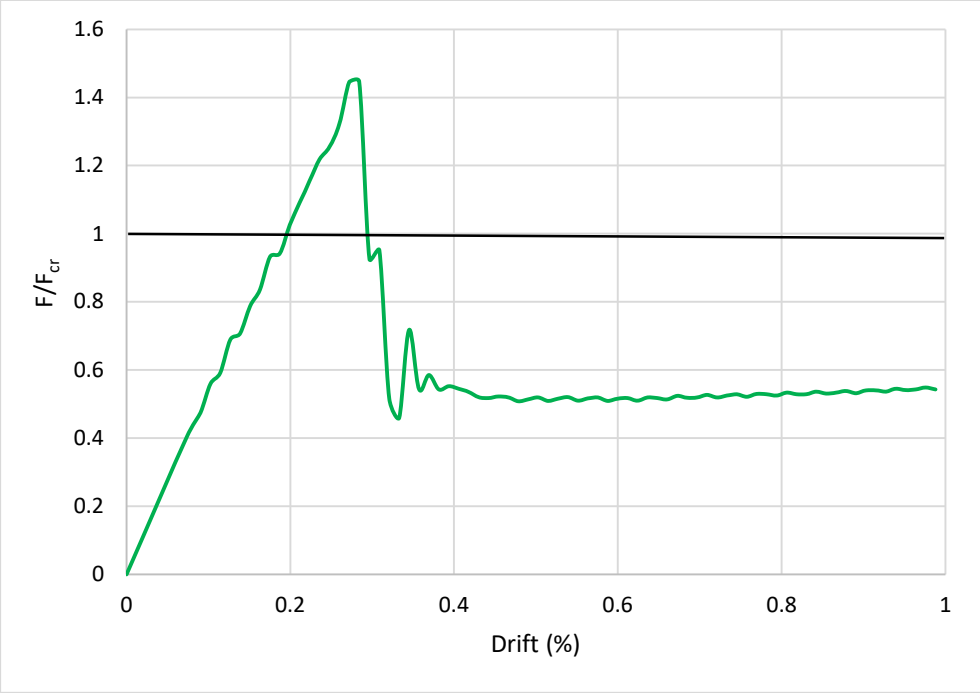

Figure A.10. Load Displacement History of W36_1_MB_C_0

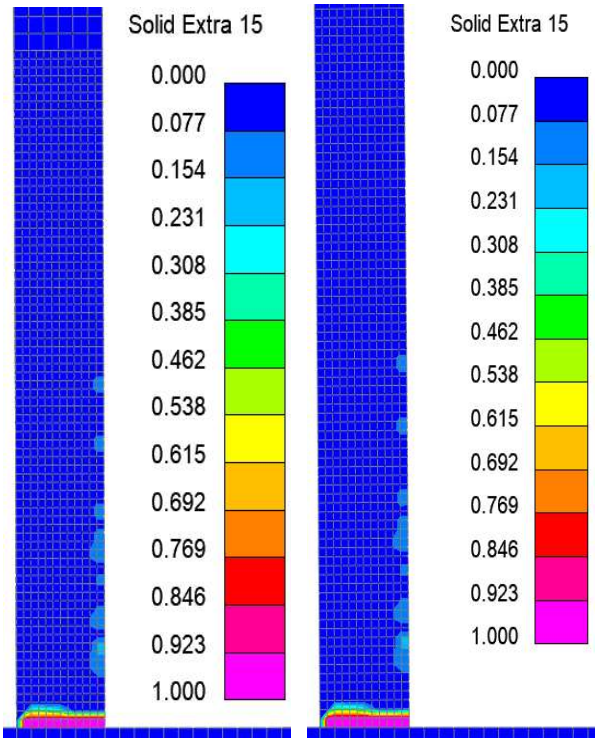

Figure A.11. Tensile Damage of W36_1_MB_C_0 at 0.5% and 1% Drift

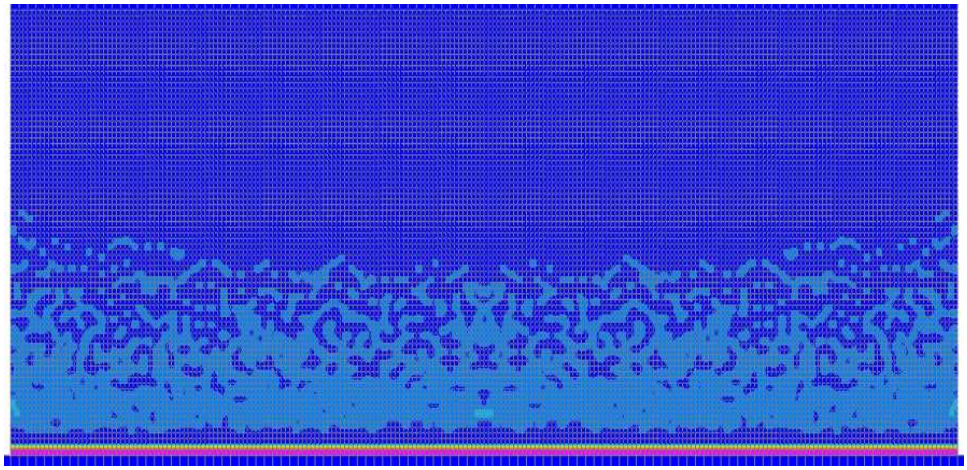

Figure A.12. Tensile Damage of W36_1_MB_C_0 at 0.5% Drift

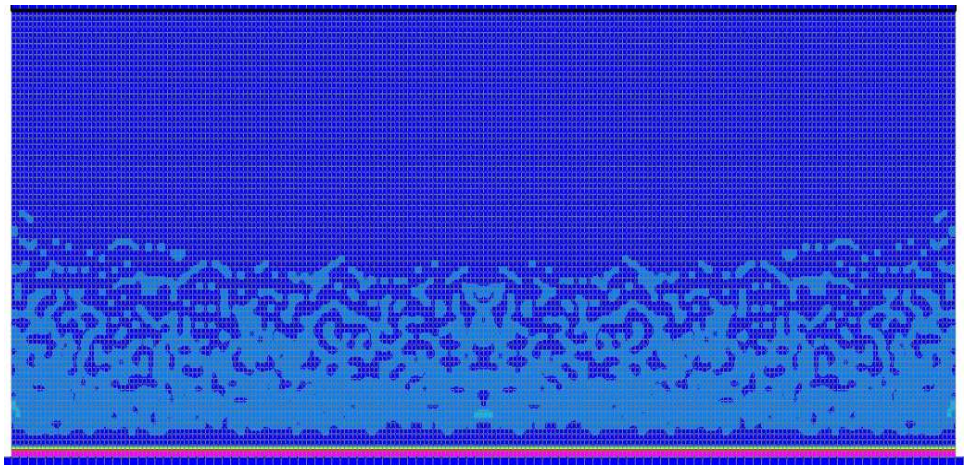

Figure A.13. Tensile Damage of W36_1_MB_C_0 at 1.0% Drift

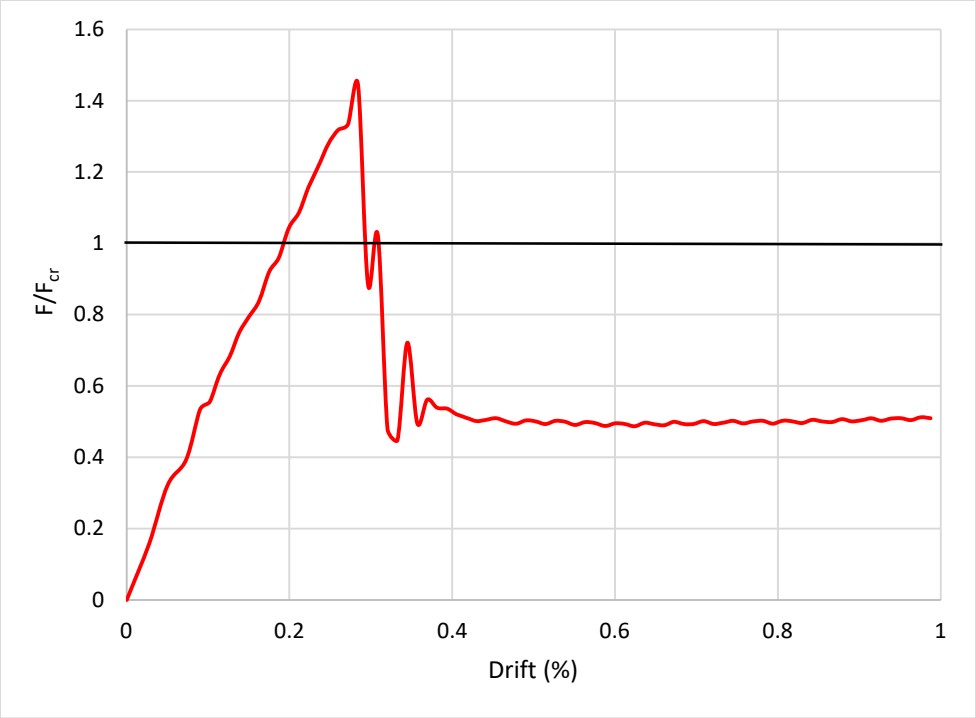

Figure A.14. Load Displacement History of W48_1_MB_C_0

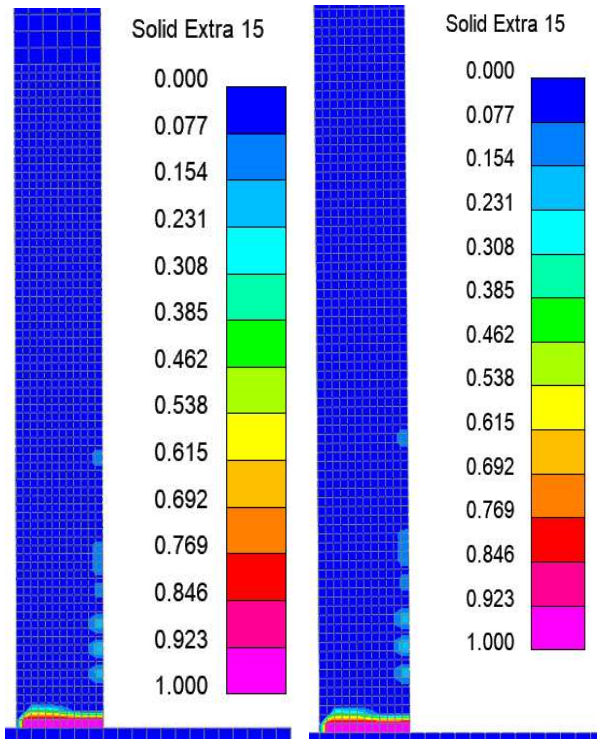

Figure A.15. Tensile Damage of W48_1_MB_C_0 at 0.5% and 1% Drift

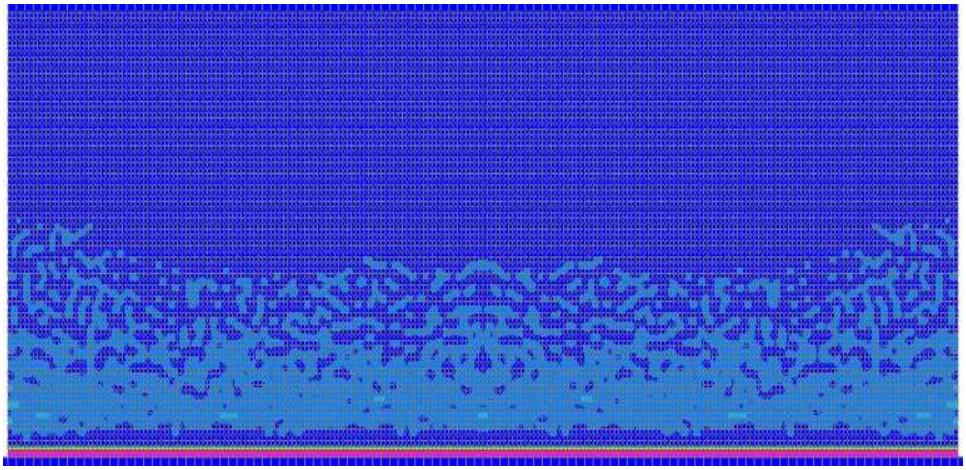

Figure A.16. Tensile Damage of W48_1_MB_C_0 at 0.5% Drift

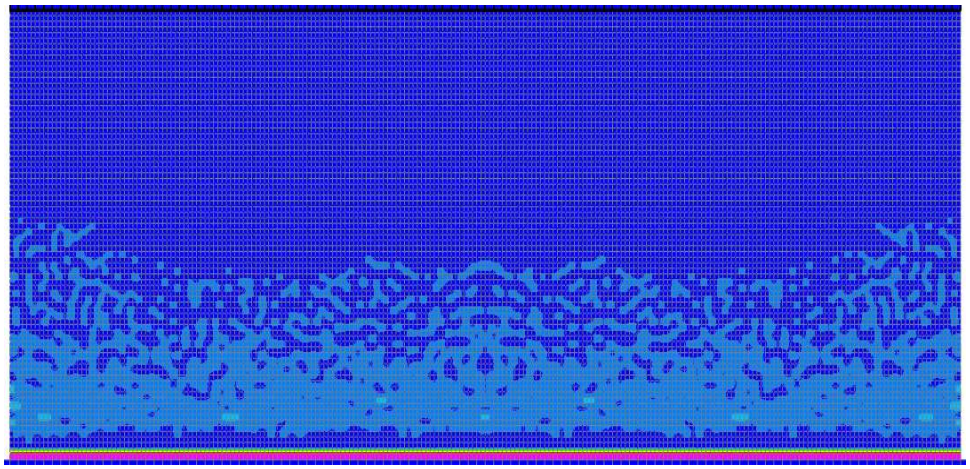

Figure A.17. Tensile Damage of W48_1_MB_C_0 at 1.0% Drift

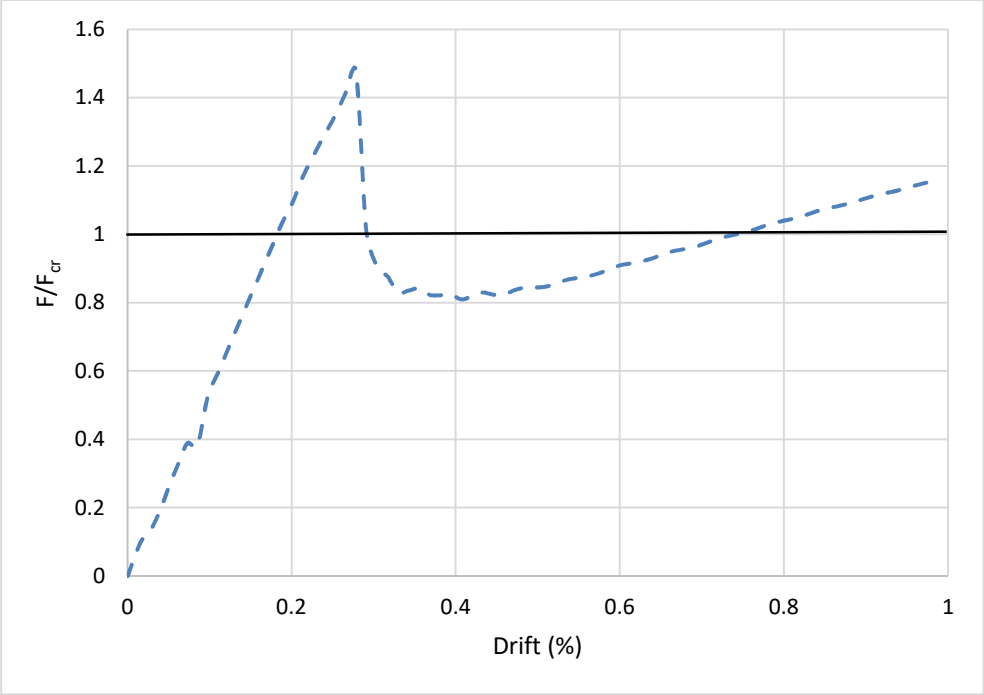

Figure A.18. Load Displacement History of W18_2_MB_C_0

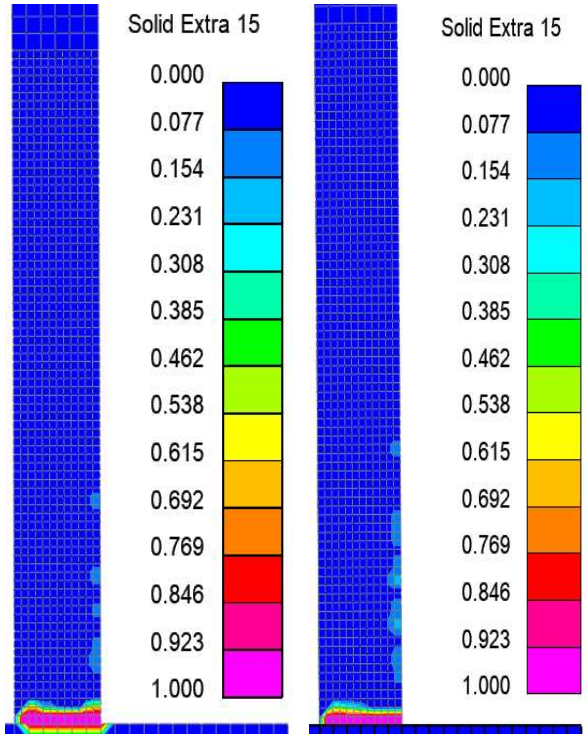

Figure A.19. Tensile Damage of W18_2_MB_C_0 at 0.5% and 1% Drift

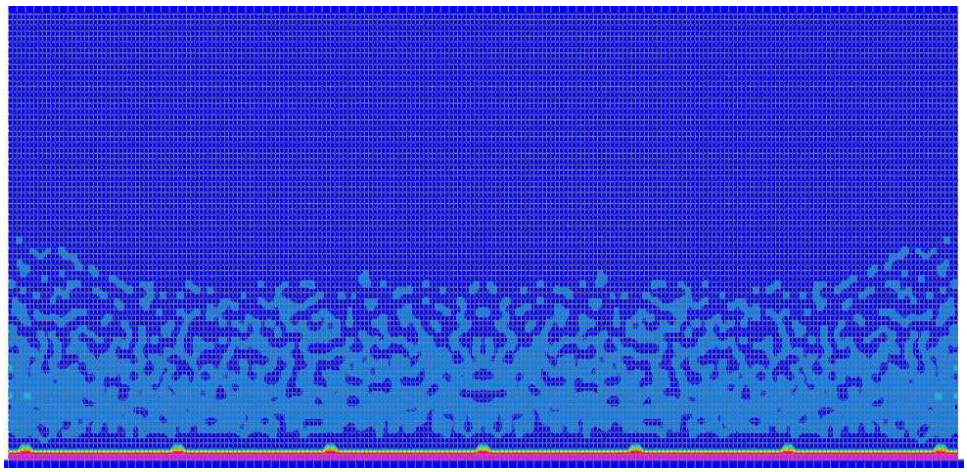

Figure A.20. Tensile Damage of W18_2_MB_C_0 at 0.5% Drift

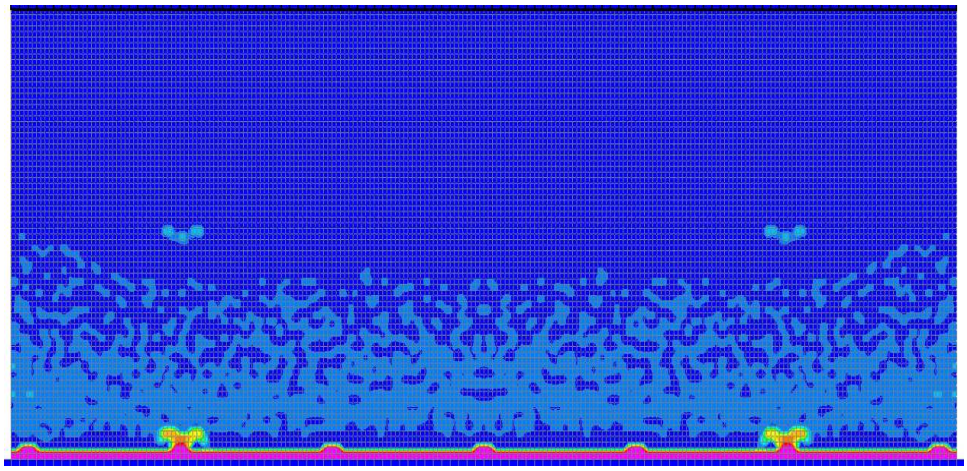

Figure A.21. Tensile Damage of W18_2_MB_C_0 at 1.0% Drift

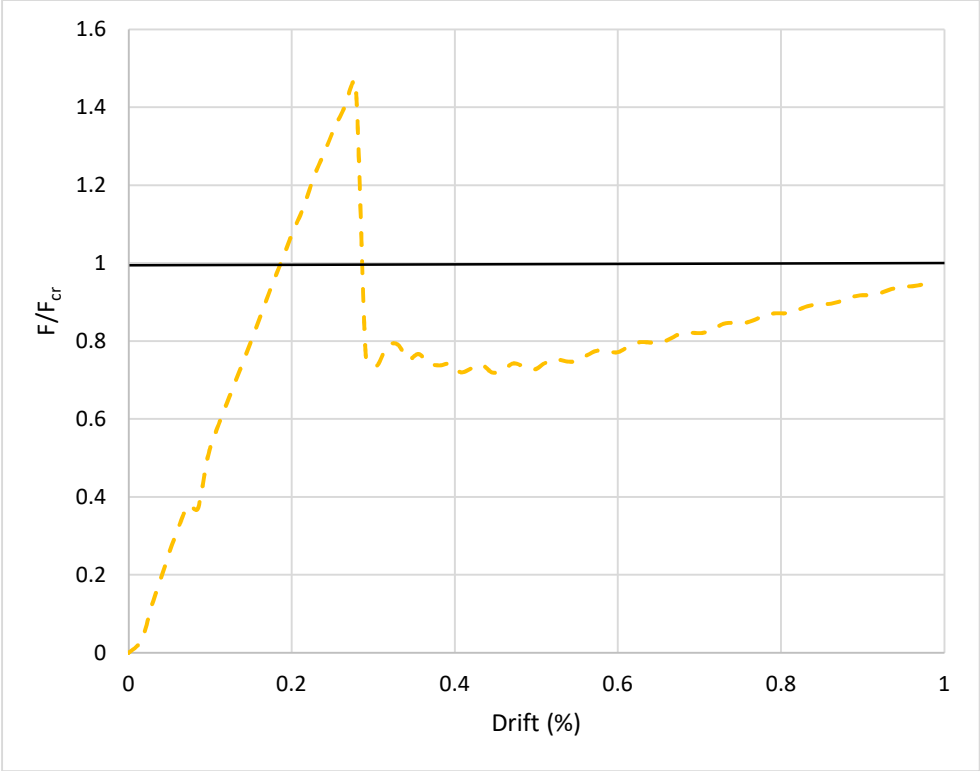

Figure A.22. Load Displacement History of W24_2_MB_C_0

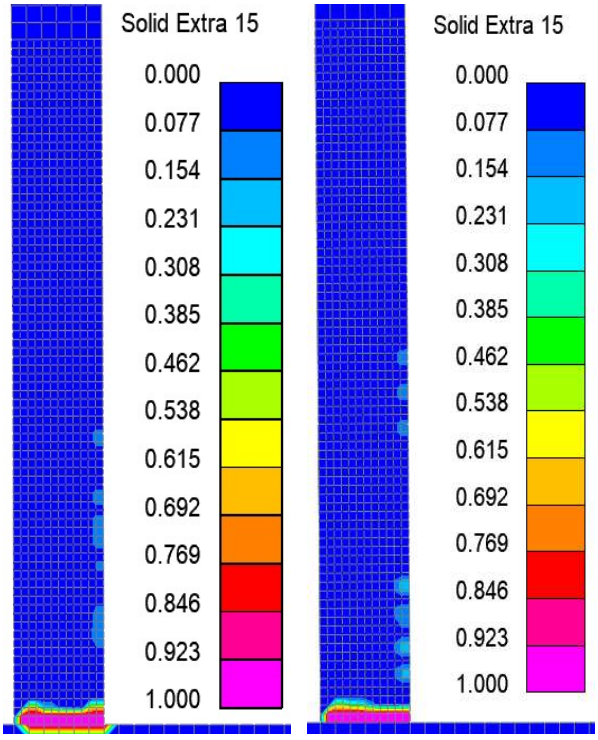

Figure A.23. Tensile Damage of W24_2_MB_C_0 at 0.5% and 1% Drift

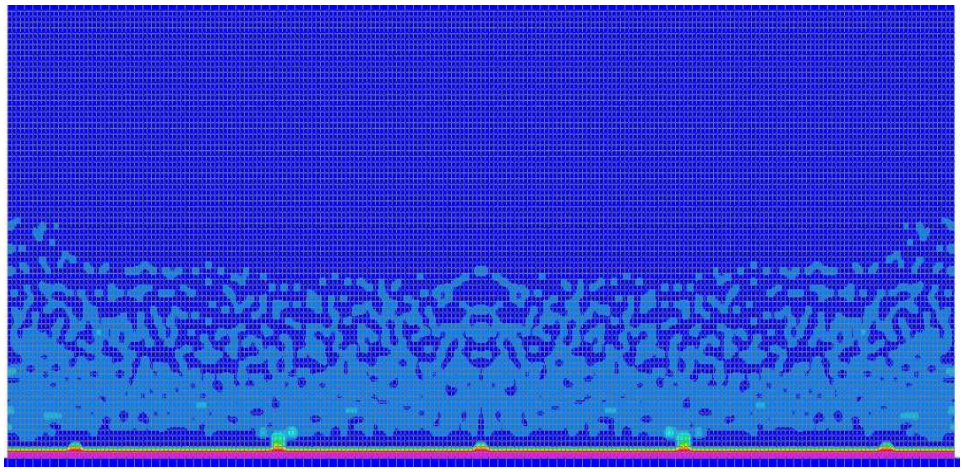

Figure A.24. Tensile Damage of W24_2_MB_C_0 at 0.5% Drift

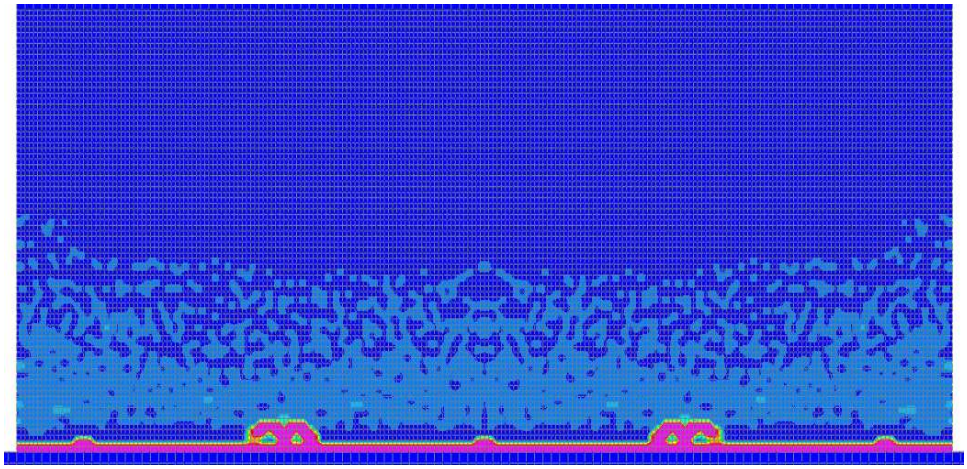

Figure A.25. Tensile Damage of W24_2_MB_C_0 at 1.0% Drift

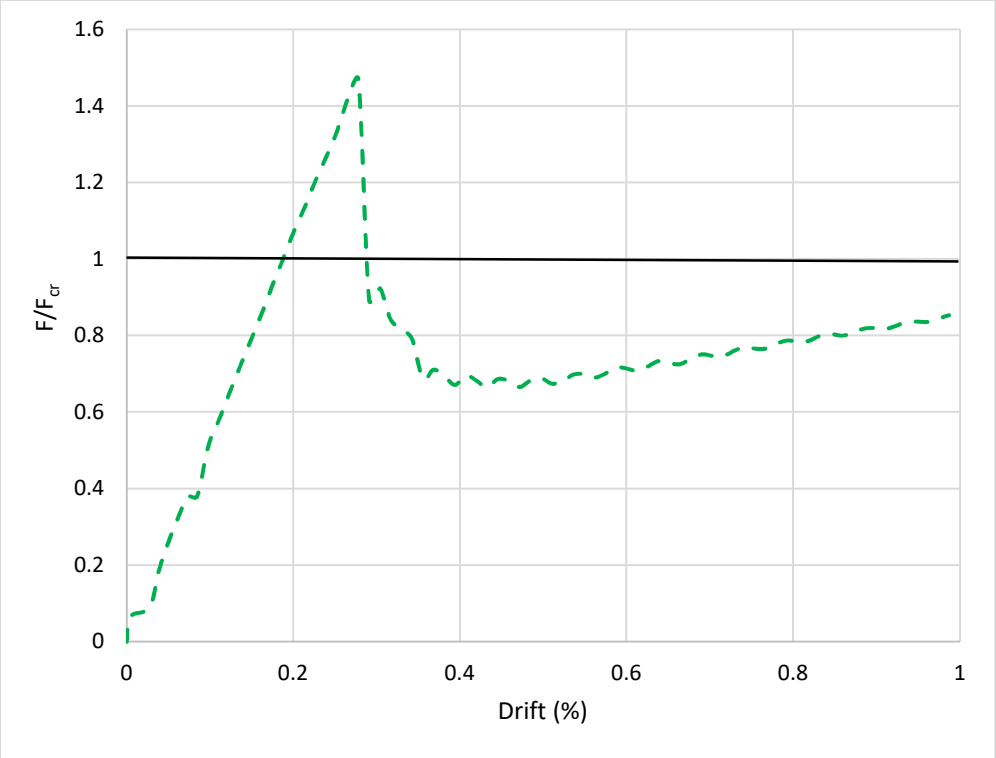

Figure A.26. Load Displacement History of W36_2_MB_C_0

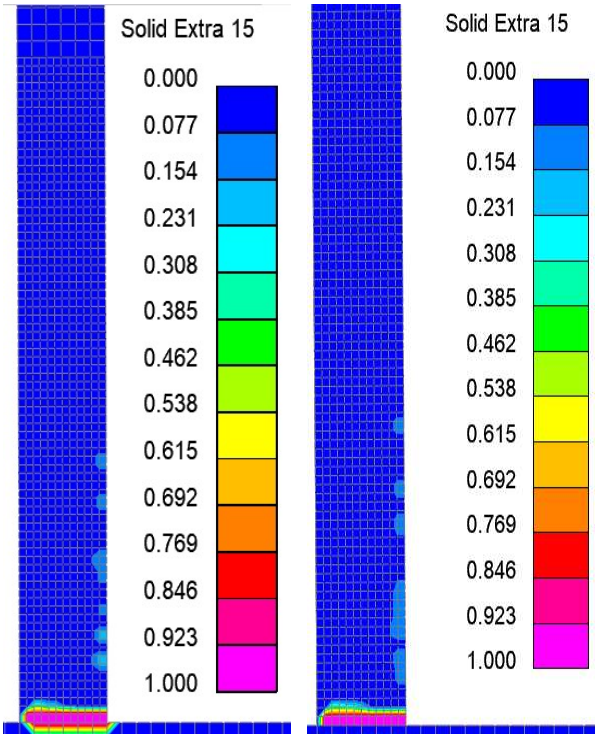

Figure A.27. Tensile Damage of W36_2_MB_C_0 at 0.5% and 1% Drift

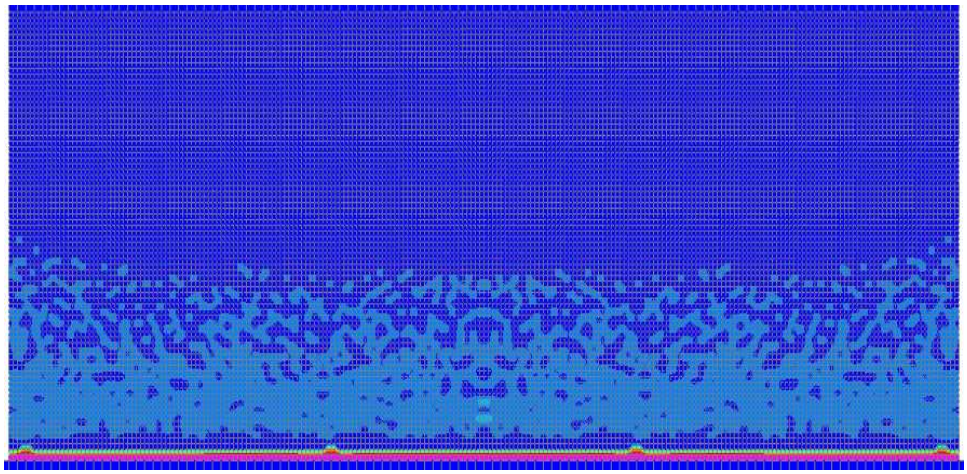

Figure A.28. Tensile Damage of W36_2_MB_C_0 at 0.5% Drift

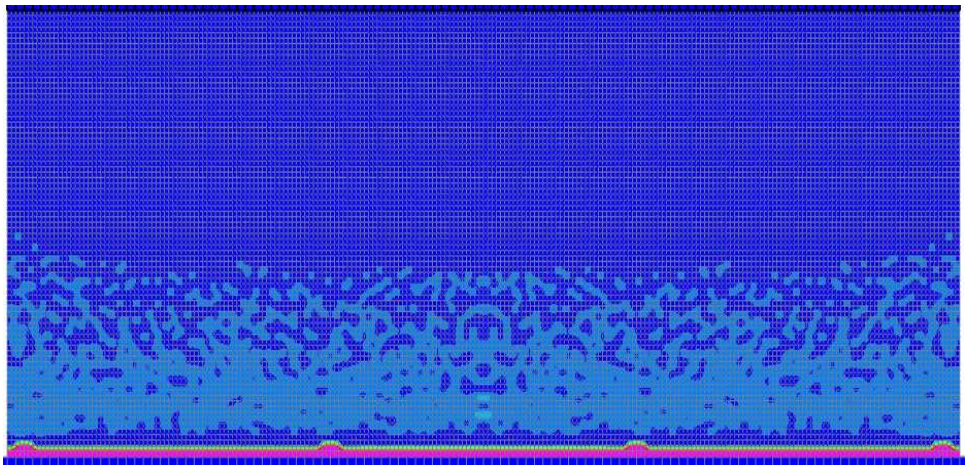

Figure A.29. Tensile Damage of W36_2_MB_C_0 at 1.0% Drift

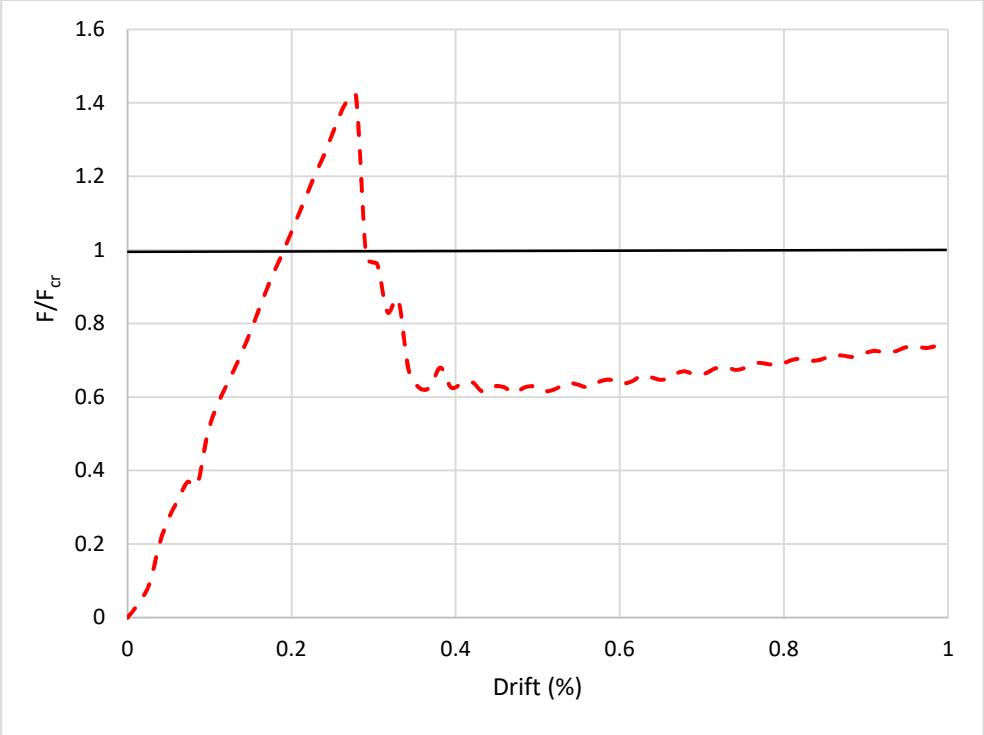

Figure A.30. Load Displacement History of W48_2_MB_C_0

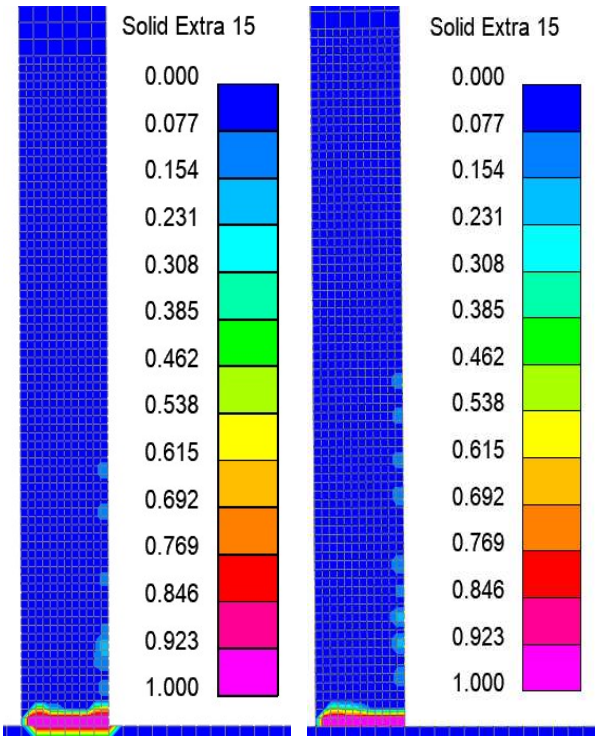

Figure A.31. Tensile Damage of W48_2_MB_C_0 at 0.5% and 1% Drift

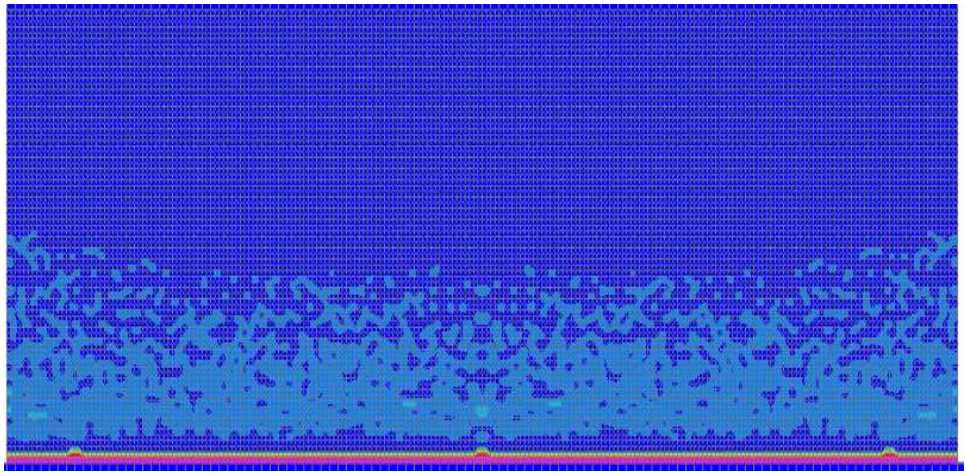

Figure A.32. Tensile Damage of W48_2_MB_C_0 at 0.5% Drift

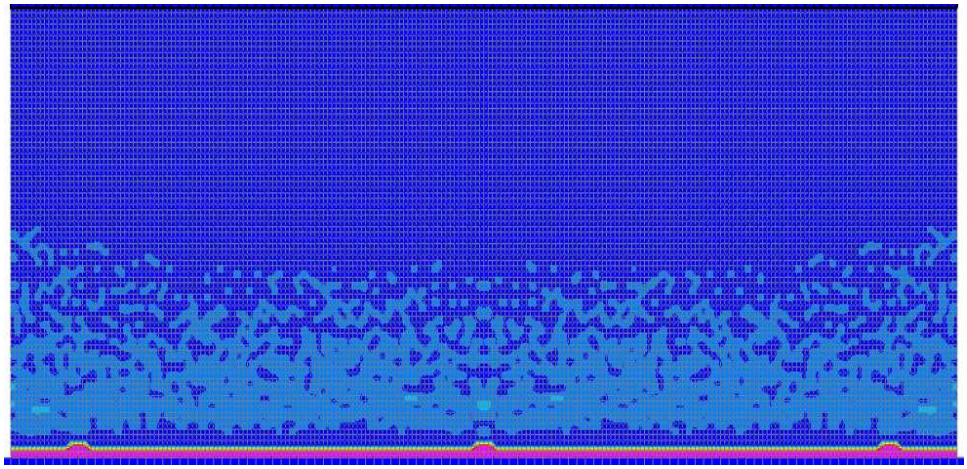

Figure A.33. Tensile Damage of W48_2_MB_C_0 at 1.0% Drift

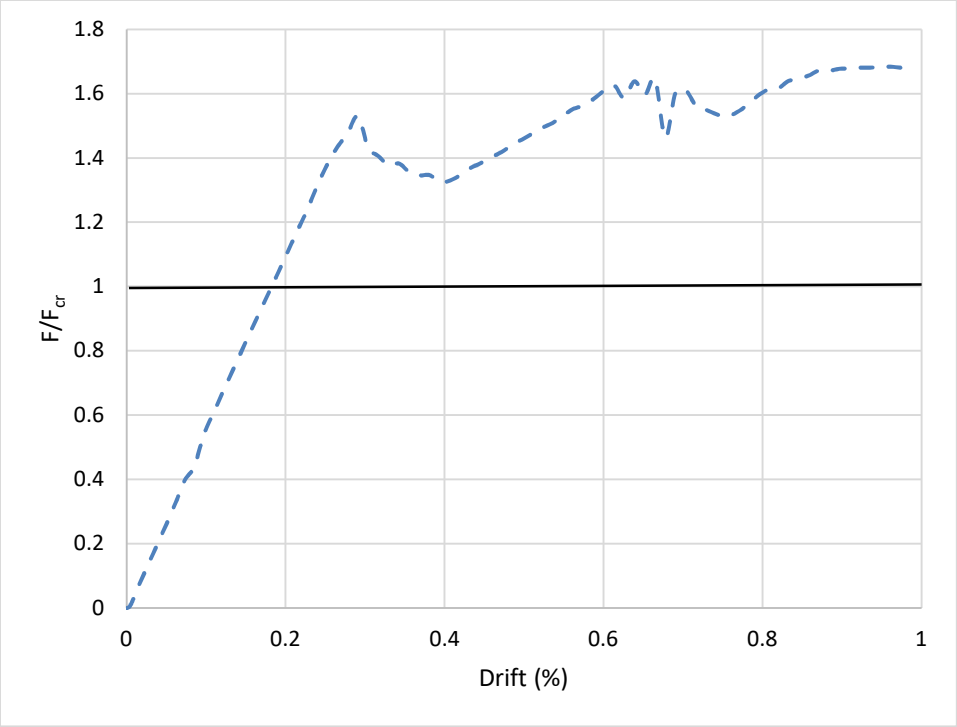

Figure A.34. Load Displacement History of W18_2_PB_C_0

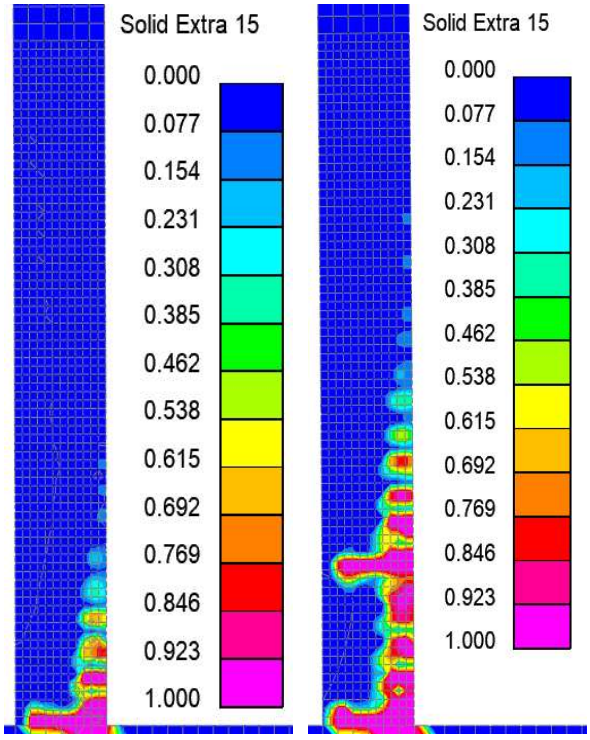

Figure A.35. Tensile Damage of W18_2_PB_C_0 at 0.5% and 1% Drift

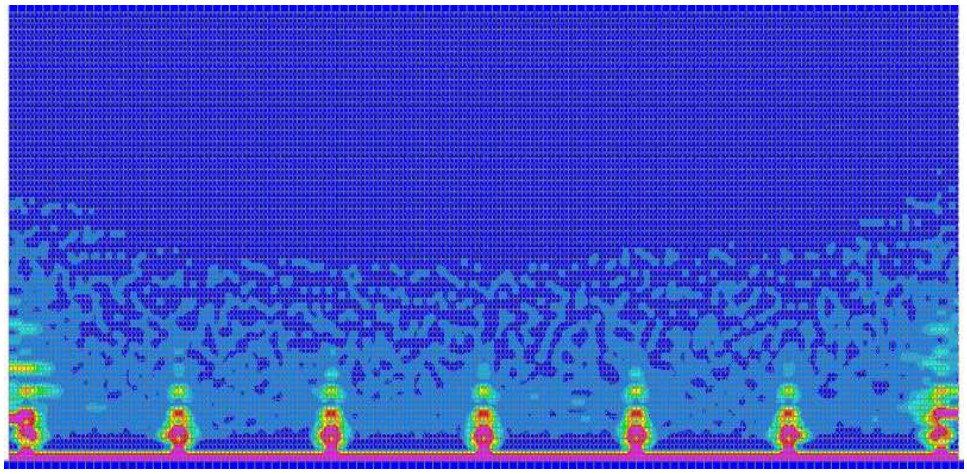

Figure A.36. Tensile Damage of W18_2_PB_C_0 at 0.5% Drift

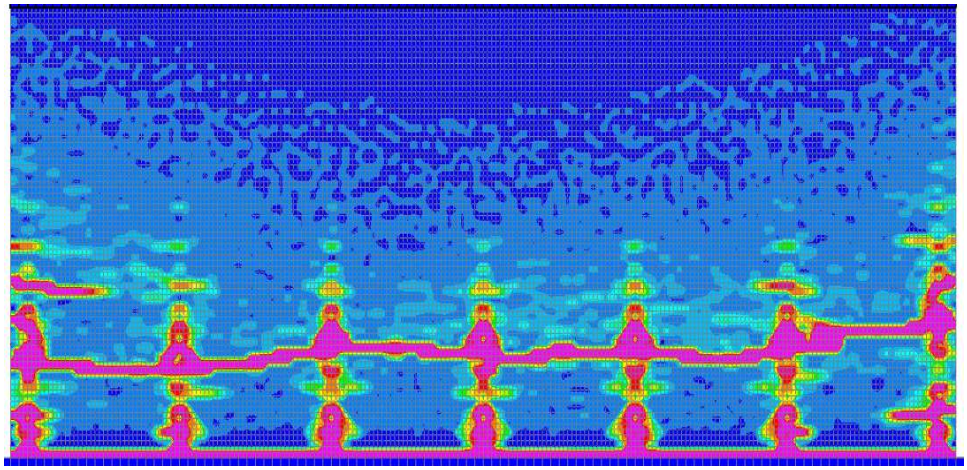

Figure A.37. Tensile Damage of W18_2_PB_C_0 at 1.0% Drift

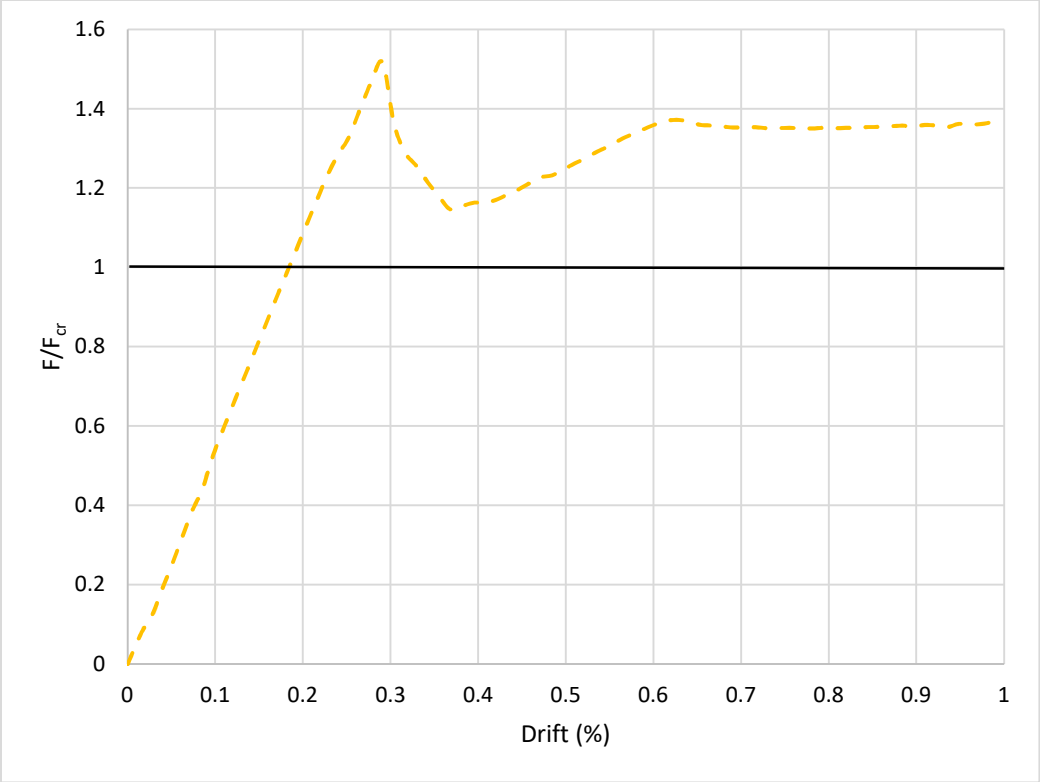

Figure A.38. Load Displacement History of W24_2_PB_C_0

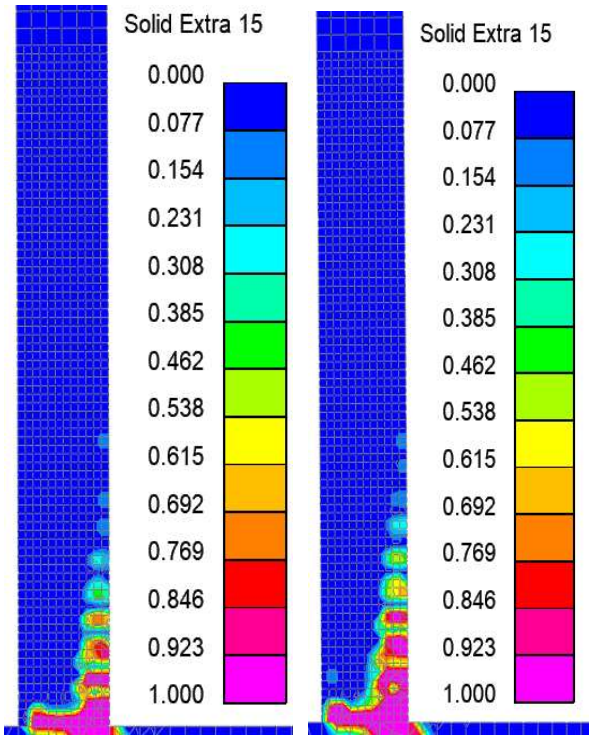

Figure A.39. Tensile Damage of W24_2_PB_C_0 at 0.5% and 1% Drift

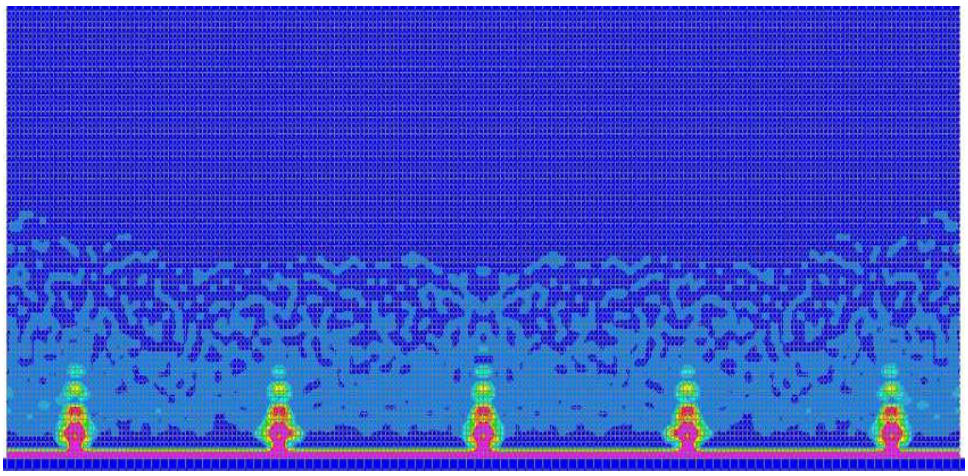

Figure A.40. Tensile Damage of W24_2_PB_C_0 at 0.5% Drift

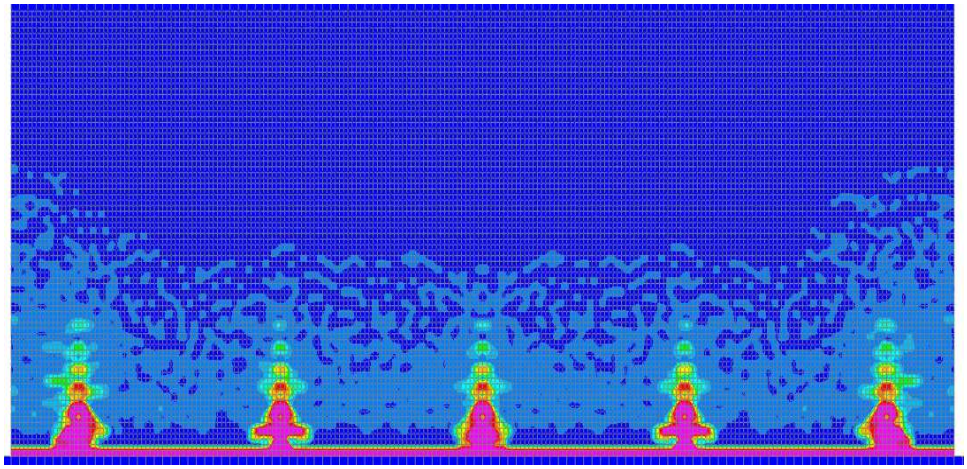

Figure A.41. Tensile Damage of W24_2_PB_C_0 at 1.0% Drift

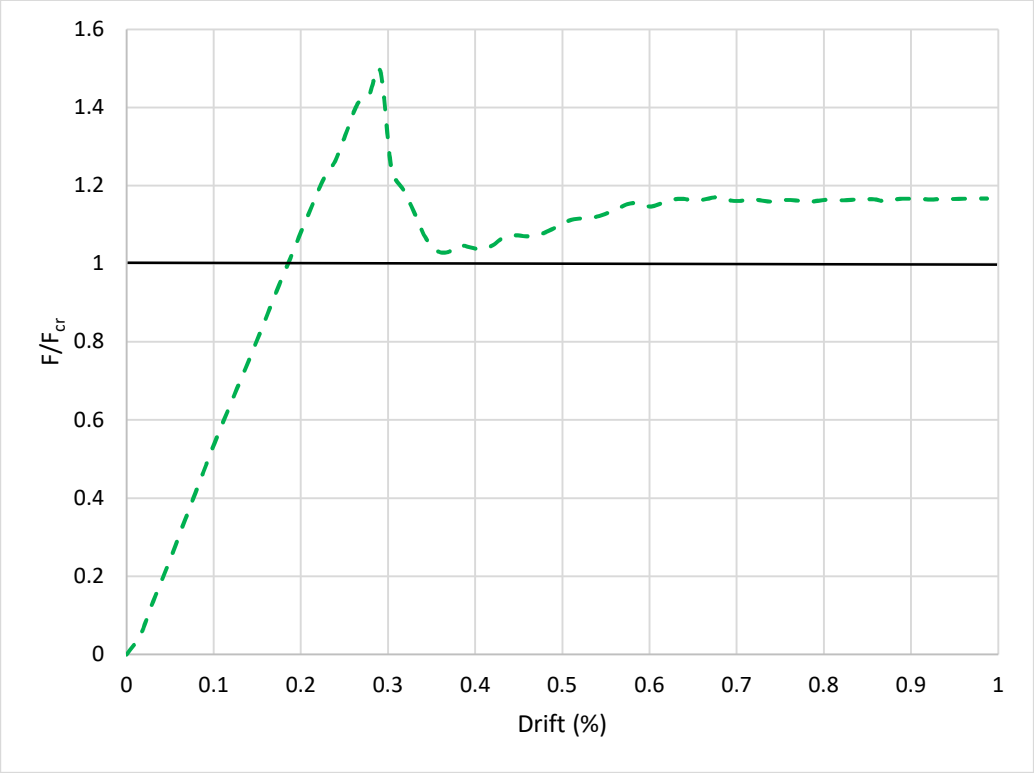

Figure A.42. Load Displacement History of W36_2_PB_C_0

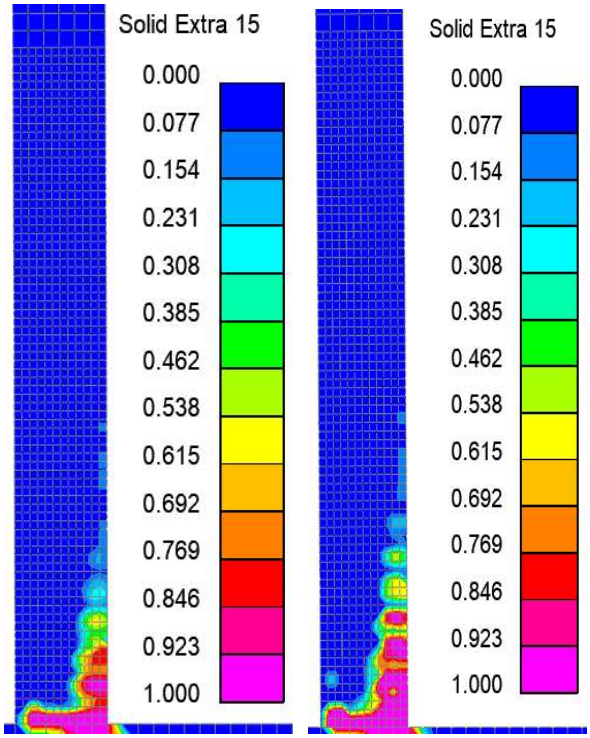

Figure A.43. Tensile Damage of W36_2_PB_C_0 at 0.5% and 1% Drift

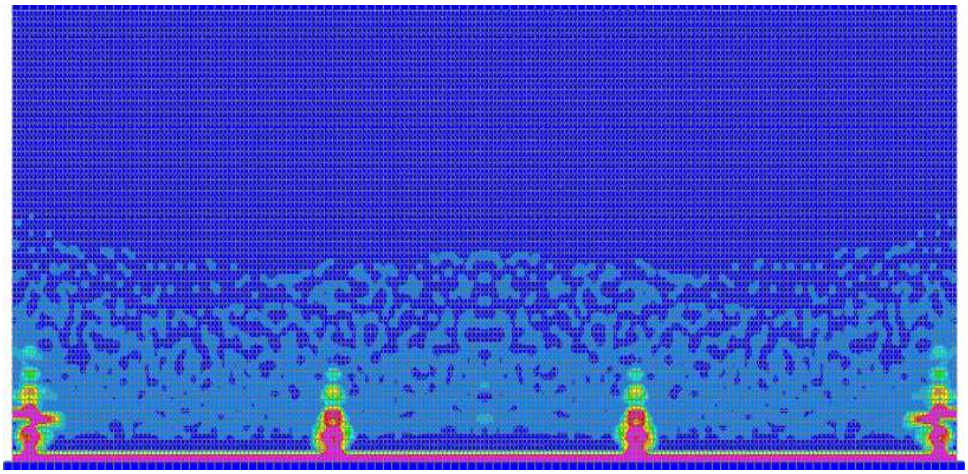

Figure A.44. Tensile Damage of W36_2_PB_C_0 at 0.5% Drift

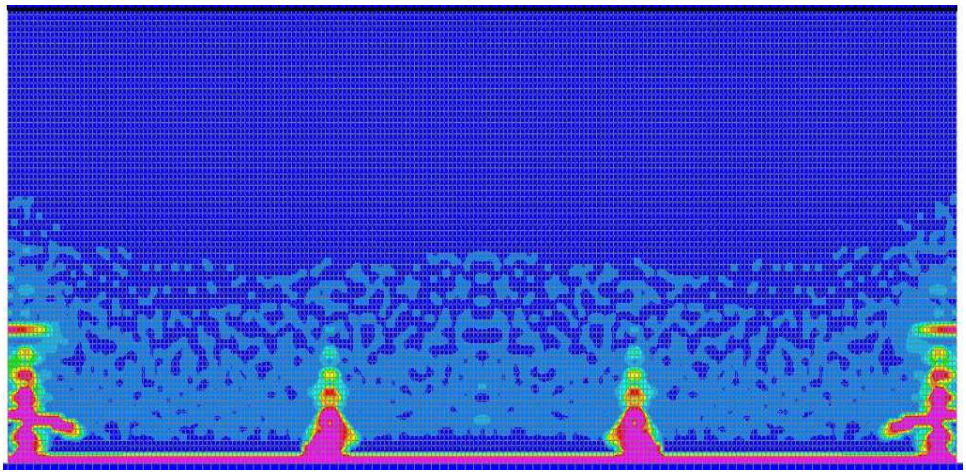

Figure A.45. Tensile Damage of W36_2_PB_C_0 at 1.0% Drift

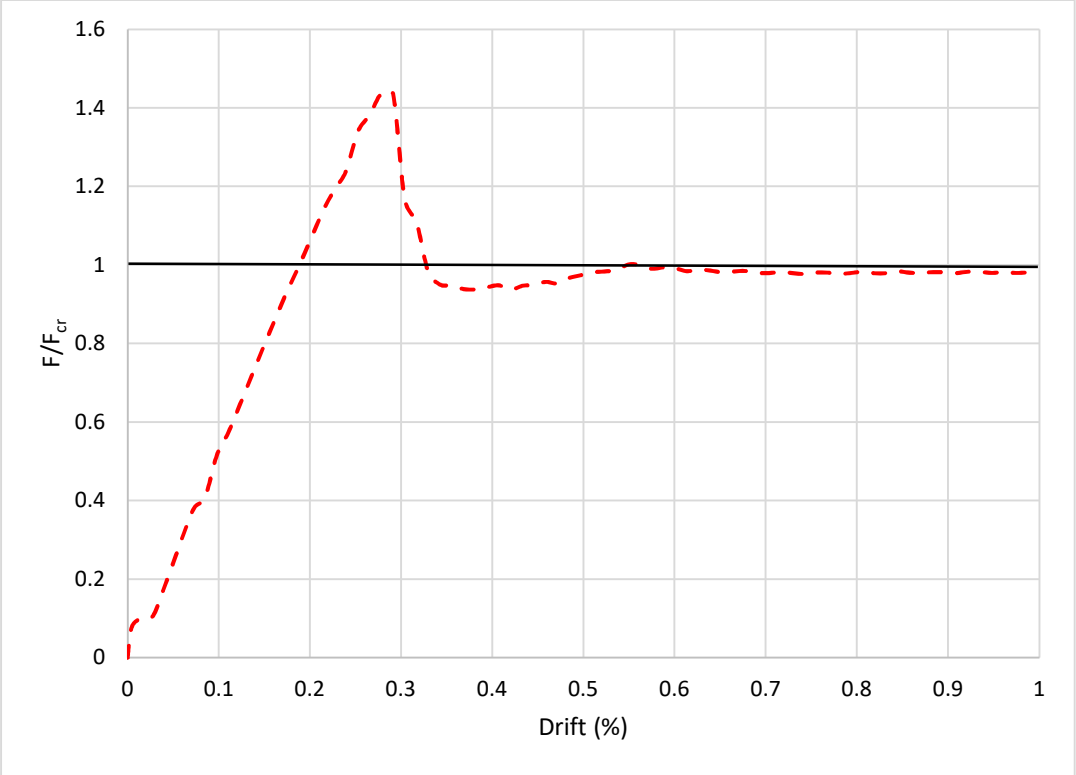

Figure A.46. Load Displacement History of W48_2_PB_C_0

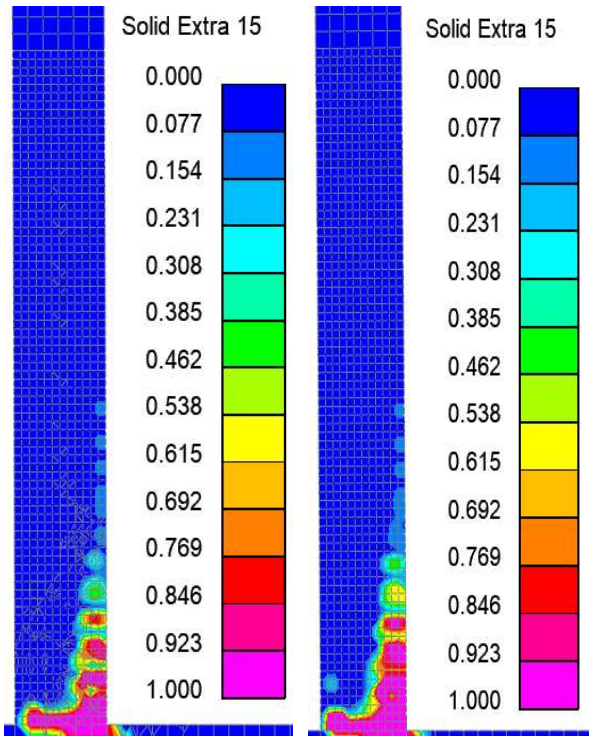

Figure A.47. Tensile Damage of W48_2_PB_C_0 at 0.5% and 1% Drift

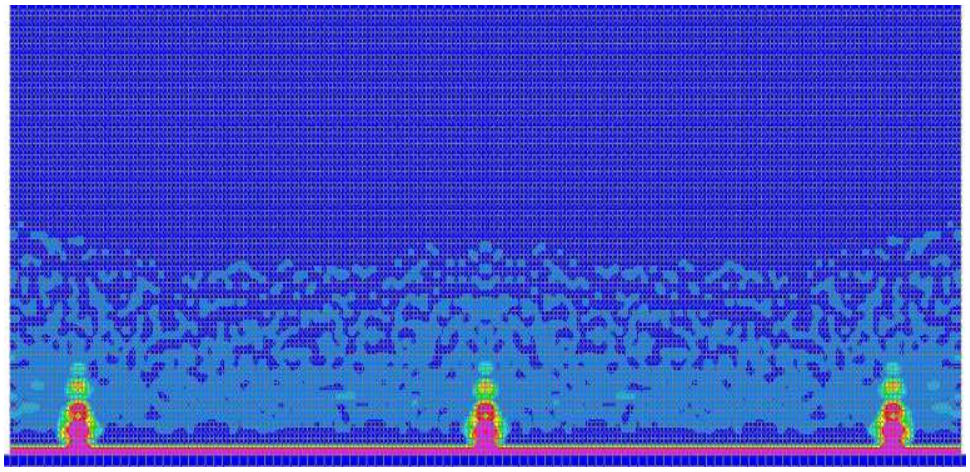

Figure A.48. Tensile Damage of W48_2_PB_C_0 at 0.5% Drift

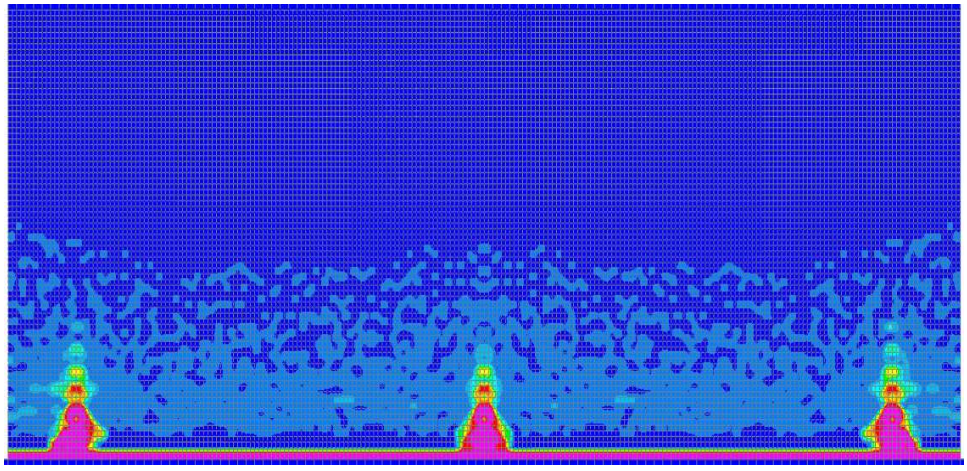

Figure A.49. Tensile Damage of W48_2_PB_C_0 at 1.0% Drift

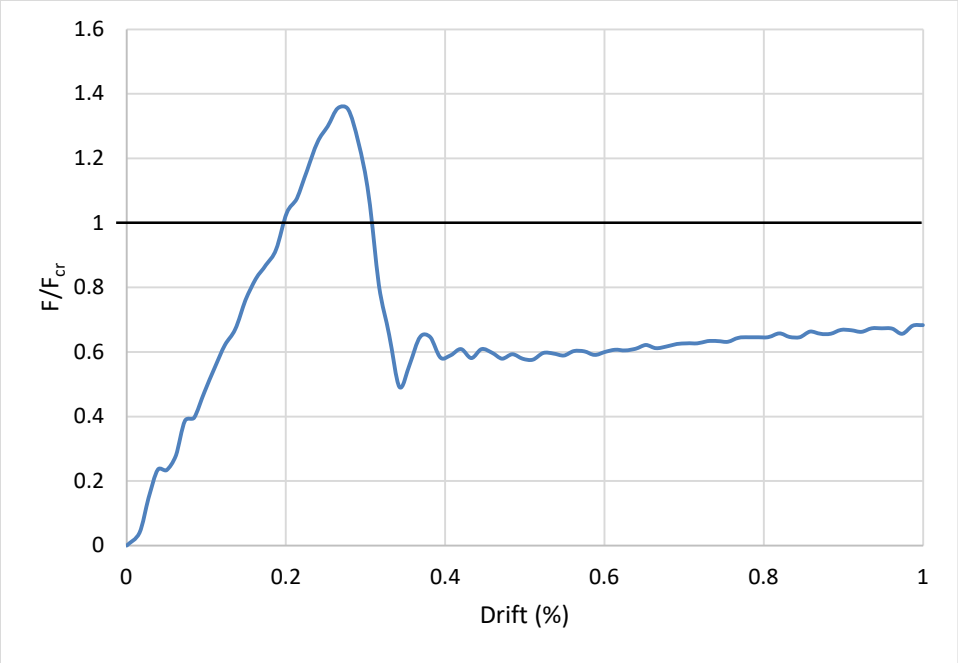

Figure A.50. Load Displacement History of W18_1_MB_S_0

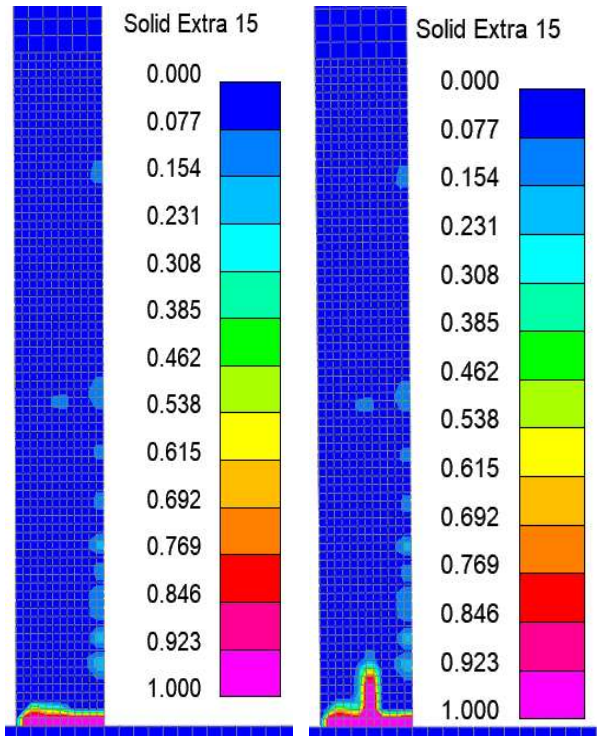

Figure A.51. Tensile Damage of W18_1_MB_S_0 at 0.5% and 1% Drift

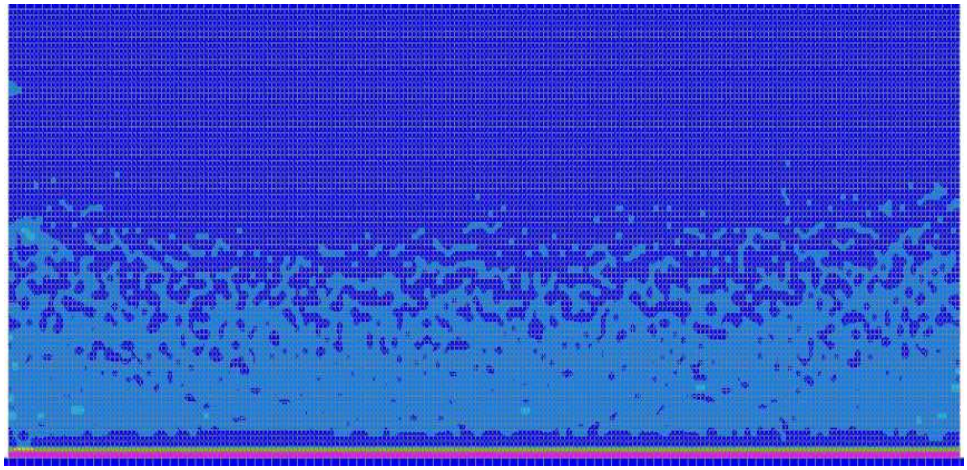

Figure A.52. Tensile Damage of W18_1_MB_S_0 at 0.5% Drift

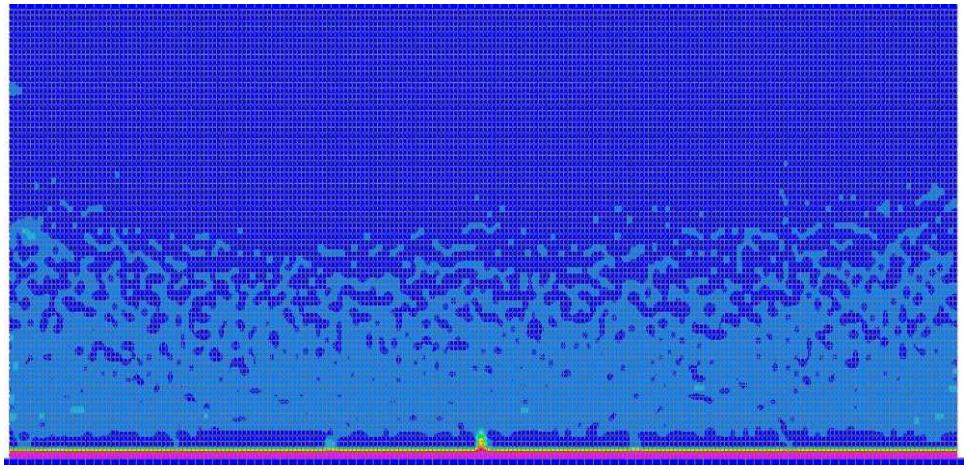

Figure A.53. Tensile Damage of W18_1_MB_S_0 at 1.0% Drift

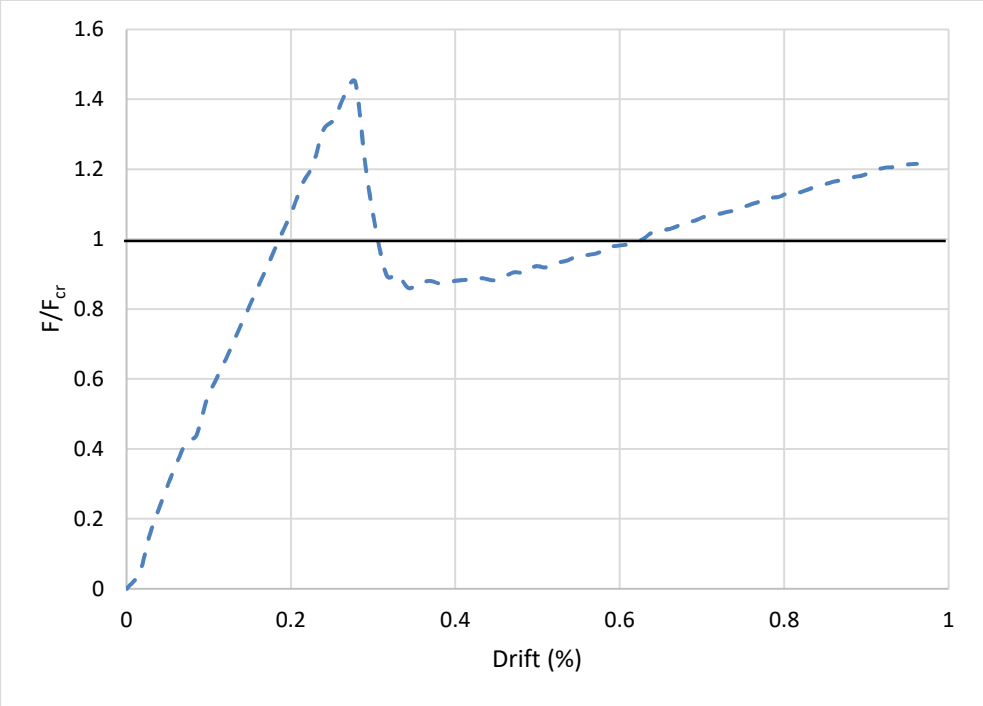

Figure A.54. Load Displacement History of W18_2_MB_S_0

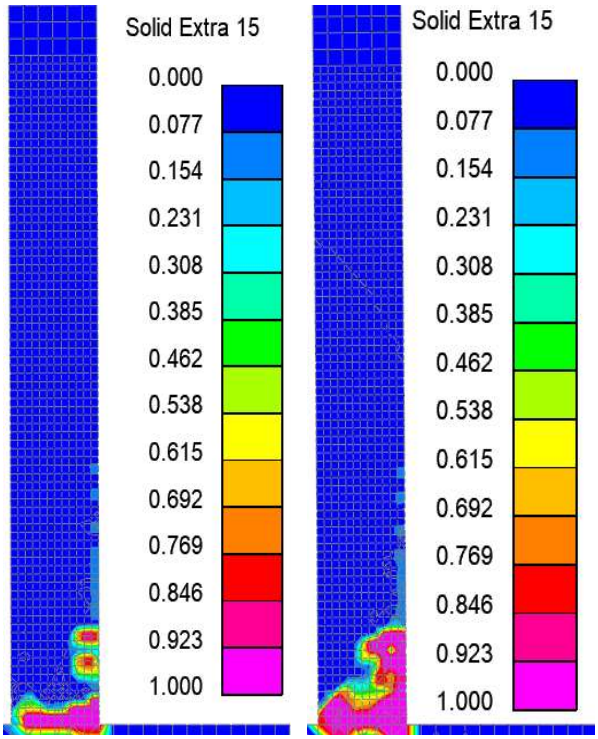

Figure A.55. Tensile Damage of W18_2_MB_S_0 at 0.5% and 1% Drift

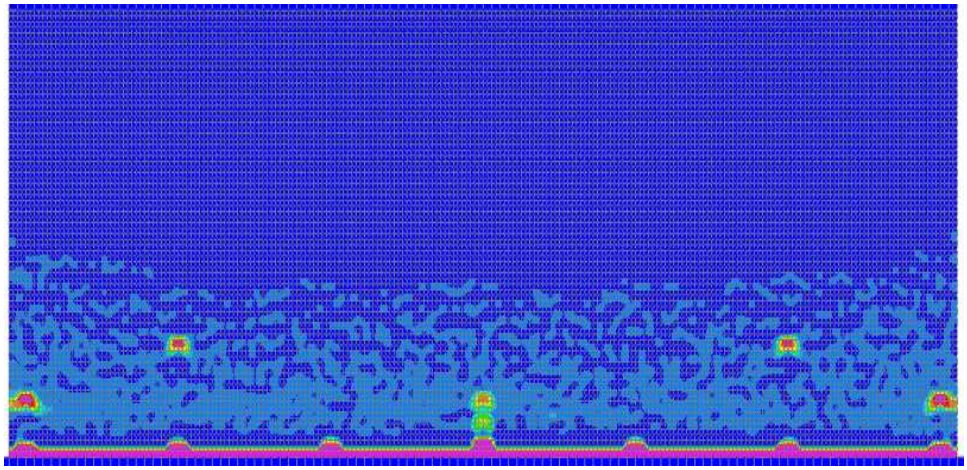

Figure A.56. Tensile Damage of W18_2_MB_S_0 at 0.5% Drift

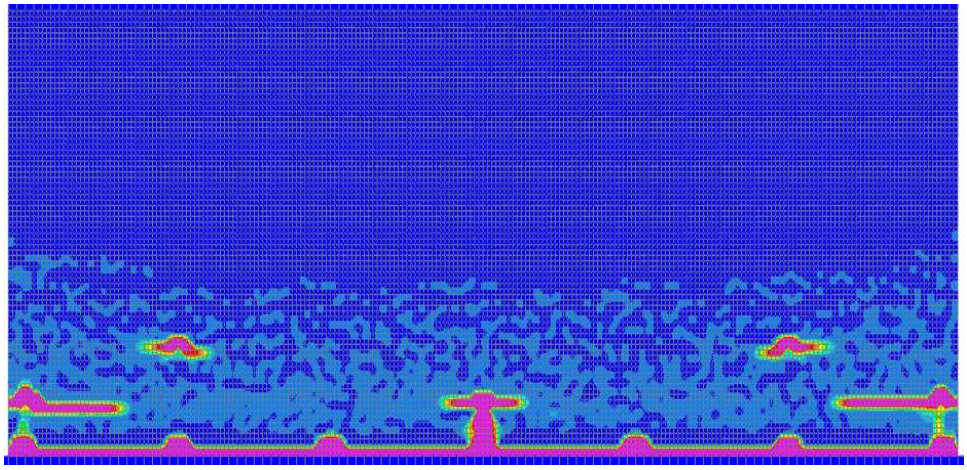

Figure A.57. Tensile Damage of W18_2_MB_S_0 at 1.0% Drift

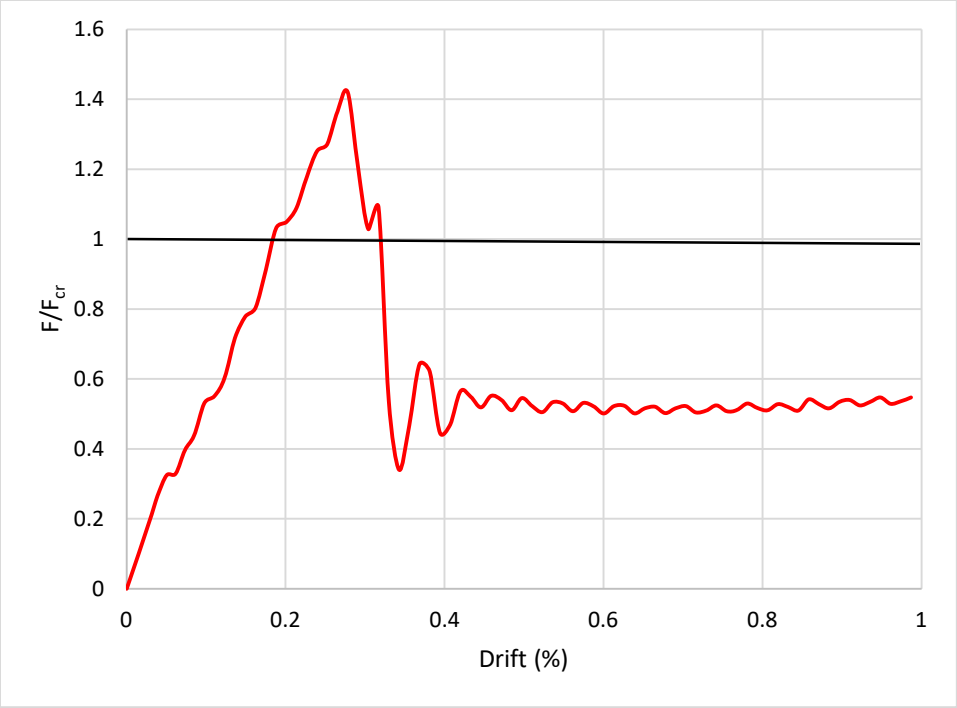

Figure A.58. Load Displacement History of W48_1_MB_S_0

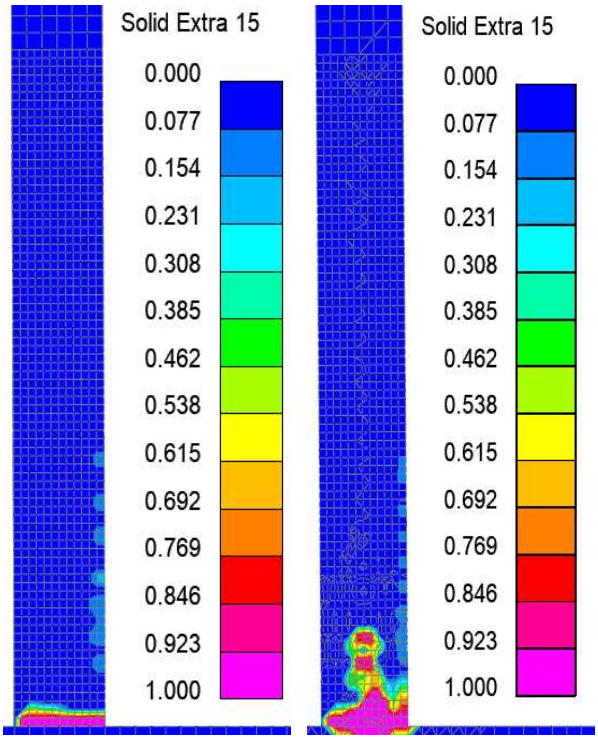

Figure A.59. Tensile Damage of W48_1_MB_S_0 at 0.5% and 1% Drift

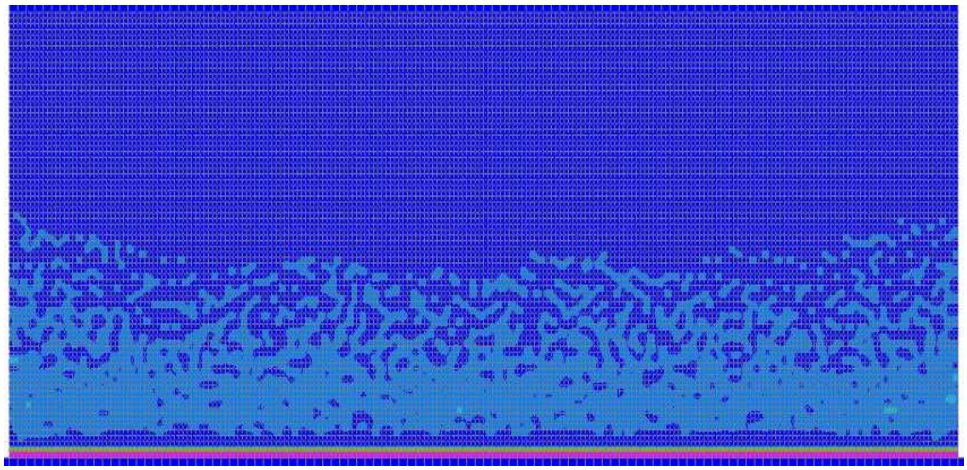

Figure A.60. Tensile Damage of W48_1_MB_S_0 at 0.5% Drift

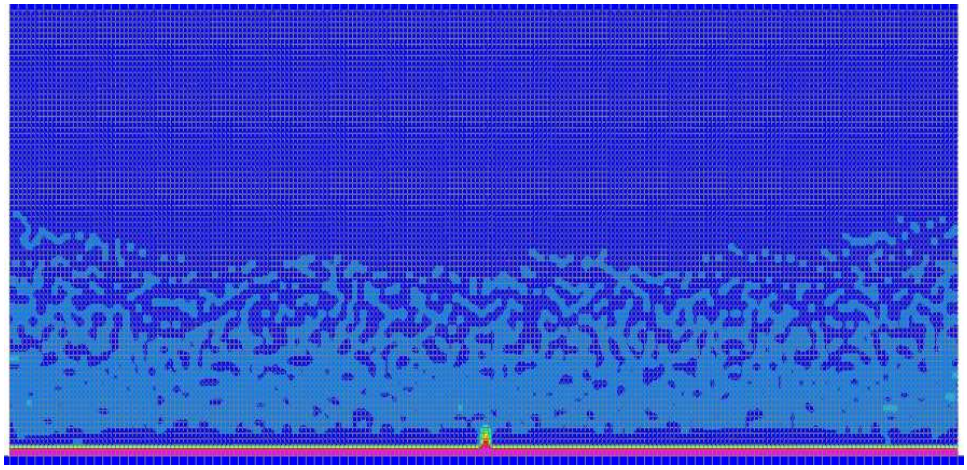

Figure A.61. Tensile Damage of W48_1_MB_S_0 at 1.0% Drift

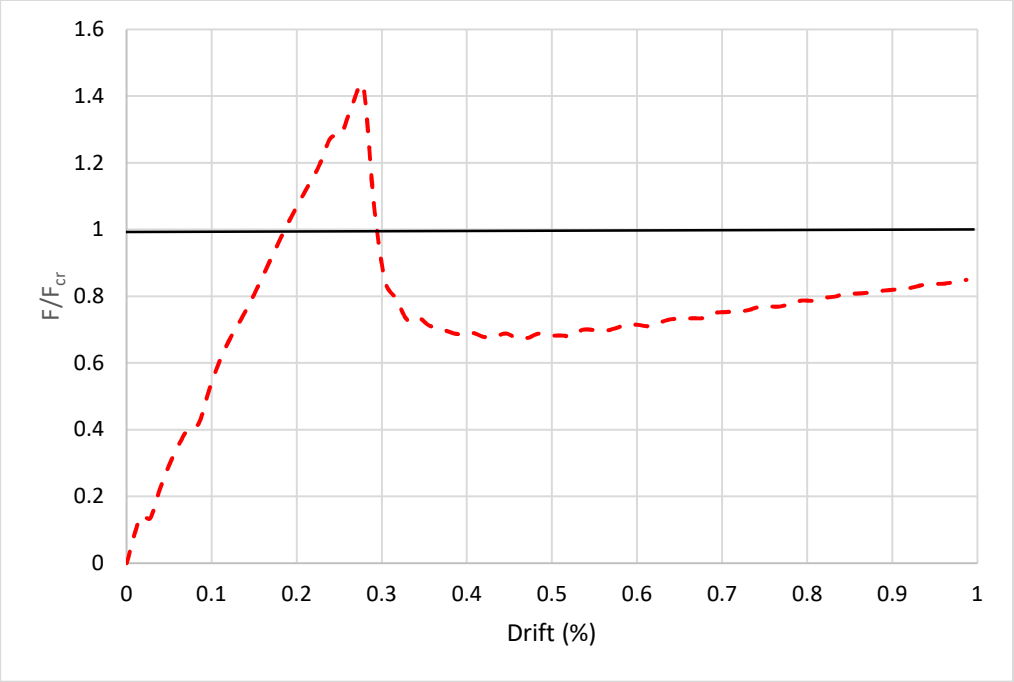

Figure A.62. Load Displacement History of W48_2_MB_S_0

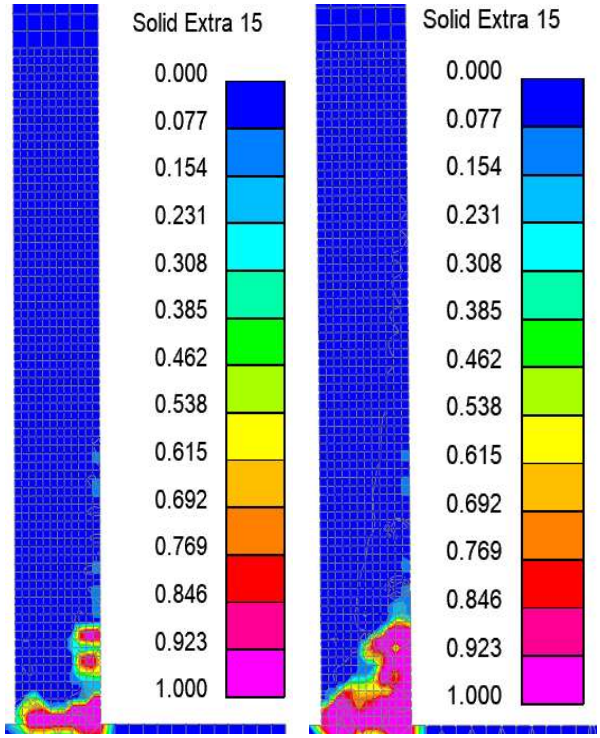

Figure A.63. Tensile Damage of W48_2_MB_S_0 at 0.5% and 1% Drift

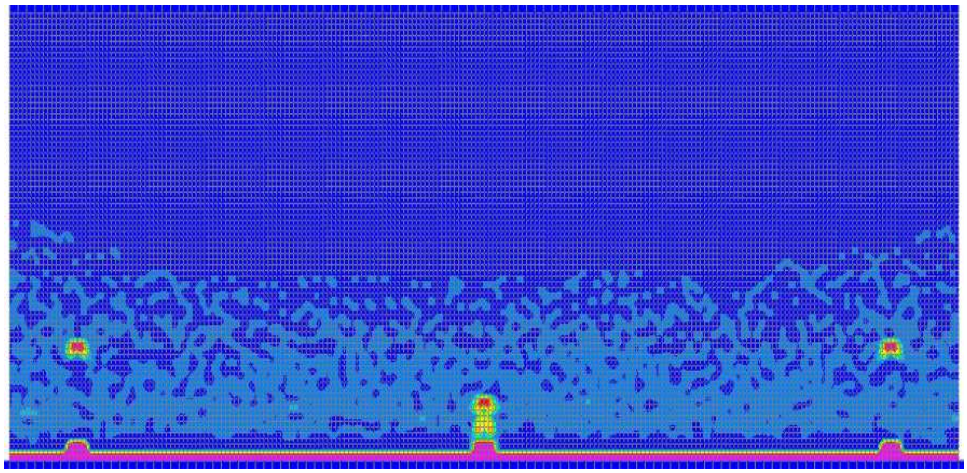

Figure A.64. Tensile Damage of W48_2_MB_S_0 at 0.5% Drift

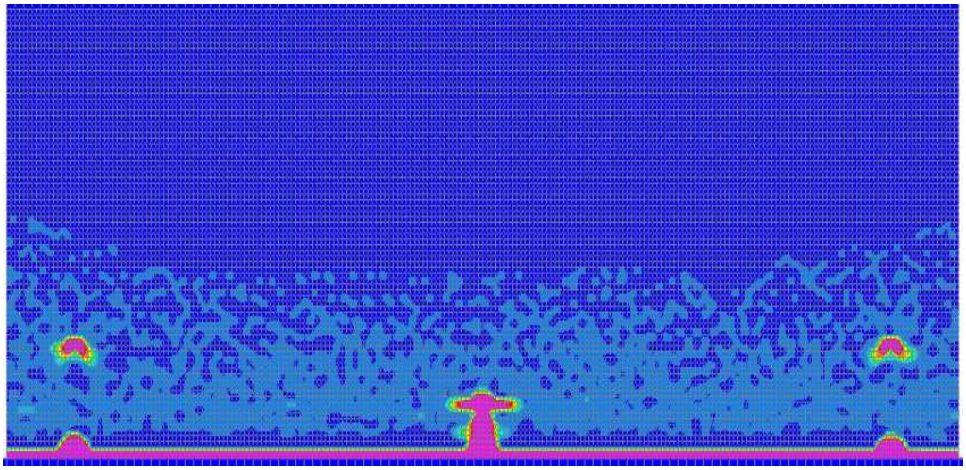

Figure A.65. Tensile Damage of W48_2_MB_S_0 at 1.0% Drift

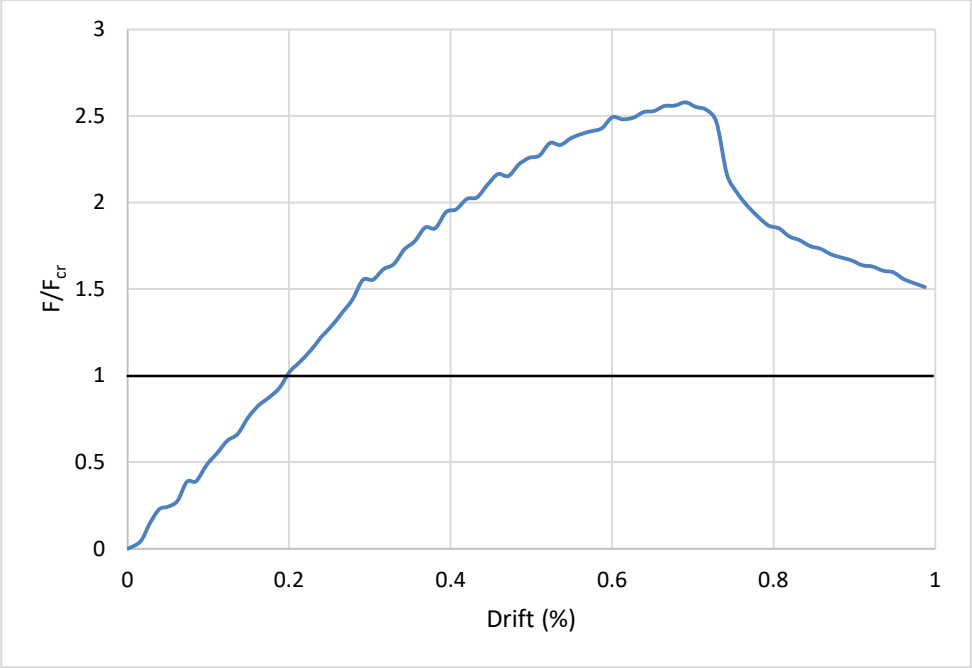

Figure A.66. Load Displacement History of W18_1_MB_S_0.5

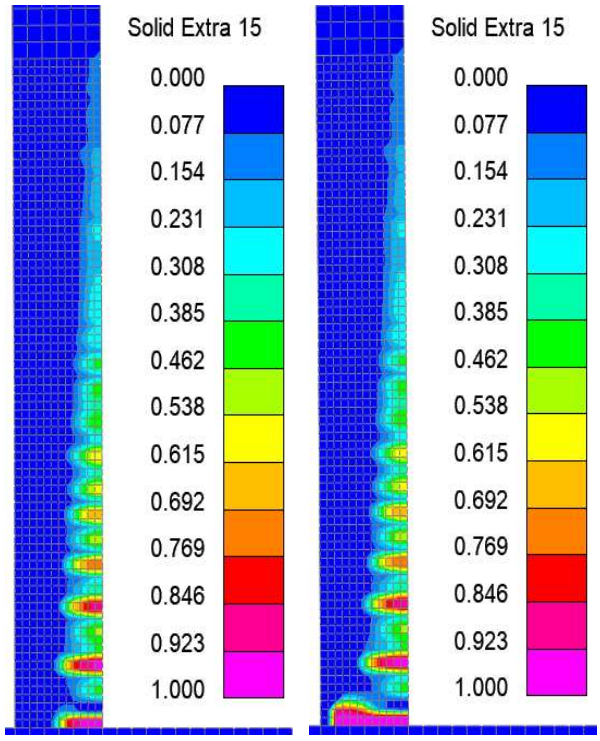

Figure A.67. Tensile Damage of W18_1_MB_S_0.5 at Peak Strength and 1% Drift

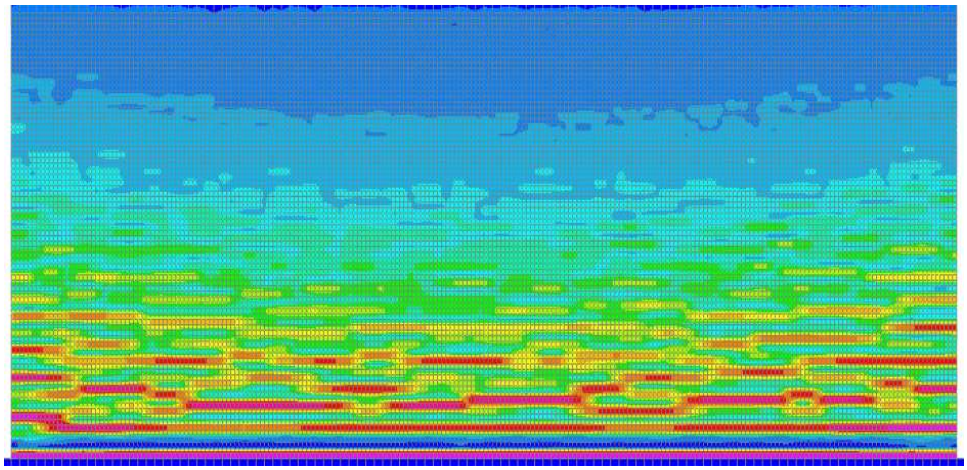

Figure A.68. Tensile Damage of W18_1_MB_S_0.5 at Peak Strength

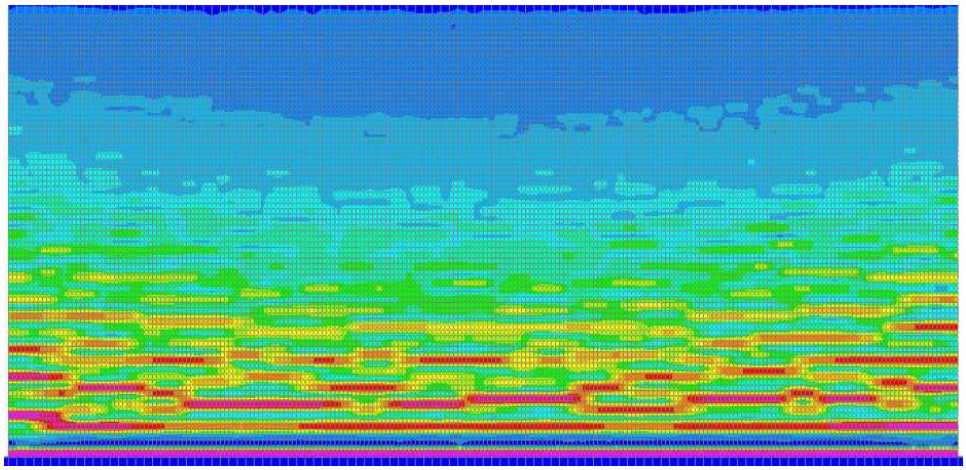

Figure A.69. Tensile Damage of W18_1_MB_S_0.5 at 1.0% Drift

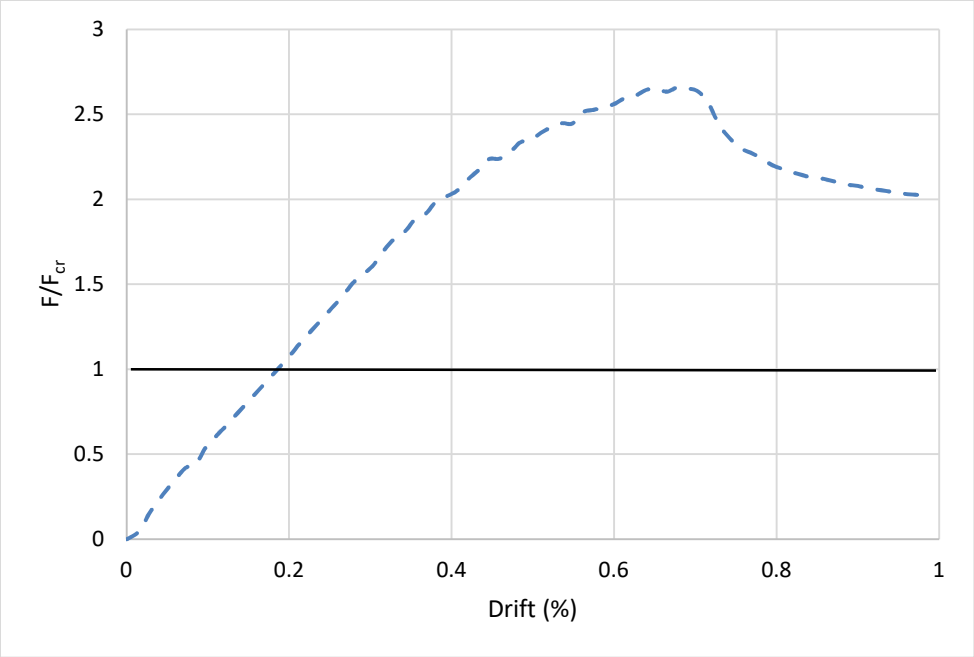

Figure A.70. Load Displacement History of W18_2_MB_S_0.5

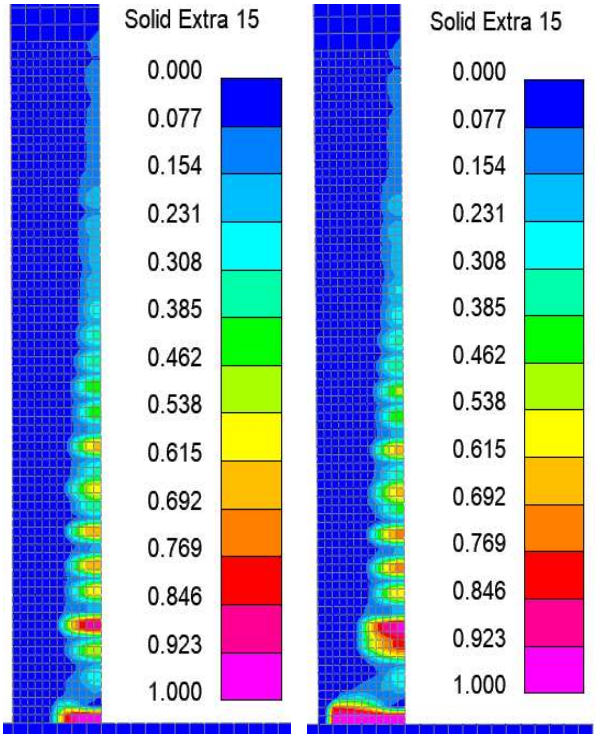

Figure A.71. Tensile Damage of W18_2_MB_S_0.5 at Peak Strength and 1% Drift

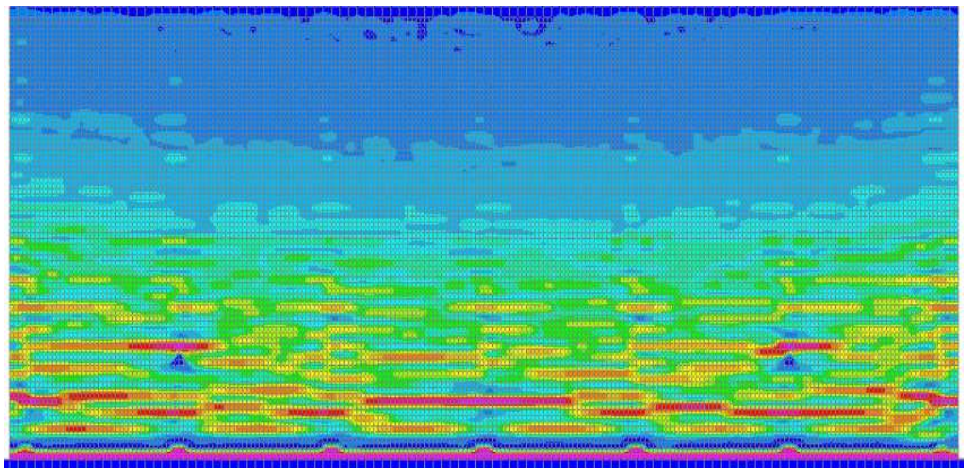

Figure A.72. Tensile Damage of W18_2_MB_S_0.5 at Peak Strength

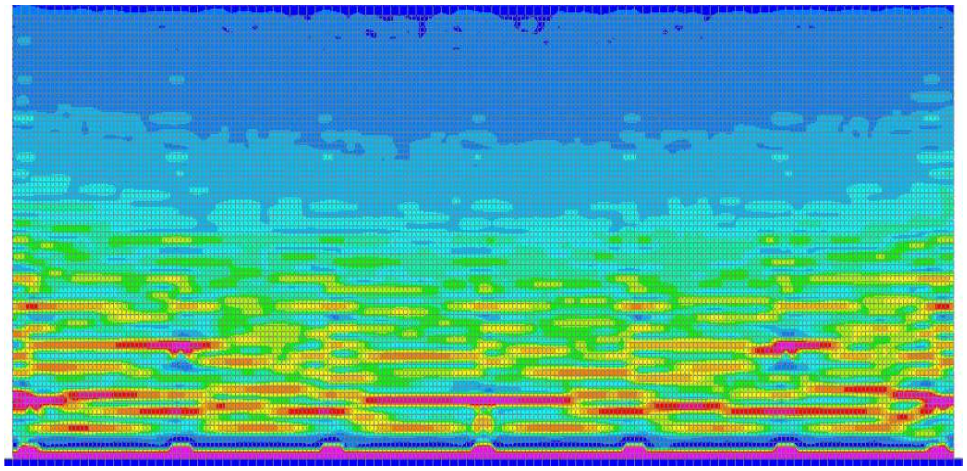

Figure A.73. Tensile Damage of W18_2_MB_S_0.5 at 1.0% Drift

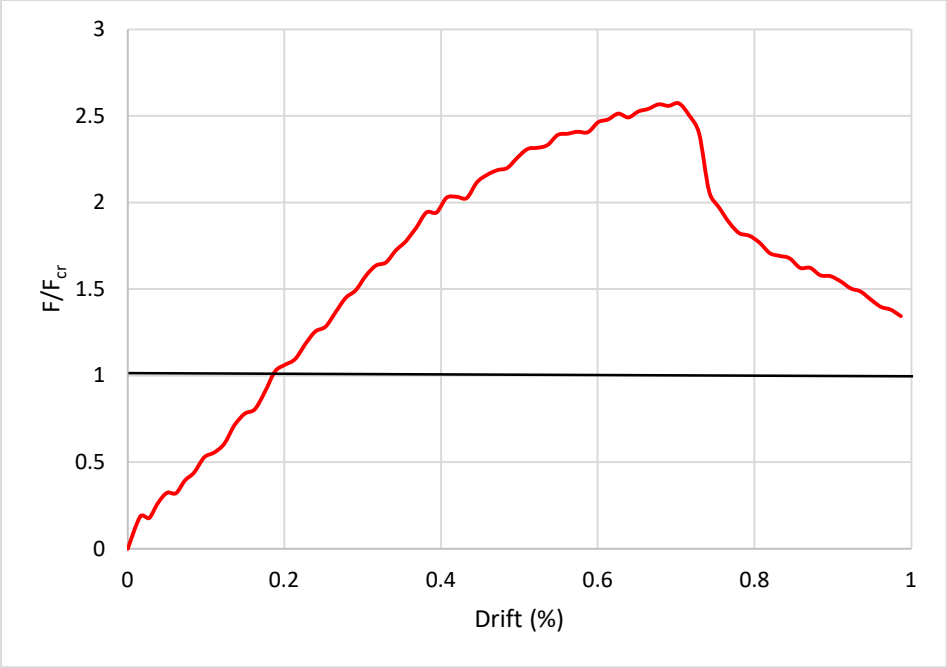

Figure A.74. Load Displacement History of W48_1_MB_S_0.5

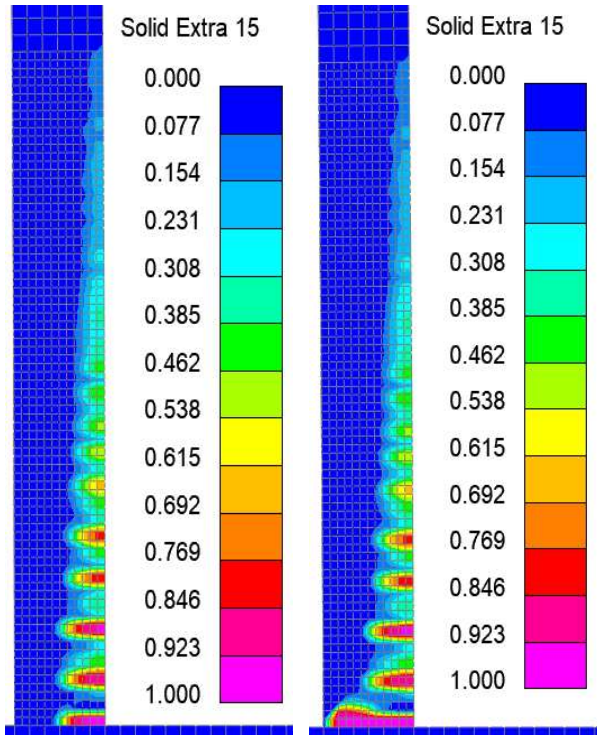

Figure A.75. Tensile Damage of W48_1_MB_S_0.5 at Peak Strength and 1% Drift

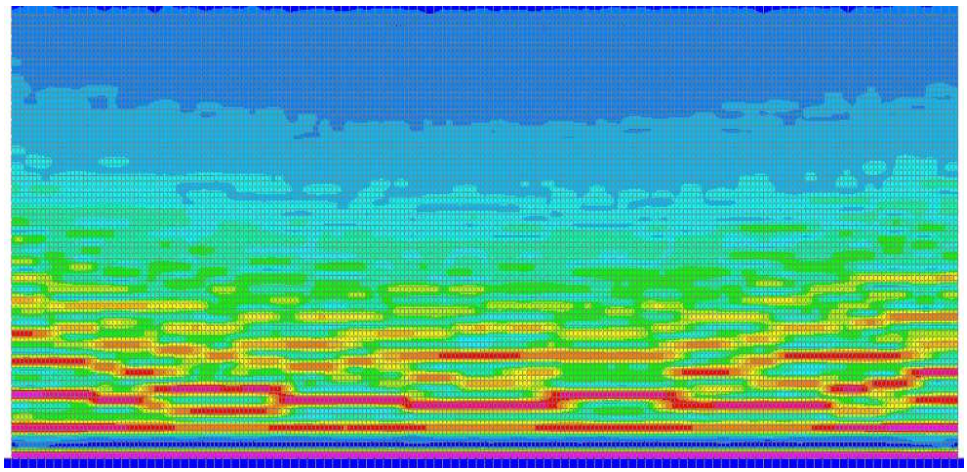

Figure A.76. Tensile Damage of W48_1_MB_S_0.5 at Peak Strength

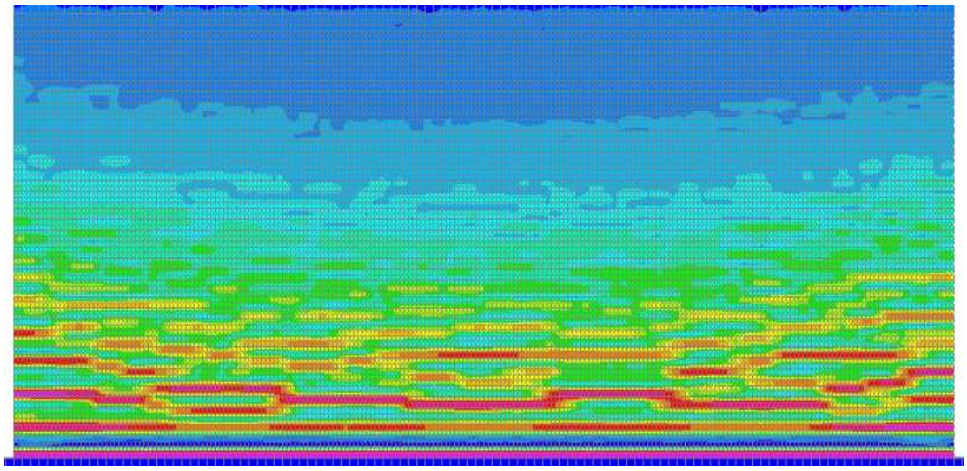

Figure A.77. Tensile Damage of W48_2_MB_S_0.5 at 1.0% Drift

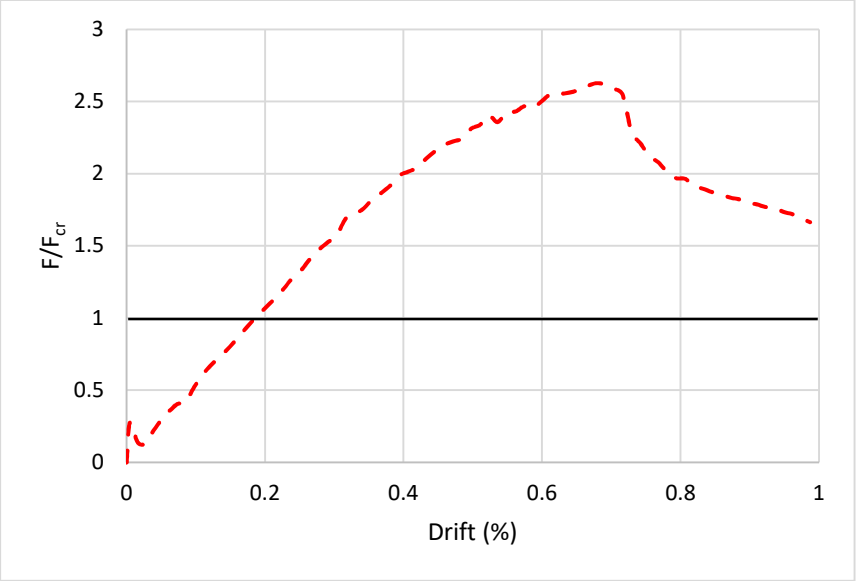

Figure A.78. Load Displacement History of W48_2_MB_S_0.5

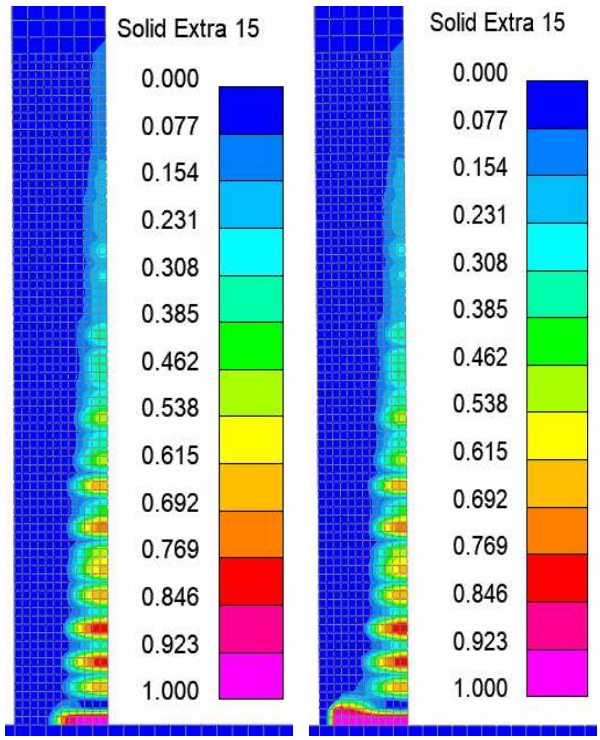

Figure A.79. Tensile Damage of W48_2_MB_S_0.5 at Peak Strength and 1% Drift

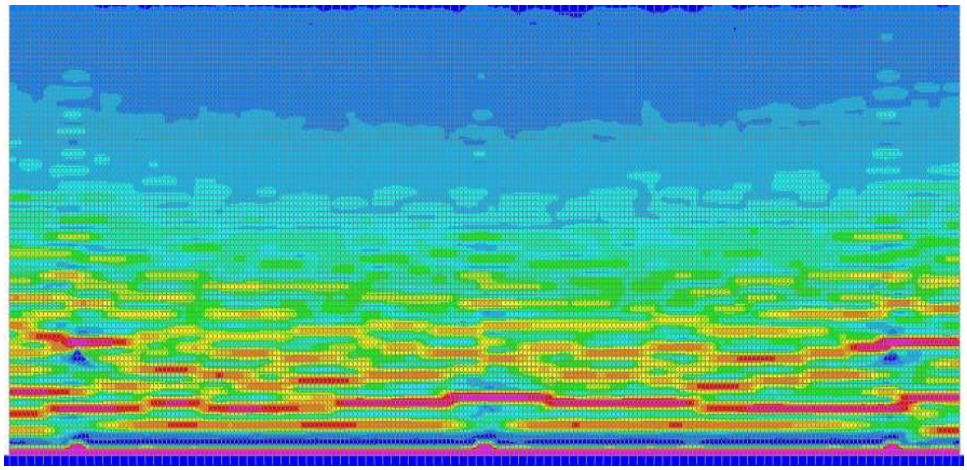

Figure A.80. Tensile Damage of W48_2_MB_S_0.5 at Peak Strength

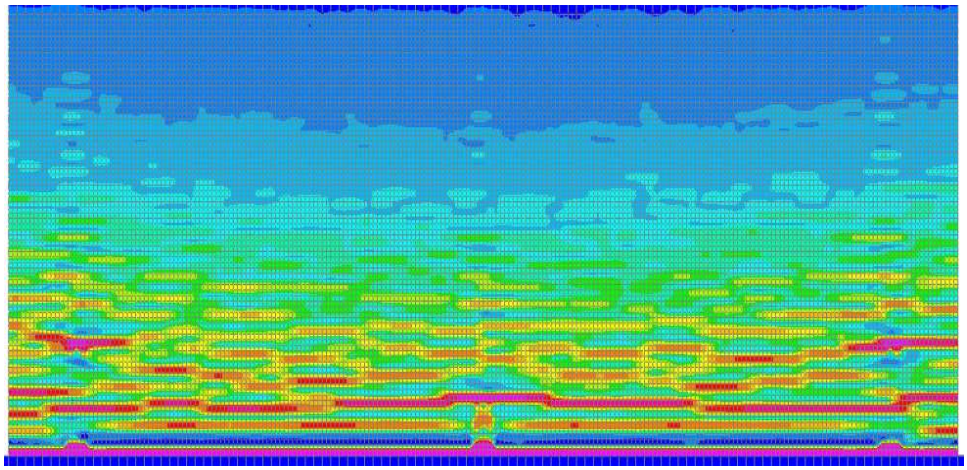

Figure A.81. Tensile Damage of W48_2_MB_S_0.5 at 1.0% Drift

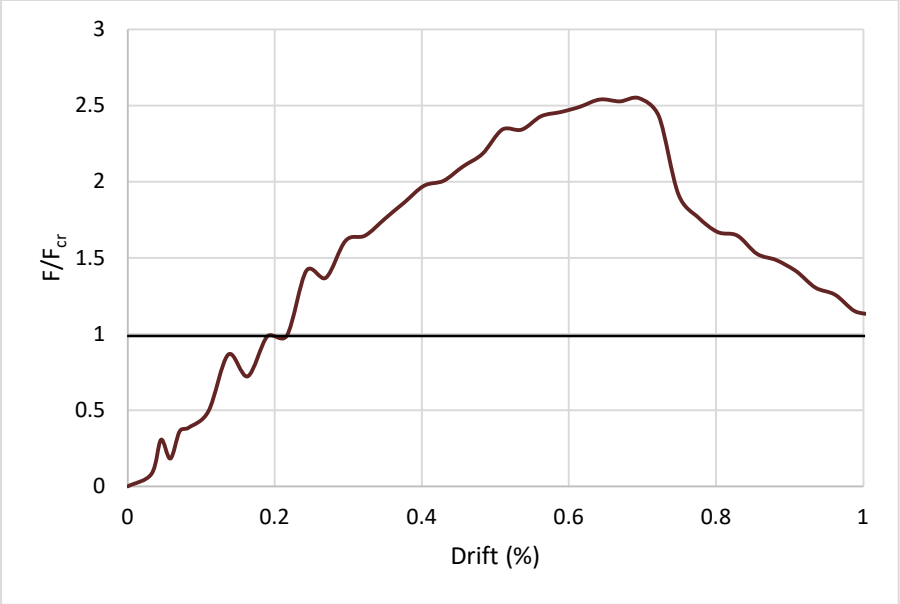

Figure A.82. Load Displacement History of W0_0_0_0_0.5

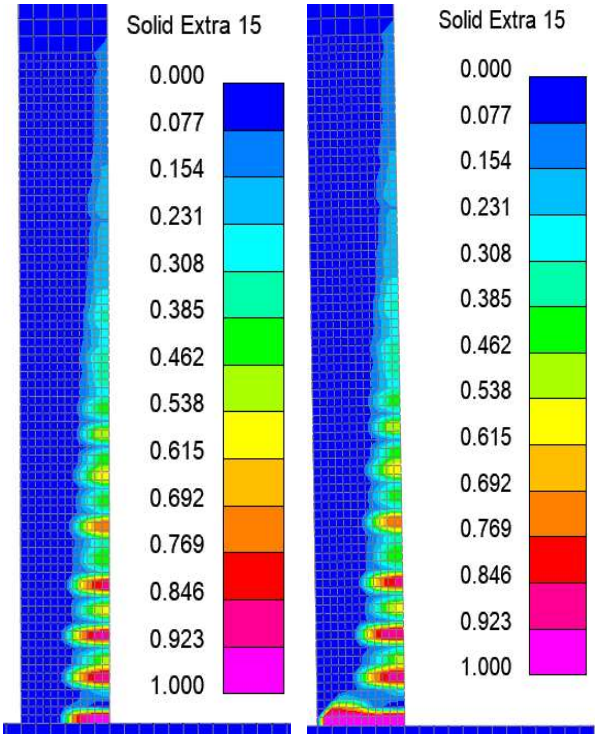

Figure A.83. Tensile Damage of W0_0_0_0_0.5 at Peak Strength and 1% Drift

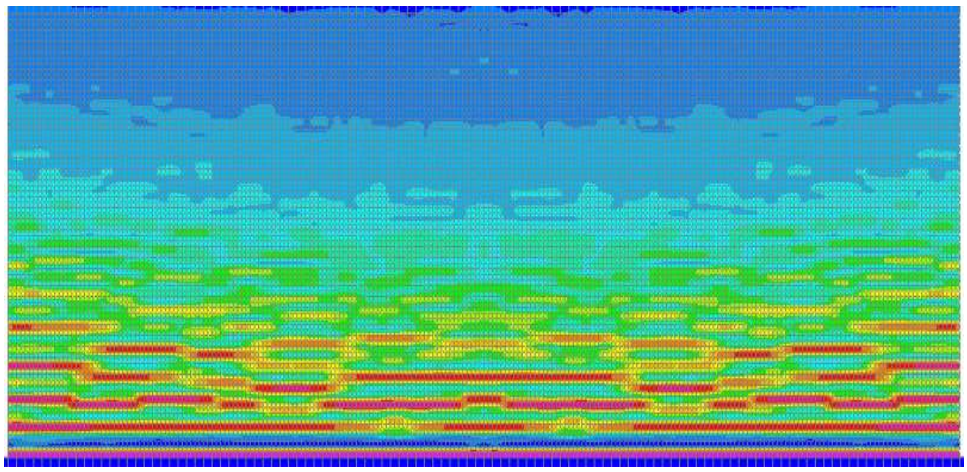

Figure A.84. Tensile Damage of W0_0_0_0_0.5 at Peak Strength

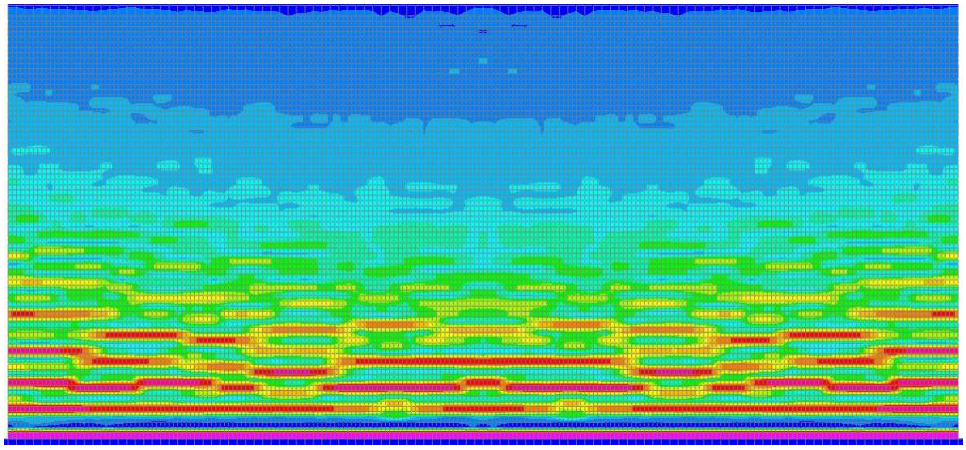

Figure A.85. Tensile Damage of W0_0_0_0_0.5 at 1.0% Drift

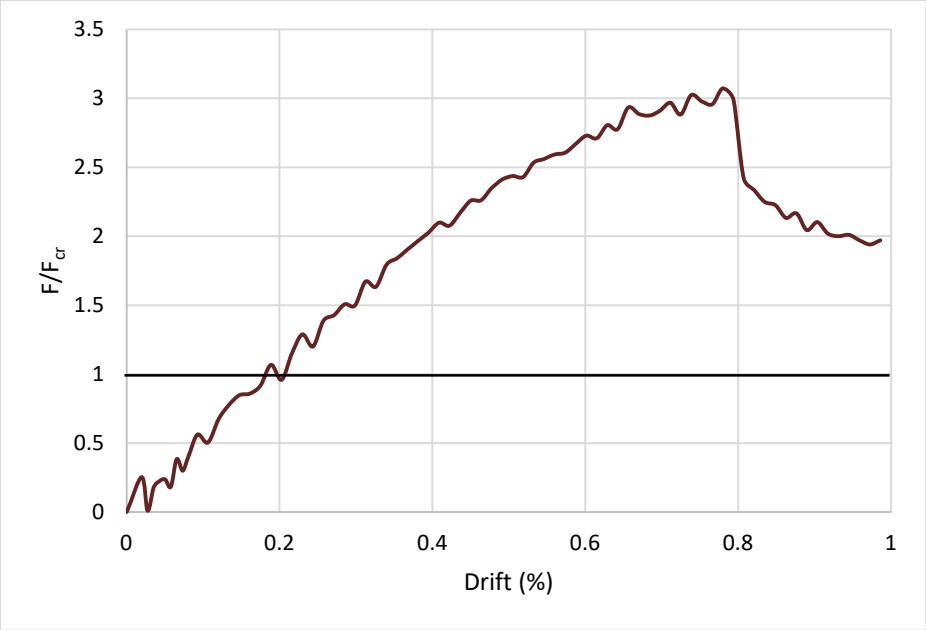

Figure A.86. Load Displacement History of W0_0_0_0_1.0

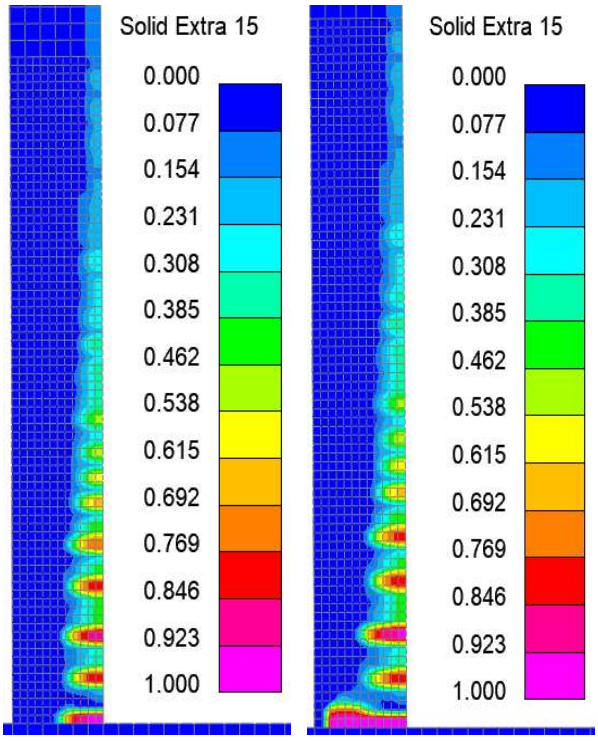

Figure A.87. Tensile Damage of W0_0_0_0_1.0 at Peak Strength and 1% Drift

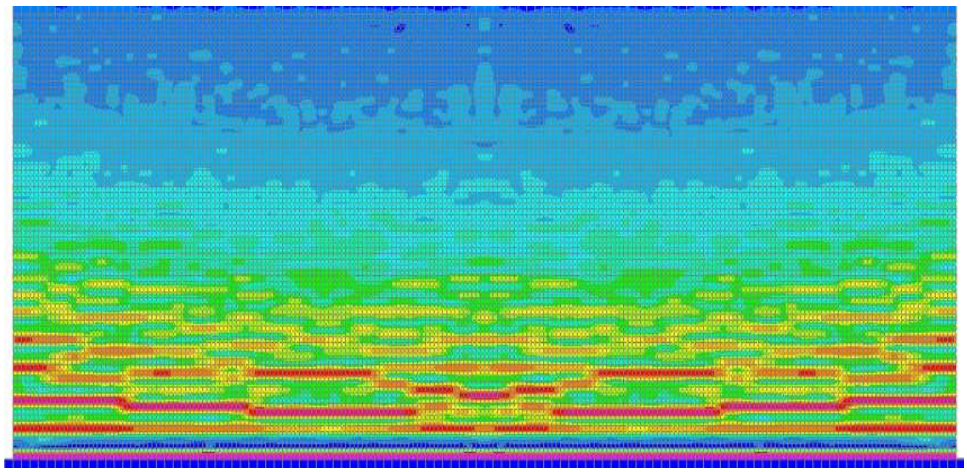

Figure A.88. Tensile Damage of W0_0_0_0_1.0 at Peak Strength

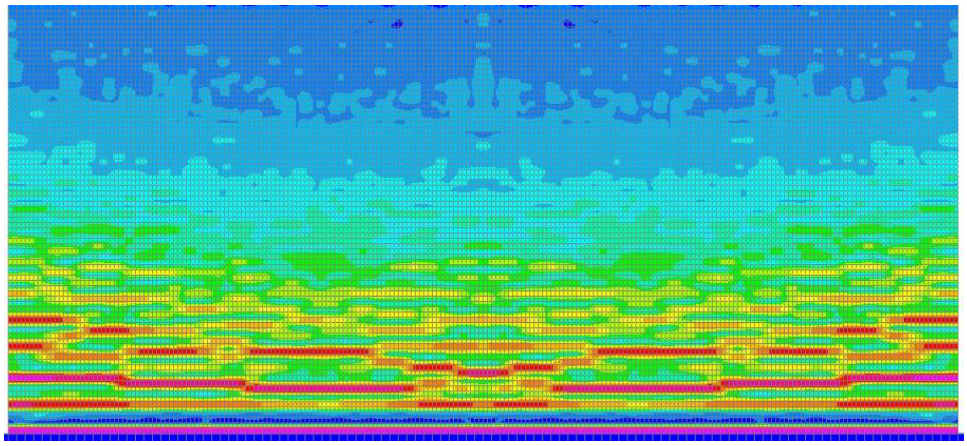

Figure A.89. Tensile Damage of W0_0_0_0_1.0 at 1.0% Drift

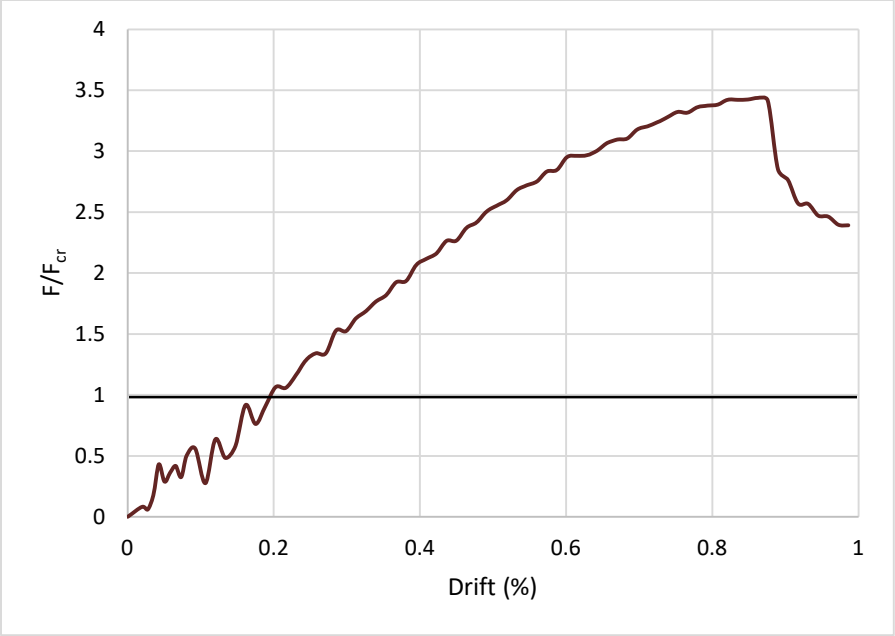

Figure A.90. Load Displacement History of W0_0_0_0_1.5

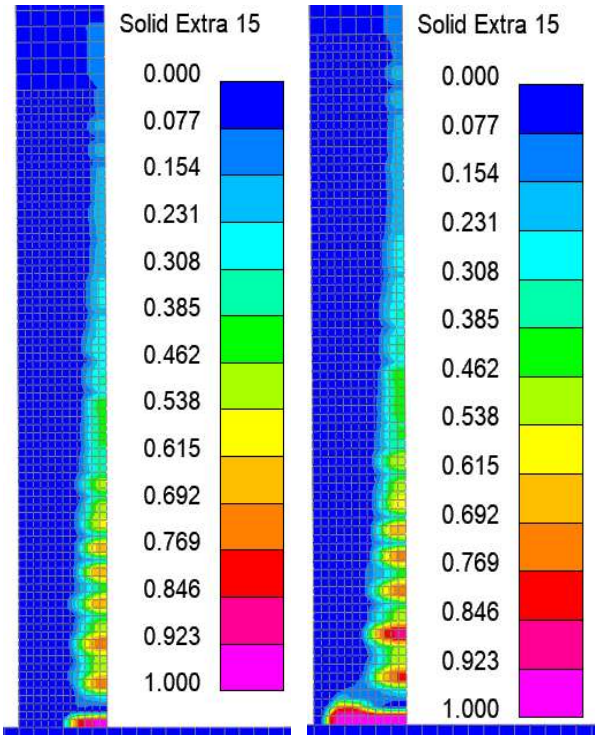

Figure A.91. Tensile Damage of W0_0_0_0_1.5 at Peak Strength and 1% Drift

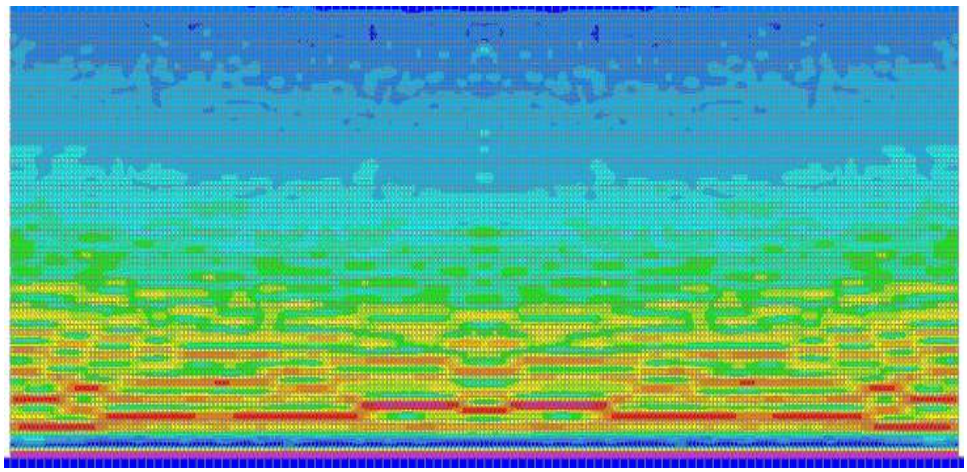

Figure A.92. Tensile Damage of W0_0_0_0_1.5 at Peak Strength

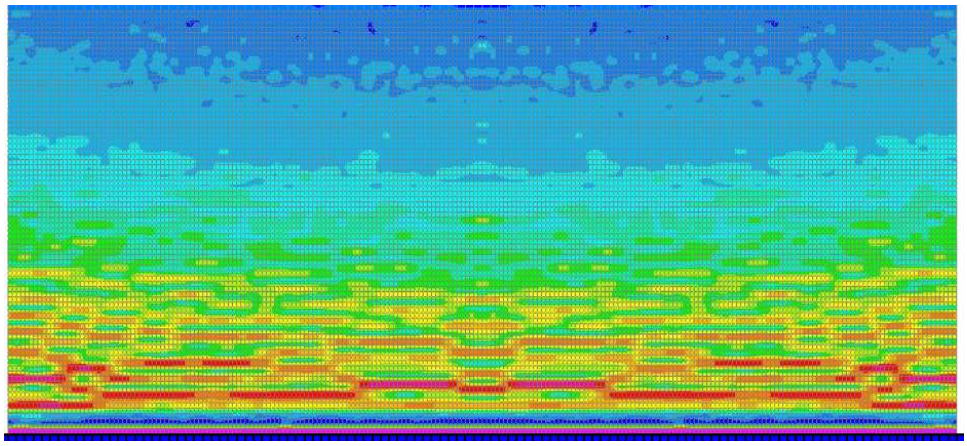

Figure A.93. Tensile Damage of W0_0_0_0_1.5 at 1.0% Drift

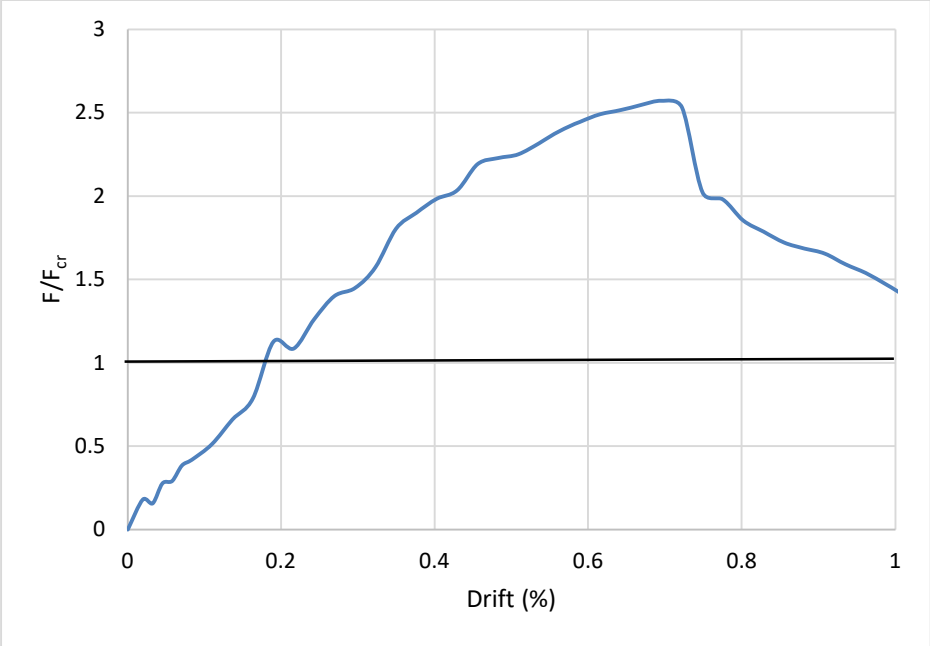

Figure A.94. Load Displacement History of W18_1_MB_C_0.5

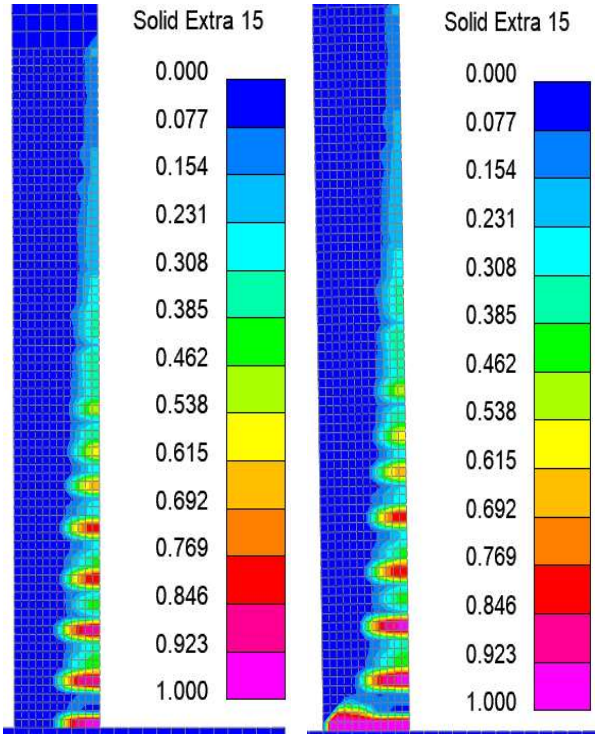

Figure A.95. Tensile Damage of W18_1_MB_C_0.5 at Peak Strength and 1% Drift

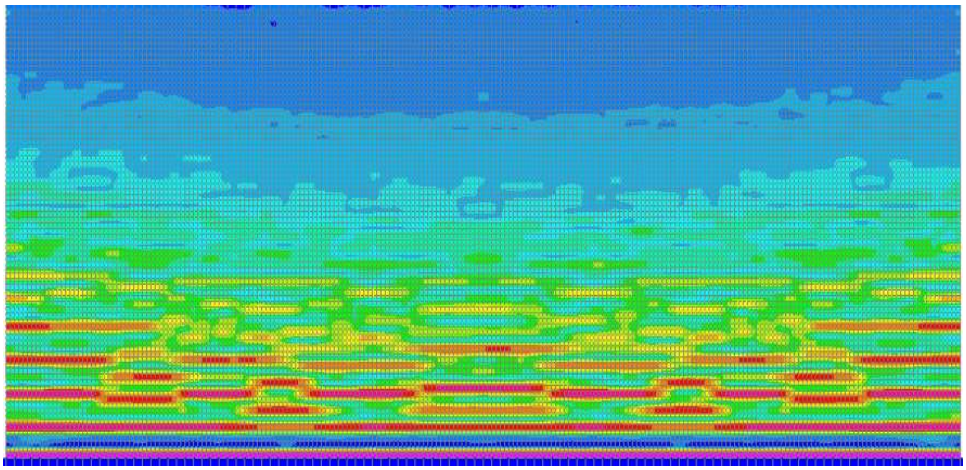

Figure A.96. Tensile Damage of W18_1_MB_C_0.5 at Peak Strength

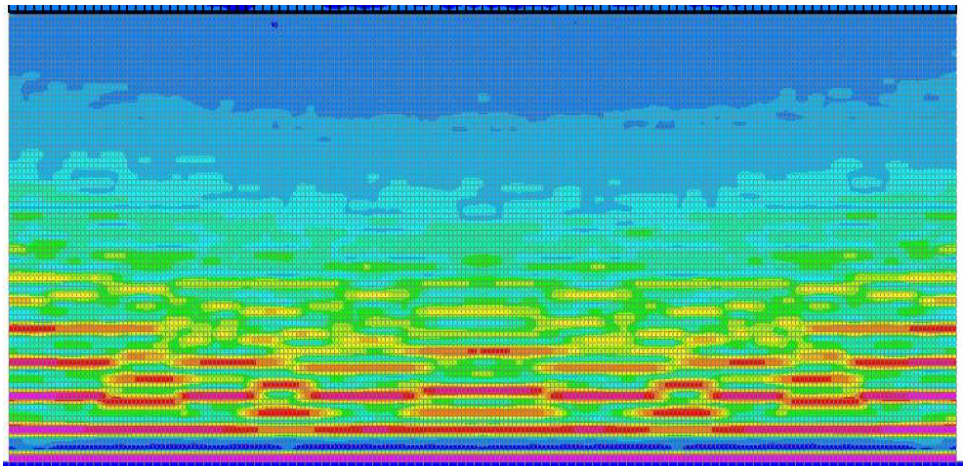

Figure A.97. Tensile Damage of W18_1_MB_C_0.5 at 1.0% Drift

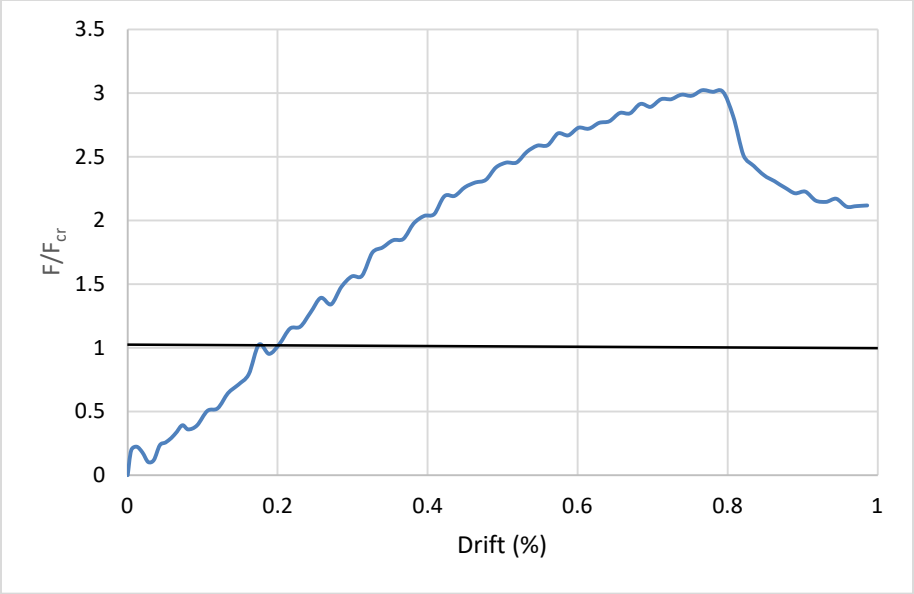

Figure A.98. Load Displacement History of W18_1_MB_C_1.0

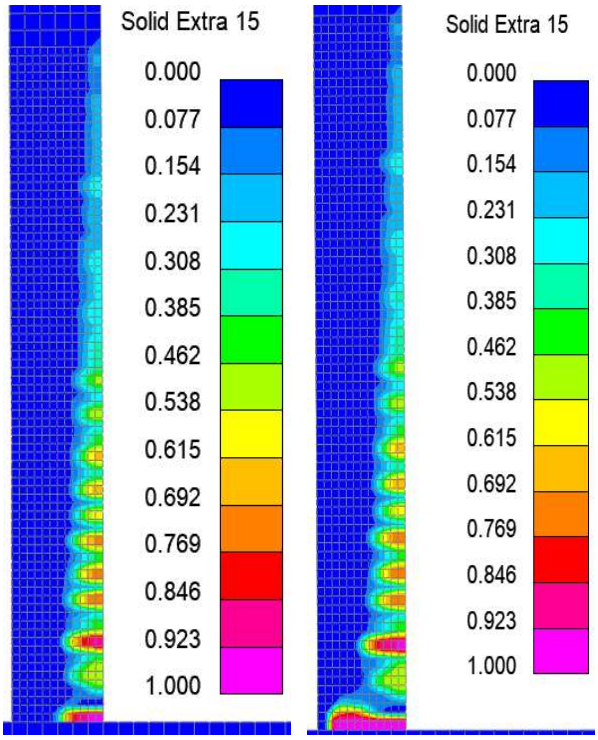

Figure A.99. Tensile Damage of W18_1_MB_C_1.0 at Peak Strength and 1% Drift

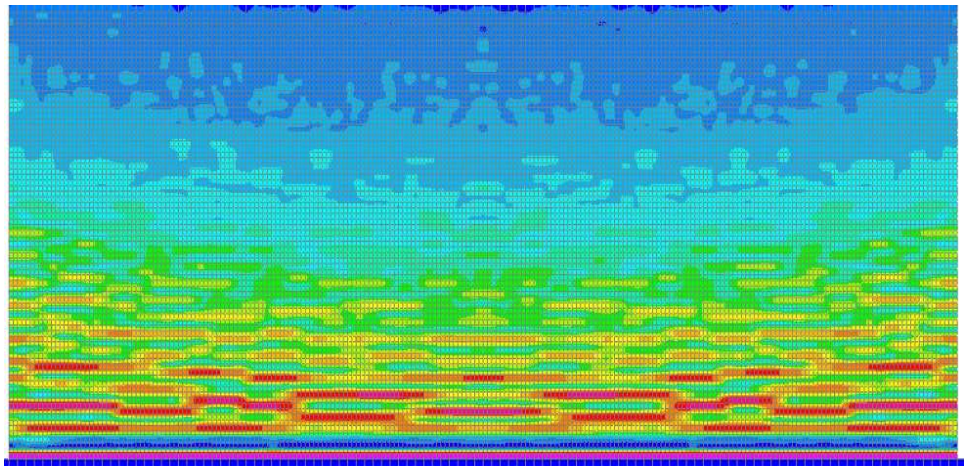

Figure A.100. Tensile Damage of W18_1_MB_C_1.0 at Peak Strength

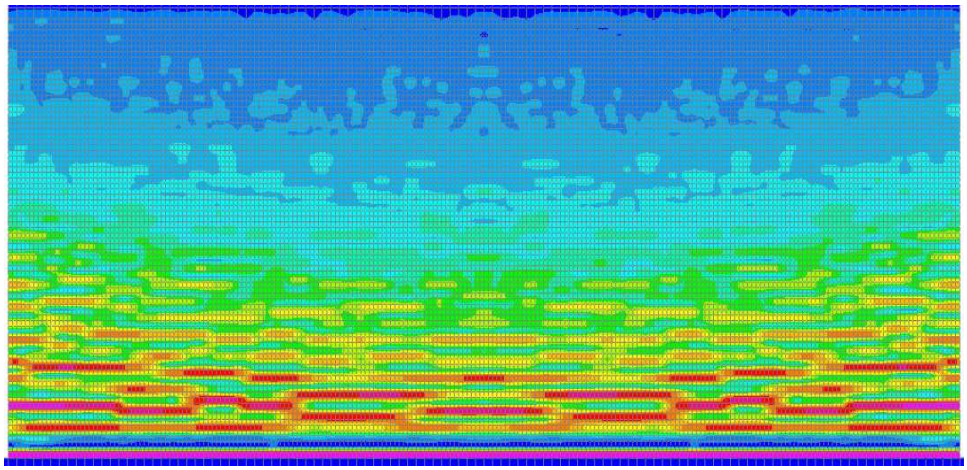

Figure A.101. Tensile Damage of W18_1_MB_C_1.0 at 1.0% Drift

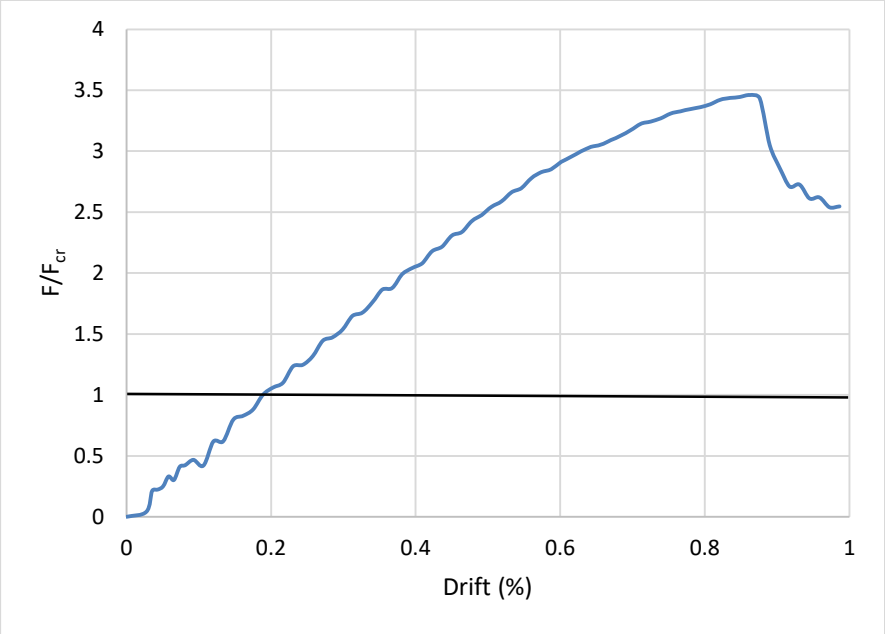

Figure A.102. Load Displacement History of W18_1_MB_C_1.5

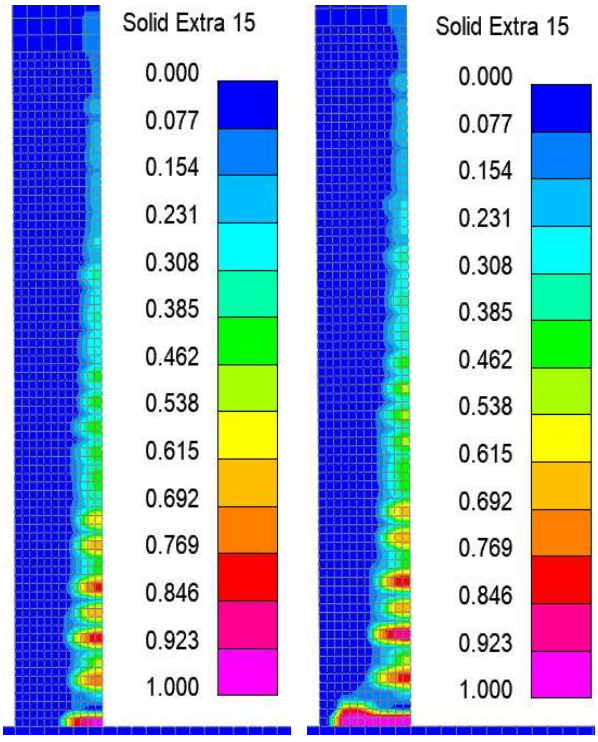

Figure A.103. Tensile Damage of W18_1_MB_C_1.5 at Peak Strength and 1% Drift

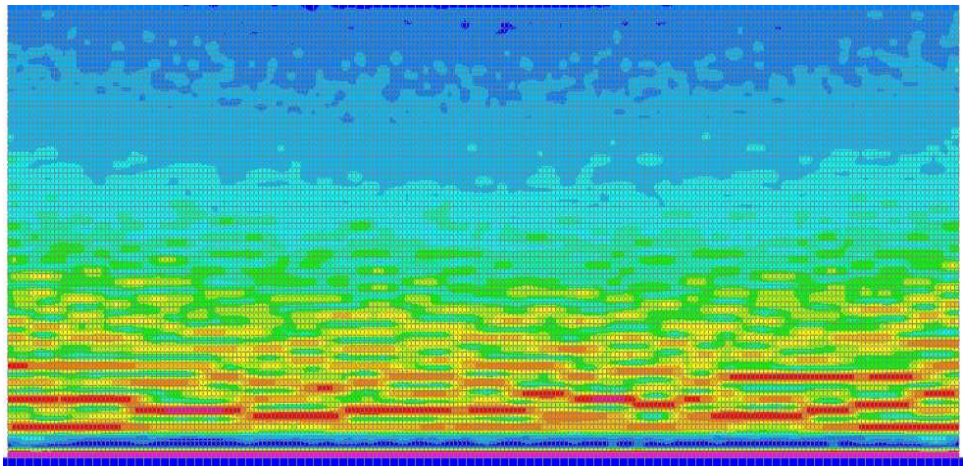

Figure A.104. Tensile Damage of W18_1_MB_C_1.5 at Peak Strength

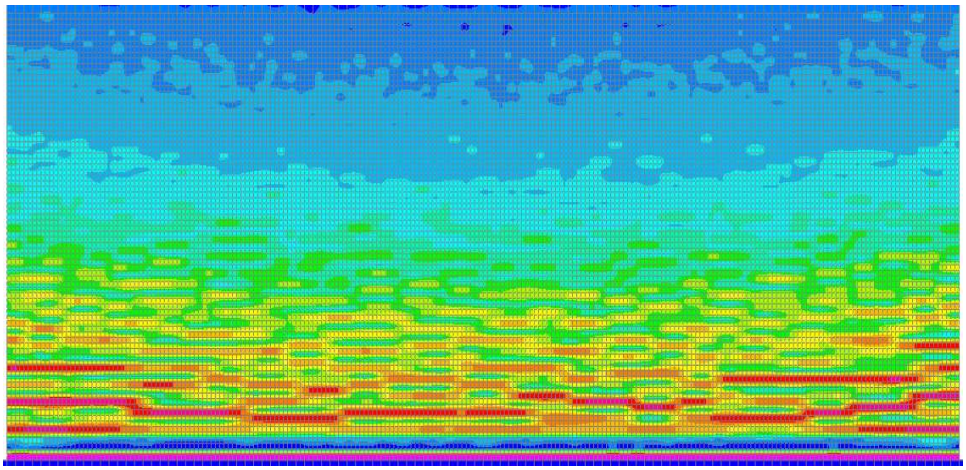

Figure A.105. Tensile Damage of W18_1_MB_C_1.5 at 1.0% Drift

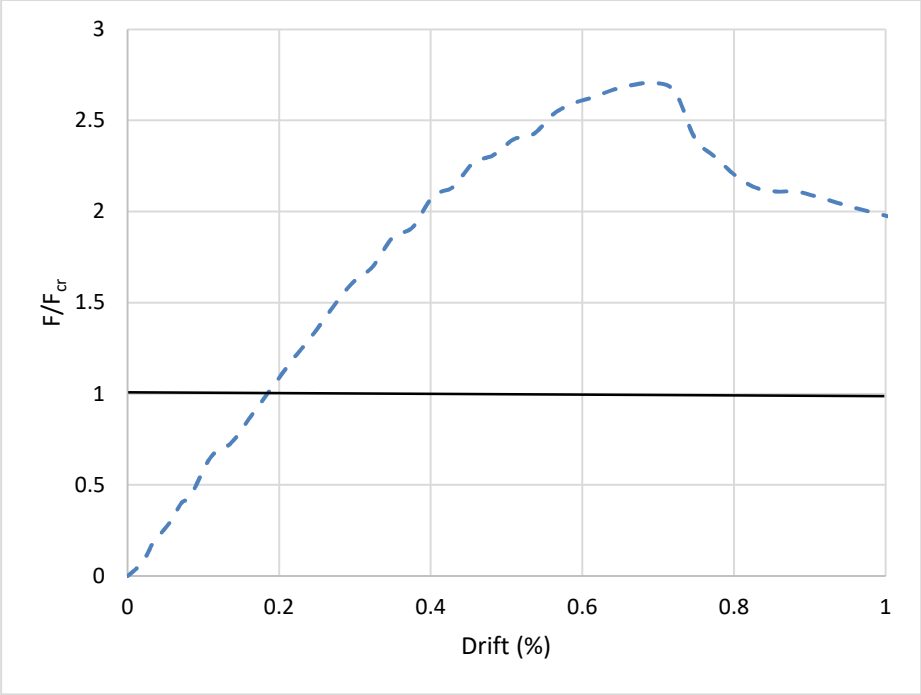

Figure A.106. Load Displacement History of W18_2_MB_C_0.5

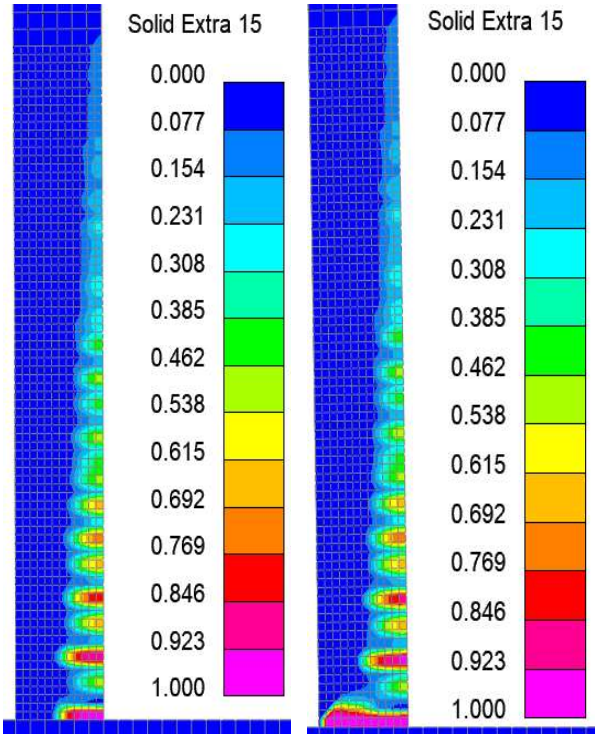

Figure A.107. Tensile Damage of W18_2_MB_C_0.5 at Peak Strength and 1% Drift

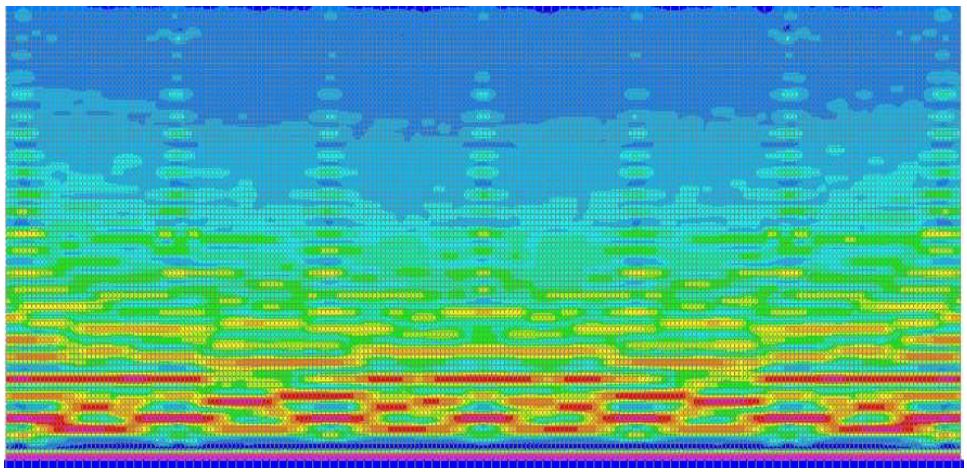

Figure A.108. Tensile Damage of W18_2_MB_C_0.5 at Peak Strength

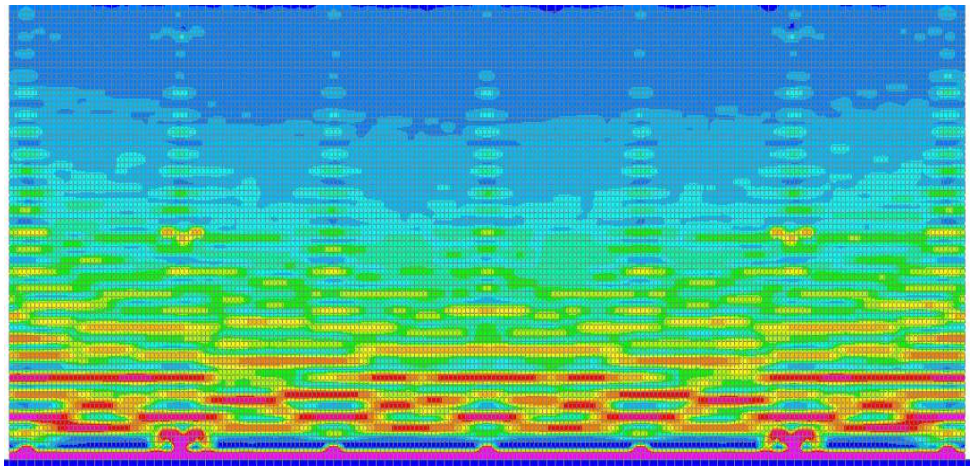

Figure A.109. Tensile Damage of W18_2_MB_C_0.5 at 1.0% Drift

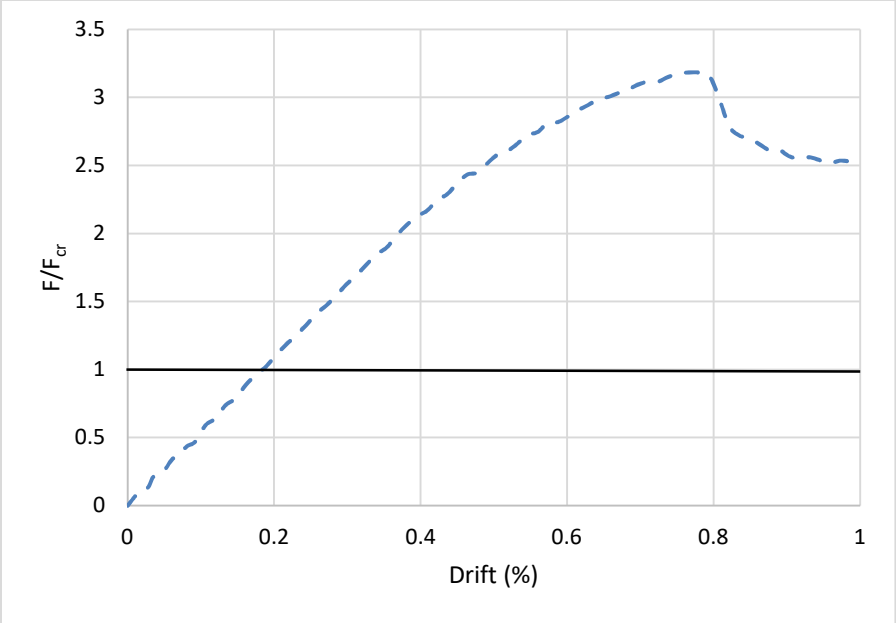

Figure A.110. Load Displacement History of W18_2_MB_C_1.0

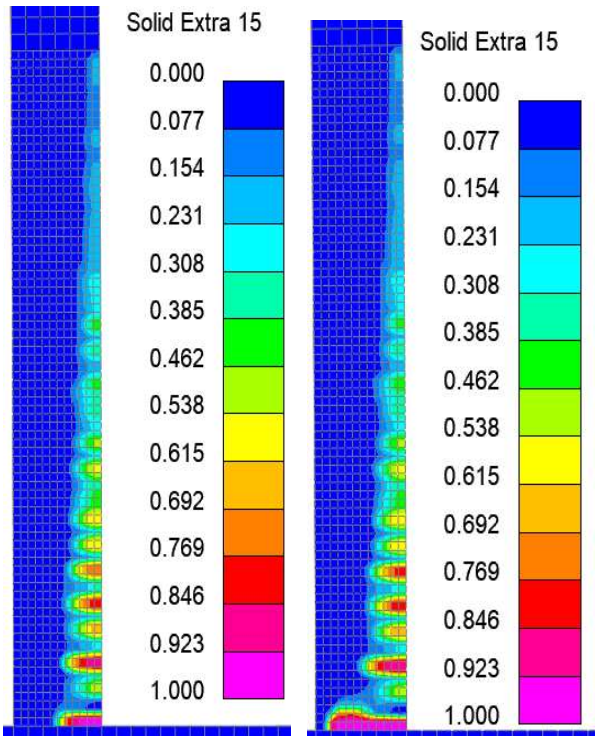

Figure A.111. Tensile Damage of W18_2_MB_C_1.0 at Peak Strength and 1% Drift

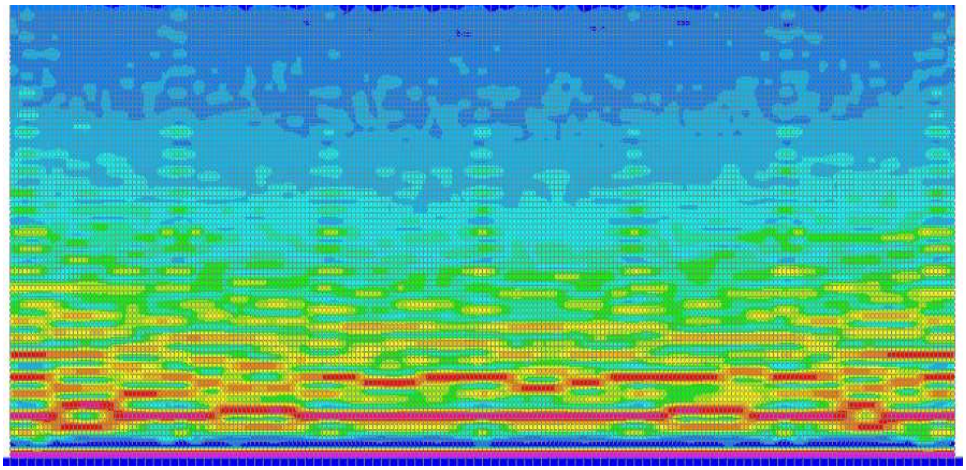

Figure A.112. Tensile Damage of W18_2_MB_C_1.0 at Peak Strength

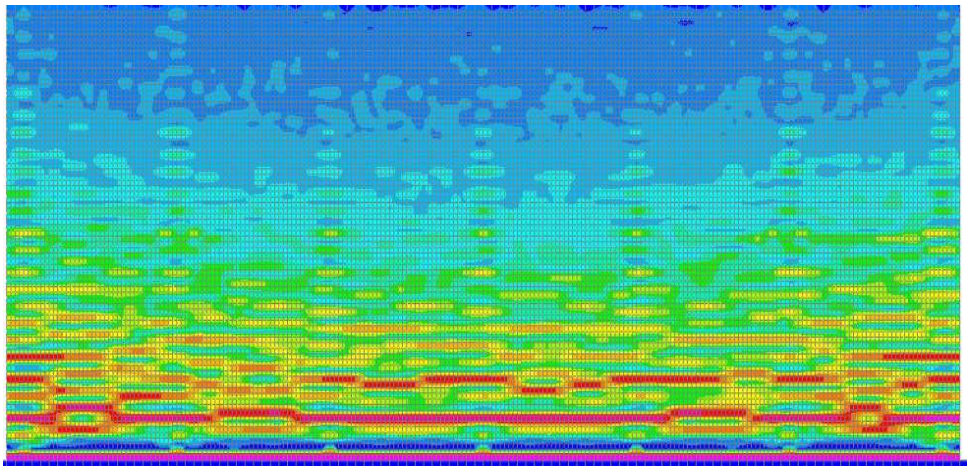

Figure A.113. Tensile Damage of W18_2_MB_C_1.0 at 1.0% Drift

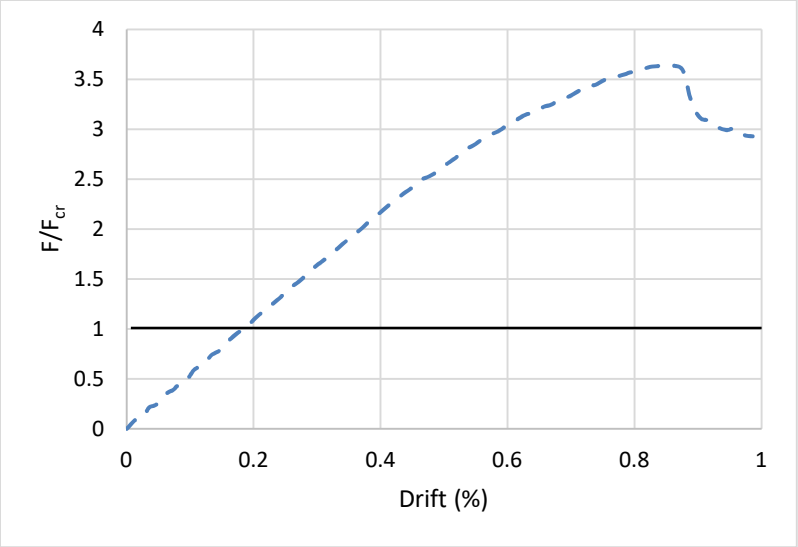

Figure A.114. Load Displacement History of W18_2_MB_C_1.5

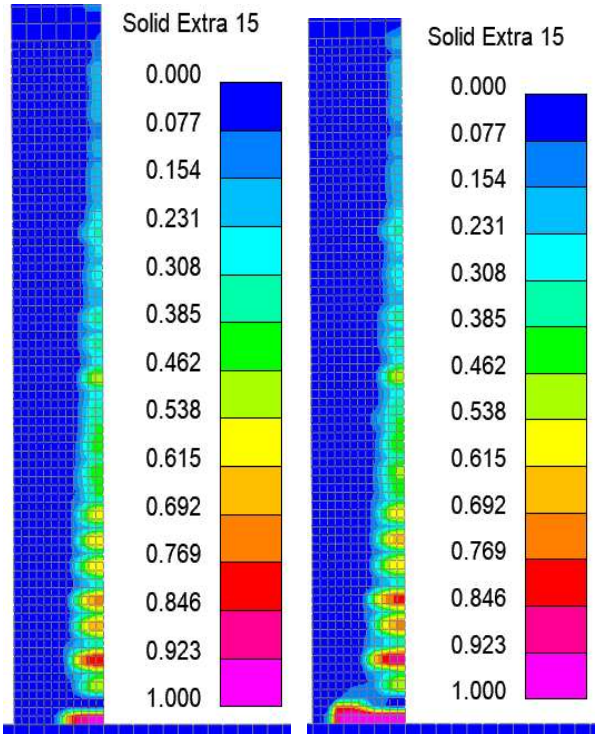

Figure A.115. Tensile Damage of W18_2_MB_C_1.5 at Peak Strength and 1% Drift

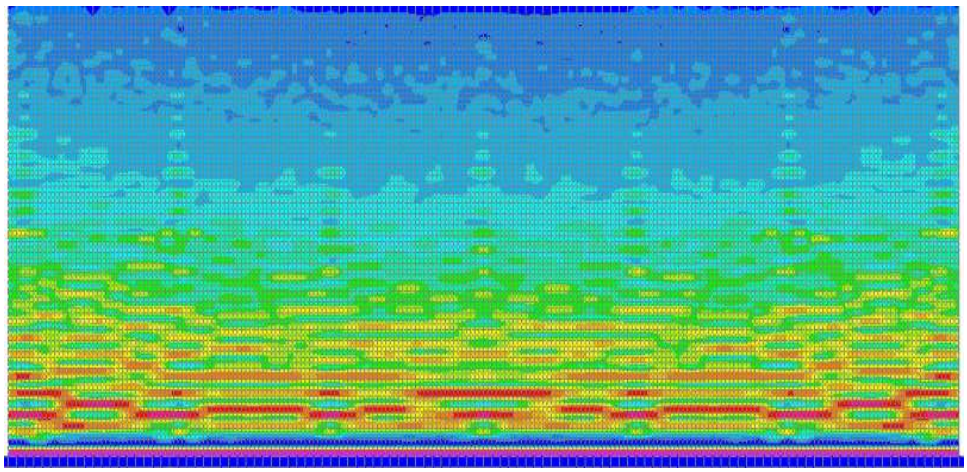

Figure A.116. Tensile Damage of W18_2_MB_C_1.5 at Peak Strength

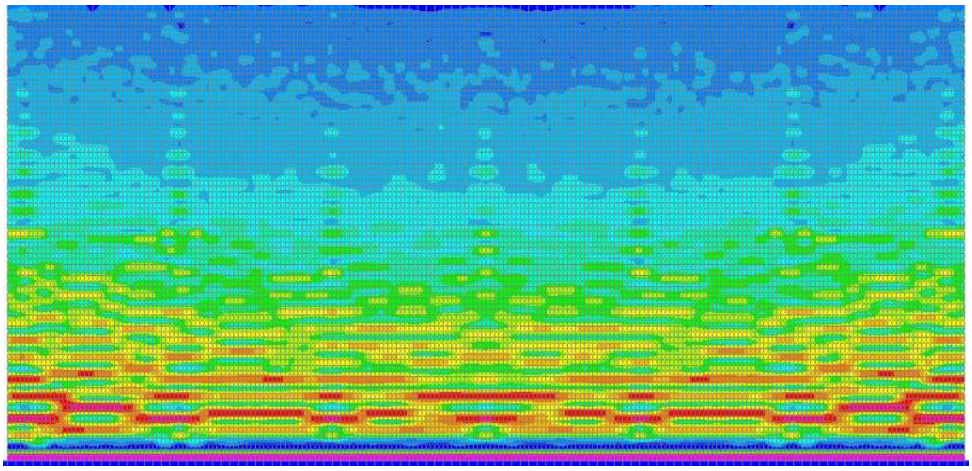

Figure A.117. Tensile Damage of W18_2_MB_C_1.5 at 1.0% Drift

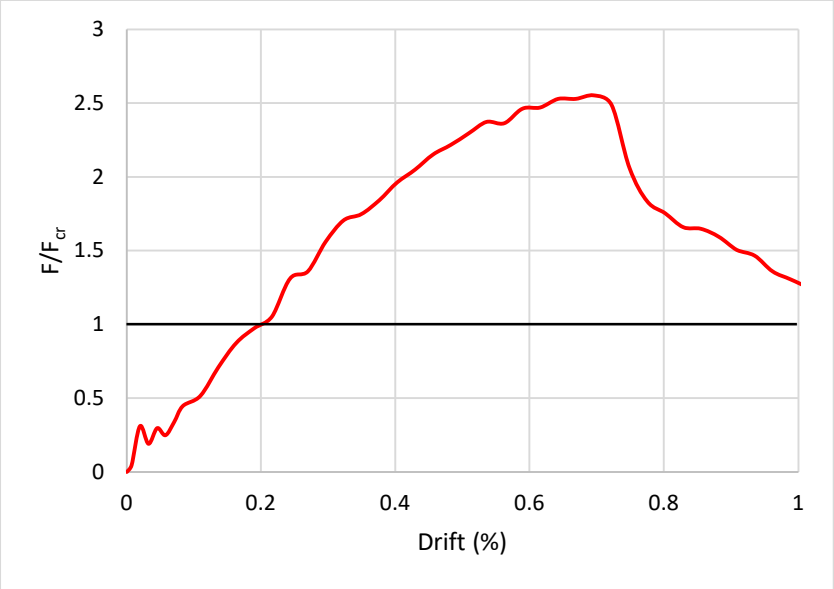

Figure A.118. Load Displacement History of W48_1_MB_C_0.5

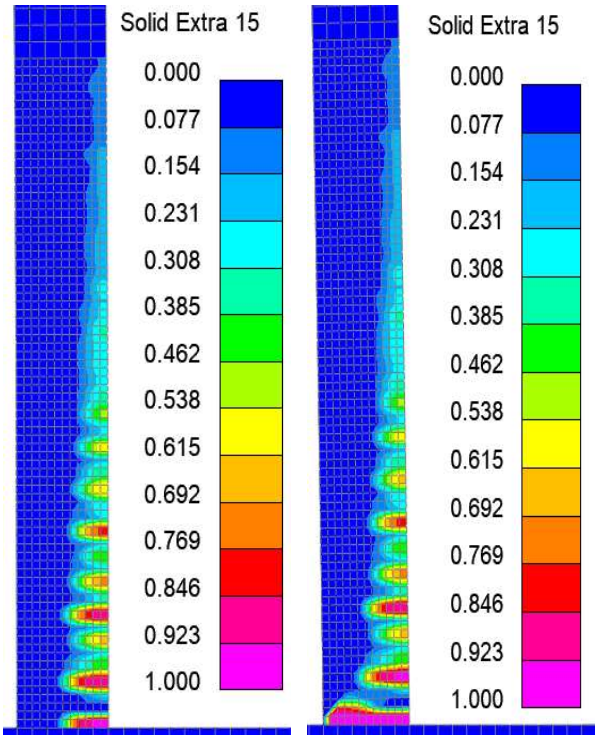

Figure A.119. Tensile Damage of W48_1_MB_C_0.5 at Peak Strength and 1% Drift

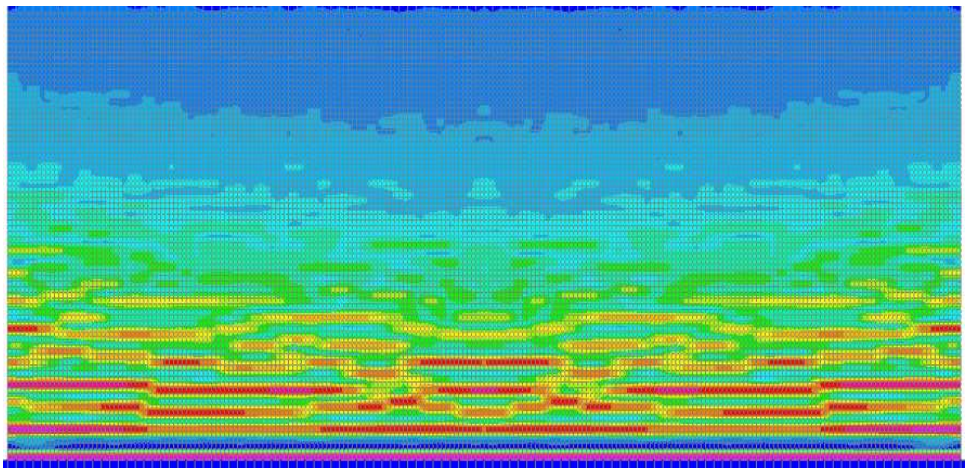

Figure A.120. Tensile Damage of W48_1_MB_C_0.5 at Peak Strength

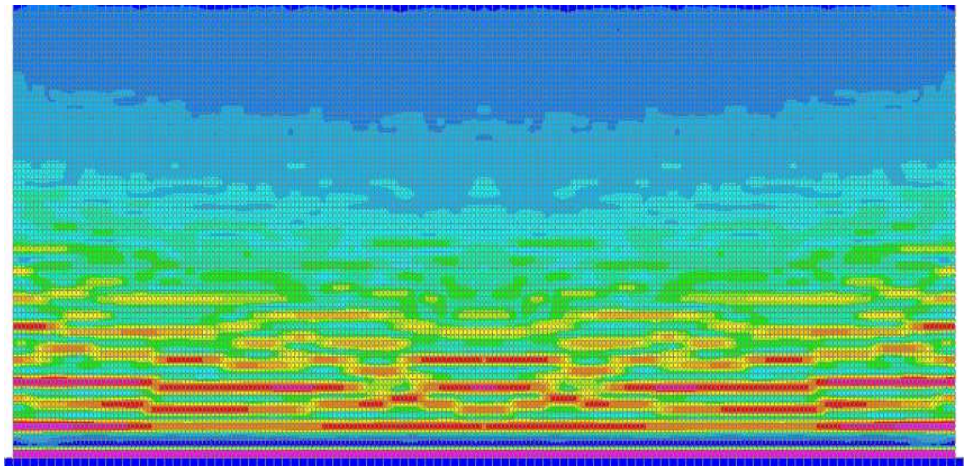

Figure A.121. Tensile Damage of W48_1_MB_C_0.5 at 1.0% Drift

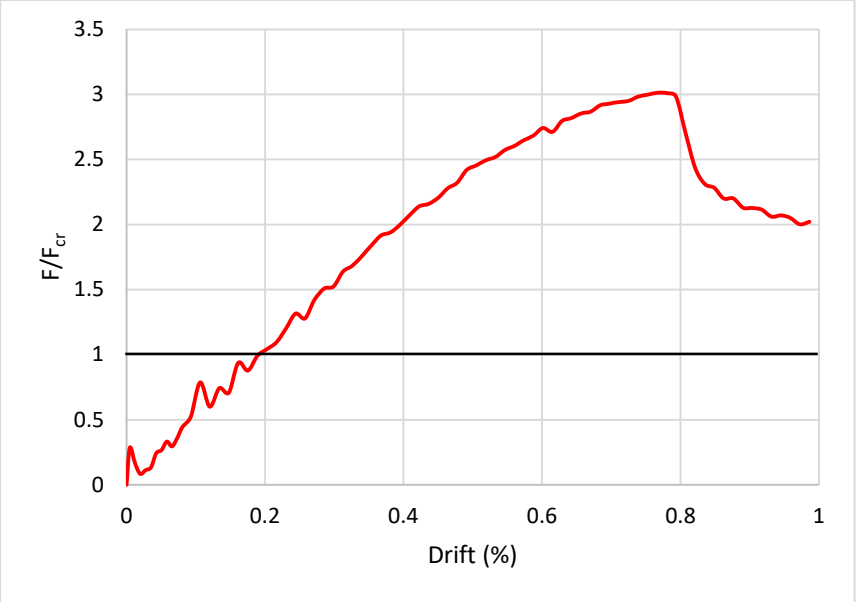

Figure A.122. Load Displacement History of W48_1_MB_C_1.0

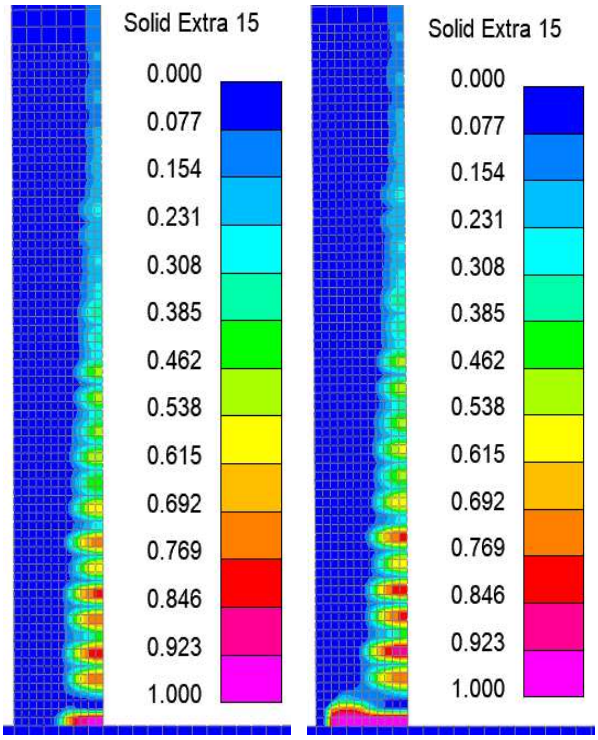

Figure A.123. Tensile Damage of W48_1_MB_C_1.0 at Peak Strength and 1% Drift

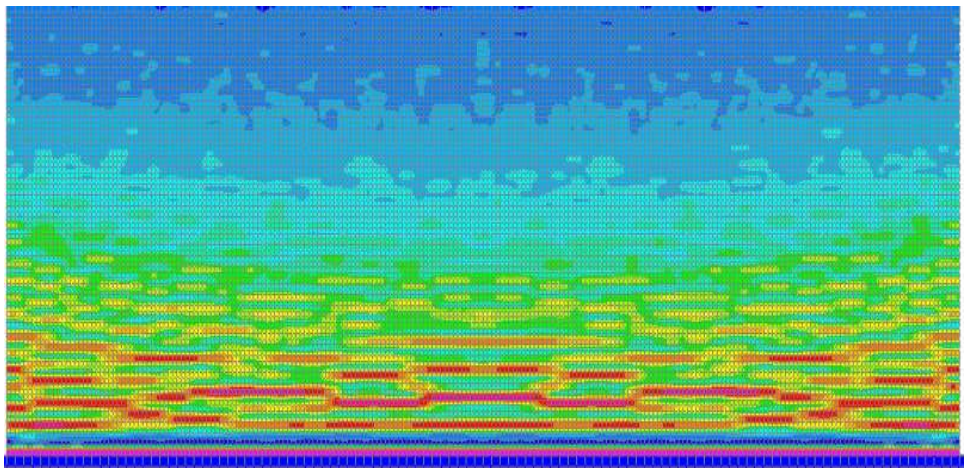

Figure A.124. Tensile Damage of W48_1_MB_C_1.0 at Peak Strength

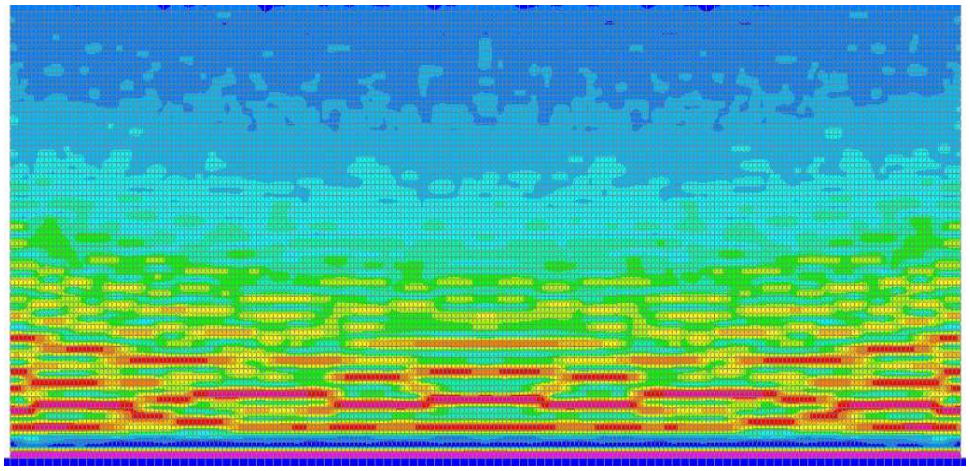

Figure A.125. Tensile Damage of W48_1_MB_C_1.0 at 1.0% Drift

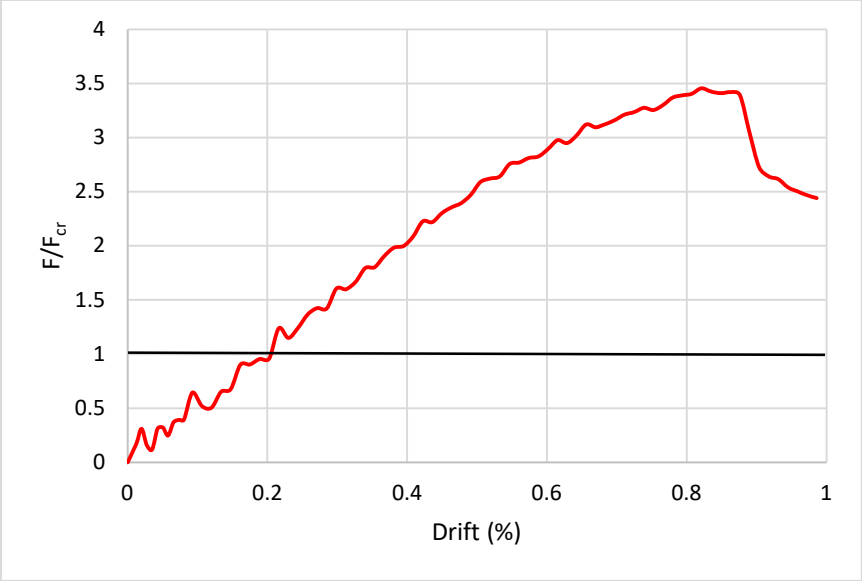

Figure A.126. Load Displacement History of W48_1_MB_C_1.5

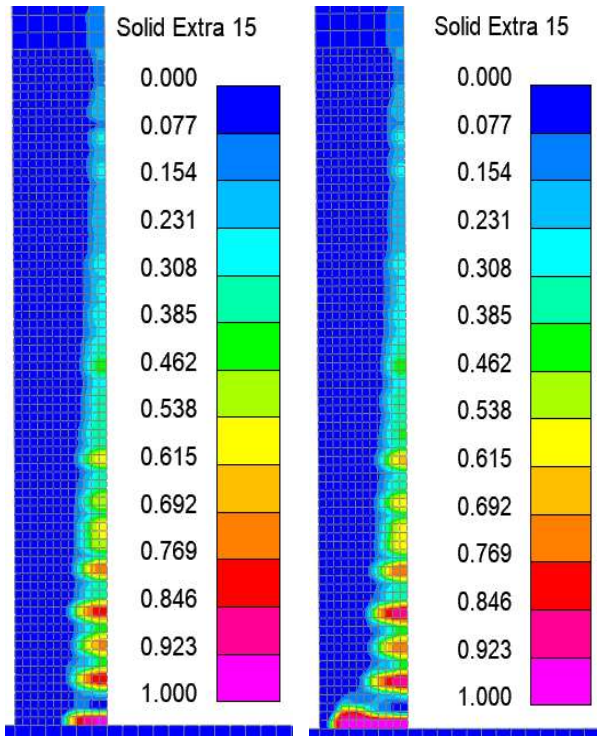

Figure A.127. Tensile Damage of W48_1_MB_C_1.5 at Peak Strength and 1% Drift

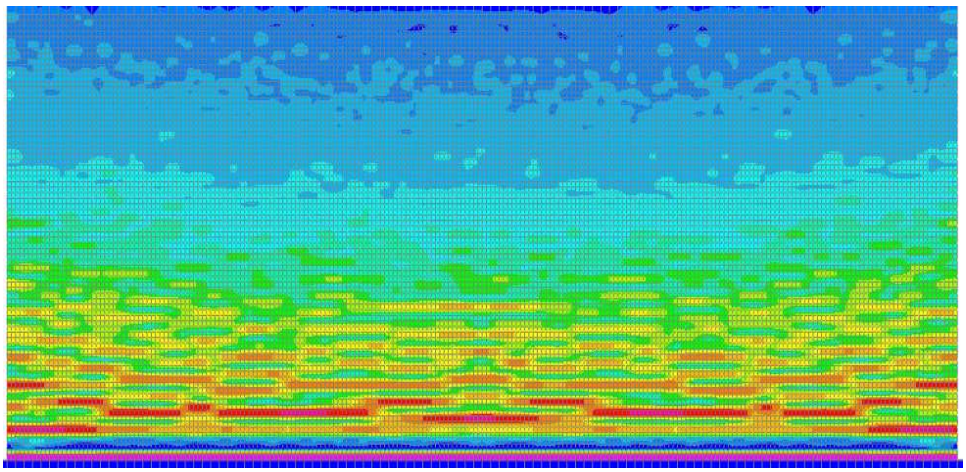

Figure A.128. Tensile Damage of W48_1_MB_C_1.5 at Peak Strength

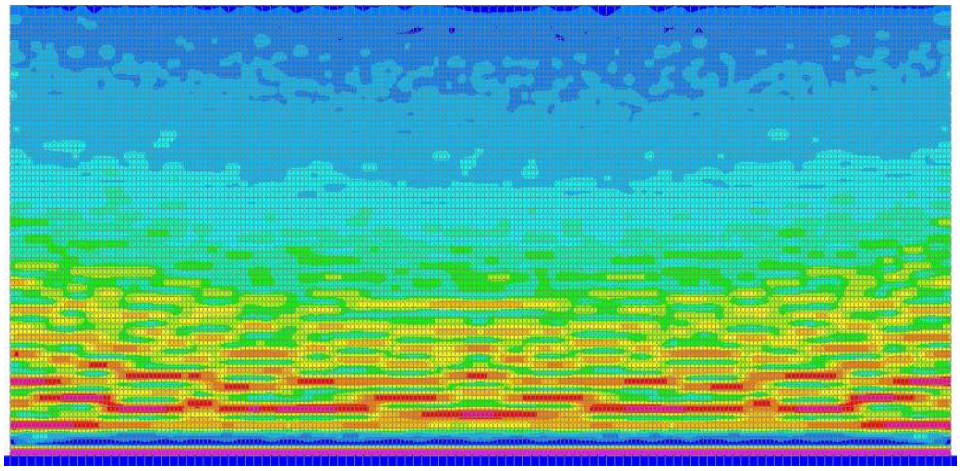

Figure A.129. Tensile Damage of W48_1_MB_C_1.5 at 1.0% Drift

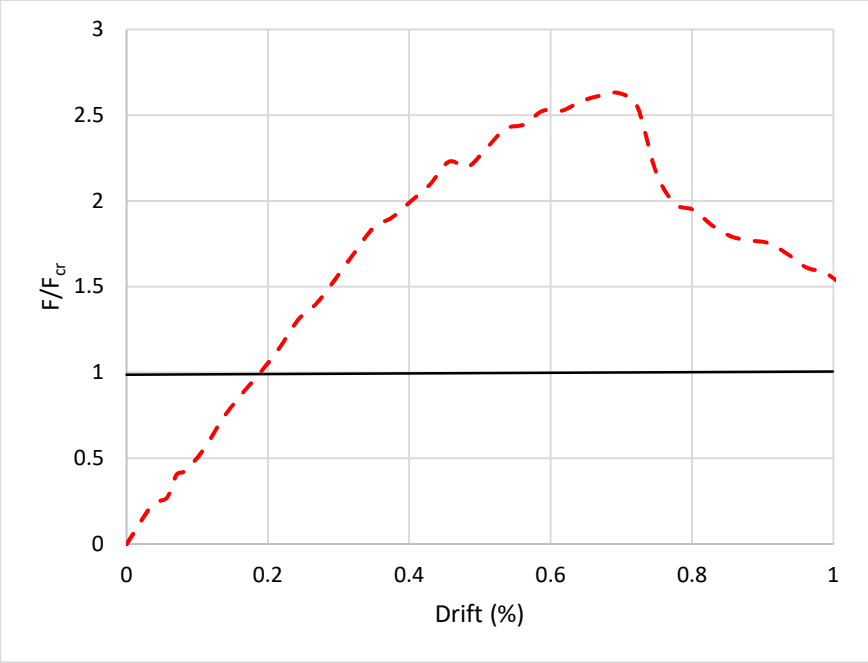

Figure A.130. Load Displacement History of W48_2_MB_C_0.5

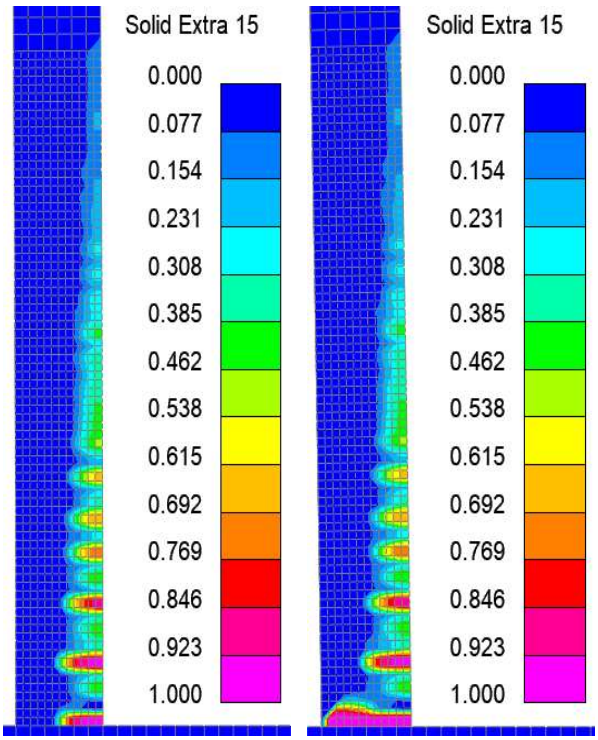

Figure A.131. Tensile Damage of W48_2_MB_C_0.5 at Peak Strength and 1% Drift

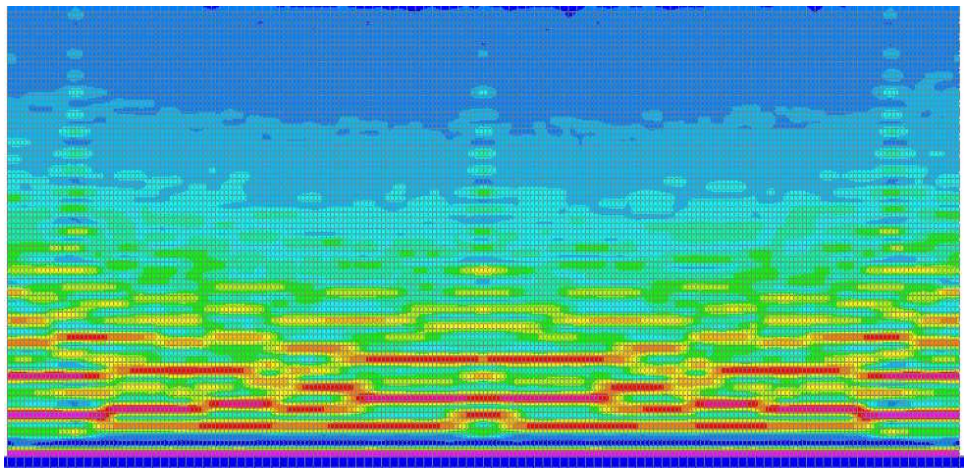

Figure A.132. Tensile Damage of W48_2_MB_C_0.5 at Peak Strength

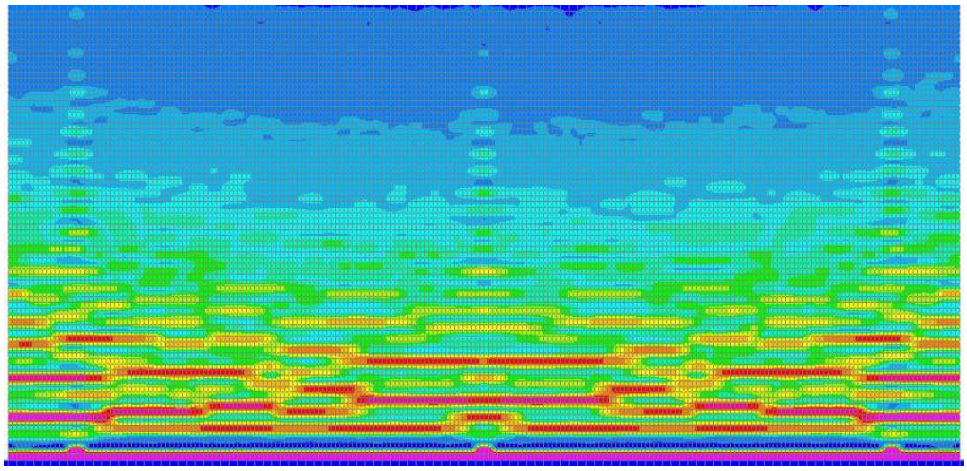

Figure A.133. Tensile Damage of W48_2_MB_C_0.5 at 1.0% Drift

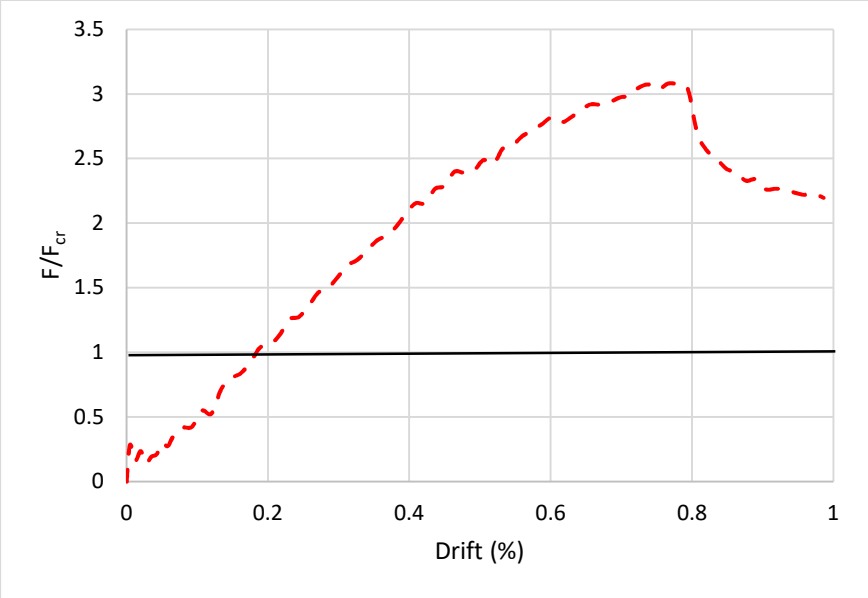

Figure A.134. Load Displacement History of W48_2_MB_C_1.0

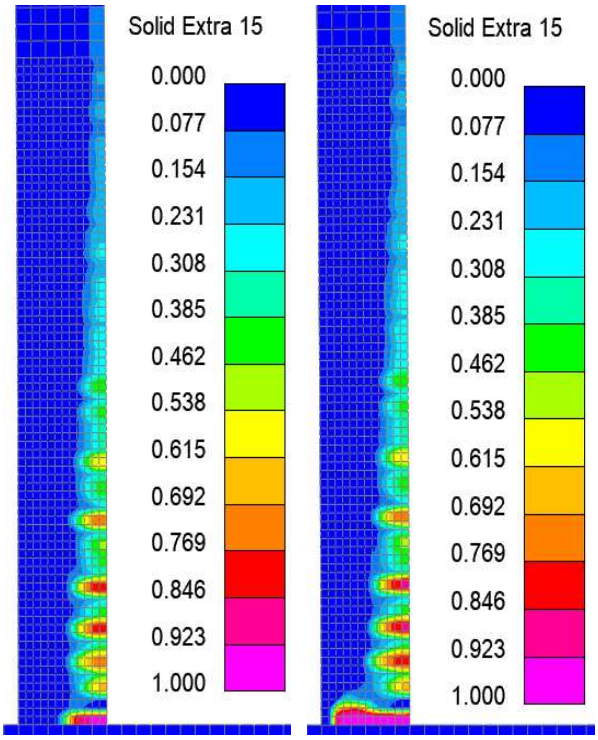

Figure A.135. Tensile Damage of W48_2_MB_C_1.0 at Peak Strength and 1% Drift

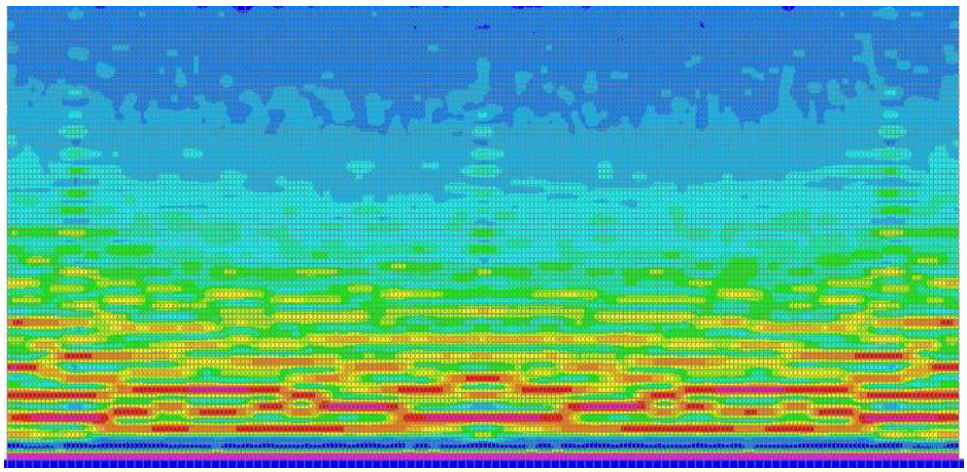

Figure A.136. Tensile Damage of W48_2_MB_C_1.0 at Peak Strength

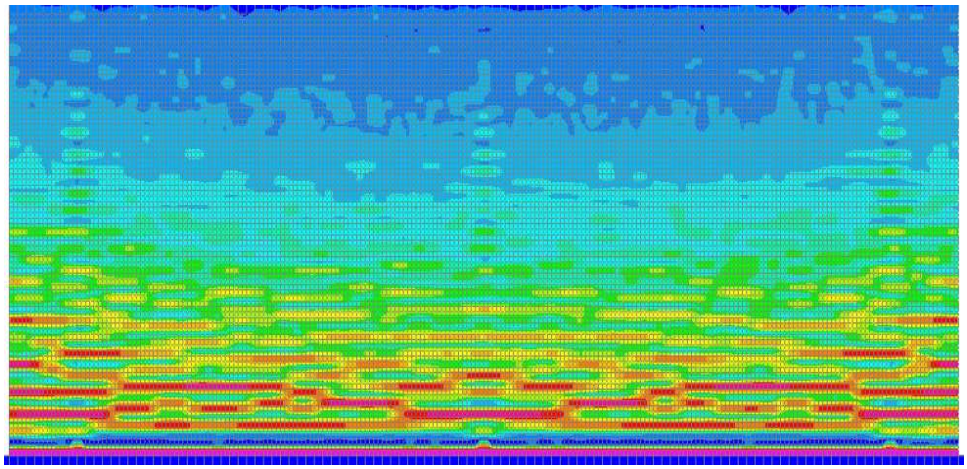

Figure A.137. Tensile Damage of W48_2_MB_C_1.0 at 1.0% Drift

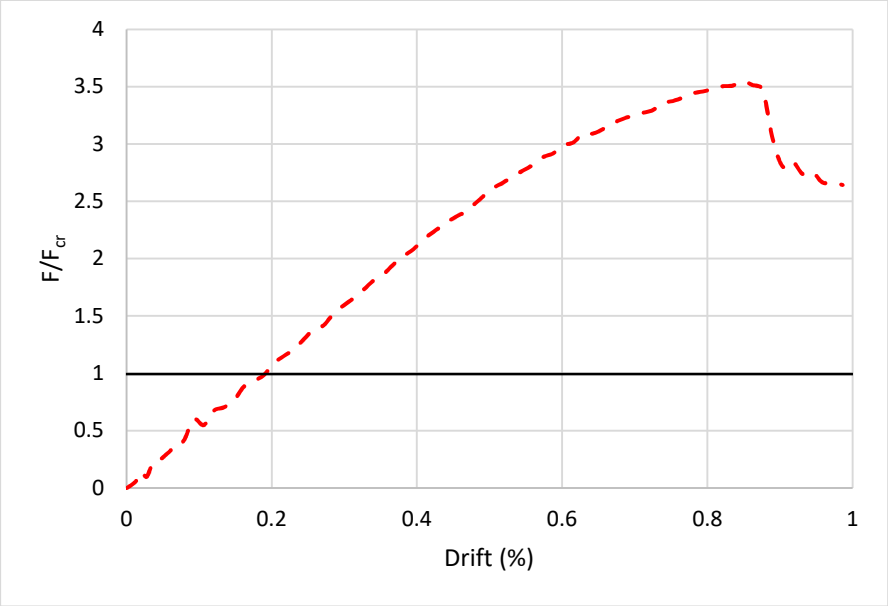

Figure A.138. Load Displacement History of W48_2_MB_C_1.5

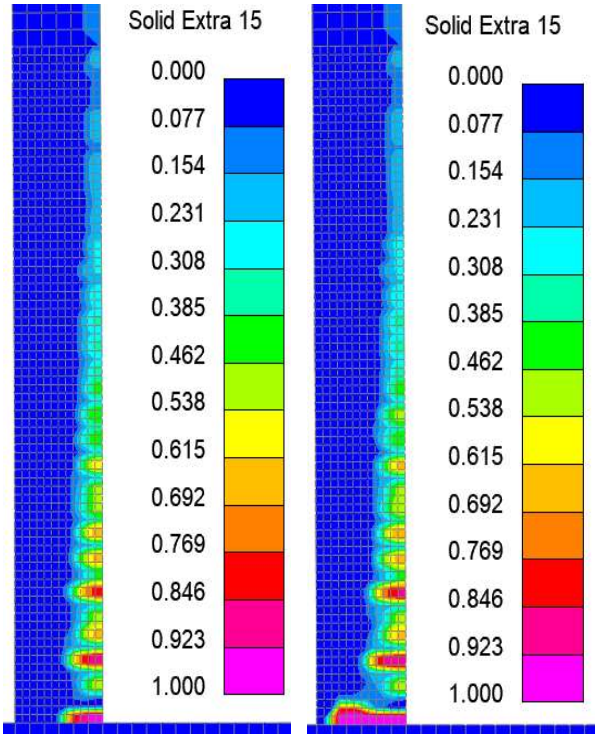

Figure A.139. Tensile Damage of W48_2_MB_C_1.5 at Peak Strength and 1% Drift

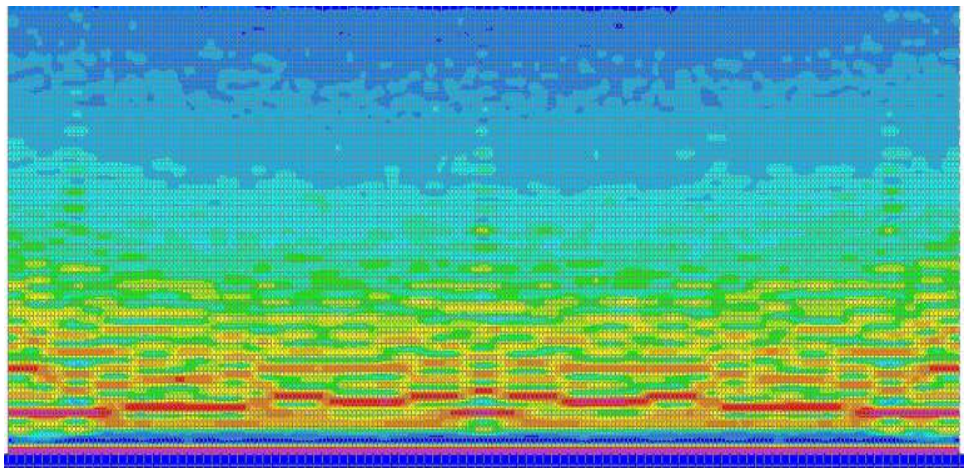

Figure A.140. Tensile Damage of W48_2_MB_C_1.5 at Peak Strength

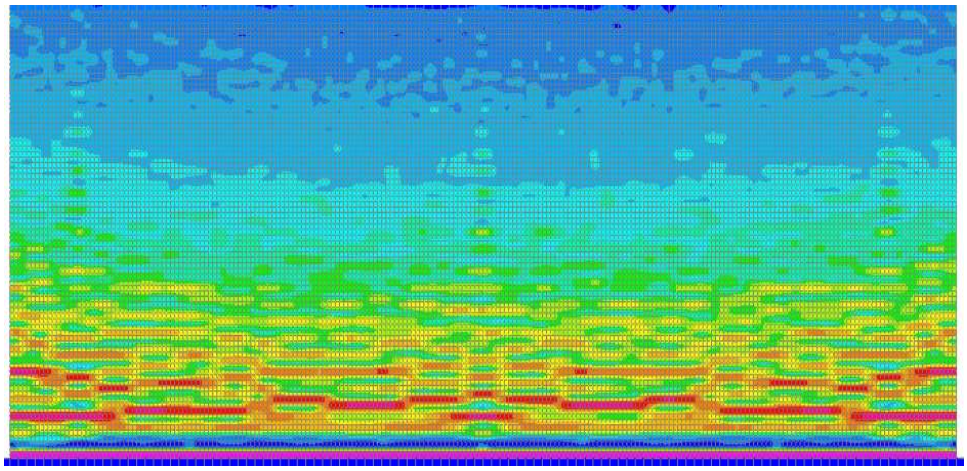

Figure A.141. Tensile Damage of W48_2_MB_C_1.5 at 1.0% Drift